Investigating the polar stratospheric vortex edge region using reanalysis and satellite tracer data

A thesis submitted in partial fulfilment of the requirements for the Degree of Doctor of Philosophy in Physics at the University of Canterbury by

Madeleine Lindsay Smith

Department of Physics and Astronomy
University of Canterbury, 2016

Abstract

Changes in the strength of the transport barrier at the edge of the stratospheric polar vortex can affect the rate at which air descends through the vortex, as well as the chemical composition of the stratosphere. We investigate methods for determining the strength of this barrier in the middle stratosphere using reanalysis data. Firstly, we develop two quantitative measures related to the strength of the barrier, which are based on a recently introduced method known as the function M derived using the path lengths of Lagrangian trajectories [de la Camara et al. 2012], and show that they are both potentially worthwhile at isentropic levels of 600-900 K. The first of these is a measure of vortex strength and permeability and the second is a measure of vortex barrier area. These measures are both calculated using an isentropic Lagrangian trajectory model based on wind velocity data from the MERRA reanalysis.

We also investigate the use of satellite data for identifying the location of the polar vortex by dividing measurements of CO and N_2O into clusters corresponding to intra- and extra-vortex air in tracer-tracer space using two different clustering schemes. This method is tested in the middle stratosphere at 700-1250 K against a potential-vorticity based method, and also against the CO probability distribution function (PDF) based method detailed in McDonald and Smith [2013]. By using different combinations of chemicals, such as CO/water, this method could be extended into the upper stratosphere, where reanalysis data becomes less reliable but chemical tracer data from satellites such as the Aura-MLS (Microwave Limb Sounder) is readily available. No clear evidence is found that this method identifies vortex air more accurately than the CO PDF-based method. However, it is shown that this method is particularly good at identifying air located outside the vortex.

Acknowledgements

I would like to thank my supervisor, Adrian McDonald, for his advice, guidance and encouragement, and for giving me the opportunity to study this important and interesting subject. I would also like to thank all those who have been members of the Atmospheric Physics group during the course of my PhD, including Nikolai Krützmann, Jack Coggins, Simon Parsons, Robert Ward, Ben Jolly, Fraser Dennison, Simon Fullick, Alexander Schuddeboom, Alex Paterson, Helena Sodergren, Ethan Dale, Andrew Ichoja, Ryan Ridden-Harper and Leon Friedrich, as well as Graeme Plank. They have all helped to create a pleasant and supportive environment to work in. I would also like to thank my fellow Physics postgraduate students more generally, including Mita Brierly, Douglas Walker, Rosa Hughes-Currie and Robert Doesburg.

In addition, I would like to thank my co-supervisors, Jenni Adams and Jack Baggaley, our Department's computer support people, Orlon Petterson and Timothy Delany, as well as Rosalie Reilly, Sharlene Wilson and Gill Evans.

Thanks to the Jet Propulsion Laboratory/NASA for providing the EOS MLS satellite data used in this research via their website, and also to the Global Modeling and Assimilation Office (GMAO) and the GES DISC for the MERRA reanalysis data. I am also grateful to the Royal Society of New Zealand for their financial support via the Marsden Fund.

Contents

List of Figures

List of Tables

Chapter 1

Introduction

The dynamics of the stratospheric winter hemisphere is dominated by a cyclonic vortex that forms each winter. The winds near the edge of this vortex are powerful enough to form an effective barrier to transport, isolating polar stratospheric air from air at lower latitudes. During winter, this isolated air descends through the vortex. These two factors both have a strong influence on the amount of air from higher-altitude regions which reaches the lower-middle stratosphere. This includes air from the mesosphere and lower thermosphere (MLT), which can contain reactive chemicals such as odd nitrogen (NO_x) that can break down ozone [Rinsland et al., 1996, Jackman et al., 2009].

The main aim of this research has been to investigate how vortex dynamics, and in particular how changes in the strength of the vortex edge barrier affect the rate of descent through the vortex. Changes in descent rate can potentially affect how much odd nitrogen produced by energetic particle precipitation (EPP-NO_x) reaches the lower stratosphere and therefore alters ozone concentrations there.

The relationship between the strength of the vortex edge transport barrier and the rate of descent through it is complex. The breaking of large-scale planetary waves in and near the polar stratosphere disrupts and weakens the polar vortex, and also drives the large-scale Brewer-Dobson stratospheric circulation that causes air to descend through the vortex. Therefore, in general, winter seasons in which the vortex is weaker than average are associated with stronger descent [Tegtmeier et al., 2008]. However, during major stratospheric sudden warming events (SSWs), when the vortex can be strongly distorted or break down entirely, the descent can be temporarily slowed or halted. This is due to the effects of planetary-wave breaking causing air to travel polewards at the altitude where the SSW occurs, leading to air above/below the SSW being pushed

upwards/downwards and thus cutting off the descent of air from above [Engel et al., 2006]. In summary, disruptions to the vortex are likely to lead to short-term reductions in descent rates, but also help drive changes in the large-scale circulation that lead to faster descent rates in the long term. After some major SSWs, a strong polar vortex can reform in the upper stratosphere within which rapid downwards transport can occur. This behaviour appears to be associated with SSWs during which the stratopause breaks down, with the temperature maximum at the top of the stratosphere disappearing [Manney et al., 2005b, 2008a, 2009b, Randall et al., 2009].

In order to find relationships between the strength of the vortex edge barrier and descent rate, it is important to find some way to measure them quantitatively. As the research progressed, a decision was made to focus on developing new methods for measuring the strength of the vortex edge transport barrier. In the lower-middle stratosphere, rates of diabatic heating/cooling are relatively slow, and it is possible to assume that the air parcels are travelling adiabatically over periods of a few weeks. In this way, it is possible to simplify most methods used to investigate transport and mixing by only looking at two-dimensional isentropic surfaces. Many of the more common methods used to investigate stratospheric transport barriers take a Lagrangian approach, tracing the trajectories of individual air parcels over time. A number of these methods are discussed in Chapter 2.2.2 of the literature review. The exploration of polar vortex dynamics began by running an isentropic parcel trajectory model which calculated trajectories using wind velocity data from the MERRA reanalysis [Rienecker et al., 2011], and using this to calculate finite-time Lyapunov exponents (FTLEs) on isentropic surfaces during the polar vortex winter seasons. FTLEs have been extensively used in the stratosphere as a measure of mixing and a method of identifying transport barriers [Bowman, 1993, Pierrehumbert and Yang, 1993, Garny et al., 2007, Beron-Vera et al., 2012]. However, it was found that, although the vortex edge transport barrier was observable in plots of Lyapunov exponents in the lower stratosphere, the results were affected by noise, and that at higher altitudes the vortex edge barrier was often not visible even when trajectories calculated using the parcel trajectory model clearly indicated the presence of a strong vortex.

We therefore investigated alternative methods that could be used to understand vortex dynamics both qualitatively and quantitatively, deciding upon a method known as the "function M". This method, which is based on the arc length of fluid parcel trajectories, was initially developed as part of research into dynamical systems [Jimenez Madrid and Mancho, 2009] and then applied to the

study of ocean dynamics [Mendoza and Mancho, 2010, 2012]. It was then introduced into the field of stratospheric polar dynamics by de la Camara et al. [2012]. The value of the function M at a given location x and time t_0 is the arc length of a fluid parcel trajectory calculated over a time period centred on t_0, where x is the parcel's location at time t_0.

The function M can be used to produce detailed maps of the stratospheric polar vortex, identifying not only the zone of strong winds near the vortex edge, but also nearby anticyclones as well as specific locations where air is entering or leaving the vortex. Two quantitative measures of vortex dynamics based on the function M were developed and tested. The first of these is based on the average value of M near the edge of the vortex and captures information about the strength of the vortex edge barrier. The second is a function M-based measure of vortex area. It was found that the area-based measure was useful for identifying SSWs within the test periods, and that the measure based on the average value of M near the vortex edge provided complementary information on the strength of the edge barrier. These measures are discussed in Chapter 3, which is an unformatted version of the paper Smith and McDonald [2014], published in the Journal of Geophysical Research - Atmospheres.

Using measures based on the function M, we were able to investigate vortex dynamics at potential temperature levels up to 900 K (in the middle stratosphere, corresponding to an approximate altitude of 31 km).

However, above this level, two different issues mean that this technique becomes less reliable. Firstly, it becomes more difficult to identify the location of the vortex edge at higher altitudes. The methods most commonly used to do this in the lower-middle stratosphere are based on potential vorticity (PV), since the vortex edge transport barrier is generally associated with a sharp gradient of PV as a function of equivalent latitude (an alternative latitude coordinate usually obtained from PV information). At higher altitudes, the position of the vortex edge becomes more difficult to determine in this way. Rather than there being a sharp boundary at the edge of the vortex associated with large PV gradients, there often appear to be two or more regions where PV values change rapidly, and no clear way of identifying which one corresponds to the true vortex edge [Manney et al., 2007]. Higher rates of filamentation from the vortex at higher altitudes also mean that it becomes more difficult to locate the vortex edge [Mitchell et al., 2010]. Above altitudes of approximately 50 km, it is no longer possible to obtain the vortex edge location using these methods because PV-based equivalent latitude is no longer a useful alternative latitude coordinate [Harvey et al., 2009]. One of the

function M-based measures of vortex barrier strength introduced in Chapter 3 (the measure based on the average value of M near the edge of the vortex), relies on a PV-based equivalent latitude method to identify the location of the vortex edge, and is thus affected by this issue. More generally, uncertainty about the location of the vortex edge will cause difficulties with many methodologies for investigating the strength of the transport barrier at that edge.

Secondly, the reanalysis wind data upon which the function M-based measures are based starts to become less reliable, as discussed in Chapter 2.3.1. However, measurements of tracer concentrations are readily available above this altitude, although their resolution is usually poorer than that available from reanalysis data at lower altitudes. Therefore, when investigating vortex dynamics in the middle-upper stratosphere, tracer-based methods are likely to be more effective than methods based on wind data from reanalyses. Chapter 2.4 contains a review of these methods. Many of these methods are based on probability distribution functions (PDFs) of measured tracer concentrations. When such a PDF is calculated over an area containing two regions with different mean tracer concentrations, it can then be used to identify which measurements were taken in which region. The spatial extent of each of the regions can then be identified based on the geographical location of each measurement. McDonald and Smith [2013] used PDFs of CO concentrations in this way to identify intra- and extra-vortex air.

In light of these issues, in the next stage of the research project, methods for locating the vortex edge using tracer mixing ratios from satellite data were investigated. Chapter 4 describes two closely related methods for identifying intra- and extra-vortex air by sorting measurements into clusters based on observed mixing ratios of carbon monoxide (CO) and nitrous oxide (N_2O).

During the polar winter, air with high concentrations of CO descends through the polar vortex, while mixing ratios are lower outside the vortex. CO is a good tracer in the stratosphere and mesosphere, and is commonly used for studies in which the descent rate of air in the upper stratosphere and mesosphere is measured. Most of the nitrous oxide within the lower-middle stratosphere has entered it through the tropical troposphere after being produced at the Earth's surface. Therefore within this region of the atmosphere concentrations of N_2O are lower inside the polar vortex than at lower latitudes. This means that at any given isentropic level, if the vortex edge barrier is reasonably wide, its location as determined using nitrous oxide is likely to be different from that found using CO data, and that determining the vortex edge position based on both tracers

may help in determining the true vortex edge location more reliably.

The methodology described in Chapter 4 was used to identify intra- and extra-vortex air at the 700, 900 and 1250 K isentropic levels in the mid-stratosphere. These levels and their corresponding approximate altitudes were chosen because they are the highest altitudes at which our clustering methods can be validated by comparing them with the vortex edge obtained using standard PV-based methods. These levels also correspond to the altitude range over which the concentrations of CO and N_2O are such that both are simultaneously useful for identifying vortex air without information derived from measurements of one tracer overwhelming results from the other. Above 1250 K (which corresponds to an approximate altitude of 40 km), the N_2O results can also be affected at some times by the descent from higher altitudes of N_2O produced as a result of energetic particle precipitation (EPP), reducing the effectiveness of N_2O as a tracer [Sheese et al., 2016].

It is hoped that by using other combinations of tracers, such as CO vs water vapour (H_2O), it will be possible to extend this methodology so that it can be used to identify intra- and extra-vortex air in the upper stratosphere where reanalysis-based methods are unreliable. Although further work needs to be done to improve the methods described in Chapter 4, this approach is a promising way to locate the position of the vortex edge barrier.

Chapter 2 of this thesis is a literature review which includes information relevant to the research carried out in Chapters 3 and 4. Chapter 3 describes research in which the use of the "function M" as a means to understand polar vortex dynamics is investigated. It includes a description of two quantitative measures related to the strength of the vortex edge barrier and the area occupied by it. This chapter is based on an unformatted manuscript version of the paper Smith and McDonald [2014], which was published in the Journal of Geophysical Research - Atmospheres (JGRA). This is very similar textually to the version submitted to JGRA immediately before final editing, but a few alterations to it have been made since, mostly in response to examiner's comments. Chapter 4 contains research on the use of satellite tracer data for locating the stratospheric polar vortex and its edge, including two closely related clustering algorithms that can be used to identify intra- and extra-vortex air. Chapter 5 describes our conclusions, as well as possible avenues for further research.

Chapter 2

Literature review

The main aim of the research contained in this thesis is to develop new methods for locating the barrier at the edge of the polar vortex and measuring changes in its permeability. If the permeability of the vortex edge barrier can be measured as a function of time throughout the stratosphere and mesosphere, then this will make it easier to understand how changes in vortex edge barrier strength affect the rate at which high-altitude air descends through the vortex and the quantity of it which reaches the stratosphere.

This review starts with a basic description of the stratosphere, followed by a discussion of the large-scale circulation in the stratosphere and mesosphere that drives descent through the polar vortices. Then stratospheric sudden warmings (SSWs), the most dramatic dynamical events in the stratosphere, are introduced. These events have a large impact upon the vortex edge barrier and a major goal of any method for measuring vortex barrier permeability will be to clearly identify them. Next, the energetic particle precipitation indirect effect (EPP IE) is discussed, since the amount of ozone-destroying chemicals that reach the lower-middle stratosphere changes depending on polar vortex dynamics.

Then methods that have been used to investigate polar vortex dynamics using data from reanalyses are reviewed. This includes the function M, which the research in Chapter 3 uses. However, as is then discussed, above the middle stratosphere reliable reanalysis data become more difficult to obtain. However, satellite observations of chemical concentrations are readily available at higher altitudes. Therefore methods for locating the extent of the vortex using chemical tracer measurements are discussed. This includes the research that will be discussed in more detail in Chapter 4.

2.1 The stratosphere

The Earth's atmosphere can be viewed as being divided into several different layers based on temperature gradient. The troposphere is the lowest layer; its circulation is dominated by large cells, within which heat is transported polewards from the tropics [Lynch and Cassano, 2006]. The layer immediately above the troposphere is the stratosphere. The transition between these layers, known as the "tropopause", is at the upper boundary of the tropospheric convection cells and is thus higher in the tropics, where the convection is stronger. It varies in altitude between about 8 km near the poles and 18 km near the equator [Shepherd, 2000]. The upper boundary of the stratosphere, referred to as the "stratopause", is at an altitude of approximately 40-50 km but can vary in response to dynamical events, particularly in the winter polar regions [Smith, 2012]. Above this, the next layer of the atmosphere is the mesosphere, followed by the thermosphere. Within the troposphere, the temperature drops with altitude, but in the stratosphere it increases with altitude, reaching a maximum at the stratopause before dropping again in the mesosphere. Figure 2.1 shows a global annual mean temperature profile based on data from the COSPAR International Reference Atmosphere (CIRA) data set, which displays the typical temperature structure of all layers of the Earth's atmosphere below an altitude of 120 km.

The stratosphere contains high concentrations of ozone (O_3), produced by the photodissociation of molecular oxygen (O_2) by ultraviolet (UV) light. This ozone then absorbs most radiation within the UV part of the spectrum and reradiates it as infrared radiation. The highest density of ozone occurs in the lower stratosphere. However, the overall density of the atmosphere declines exponentially with altitude, and the altitude where the proportion of ozone as a fraction of the molecules in the atmosphere is greatest is at approximately the altitude of the stratopause. Therefore, the heating due to ozone has its maximum effect upon air temperature at this altitude, causing the temperature maximum there. At each altitude, the heating rate due to absorption of UV light by ozone depends on the density of ozone and the flux of UV light at that level. The range of altitudes where this heating rate is highest is often referred to as the "Chapman layer" [Andrews, 2010, Solomon, 2010].

The majority of air entering the stratosphere arrives from the tropical troposphere. As air from this region rises, it cools and dehydrates since the maximum amount of water vapour that the air can hold decreases. At the tropical tropopause, temperatures are so low that most of the remaining water freezes

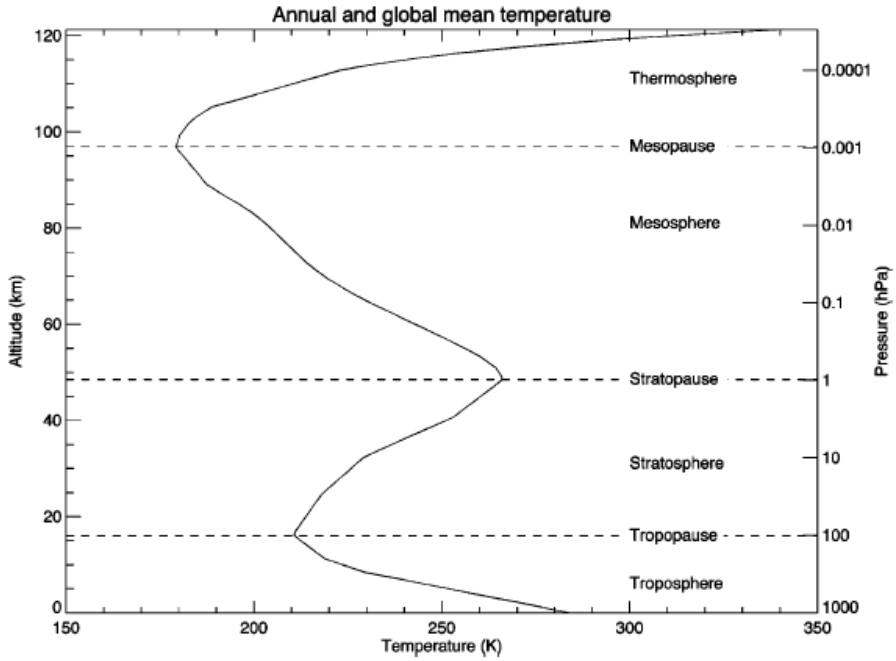

Figure 2.1: Global annual mean temperature profile from the COSPAR International Reference Atmosphere (CIRA) data set (figure taken from Shepherd [2003], which references Fleming et al. [1990]).

out [Andrews et al., 1987]. Due to this, the stratosphere is much drier than the troposphere.

Within the atmosphere, the rate at which temperature decreases with altitude is referred to as the lapse rate Γ. If a dry air parcel is disturbed adiabatically upwards from its original position, then it will expand and cool according to the dry adiabatic lapse rate of $\Gamma_d = 9.8\ K/km$. If $\Gamma < \Gamma_d$, then the temperature inside the displaced parcel will be cooler than the outside air, and the atmosphere is referred to as being statically stable. In order to maintain the same pressure as the surrounding air, the cooler air inside the parcel must be denser than the air outside. Gravity then pulls this heavier air downwards, acting as a restoring force. Similarly, if the parcel is displaced downwards, a restoring force due to gravity will cause it to rise again. This means that if parcels of air are vertically displaced, e.g. as they flow over a mountain range, this restoring force can set off atmospheric waves, referred to as gravity waves, that cause the parcels to oscillate vertically and which can potentially travel over large distances. Areas where $\Gamma > \Gamma_d$ are unstable are generally associated with convection. In the stratosphere, the lapse rate Γ is negative, meaning that it is a very stable area.

This causes vertical transport in the stratosphere to be relatively slow and its structure to be stratified into layers.

In order to understand vertical transport within the atmosphere, it is important to understand the concept of potential temperature. The stratosphere is dry enough so that the effect of moisture can be neglected when calculating this. The dry potential temperature of an air parcel is the temperature that it would have if it were adiabatically (without any exchange of heat energy between itself and its surroundings) brought down to a reference pressure level (usually 1000 mb is chosen since this is the approximate pressure at ground level). It can be described by the equation:

$$\theta = T\left(\frac{p_0}{p}\right)^{\frac{c_p - c_v}{c_p}},$$

where T is the physical temperature of the air parcel, p is the pressure experienced by the parcel, and p_0 is the reference pressure level. c_p and c_v are the specific heat capacity of dry air at constant pressure and at constant volume, respectively. Potential temperature is important because it allows changes in air temperature due to vertical displacement of air parcels to be separated from changes due to heat energy actually entering or leaving the air parcel. If an air parcel is displaced vertically without exchange of energy with its environment then its physical temperature will change but its potential temperature will not; the potential temperature of dry air will only change if an outside influence causes it to be heated or cooled.

Weather events in the troposphere can produce waves which propagate upwards and affect the stratosphere. As such waves travel upwards, the refractive index experienced by them at each altitude level depends on the difference between the zonal phase velocity c of the wave and the zonal mean wind velocity $\underline{u}$ of the surrounding air. If $\underline{u} - c < 0$ or $> U_c$, where U_c is a critical velocity depending on the horizontal scale of the wave, then the refractive index becomes imaginary and the wave experiences partial or total reflection [Charney and Drazin, 1961, McDonald et al., 2011]. A wave with a negligible zonal phase velocity can then propagate through a region of westerly winds, if their zonal velocity is not too large, but not through a region of easterly winds. The critical velocity U_c is largest for waves with very long wavelengths, such as Rossby or planetary waves; this means that the range of phase velocities that can propagate into the stratosphere is larger for these waves and that more of them reach the stratosphere [Plumb, 2010]. When the amplitudes of these waves become large, they can break. This

often occurs within a region of the stratosphere called the "surf zone" [McIntyre and Palmer, 1983, Plumb, 2002], where the background zonal winds favour the propagation of planetary waves according to the conditions discussed above [Holton, 1992]. The surf zone covers a wide region of the winter hemisphere mid-latitudes. It is bounded on one side by the tropical stratosphere, and on the other by the polar vortex. The stratosphere is then divided into four different dynamically distinct areas, the summer hemisphere, the tropical stratosphere, the surf zone, and the polar vortex [Plumb, 2002].

Within the stratosphere, transport along lines of latitude (zonal transport) is rapid, with air parcels circling the globe within days or weeks. However, transport along lines of longitude (meridional transport) is much slower. This is because, in order for air to move meridionally, it must gain or lose angular momentum. Air within the atmosphere has angular momentum due to the Earth's rotation, with air near the equator having the most.

When waves break and dissipate in the surf zone, this causes a transfer of momentum to the surrounding air that helps drive the overall circulation of air in the stratosphere. In the lower stratosphere, air rises from the tropical troposphere, travels polewards, and then returns to the troposphere at higher latitudes in both hemispheres, while in the middle-upper stratosphere the air only travels polewards and sinks in the winter hemisphere [Smith, 2012, Butchart, 2014]. In the lower stratosphere, some breaking and stirring due to synoptic waves takes place in both hemispheres, while in the mid-upper stratosphere wave-breaking is dominated by large waves in the surf zone of the winter hemisphere. It takes on the order of a decade for air to undergo this cycle. This is known as the Brewer-Dobson circulation [Brewer, 1949, Dobson, 1956, Dunkerton, 1978, Holton et al., 1995, Butchart, 2014, Cohen et al., 2014]. The Brewer-Dobson circulation is stronger during the Northern Hemisphere winter than in the Southern Hemisphere since more wave breaking in the surf zone occurs to drive it. This is because the topography in the Northern Hemisphere is more varied; it has large mountain ranges that disturb passing air upwards, giving rise to planetary waves, as well as large continents whose temperature differences with surrounding oceans can also cause them.

The strong mixing in the surf zone does not appear to extend into the subtropics; there is considerable evidence that there is a mixing barrier between the surf zone and the subtropical region, and also a barrier at the edge of the subtropics in the summer hemisphere [Neu et al., 2003]. This region is sometimes referred to as the "tropical pipe" [Plumb, 1996].

2.2 The stratospheric polar vortices

2.2.1 Dynamics of the polar vortices

In the Earth's polar regions, air rotates rapidly around the poles, creating the winter stratospheric polar vortex. The strong westerly winds at the edge of the polar vortex form a transport barrier separating intra and extra-vortex air. The Brewer-Dobson circulation causes air to descend through the polar vortex.

The winter stratospheric polar vortex also extends into the mesosphere. In the mesosphere, air rises from the summer pole and moves horizontally to the winter pole, where it sinks [Smith, 2012]. This circulation is caused by the propagation of gravity waves upwards from the troposphere. If the phase velocity of a gravity wave matches the mean velocity of the air it is propagating through, then it cannot propagate any further. Therefore upwards-travelling gravity waves are partially blocked from propagating through the stratosphere, depending on their phase velocities. In the winter hemisphere, the prevailing westerly winds associated with the polar vortex block eastward-travelling gravity waves, while in the summer hemisphere westwards gravity waves are blocked by easterlies. Since meridional transport in the stratosphere is slow, meridionally-propagating gravity waves (travelling north or south) are less affected. When the gravity waves that make it through the stratosphere finally do break higher up in the mesosphere, the differences in their directions of propagation between hemispheres drives the circulation in the mesosphere [Smith, 2012]. These breaking waves induce a westward force in the winter hemisphere and an eastward force in the summer hemisphere, which both cause the mean circulation to flow towards the winter pole [Plumb et al., 2002]. The local temperature maximum constituting the winter polar stratopause is produced by adiabatic heating as air sinks near the pole, driven by this circulation [Hitchman et al., 1989]. In general, descent through the polar vortices is driven by a combination of forcing from planetary waves breaking in the stratospheric surf zone, and gravity wave breaking driving descent from the mesosphere.

A large amount of mesospheric air has been observed to descend into the stratosphere via the polar vortex every winter. Russell et al. [1993] observed methane concentrations in the middle stratospheric polar vortex during October 1991 that were as low as those typically observed in the mesosphere, using the HALOE instrument on the UARS satellite. Fisher and O'Neill [1993] followed up on this research by using a simulation to model the trajectories of air parcels ini-

tialized in the mesosphere to observe their descent. They observed a "systematic poleward and downward drift of air from the mesosphere into the polar vortex in the stratosphere". The poleward transport in the mesosphere was rapid and the rate of descent in the upper stratosphere was approximated to be about 12 km per month. Polewards and downwards transport still took place lower down in the stratosphere, but at a slower rate. They found that mesospheric air reached the mid stratosphere after only a few months. Randel et al. [1998] also observed air low in methane descending within the lower stratosphere based on data from the HALOE instrument onboard the UARS satellite.

There are two major types of methods that have been used to investigate the rate of descent through the polar vortices [Tegtmeier et al., 2008]. The first is to use radiative transfer models to calculate rates of diabatic descent [Rosenfield et al., 1994, Manney et al., 1994b, Tegtmeier et al., 2008], and the second is to use tracer measurements to observe the rate of descent [Randel et al., 1998, Greenblatt et al., 2002b, Filipiak et al., 2005, Engel et al., 2006]. The rates of descent are commonly expressed in terms of a rate of change in potential temperature, because in the stratosphere, descent of air parcels over a period of time is always associated with the air parcels losing heat diabatically. Applying a radiative transfer model to obtain descent rates in these circumstances requires detailed information about temperatures, as well as about the concentrations of gases such as water vapour, ozone, carbon monoxide and CFCs [Tegtmeier et al., 2008]. A common tracer-based method used to determine rates of descent is to plot measured tracer volume mixing ratios (VMRs) as a function of potential temperature and time. Then the rates at which the potential temperatures associated with each tracer VMR value change with time can be used to find diabatic cooling rates as a function of tracer VMR and time. Figure 2.2 shows an example of such a plot.

The powerful winds at the edge of the winter stratospheric polar vortex are a strong barrier to transport at the vortex edge. This confines high-altitude air within the vortex as it descends. However, dynamical events can cause disruptions to this barrier. The most dramatic events are known as stratospheric sudden warmings (SSWs). These events are in general caused by disturbances due to large-scale planetary waves breaking in the surf zone. At the altitude of the breakdown, air travels polewards, causing air above the SSW to travel upwards and cool, and air below the SSW to descend and warm. Hence an SSW causes warming in the stratosphere and cooling in the mesosphere [Labitzke, 1972, Engel et al., 2006].

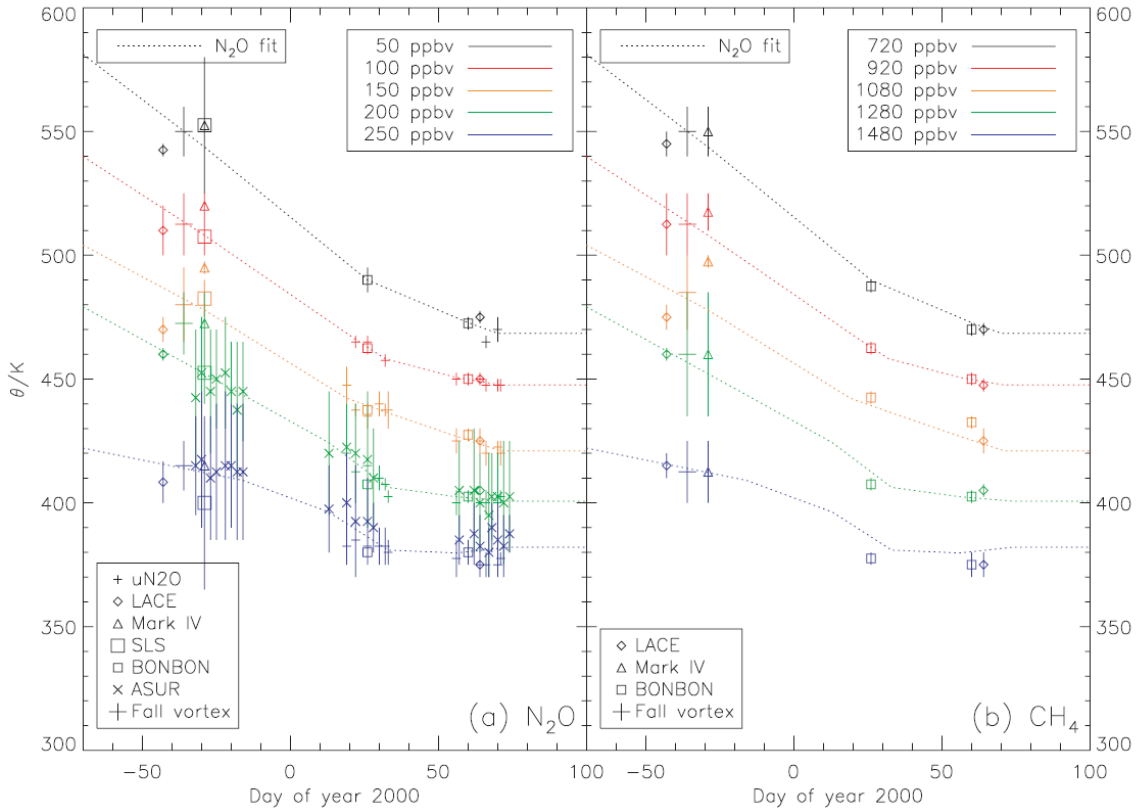

Figure 2.2: An example, from Greenblatt et al. [2002b], showing how tracer measurements (of N_2O and CH_4) can be plotted as a function of potential temperature θ and time in order to obtain descent rates, using measurements from a wide variety of sources (shown in the legends, see Greenblatt et al. [2002b] for more details). Approximate descent rates, as a function of θ, can be found from the gradients of the tracer isopleths.

Stratospheric sudden warmings vary in the level of disruption that they cause to the polar vortices. In terms of their severity they can be divided into major and minor warmings. A minor warming generally causes only a temporary weakening of the zonal winds at the polar vortex edge, while major warmings cause more serious disruptions, such as the vortex being pushed off the pole, splitting into two, or even disintegrating completely. There are several competing official definitions of what constitutes a major SSW. The World Meteorological Organization's (WMO) Commission for Atmospheric Sciences adopted a definition that deems an SSW to be major if "at 10 mb or below the latitudinal mean temperature increases poleward from 60 degrees latitude and an associated circulation reversal is observed (i.e., mean westerly winds poleward of 60° latitude are succeeded by mean easterlies in the same area)" [McInturff, 1978, Flury et al., 2009]. Since then, a number of similar definitions have been put forward. The most commonly used definition in recent times is that of Charlton and Polvani [2007], who defined a major SSW to take place when the zonal mean zonal winds at 10 hPa (equivalent to a potential temperature of about 900 K or an altitude of 31 km) and 60° N become easterly, rather than westerly as is usually the case during the vortex season. They define the first date for which these conditions are satisfied to be the "central date" of the major SSW. Lists of SSW definitions have recently been compiled by Butler et al. [2015] and Palmeiro et al. [2015], as well as lists of the SSWs found using a number of different definitions. It was found that the definition used to find major SSWs has a clear effect upon how many of them are identified. For example, the McInturff [1978] and Charlton and Polvani [2007] definitions show a pronounced dip in the number of major SSWs found in the 1990s which is not observed when other definitions are used [Butler et al., 2015].

Major stratospheric sudden warmings occur regularly in the Northern Hemisphere but very rarely in the Southern Hemisphere. Since regular measurements of stratospheric dynamics began, only one major stratospheric sudden warming has been observed in the Southern Hemisphere. This event caused the vortex to split into two during the last two weeks of September 2002 [Varotsos, 2002, Simmons et al., 2004, Glatthor et al., 2005, Manney et al., 2005a].

Some SSWs, especially major SSWs, are associated with what is called an elevated stratopause (ES) event. Normally the stratopause, the area of temperature maximum which defines the upper boundary of the stratosphere, occurs at an altitude of approximately 40-50 km. However, during some SSWs, the amount of westward-travelling gravity waves that reach the mesosphere and break there

is reduced because SSW-induced changes in the zonal winds cause them to be filtered out as they pass through the stratosphere [Siskind et al., 2007]. Since it is the breaking of these waves that drives the mesospheric circulation which leads to the formation of the temperature maximum at the winter polar stratopause, during some SSWs this temperature maximum can disappear before reforming at a greatly elevated altitude of approximately 80 km [Manney et al., 2009b, Randall et al., 2009, France and Harvey, 2013]. For example, during the extremely strong major SSW that occurred in January 2009, the stratopause reformed at 80 km; this altitude is usually well into the mesosphere [Manney et al., 2009b, Randall et al., 2009].

Major SSWs, especially those involving an elevated stratopause event, are often associated with enhanced descent as the vortex reforms. For instance, after the major SSWs in early 2004, 2006 and 2009, which all involved ES events and were of unprecedented strength, an unusually strong vortex reformed in the upper stratosphere and was associated with strong descent of odd nitrogen chemical species and carbon monoxide [Manney et al., 2005b, 2008a, 2009b, Randall et al., 2009].

The descent of air from higher altitudes within the stratospheric polar vortices means that air within the polar vortex can be very different chemically from air outside it. Chemicals present in the mesosphere can descend into the stratosphere this way, while at the vortex edge strong winds form a barrier, creating a "containment vessel" which prevents this chemically distinct air from leaking out. An example of this is how chemically reactive odd nitrogen and similar chemicals produced in the mesosphere and lower thermosphere (MLT) can reach the lower stratosphere via descent through the vortex.

Energetic charged particles from the solar wind can produce a variety of chemical species when they interact with the Earth's atmosphere. Among these, odd nitrogen (NO_x) and odd hydrogen (HO_x) are particularly important since they can break down ozone catalytically [Sinnhuber et al., 2012]. Here, *odd nitrogen* refers to N, NO and NO_2 and *odd hydrogen* refers to H, OH and HO_2. Ozone has a very significant influence on the structure and dynamics of the stratosphere, since its absorption of UV and infrared radiation has a heating effect, causing temperatures to rise with altitude within this layer of the atmosphere [Andrews et al., 1987]. Therefore, if odd nitrogen and hydrogen produced by this energetic particle precipitation (EPP) is able to reach the stratosphere, it could have an effect on stratospheric temperature and dynamics. This is referred to as the EPP indirect effect (EPP IE) [Solomon et al., 1982, Randall et al., 2007].

Odd nitrogen produced by EPP (EPP-NO_x) is the result of a process which begins with the dissociation and/or ionization of molecular nitrogen, after which subsequent chemical reactions can create more NO_x [Rusch et al., 1981]. EPP produces odd hydrogen (EPP-HO_x) as a result of complex ionic reactions [Thorne, 1980, Jackman et al., 2011].

Odd hydrogen has a lifetime of a few hours at most in the mesosphere [Jackman et al., 1995] therefore the general consensus is that HO_x produced by EPP will not last long enough to be transported into lower levels of the atmosphere. However, observations have shown that EPP-HO_x from solar proton events (SPEs) can cause significant ozone reductions in the mesosphere and upper stratosphere that can last for up to a few days [Jackman et al., 2001].

It was originally thought that EPP-NO_x produced in the MLT also had a lifetime that was too short to allow any significant amount of it to reach the stratosphere [Thorne, 1980]. This is due to photodissociation in the middle to upper mesosphere and the thermosphere. The photodissociation of NO produces atomic nitrogen in its ground state, which then reacts with NO and NO_2 and is the major sink for NO_x in this region [Thorne, 1980, Solomon et al., 1982]. As a result, NO_x at this altitude has a lifetime of at most a few days in sunlit areas [Randall et al., 2007]. However, during winter, there are long periods of time over which the areas near the poles are not exposed to sunlight. The lifetime of NO_x is then significantly longer in these locations (on the order of weeks [Randall et al., 2009]), which would make it possible for significant quantities of it to be advected to the stratosphere if favourable dynamical conditions exist. Once in the stratosphere, the NO_x has a lifetime on the order of a year [Solomon et al., 1982, Randall et al., 2009] and its effects can be long-lasting. Other factors suggesting that EPP-NO_x can reach the stratosphere are that in the stratosphere and MLT, the prevailing direction of vertical motion is downwards during the winter [Solomon et al., 1982], and also that the Earth's magnetic field tends to guide EPP to the poles.

Solomon et al. [1982] were the first to discuss the possibility of significant amounts of EPP-NO_x reaching the stratosphere in this way. Since then many observations have been made which show NO_x from the mesosphere and above reaching the stratosphere [Russell et al., 1984, Jackman et al., 1995, Randall et al., 1998, 2001, 2007, Siskind et al., 2000, Seppala et al., 2004]. The large number of observations of the EPP IE constitutes firm evidence that the effect exists.

Randall et al. [2007] used data from the HALOE instrument to estimate the amount of EPP-NO_x reaching the stratosphere in the Southern Hemisphere each

winter during 1992-2005 (an entire solar cycle). The correlation between the estimated amount of EPP-NO_x and several measures of EPP intensity was found to be stronger (0.85-0.88) than the correlation between it and the estimated vortex area (0.68), implying that for the Southern Hemisphere, the strength of the EPP IE depends more on the amount of EPP-NO_x produced in the MLT than it does on the dynamics of the polar vortex. This may be because these dynamics are much less variable in the Southern Hemisphere than in the Northern Hemisphere. The earlier paper by Siskind et al. [2000] also finds a correlation between the EPP IE and a measure of solar activity (the A_p auroral index).

The EPP IE is just one example of how air descending from higher altitudes can impact upon the chemistry of the stratosphere. The chemical composition of mesospheric air differs from that of stratospheric air, and therefore the chemistry of the lower stratosphere during the polar winter can be greatly affected by the rate at which mesospheric air descends through the polar vortex and whether it remains isolated within the vortex edge barrier or is mixed out of the vortex, as can happen during events such as SSWs. In order to understand how the dynamics of the polar vortex affects downwards transport within it, it is important to be able to locate the edge of the polar vortex at all altitudes from the lower stratosphere up into the mesosphere and to measure the strength of the barrier at its edge.

2.2.2 Transport on isentropic surfaces

To begin with, we discuss a few techniques that have been used to simplify the task of modelling and understanding the dynamics of the stratospheric polar regions. Within the stratosphere, due to the relatively slow diabatic transport, it is often possible to approximate the motion of air parcels by assuming that it is adiabatic over relatively short time periods. The modelled air parcels are then confined to an isentropic, approximately horizontal surface of constant potential temperature. In the lower stratosphere, at potential temperatures of 500 K and below (altitudes below about 20 km), this approximation has been successfully used over periods of a month or more [Bowman, 1993, McKenna et al., 2002], since air parcels generally stay on isentropic surfaces unless they gain or lose heat energy. However, in the middle stratosphere, at potential temperatures of 700-800 K, for individual parcels this approximation is only really justified over periods of approximately 7-10 days [Pierce et al., 1994, Morris et al., 1995, 2002]. However, if many trajectories are used and the results are considered in

a statistical manner, isentropic approximations can be useful over longer periods [Morris et al., 1995, Ajtić et al., 2004]. This approximation greatly simplifies the process of computing trajectories and makes it possible to investigate horizontal motion in isolation from vertical motion, which is relatively difficult to compute.

In the surf zone, breaking planetary waves trigger large scale mixing on isentropic surfaces. These also erode the edge of the polar vortex, stripping away filaments of air that are then mixed into the surf zone. Over time, this erosion can cause the vortex to shrink [McIntyre and Palmer, 1984], particularly if the amplitude of the waves is large. The forcing by planetary waves can also distort the vortex, causing its boundary to bend and/or shift off the pole and disrupting the vortex's zonal symmetry. This can make it difficult to easily describe the exact position of the vortex and its edge, since it is not possible to simply define these using physical latitudes. A way to get around this problem is to convert to a new coordinate system in which the zonal symmetry of the vortex and its environs is restored.

The most popular way to do this is to convert to an alternative latitude coordinate known as equivalent latitude. This is most commonly based on potential vorticity (PV), a quantity proportional to the dot product of absolute vorticity and the gradient of potential temperature which is defined by

$$q = \frac{1}{\rho}(2\mathbf{\Omega} + \nabla \times \mathbf{u}) \cdot \nabla\theta,$$

where ρ is the air density, $\mathbf{\Omega}$ is the Earth's angular velocity, $\nabla \times \mathbf{u}$ is the curl of the air velocity and $\nabla\theta$ is the gradient of potential temperature. In the absence of diabatic heat transfer or friction, potential vorticity is conserved for air parcels. This means that over timescales of a few days to approximately a week, PV can be used as a tracer in the stratosphere [Haynes and McIntyre, 1987, Baker and Cunnold, 2001, Waugh and Polvani, 2010]. Absolute values of PV are greatest near the poles, and the transport barrier at the edge of the polar vortex is associated with sharp gradients of PV which then further impede transport across the barrier [Butchart and Remsberg, 1986, Waugh and Polvani, 2010]. Values of PV increase with altitude in the winter hemisphere, since high-PV air can be advected by diabatic downwards descent within the vortex region; this leads to a further increase in absolute PV values within the vortex [Waugh and Polvani, 2010], which again makes it more difficult for extra-vortex air parcels to enter the vortex.

Equivalent latitude can be calculated based on gridded PV data covering one

of the Earth's hemispheres at any given altitude by first determining the surface area associated with each grid point. Then, for any given PV value q^*, the total surface area A^* which corresponds to absolute PV values above q^* is summed. The equivalent latitude corresponding to q^* is then:

$$\varphi_e^* = \arcsin\left(1 - \frac{A^*}{2\pi r}\right),$$

which is the latitude that the edge of a zonally symmetric region with surface area A^* would have (where r is the Earth's radius) [Butchart and Remsberg, 1986, Haynes and Shuckburgh, 2000, Allen and Nakamura, 2003]. In this way, an equivalent latitude can be assigned to any PV contour. Since flow in the stratosphere generally follows PV contours, using a coordinate system based on equivalent latitude can greatly simplify the description of dynamical structures in the stratosphere. For example, the location of the polar vortex edge can be specified by a PV/equivalent latitude contour that bends and distorts with the vortex as it is disturbed by planetary waves.

Equivalent latitude can also be calculated using dynamical variables or quantities other than PV. For example, in theory tracer concentrations could be used, with the tracer-equivalent latitude being determined by summing the areas associated with tracer concentrations above or below a certain threshold [Butchart and Remsberg, 1986, Haynes and Shuckburgh, 2000]. In practice, it is difficult to do this using directly measured tracer concentrations, as tracer measurements from observations do not generally come in the form of gridded data. However, Allen and Nakamura [2003] do this by using an artificial tracer which is advected over time using an advection-diffusion model, and define an alternative equivalent latitude based on concentrations of this tracer. This is called the tracer equivalent latitude (TrEL) [Allen and Nakamura, 2003, Allen et al., 2012].

We will now discuss the types of methods that have been previously used to identify the location of the vortex edge and the strength of the associated transport barrier. The most common method used to identify the location of the vortex edge barrier is based on plotting potential vorticity as a function of equivalent latitude. It was first developed by Nash et al. [1996]. Since the vortex edge is associated with a very sharp gradient of PV, a plot of the gradient of PV vs equivalent latitude should peak in the vicinity of the vortex edge. The equivalent latitude of the vortex edge is then taken to be the value associated with this peak. If there is more than one peak to choose from, the average wind speed along the equivalent latitude isolines can be used to select the correct one,

since wind speeds also maximise near the vortex edge [Nash et al., 1996, Mitchell et al., 2010]. According to Steinhorst et al. [2005], the maximum value of the PV gradient with respect to equivalent latitude can also be used as a measure of the permeability of the vortex edge barrier. A common variation on this technique is to multiply the gradient of PV with the average wind speed function in a pointwise way to get a function known as the "impermeability", which is a function of equivalent latitude. The equivalent latitude isoline associated with the maximum of this function is then determined to be the location of the vortex edge [Ajtić et al., 2003, Smith and McDonald, 2014]. A simpler method that has also been commonly been used is to simply choose a particular PV contour at a given altitude to be the vortex edge location and then to use it for all days during the polar vortex season [Manney et al., 1994a, Waugh and Randel, 1999, Müller and Günther, 2003, Matthewman et al., 2009].

Nash et al. [1996] originally applied this method for locating the vortex edge in the lower stratosphere. According to Mitchell et al. [2010], at higher altitudes such as in the middle stratosphere this method becomes more difficult to apply, since at higher altitudes more filamentation occurs, as thin streamers of high-PV air are mixed into the surf zone. Above approximately 50 km, the usefulness of equivalent latitude based on PV breaks down since the relationship between PV values and physical latitude is no longer monotonic [Harvey et al., 2009].

Many methods used to investigate the dynamics within the stratosphere, including some which can be used to help identify the location and strength of the vortex edge barrier, use Lagrangian models in which a set of initial points are chosen to represent parcels of air and then wind velocity data from reanalyses or other sources is used to calculate the trajectories of the parcels over time. One such method is to trace the evolution of material contours (usually PV contours are used) and measure their rate of lengthening with time as mixing occurs. This is done by representing the contour as a series of particles and advecting them using a trajectory model. The vortex barrier will then be the contour for which the rate of lengthening is at a minimum [Chen, 1994, Norton, 1994, Waugh and Plumb, 1994, Waugh et al., 1994, Appenzeller et al., 1996, Baker and Cunnold, 2001]. Another, very commonly used, method for identifying transport barriers such as those at the polar vortex edge is effective diffusivity, which also defines the barriers as those contours for which contour lengthening associated with mixing is slowest [Nakamura, 1996, Nakamura and Ma, 1997, Haynes and Shuckburgh, 2000, Allen and Nakamura, 2001, Roscoe et al., 2012]. For both of these methods, the rate of contour lengthening at the vortex edge barrier can also be used as a

quantitative measure of barrier strength, with a slower rate relating to a stronger barrier [Chen, 1994, Allen et al., 1999].

Trajectory-based methods can also be used to improve the resolution of plots based on observational data. One such method, known as trajectory mapping, works by collecting observations over a time period of some days and then running a trajectory model to predict where the air parcels associated with these observations will end up at a specific time. This allows information gathered over a long period to be used to gain additional information about conditions on one specific day [Pierce et al., 1994, Morris et al., 1995, 2000, McDonald and Smith, 2013]. These methods assume that the observational data associated with each air parcel will be conserved over the time period that the trajectories are calculated over. A variation on this method is to initialize air parcels on a grid at some specific time, and then observe where a trajectory model based on wind velocity advects them at a later time. This is known as "domain filling" [Fisher and O'Neill, 1993, O'Neill et al., 1994]. Although in the examples referred to here the parcels are only being initialized at a single initial time t_1, meaning that when the results are observed at a later time t_2 there will be no increase in the number of data points used, it is still possible to see extra fine-scale structure at t_2 that would not otherwise be observable, such as thin filaments of high PV [O'Neill et al., 1994]. This is because most gridded observational data have relatively poor resolution and fine structure does not show up; however over time as the initial data points are chaotically stirred by the wind fields there is a "cascade" towards small-scale structure. The results of the original "domain filling" technique provide results at t_2 that are not gridded. But a modification of this technique, known as reverse domain filling (RDF), instead sets up a grid of points at t_2, calculates back trajectories for each of the points, and matches them with observations made in the past. This results in a coherent grid of data at t_2 with no gaps [Sutton et al., 1994, Schoeberl et al., 2006].

Another trajectory-based method that is very commonly used relies on Lyapunov exponents. The basic idea behind Lyapunov exponents is to initialize two air parcels at nearby points in a particular location so that they are a short distance $\Delta x(t_0)$ apart at time t_0, advect them both using a trajectory model, and observe how the distance between them changes. For two points which are an infinitesimal distance apart at time t_0, the Lyapunov exponents are defined by

$$\lambda = \lim_{t\to\infty} \frac{1}{t - t_0} \ln \frac{|\delta x_i(t)|}{|\delta x_i(t_0)|},$$

as the time t tends to infinity [Garny et al., 2007]. The number of Lyapunov exponents is the same as the dimension of the system, but for most practical purposes, only the Lyapunov exponent with the largest value counts. If the Lyapunov exponent is calculated for air confined to a two dimensional isentropic surface, the flows are incompressible and therefore the second Lyapunov exponent provides no additional information. For air confined to an isentropic surface [Pierrehumbert and Yang, 1993], the Lyapunov exponent will in general be positive if the distance between the two air parcels increases with time, negative if they converge with time, and zero if they stay the same distance apart even as $t \to \infty$.

For any dynamical system that is well-mixed over a long time scale, the Lyapunov exponents at all locations will eventually average out into a uniform distribution [Joseph and Legras, 2002]. The Earth's atmosphere is affected by this issue, and therefore Lyapunov exponents calculated over very long periods are not useful for understanding its dynamics. For any two test air parcels in the Earth's atmosphere, if their trajectories are traced over a long enough time period, they will eventually diverge, and because the atmosphere is well-mixed over long time periods, eventually the distance between the air parcels will become random as the two parcels are advected separately around the globe.

A related issue can also cause problems when calculating Lyapunov exponents over finite time periods. When attempting to identify features such as transport barriers and regions of mixing in the atmosphere, Lyapunov exponents are only useful when the pair of test air parcels remains close enough together. Once the two air parcels are far enough apart, changes in the distance between them may have little bearing on local dynamical conditions associated with either of the test trajectories. In order to avoid that, in most work done using Lyapunov exponents in the stratosphere, the distance between the trajectories is reset to its minimum after an interval of a few days. The approximate Lyapunov exponent can then be computed using

$$\lambda = \frac{1}{nT} \sum_{k=1}^{n} \frac{\delta x(kT)}{\delta x(t_0)},$$

where T is the length of the interval between resets, n is the total number of intervals the parcel was advected over, $\delta x(t_0)$ is the initial distance between the two parcels and $\delta x(kT)$ is the distance between the parcels after k time intervals. This is the finite time Lyapunov exponent or FTLE. It is also possible to instead reset the distance between the test air parcels once the distance between the two air parcels reaches a certain threshold. This gives the finite size Lyapunov

exponent or FSLE [Joseph and Legras, 2002].

If this approximate Lyapunov exponent is calculated on a grid over an isentropic surface, high positive values of the Lyapunov exponent will be associated with enhanced mixing as air parcels which were initially close together are separated, while the polar vortex barrier edge should, at least in theory, coincide with minima in the field of Lyapunov exponents. Papers that have used Lyapunov exponents to identify the vortex edge and other barriers in the stratosphere include [Bowman, 1993, Garny et al., 2007, Beron-Vera et al., 2012, Olascoaga et al., 2012].

The atmosphere can be considered to be a chaotic system, and Lyapunov exponents can be used to help identify features called Lagrangian coherent structures (LCS). These structures play a role in organizing fluid flow within dynamical or chaotic systems such as the stratosphere. They include hyperbolic invariant manifolds. These cannot be crossed by fluid parcels and thus can be considered to be barriers. Unstable manifolds attract nearby fluid parcels, while stable manifolds repel them, but neither type of manifold can be crossed by a fluid parcel so both can be considered to be types of barrier. Joseph and Legras [2002], de la Camara et al. [2010] and Beron-Vera et al. [2012] have located these structures using Lyapunov exponents.

In a two-dimensional system such as an isentropic layer of the stratosphere, the stable and unstable manifolds are one-dimensional lines that are advected by the fluid flow over time. When a stable and an unstable manifold cross, if an air parcel near the stable manifold approaches the crossing point, it will be repelled by the stable manifold and attracted by the unstable manifold. However it cannot cross either manifold, and will end up travelling away from the crossing point along the unstable manifold. Figure 2.3 is a diagram from de la Camara et al. [2010] showing how such an event would evolve over time. The trajectory traced out over time by the intersection point between the two manifolds is referred to as a hyperbolic or distinguished hyperbolic trajectory [Jimenez Madrid and Mancho, 2009, de la Camara et al., 2010]. The sudden changes in direction experienced by fluid parcels near the intersection point are likely to be associated with strong mixing. If a stable and unstable manifold intersect at the edge of the polar vortex, this is likely to lead to air parcels entering and/or leaving the vortex [de la Camara et al., 2010].

Other types of Lagrangian coherent structures include elliptic LCSs, which correspond to trajectories within a Lagrangian vortex, and parabolic LCSs, which correspond to Lagrangian jet cores. It should be possible to find both of these

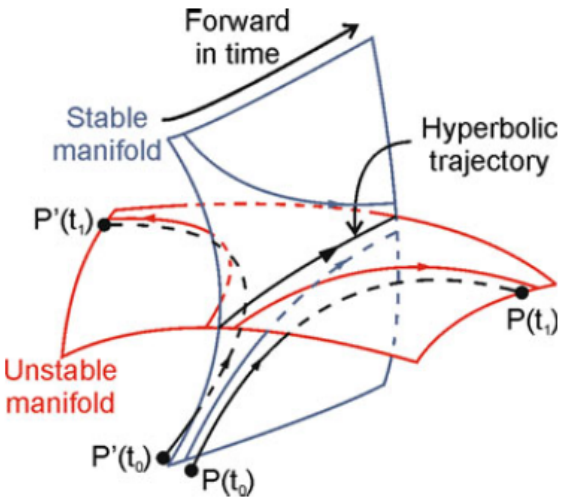

Figure 2.3: Behaviour of the hyperbolic trajectory and the trajectories on and near the stable and unstable manifolds. Two trajectories starting from nearby initial conditions across the stable manifolds will diverge after a sufficient time period. This figure and caption reproduced from de la Camara et al. [2010] with permission of Springer.

types of LCS within the barrier region of the polar vortex; so they could potentially be useful for locating the vortex edge barrier. These are described in detail by Haller [2015] along with methods for locating them. In the theory of dynamical systems, many methods for identifying organizing structures and barriers were originally designed to be applied only to periodic or time-independent flows, rather than real geophysical flows which are aperiodic. The study of Lagrangian coherent structures is part of a body of work which aims to discover generalized methods for locating these structures within aperiodic flows. Another useful approach within this area is discussed by Wiggins and Mancho [2014], who review a theorem which can be used to mathematically describe a realistic transport barrier which may only exist for a finite amount of time.

Another, more recently developed method that is potentially very useful for investigating stratospheric dynamics is known as the function M. This function was first defined by Jimenez Madrid and Mancho [2009] while looking for methods that could be used to find distinguished hyperbolic trajectories. The function M is based on the arc length of trajectories taken over a given time interval. The value of M at a position $\mathbf{x} = (x_1, x_2)$ in two-dimensional space and at a time t_0 is given by the Euclidean arc length of a trajectory calculated over a time period $(t_0 - \tau, t_0 + \tau)$, where τ is some constant time period which in the case of the

stratosphere is usually measured in days.

$$M_\tau(\mathbf{x}, t_0) = \int_{t_0-\tau}^{t_0+\tau} dt \sqrt{\left(\frac{dx_1(t)}{dt}\right)^2 + \left(\frac{dx_2(t)}{dt}\right)^2}$$

Plots of the function M can be used to create detailed maps of the stratospheric polar vortex, since regions where M is larger correspond to locations where air parcels have travelled a longer distance over the time period $(t_0 - \tau, t_0 + \tau)$, while regions where M is smaller correspond to the locations of air parcels that have spent time in the calmer regions outside the vortex or in its core. The function M was first used in this way by de la Camara et al. [2012]. The region of high wind speeds near the vortex edge can clearly be seen in such plots. Sharp gradients in the function M correspond to boundaries between dynamically distinct areas associated with stable or unstable manifolds. Hyperbolic trajectories can often be clearly identified on such plots by observing where these manifolds cross. Figure 2.4 shows an example from de la Camara et al. [2012] in which the ring of high M values associated with the vortex edge is clearly visible, as well as a crossing point between stable and unstable manifolds. As the time period over which M is calculated increases, these dynamical features become more clearly visible. The elliptic and parabolic LCSs described by Haller [2015] and references therein have only been introduced into the literature recently, therefore attempts have yet been made to identify these features in maps of the function M. However, since the ring of high M values corresponds to a zonal jet associated with strong wind speeds, a parabolic LCS or zonal jet core is likely to be located within it. A family of elliptic LCSs should also be located within the region occupied by the vortex and its edge. Although the function M can be useful for identifying hyperbolic LCSs [de la Camara et al., 2012, 2013], it is a heuristic method that may give false positives or negatives under some circumstances, or give different answers depending on the frame of reference used [Haller, 2015, Ruiz-Herrera, 2015].

Chapter 3 contains more information on the function M, its interpretation and its applications. In addition to being useful for creating detailed maps of the polar vortex and identifying mixing regions associated with hyperbolic trajectories, it can also potentially be used as a basis for developing quantitative measures of barrier strength, since high values of M are in general associated with the region of high winds that gives rise to the vortex edge barrier.

One issue with methods involving computation of many trajectories based on

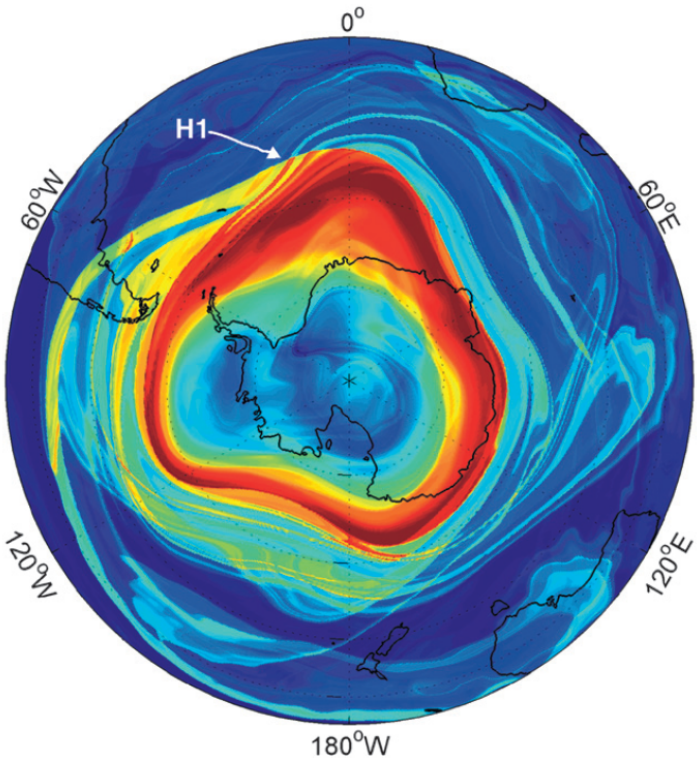

Figure 2.4: This figure, from de la Camara et al. [2012], shows the function M plotted over a month-long period centred on 1 Nov 2005 on the 475 K isentropic surface (corresponding to an approximate altitude of 18.5 km and pressure level of 70 hPa). Here t_0= 1 Nov 2005 and τ = 15 days. H1 marks the location of a hyperbolic trajectory.

wind velocity data, such as Lyapunov exponents, the function M, and methods based on advection of material contours, is that they are computationally expensive, as will be mentioned in Chapter 3. The function M is less computationally expensive than Lyapunov-based methods, since it only requires one trajectory to be calculated for each air parcel being advected, while Lyapunov-based methods require at least two [Mendoza and Mancho, 2010]. Tracer-based methods, which will be discussed later, require much less computational time [Krützmann et al., 2008].

The methods for investigating vortex dynamics that have been discussed in this section are effective throughout the lower-middle stratosphere, but can run into difficulties when applied at higher altitudes. Firstly, the rate of vertical transport within the vortex increases with height and the isentropic approximation is valid over shorter timescales. At levels above approximately 900 K (about 32 km altitude), it becomes more difficult to justify using this approximation, and accounting for vertical transport becomes more important. Above an altitude of approximately 50 km, near the stratopause, equivalent latitudes based on potential vorticity (PV) are no longer useful since the highest values of PV are no longer located near the poles [Harvey et al., 2009]. Secondly, above approximately 900 K, the gridded wind data from reanalyses that is usually used when applying these methods starts to become less reliable. This issue will be discussed in more detail in Chapter 2.3.1 and is particularly problematic for methods that use trajectory models.

2.3 Availability and reliability of data in the mid-stratosphere and above

2.3.1 Reanalysis data

In general, the methods discussed above for investigating the behaviour of the polar vortex and its barrier rely on the availability of reliable gridded wind velocity and/or potential vorticity (PV) data on isentropic surfaces. In particular, the methods which use Lagrangian models need detailed wind velocity information in order to determine the trajectories of air parcels. For altitudes at and below the middle stratosphere, this data is most commonly obtained from reanalysis datasets. A reanalysis dataset is a global climate model (GCM) that is forced by real observations from a variety of sources. It is constructed in order to give the

best possible description of the state of the Earth's atmosphere over the timespan that it covers (usually at least several decades).

Current reanalyses in mainstream use include the Modern-Era Retrospective analysis for Research and Applications (MERRA) produced by NASA's Global Modeling and Assimilation Office (GMAO) [Rienecker et al., 2011] and the ERA-Interim reanalysis produced by the European Centre for Medium-Range Weather Forecasts (ECMWF) [Dee et al., 2011], as well as the Climate Forecast System (CFS) reanalysis from the National Centers for Environmental Prediction [Saha et al., 2010, 2014] and the new JRA-55 Reanalysis from the Japan Meteorological Agency (JMA) [Kobayashi et al., 2015]. In general, reanalyses are produced using a combination of a forecast model and/or GCM, coupled with a data assimilation system (DAS), which is used to incorporate the observations into the model.

The MERRA reanalysis is based on version 5.2.0 [Rienecker et al., 2008] of the Goddard Earth Observing System Data Assimilation System Version 5 (GEOS-5 DAS). This includes a GCM as well as a DAS [Rienecker et al., 2011]. A wide variety of data products associated with the MERRA reanalysis are available, including gridded wind velocity components and temperatures. These are available on either the 72 vertical levels native to the GEOS-5 model with the top level corresponding to 0.01 hPa (∼81 km altitude), or a set of 42 pressure levels with the top level at 0.1 hPa (∼64 km). The horizontal grid has a resolution of $\frac{2}{3}^\circ$ longitude by $\frac{1}{2}^\circ$ latitude [Lucchesi, 2012]. Data from MERRA is available from 1979 until February 2016, after which it will be superseded by the next-generation MERRA2 reanalysis, which assimilates a wider range of satellite measurements and uses updated model parameterizations [Bosilovich et al., 2015, Molod et al., 2015].

The ERA-Interim reanalysis is based on ECMWF's Integrated Forecast System (IFS) and was originally designed as a bridge between the previous ERA-40 reanalysis [Uppala et al., 2005] and the new ERA-20C reanalysis, currently in production, that is designed to cover the entire 20th century. It covers the same time period (1979-present) as MERRA [Dee et al., 2011]. The reanalysis model has 60 vertical levels with the top level at 0.1 hPa. Data on temperatures and wind velocities are available on these native levels, or on a set of pressure levels ranging from 1000-1 hPa, or on potential temperature levels ranging from 265-800K. For these fields, the data is expressed in terms of spherical harmonic components, truncated at a wavenumber of 255 (T255 spectral resolution), which corresponds to a horizontal resolution of approximately 80 km [Berrisford et al., 2011] (also see the ECMWF website about ERA-Interim,

http://www.ecmwf.int/en/research/climate-reanalysis/era-interim).

The CFSR reanalysis dataset from NCEP has a horizontal resolution of T382 or 38 km, the most detailed horizontal resolution of any of the reanalyses. Its top vertical model level is at about 0.266 hPa, although the reanalysis is only scientifically usable up to 1 hPa [Saha et al., 2010]. It also runs from 1979 to the present day. However, the new JRA-55 reanalysis starts in 1958, which is the first year when routine radiosonde observations became available globally [Kobayashi et al., 2015]. It has a spectral resolution of T319, which corresponds to a horizontal resolution of ∼55 km, and its top level is at 0.1 hPa.

Most of the reanalyses cover a time period of at least several decades and are designed so that, as much as possible, errors caused by changes in the way that observations are made over that time period or by changes in the types of data available are avoided. They all assimilate data from a wide variety of sources, including radiosondes, ground, aircraft and ship observations, and observations from numerous satellites. Radiosonde observations are important at altitudes up to about 30 km, but are rarely available higher up [Le Pichon et al., 2015]. The satellite data used typically includes atmospheric motion vectors from satellite imagery, ocean surface wind speeds, radiances, ozone data, and more recently, atmospheric refractivities from radio occultation (RO) observations. Of these, the radiance and ozone data are the most relevant for the middle atmosphere.

In the stratosphere, satellite observations of wind velocities are generally not available; the MODIS instrument onboard NASA's Terra and Aqua satellites, which measures winds by tracking the motion of clouds, can only obtain these at pressure levels below 250 hPa (approximately equivalent to a potential temperature of 320 K or an altitude of 10.5 km) [Rabier et al., 2010]. However, measurements of temperature and/or geopotential height can be used to derive approximate wind velocities (geostrophic winds) under the assumption that the pressure gradient force and the force due to the Coriolis effect are balanced [Oberheide et al., 2002, Remsberg et al., 2003, Livesey et al., 2015]. Reanalysis wind fields in the stratosphere depend largely on information derived using this method, as well as on observations from radiosondes at locations and altitudes where these are available.

At low latitudes the balance conditions do not constrain the wind fields to the same degree that they do elsewhere. This has a negative effect upon the reliability of wind fields there [Rienecker et al., 2011], even in the lower stratosphere [Podglajen et al., 2014]. However, when comparing rocketsonde observations from Thumba, India (at 8.5° N) with MERRA reanalysis data, Kishore Kumar et al.

[2014] did find a fairly good agreement between the zonal winds up to an altitude of 60 km (corresponding to a pressure level of about 0.3 hPa), although the agreement between real and modelled meridional winds was very poor.

Many, if not most, of the middle atmospheric radiances assimilated into the reanalyses come from instruments onboard National Oceanic and Atmospheric Administration (NOAA) satellites, including Stratospheric Sounding Units (SSU), Microwave Sounding Units (MSU), and Advanced Microwave Sounding Units (AMSU) [Kobayashi et al., 2009, Dee et al., 2011]. The SSU instruments made stratospheric temperature observations using three different channels, with the range of pressures covered by each channel described using a weighting function. The three weighting functions for the channels were centred at approximately 15, 5, and 1.5 hPa (corresponding to altitudes of about 29, 35 and 45 km), covering much of the middle-upper stratosphere [Saha et al., 2010, Nash and Saunders, 2015]. The AMSU-A instruments are designed to measure temperature profiles from the surface up to a pressure level of 3 hPa ($\sim$ 45 km). These instruments therefore can take measurements at altitudes up to the upper stratosphere, but do not extend into the mesosphere. They have relatively poor resolution since they are nadir-sounders that look downwards at the atmosphere. The uppermost channels of these instruments measure temperatures averaged over a layer in the stratosphere that is about 20 km deep [Manney et al., 2009a]. Overall, despite the inclusion of observations from these instruments, data coverage in the stratosphere is relatively sparse, and the reanalysis models are not as well constrained by observations as they are at lower altitudes [Kobayashi et al., 2009, Dee et al., 2011]. The mesosphere is largely unconstrained by observations [Manney et al., 2009a]. Temperatures from limb-sounding instruments, which have better vertical resolution (but worse horizontal resolution) and can make measurements at higher altitudes, have not been assimilated into mainstream reanalyses until now. However, this does mean that results from them can provide an independent check upon temperatures from these reanalyses. Limb sounders will be discussed in more detail in Chapter 2.3.2. The new MERRA-2 reanalysis now includes temperature and ozone data from the Microwave Limb Sounder onboard NASA's Aura satellite, which will improve its accuracy and reliability in the stratosphere and mesosphere during the time period when data from this satellite is available [Bosilovich et al., 2015].

There is considerable overlap between the datasets used by each reanalysis. For example, the data sources used in the NCEP-CFSR reanalysis are very similar to those used by MERRA [Saha et al., 2010, Rienecker et al., 2011]. The data

sources available have changed over time. For example, 1979 was the first full year in which comprehensive satellite data became available from the NOAA polar-orbiting weather satellites, causing a great improvement in the quantity of observations available for assimilation, as well as the coverage in the previously poorly-observed southern polar regions and the upper stratosphere [Simmons et al., 2004].

All of the reanalyses listed above use automated schemes for correcting biases in the satellite data that they use. In the stratosphere, most of the reanalysis data comes from the satellite instruments described above. These are all subject to biases, and these biases differ depending on the instruments used. Even identical instruments on different satellites can have different biases, and in addition, these biases can vary with respect to time [Kobayashi et al., 2009]. The bias correction schemes rely on there being a reliable source of unbiased data to compare the satellite results to. This can either be from the underlying GCM model or from measurements. But in the upper stratosphere, the underlying GCMs often have large biases [Kobayashi et al., 2009, Rienecker et al., 2011]. Non-satellite measurements such as rocketsondes and lidars provide reliable in situ data, but there are not enough of them to be useful as a reference for the correction scheme [Kobayashi et al., 2009]. If there was a source of satellite temperature data available with bias that was consistent over the entire period of a reanalysis, then it would be possible to use that as a baseline for the bias-correction scheme, but since satellite instruments have relatively short lifetimes, that is not possible [Rienecker et al., 2011]. Observations of atmospheric refractivity from radio-occultation (RO) satellites using GPS data have biases small enough to be very useful for the correction schemes, but the first of these, the CHAllenging Minisatellite Payload (CHAMP) mission, was launched in 2000; therefore it is not possible to use GPS-RO satellite data as a baseline before then. When the automated bias correction scheme is applied to stratospheric temperature measurements, it tends to push the results towards those that would have been obtained from the underlying GCM, leading to biases. In the NCEP-CFSR reanalysis, applying the automated bias correction procedure to SSU radiances led to a spurious warming trend in the upper stratosphere, although this is likely to be remedied in future NCEP reanalyses [Saha et al., 2010]. In order to avoid issues such as these, the MERRA and ERA-Interim analyses did not apply the bias correction scheme to their highest-altitude satellite measurements [Dee et al., 2011, Rienecker et al., 2011].

Due to the lack of assimilated data above the middle stratosphere, and par-

ticularly in the mesosphere, it is to be expected that the reanalyses may become less accurate at higher levels. In the upper stratosphere and mesosphere, there are few non-satellite based measurements that are not already assimilated into the reanalyses and can thus be used for testing them. However, Kishore Kumar et al. [2014] made such observations, as mentioned earlier, as well as Le Pichon et al. [2015], who used a range of ground-based observations including lidar from the Haute-Provence Observatory in mid-latitudes. During January-July 2013, Le Pichon et al. [2015] compared temperatures and winds from MERRA and observational ECMWF analyses with their own observations. The temperatures agreed well up to an altitude of 40 km, but began to diverge above that. At 40-45 km, the worst agreement was in January, a month during which there was a major SSW, and in winter more generally. Much of the difference between models and observations during this period was attributed to variability on time-scales of a few days associated with planetary waves which were present in the observations but not to the same degree in the models, implying that the models have problems with representing planetary waves accurately at these altitudes.

There has, however, been a considerable amount of work in which satellite measurements of temperatures and winds have been compared with reanalysis results. Most of these comparisons have been carried out using the operational analysis products, rather than the reanalyses themselves. The operational products are similar to their corresponding reanalyses, except that the methods by which they are produced are continually updated as methods and observations are improved over time, without regard to consistency of the product over long time scales. During the validation study for version 2.2 of the temperature data from the Microwave Limb Sounder (MLS) onboard NASA's Aura satellite, comparisons were made with an ECMWF operational analysis and with a GEOS-5 based reanalysis (similar to MERRA) [Schwartz et al., 2008]. The most striking differences between the MLS and GEOS-5 temperatures were a vertically oscillating bias of amplitude $\leq$4 K in the upper troposphere and lower stratosphere and a large bias of approximately 10 K near the poles at the top of the stratosphere (at a pressure level of 1 hPa), except during summer [Schwartz et al., 2008]. The oscillating bias is almost certainly due to a problem with the MLS data rather than with the GEOS-5 model, since it is also evident in comparisons between MLS and other satellites. However, it is not clear from the validation exercise alone whether the large bias at higher altitudes, with the GEOS-5 temperatures being cooler than those from MLS, is an issue with the reanalysis or with the MLS data. The agreement between the ECMWF analysis and the satellite data

was good up to 10 hPa in the middle stratosphere (about 900 K or an altitude of 31 km), but got worse in the upper stratosphere and mesosphere, including at 1 hPa (near the stratopause at about 49 km) in the Southern Hemisphere winter, where once more the bias reached 10 K or more.

Manney et al. [2008b] compared results from ECMWF and GEOS-5 operational analyses with satellite data from the MLS and SABER instruments during the 2005/2006 Northern hemispheric winter, which contained a major SSW in late January associated with an elevated stratopause event (ES). They found that before the SSW, the stratopause altitude according to the analysis data agreed fairly well with the satellite data. However, the location and strength of the reformed stratopause after the SSW was different both between each the analyses and between the analyses and the satellite data. After the SSW, the analysis zonal mean wind velocities and radiative cooling rates also differed from those calculated using satellite data. The GEOS-5 cooling rates were near zero at 1 hPa (the pressure value where the stratopause would usually be), which is not realistic, and there was too much diabatic cooling higher up, between 0.4-0.03 hPa. The ECMWF analysis cooling rates fared better, agreeing well with the satellite results up to 0.1 hPa and only showing a serious bias at pressures higher in altitude than 0.03 hPa [Manney et al., 2008b]. These differences can lead to considerable biases in descent rates calculated using information from the analyses [Manney et al., 2008b]. When the SLIMCAT chemistry model was run over the 2006 SSW period using wind and temperature data from the ECMWF analysis, modelled descent of mesospheric CO and H_2O after the SSW was markedly delayed compared to what happened in actuality, and was too strong when it did occur [Manney et al., 2009a]. Manney et al. [2009b] found similar discrepancies between GEOS-5 analysis data and MLS satellite data during and after the 2009 SSW, including the post-SSW stratopause reforming at too low an altitude and the vortex re-establishing itself too late.

It is clear that reanalysis data can become particularly unreliable in the polar upper stratosphere and lower mesosphere (USLM) during and after large dynamical events such as major SSWs. However, it may be possible to construct new analyses that are designed to work better at higher altitudes. Over recent years, a considerable amount of research has been done in which winds and temperatures from MLS and SABER have been assimilated into the Canadian Middle Atmosphere model [Polavarapu et al., 2005], the Advanced Level Physics High-Altitude prototype of the Navy Operational Global Atmospheric Prediction system (NOGAPS-ALPHA) [Eckermann et al., 2008, Hoppel et al., 2008, Coy

et al., 2011], and the Whole Atmosphere Community Climate Model (WACCM) [Pedatella et al., 2014]. Eckermann et al. [2008] were able to show agreements between the improved analysis model and independent measurements of mesospheric clouds, as well as MLT wind patterns observed by meteor radar. Coy et al. [2011] used the improved NOGAPS-ALPHA model to observe a reversal of upper mesospheric winds that occurred a week before the major SSW in January 2009 and to investigate its probable cause.

2.3.2 Satellite data

In order to better understand the dynamics of the polar vortices in the stratosphere and mesosphere, data is vital, but as we have seen, reanalysis data becomes less reliable and readily available from the mid-stratosphere upwards. Because of this, direct satellite measurements become relatively more important at these higher altitudes. Ground and air-based measurements can also be important, but cannot simultaneously provide both a continuous record and a wide spatial range. Measurements from recent balloon campaigns such as VORCORE [Hertzog et al., 2007], Concordiasi [Rabier et al., 2010] and the Google Loon project are generally not available at pressures below about 50 hPa, which corresponds to a potential temperature level of approximately 500 K and is in the lower stratosphere.

As mentioned in Chapter 2.3.1, direct measurements of wind velocities are generally not available. However, it is possible to obtain some direct measurements of mesospheric wind speeds using the Microwave Limb Sounder (MLS) onboard NASA's Aura satellite [Limpusavan et al., 2005, Wu et al., 2008], with the method being most useful in the mid-high mesosphere (roughly 70-90 km). Measurements of middle-atmospheric temperatures and chemical concentrations are much more readily available from a range of different instruments onboard a number of satellites. Measurements from altitudes corresponding to pressure levels of 10 hPa and lower are of particular interest because these correspond to altitudes where reanalysis datasets start to become less reliable.

Some of the most comprehensive measurements of temperatures and tracer mixing ratios come from the Microwave Limb Sounder (MLS) instrument onboard NASA's Aura satellite [Waters et al., 2006]. Measurements of CO, N_2O and H_2O from this instrument have been used for the research described in Chapter 4, in which tracer concentrations are used to identify air belonging to the polar vortex and therefore provide information on its location. The Aura-MLS instrument is mounted on one end of the satellite, pointing at the Earth's horizon, where it can

observe a cross-section of the atmosphere up to an altitude of approximately 90 km [Livesey et al., 2011].

It measures thermal emissions of microwave radiation from molecules in the atmosphere, which allow it to obtain vertical profiles of temperatures, pressures and cloud ice water content, as well as volume mixing ratios for a wide variety of gases. Aura-MLS profiles of geopotential height are also available, which are derived from temperature, pressure and the satellite ephemeris data. The satellite was launched on 15 July 2004, and the MLS instrument began making scientific observations during August of that year [Waters et al., 2006].

The Aura satellite has been launched into a polar retrograde orbit at an inclination of 98° and an altitude of 705 km, which allows it to make observations over a latitudinal range of 82° S to 82° N during each orbit. Its orbit is sun-synchronous, so the satellite always makes its measurements at the same local solar times each day during each of its orbits, which have a period of 98.8 minutes. The MLS instrument scans the Earth's limb vertically 240 times during each orbit, producing approximately 3500 vertical profiles per day. The number of measurements made is the same at each latitude covered, which means that the spatial coverage is more detailed near the poles.

The raw spectral data from the satellite instrument then undergoes several levels of processing to produce different types of scientifically useful data files, including calibrated and geolocated microwave radiances (Level 1 data, available from the EOS MLS team at NASA's Jet Propulsion Laboratory (JPL) by request) and vertical profiles of a variety of geophysical products and chemical mixing ratios (Level 2 data), available from the EOS-MLS project website (http://mls.jpl.nasa.gov/data) and the NASA Goddard Space Flight Center Data and Information Services Center (http://disc.gsfc.nasa.gov). The most recent version of the Level 2 data files is v4.2 [Livesey et al., 2015]. Version 3.3 data [Livesey et al., 2011] is used in Chapter4 of this thesis.

The vertical profiles of temperatures, chemical mixing ratios and other geophysical data fields produced using the Aura-MLS data are given on a set of vertical levels divided according to a logarithmic vertical pressure scale. The pressure levels range from 316-0.0032 hPa, but for each product the data is only scientifically useful over a subset of these levels. The temperature and geopotential height, from which it should be possible to derive information on wind velocities using balanced winds, are available up to an atmospheric pressure level of 0.001 hPa, which corresponds to an altitude of roughly 97 km, near the top of the mesosphere. Aura-MLS measures a wide variety of chemicals. Out of these,

carbon monoxide (CO) is known to be a useful tracer in the upper stratosphere and lower mesosphere (USLM) [Manney et al., 2009a], and N_2O is a useful tracer in the lower-middle stratosphere [Sparling, 2000, Jin et al., 2009, Sheese et al., 2016]. Water vapour (H_2O) can also be useful at some altitudes, even though it is more affected by chemical reactions than the other two chemicals and thus does not always meet the usual criteria for being a good tracer [Manney et al., 2009a, Lee et al., 2011, Straub et al., 2012]. MLS measures H_2O up to an altitude corresponding to a pressure level of 0.002 hPa.

Aura-MLS measures CO up to an altitude of approximately 90 km, which is in the upper mesosphere and corresponds to a pressure level of 0.0046 hPa. From the upper troposphere to the lower mesosphere, the vertical resolution of the measurements ranges from 3.5 to 5 km, meaning that the results at each Aura-MLS pressure level are averaged over a layer of air with that thickness. Errors from random noise and smoothing effects for the CO product are such that at low latitudes, the error can often be greater than the value of the mixing ratios, since concentrations of CO in the middle-atmospheric low latitudes are lower than elsewhere. This means that in order to get useful results, it is necessary to average over many profiles by, for example, taking zonal daily means. The polar winter regions, where CO concentrations are much larger due to descent from higher altitudes, are not affected by this problem [Pumphrey et al., 2007, Livesey et al., 2011, 2015]. The Aura-MLS CO data is affected by an issue in which negative CO concentrations often occur below a pressure level where CO concentrations are high. This is particularly notable in the polar vortex region, and means that as high values of CO descend to lower altitudes during the polar winter, negative CO concentrations will often be observed immediately before CO-enhanced air reaches each level. In Chapter 4, where Aura-MLS CO and N_2O concentrations are used to identify air belonging to the polar vortex, negative mean CO concentrations are observed within air assigned to the vortex immediately before the CO enhancement period at each isentropic level studied, showing that the Aura-MLS CO data we use is affected by this issue.

During the validation study for version 2.2 of the CO data [Pumphrey et al., 2007], the Aura-MLS CO data was compared with measurements made by the Fourier Transform Spectrometer onboard the Atmospheric Chemistry Experiment (ACE-FTS) [Bernath et al., 2005] and the Sub-Millimetre Radiometer (SMR) onboard the Odin satellite [Murtagh et al., 2002]. The v2.2 Aura-MLS mixing ratios were found to be positively biased by 25-50% compared with the ACE-FS results. However, for newer versions of the CO product, the biases have been

reduced and are now closer to 20%. In relation to the Odin-SMR results, a very large positive bias was found in the mesosphere, reaching 100% in places, but it is likely that these are due to systematic biases in the SMR data rather than the MLS results [Pumphrey et al., 2007]. Overall, the comparison suggests that Aura-MLS CO concentrations in the mesosphere have a positive systematic error of 20-50%, which needs to be taken into account when carrying out research based on this data [Livesey et al., 2011, 2015].

MLS measures N_2O up to an altitude equivalent to a pressure level of 0.46 hPa, which is in the lower mesosphere and corresponds to a potential temperature of about 2500 K. At most altitudes, the vertical resolution of the N_2O data is 4-6 km. Comparisons between the v2.2 Aura-MLS N_2O data, and results from ACE-FTS, Odin-SMR and the Michelson Interferometer for Passive Microwave Sounding (MIPAS) show that at altitudes above those corresponding to the 100 hPa/ 16 km pressure level, systematic biases between the Aura-MLS N_2O measurements and those obtained using other instruments are all within 5% [Lambert et al., 2007, Livesey et al., 2011, 2015]. In August 2013, the frequency band used to make measurements of N_2O mixing ratios had to be changed after results from the 640-GHz radiometer used up until that time began to suffer from ageing affects. From that point, N_2O measurements were instead obtained using the 190-GHz radiometer, leading to small reductions in precision and resolution [Livesey et al., 2015]. This does not impact on our results in Chapter 4, which use data from 2005-2010.

The satellite data used in Chapter 4 of this thesis was all obtained from the Aura-MLS instrument. However there are a number of other instruments in orbit which provide tracer data that can be useful for studies of this type. Here we describe some of the relevant satellite systems that were considered for later investigation.

Also on board the Aura satellite is the High Resolution Dynamics Limb Sounder (HIRDLS), a limb-scanning infrared radiometer which operated from 29 January 2005 to 17 March 2008. After launch, it was found that the instrument's viewing aperture was mostly obstructed by a loose piece of plastic, causing problems with the measurements. However, it was still possible to make observations through a small portion of the aperture, and by applying correction algorithms to account for the effect of the blocking material upon the radiances, it was possible to retrieve scientifically useful data for most of the intended chemical species. As a side effect of the blockage, the HIRDLS instrument was not able to take measurements at latitudes polewards of 63° S, which means that it

cannot view the Southern Hemisphere polar regions [Gille and Gray, 2013].

The HIRDLS instrument produced approximately 5600 profiles per day. This is considerably more than MLS, which produces 3500 profiles/day, and means that when HIRDLS data is available it generally has better resolution both horizontally and vertically compared to MLS. However, the short time period over which it operated and the lack of measurements in the southern polar regions is a limiting factor on its usefulness.

The Fourier Transform Spectrometer (FTS) is part of the Atmospheric Chemistry Experiment (ACE) onboard the Canadian satellite SCISAT-1, which was launched on 12 August 2003. ACE-FTS began routine operations during February 2004 and is still operational to this day. Unlike MLS and HIRDLS, which work by measuring emission spectra from the Earth's limb, ACE-FTS is a solar occultation instrument which observes the Earth's limb during sunrises and sunsets to obtain absorption spectra [Bernath et al., 2005]. During most of its orbits, it measures one sunrise and one sunset. Since its orbital period is 97.7 minutes, it can observe up to 30 occultations per day [Sica et al., 2008]. The limited number of observations mean that the data produced by this instrument is not by itself detailed enough to be useful for many of the tracer-based methods for investigating vortex dynamics that will be discussed in Chapter 2.4.

However, ACE-FTS also measures profiles of (NO_2) and (NO) up to altitudes of 45 and 105 km, respectively [Hughes and Bernath, 2012]. This, coupled with the fact that the high inclination of the SCISAT satellite's orbit means that more than half of the vertical profiles from ACE-FTS are from the polar regions [Sica et al., 2008], means that ACE-FTS can be used to measure EPP-NO_x descending from higher altitudes [Rinsland et al., 2005, Randall et al., 2006, 2009] .

The Michelson Interferometer for Passive Atmospheric Sounding (MIPAS) instrument, onboard the European Space Agency's (ESA) Envisat satellite, was launched on 1 March 2002 and operated until 8 April 2012.

MIPAS was an unusually flexible instrument, designed so that its standard scan could be adjusted in flight. MIPAS was capable of making measurements up to an altitude of 160 km, which is in the lower thermosphere. By adjusting its azimuthal mirror, it was capable of taking measurements from any latitude including directly at the poles; without the adjustable mirror, its latitudinal range would have been 80°S - 80°N, approximately the same as Aura-MLS [Fischer et al., 2008].

The Sounding of the Atmosphere using Broadband Emission Radiometry (SABER) instrument, onboard NASA's Thermosphere-Ionosphere-Mesosphere

Energetics and Dynamics (TIMED) satellite, was launched in December 2001 and is still producing results to this day. It is an infrared limb sounder, and has been specifically designed with the intention of providing information on temperatures and winds in the mesosphere and lower thermosphere; it can scan a vertical range from 10-180 km. It also measures concentrations of some chemicals such as ozone, carbon dioxide, and water vapour. Its orbit has an inclination of 74.1° (see http://saber.gats-inc.com/index.php), and the instrument is pointed at right-angles to the direction of the satellite's travel. This means that it cannot survey the entire globe continuously. Instead, over a period of approximately 60 days, it takes measurements over a latitudinal range between 83°N - 52°S, and then for the next ∼60-day period flips its coverage so that it measures from 52°N-83°S [Remsberg et al., 2008]. This is a disadvantage for studying events near the poles.

Before continuing on to discuss how the tracer measurements from these satellites can be used to investigate vortex dynamics, we briefly digress to discuss whether temperature and wind information from these satellites could be used to implement some of the trajectory-based methods for investigating the polar vortex described in Chapter 2.2.2. In theory, if information on wind velocities can be obtained at a high enough resolution, it should be possible to use that to run a trajectory model including the upper stratosphere and lower mesosphere. At these altitudes, the isentropic approximation breaks down, and vertical motion would need to be accounted for even over relatively short time scales, so the model would need to be three dimensional. Many of the methods used for investigating vortex dynamics that are described in Chapter 2.2.2 rely on trajectory models and it may be possible to adapt some of them to work in three dimensions. The Aura-MLS and SABER instruments all provide temperature data at these altitudes that can be used to derive winds [Manney et al., 2009a], and data from MIPAS and HIRDLS could also potentially be used. The limb-viewing satellites listed above have a more limited horizontal resolution than nadir viewers, and it is possible the data obtained this way may not be detailed enough for running a 3D trajectory model. However, if temperature information from these satellites could be used to create reanalyses which are reliable in the upper stratosphere and lower mesosphere (USLM), as discussed in Chapter 2.3.1, these could potentially provide data with the required resolution.

The satellites discussed above also measure concentrations of a wide variety of chemicals, some of which are useful tracers for investigating polar stratospheric dynamics. These can be particularly useful for identifying the location of the polar

vortex edge, and tracer-based methods for doing this will be discussed further in Chapter 2.4. Each chemical has a different distribution with respect to altitude, and different sources and sinks. Therefore the locations and altitudes where each individual tracer is useful vary. As a general rule, a chemical is a useful tracer within a given region if its lifetime is longer than the typical timescale over which transport occurs within that region. However, if a chemical is being produced in a given region, this can cause problems when attempting to use it as a tracer there. For locating the vortex edge, chemicals which have different concentrations inside and outside the vortex are particularly useful. This often happens when high-altitude air descends within the vortex during the polar winter. It can also occur when low-altitude air enters the stratosphere via the tropical tropopause.

One such tracer is carbon monoxide (CO). The majority of the carbon monoxide in the middle atmosphere is produced by the photolysis of carbon dioxide (CO_2) in the mesosphere and lower thermosphere [Allen et al., 1999, Filipiak et al., 2005, Engel et al., 2006]. Some CO is also produced in the middle stratosphere due to oxidation of methane, especially in the tropics at an altitude of about 30 km [Allen et al., 1999]. CO is also produced at the surface due to natural processes and combustion, but little of it reaches the stratosphere [Allen et al., 1999]. The major sink of carbon monoxide in the mesosphere and lower thermosphere is breakdown due to reactions with hydroxyl (OH) in sunlit regions, which once more produce carbon dioxide. In the winter polar stratosphere and mesosphere, the lifetime of CO is considerably longer than a month, making it a very useful tracer [Minschwaner et al., 2010]. When light returns to the polar regions in spring, this lifetime drops to about 20 days. This is still comparable with typical timescales for vertical and horizontal travel, which range from weeks to months, so CO can still be useful for investigating transport and dynamics under these circumstances [McDonald and Smith, 2013]. However, when using CO to investigate vortex dynamics during late winter and spring, the fact that CO in sunlit areas may be broken down over time by this loss process may need to be taken into account [Minschwaner et al., 2010].

In the mesosphere, the prevailing flow advects carbon monoxide towards the winter polar regions, where its lifetime is greatly increased, meaning that CO mixing ratios in the polar winter mesosphere are higher than at lower latitudes [Engel et al., 2006], and also meaning that CO is a particularly good tracer in the polar winter regions [Allen et al., 1999]. During the polar winter, descent of high-altitude air through the stratospheric polar vortex advects this air to the stratosphere, where the extra-vortex air has lower concentrations of CO [Engel

et al., 2006]. Since this descending air can reach quite low altitudes, differences in CO mixing ratios between intra and extra-vortex air can potentially be used to identify vortex air throughout the stratosphere. Carbon monoxide is a particularly useful tracer at and above the altitude of the middle stratosphere, because concentrations of it increase with height, while concentrations of most other stratospheric tracer decrease with height and are thus harder to measure [Allen et al., 1999]. Carbon monoxide has been used in a number of studies to measure diabatic descent rates of air through the vortex in the upper stratosphere and lower mesosphere [Allen et al., 2000, Filipiak et al., 2005, Funke et al., 2009, Lee et al., 2011]. Plots of CO concentrations have also been extensively used in a qualitative way to investigate vortex dynamics for altitudes ranging from the mid-stratosphere to the stratopause [Allen et al., 1999, Filipiak et al., 2005, Lee et al., 2011].

Another stratospheric tracer, nitrous oxide (N_2O), is primarily produced at the Earth's surface. It then enters the stratosphere via the tropical tropopause and follows the residual mean circulation to higher latitudes. Since it is broken down by sunlight, especially at higher altitudes, concentrations of N_2O in the stratosphere are highest at lower altitudes and latitudes [Jin et al., 2009]. Some nitrous oxide is also produced in the mesosphere and lower thermosphere as a result of energetic particle precipitation (EPP) [Funke et al., 2008, Sheese et al., 2016].

The main process by which N_2O is destroyed is photolysis. However, some N_2O reacts with excited oxygen in the stratosphere to produce nitric oxide (NO). The chemical lifespan of nitrous oxide in the atmosphere decreases with altitude. In the lower stratosphere its lifetime is measured in years, but it only persists for a few weeks in the upper stratosphere and mesosphere [Jin et al., 2009]. Since, in the middle atmosphere, the lifetime of nitrous oxide (N_2O) is the same or greater than the typical period over which air in this region of the atmosphere undergoes significant advection and mixing, N_2O is a good tracer there [Jin et al., 2009]. Because concentrations of nitrous oxide are lower inside the vortex than outside, it can also be used to help identify the vortex edge. During the polar winter, N_2O profiles are also commonly used to help derive descent rates for air parcels within the polar vortex [Bauer et al., 1994, Greenblatt et al., 2002b, Plumb et al., 2002, Kawamoto et al., 2004]. However, above the mid-stratosphere, it becomes more challenging to use nitrous oxide as a tracer. Firstly, as concentrations of nitrous oxide continue to decrease with altitude, it becomes more difficult to distinguish N_2O concentrations in extra-vortex air from those in intra-vortex air. Then,

near the stratopause, N_2O concentrations in the winter polar region can begin to increase again due to air rich in EPP-produced N_2O descending through the vortex. Depending on the dynamics of each winter season, the N_2O rich air can reach altitudes as low as 40 km (approximately 1250 K) in the upper stratosphere [Sheese et al., 2016], with the N_2O descending furthest during years affected by major SSWs. This non-monotonic behaviour means that above this altitude great care must be taken when using N_2O as a tracer. It is also possible that during periods when this descent is occurring and concentrations of N_2O within the mesospheric winter polar vortex are enhanced, N_2O could then become a useful tracer at altitudes above the stratopause.

The distribution of water vapour with respect to altitude is more complex than for the other tracers, and at some altitudes within the stratosphere it is affected by chemical reactions. However, at some altitudes differences in water vapour concentrations across the vortex edge can still be used to identify air belonging to the vortex, even if it does not always satisfy the definition of a tracer.

In the mesosphere, concentrations of water vapour (H_2O) are lower than in the stratosphere [Engel et al., 2006] and decrease with height, since it is broken down by photolysis, especially at altitudes above about 80 km [Lee et al., 2011]. However, water vapour still survives for weeks in the upper mesosphere and months in the lower mesosphere. Since this is longer than the typical timescales over which transport occurs there, this means that water vapour is a tracer in the mesosphere. During the polar winter, air descending from the upper mesosphere is very dry and can therefore be used as a tracer to investigate descent rates and potentially to identify vortex air.

In the middle stratosphere, the oxidation of methane (CH_4) is a source of water vapour [Straub et al., 2012]. This causes concentrations of water vapour to increase with height within the stratosphere. Therefore, in the lower-middle stratosphere, vortex air descending from above is often moister than the surrounding air and this can be used to identify vortex air [Lee et al., 2011]. But where mixing ratios of water vapour maximize due to production by oxidation of methane, water vapour is not a good tracer [Lee et al., 2011]. So at any given time, the vertical distribution of water vapour within the winter polar vortex will be such that air within the vortex will be moister than the surrounding air up to a certain altitude, will have approximately the same concentration of water vapour both inside and outside the vortex where the maximum due to methane oxidation occurs, and then the vortex air will be dryer than the surrounding air above that altitude. The altitude where the distribution flips over, though, will

tend to vary with time as the descent through the vortex continues. Therefore, water vapour can be a useful tracer at both high and low altitudes within the middle atmosphere, but care must be taken when using it.

The formation of polar stratospheric clouds during winter is also an important sink of water vapour in the lower stratosphere. There are several different types of PSC which are each chemically different. When temperatures in this region decrease below the frost point, PSCs comprised of ice form, causing considerable dehydration of lower polar stratospheric air during some periods of winter [Nedoluha et al., 2003, McDonald et al., 2009].

The EPP IE, described in Chapter 2.2.1, causes relatively high concentrations of odd nitrogen to descend through the vortex from the MLT during the polar winter. This can be measured by instruments such as HIRDLS, ACE-FTS and MIPAS and could potentially be used to help identify the vortex edge at high altitudes during the polar winter since concentrations of it are much higher within the vortex than outside it during that period. However the fact that it breaks down rapidly when exposed to sunlight may lead to problems with using it this way once parts of the polar vortex become sunlit in spring. Also, the amount of EPP-NO_x produced in the mesosphere and thermosphere varies depending on changes in geomagnetic activity and the solar wind, and the amount of it that reaches the stratosphere and mesosphere depends both on the amount produced and on the dynamics of the polar vortex [Sinnhuber et al., 2012]. Both of these factors mean that the usefulness of EPP-NO_x for identifying the vortex edge may potentially vary with time.

2.4 Tracer-based methods for investigating vortex dynamics

As discussed above, satellite observations of chemical observations are readily available in the middle-upper stratosphere, while gridded reanalysis temperature and wind fields are less reliable. Therefore, in order to investigate the dynamics of the polar stratosphere at these altitudes, methods based on tracer observations are likely to give the most reliable results. Also, tracer-based methods can often provide useful information about stratospheric dynamics while requiring little or no additional information other than the satellite observations themselves; in this section, we will focus on these.

One way to learn about the dynamics of a region using tracers is to look

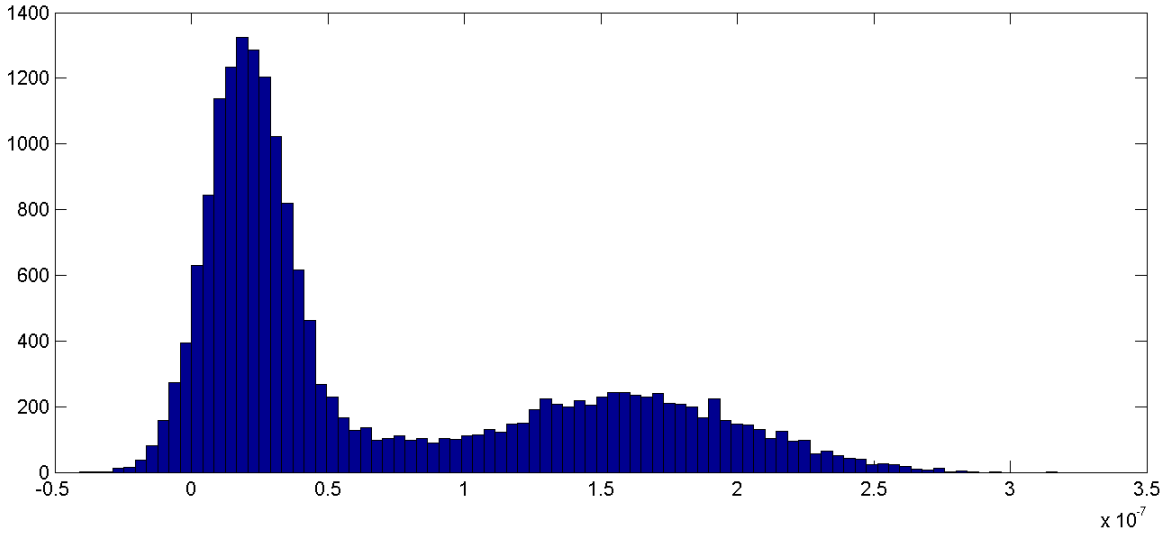

Figure 2.5: PDF of CO concentrations (vmr) for 16th August 2009 over the Southern Hemisphere at a potential temperature of 900 K (approximately 31 km altitude or 10 hPa), based on observations from the Aura-MLS satellite.

at the probability distribution function (PDF) of concentrations of that tracer. Figure 2.5 shows an example of such a PDF, based on measurements of carbon monoxide (CO) from the MLS instrument onboard the Aura satellite, over the Southern Hemisphere at a potential temperature of 900 K (approximately 31 km altitude) for the 16th of August 2009. For this day, the distribution is bimodal, with two roughly Gaussian peaks corresponding to relatively high and low CO values, which are separated by a minimum with few observations. This distribution does include some negative values; this is because the measurements are affected by some noise, and removing these measurements would affect the statistical properties of the results [Livesey et al., 2011]. Mid-August is well within the Southern Hemisphere polar vortex season, and air enriched with CO will be descending from higher altitudes; therefore the region of high CO values shown here should correspond to intra-vortex air. The measurements of low-CO air should then correspond to air outside the vortex. The valley of intermediate values then corresponds to a mixing barrier between the two regions.

The minima of tracer PDFs such as these can be used to identify transport barriers in the stratosphere such as the polar vortex edge barrier and the boundary between mid-latitudes and the subtropical regions, as stated in Sparling [2000], a review paper which discusses a number of ways that PDFs can be useful for investigating stratospheric dynamics.

Sparling [2000] describes some methods for obtaining the approximate phys-

ical latitude of transport barriers from PDFs. Firstly, if the mixing value χ_{min} associated with a minimum in the PDF $P(\chi)$ can be identified, we can gain insight into the position of the transport barrier associated with that minimum by taking tracer measurements from a small interval centred on χ_{min} and looking at the PDF of their latitudes. The range of latitudes spanned by measurements within this interval is referred to as the "support" for measurements in the neighbourhood of χ_{min} and the PDF of the latitudes is referred to as a "conditional PDF". The most probable latitude for the observations within this conditional PDF can then be taken to be the most likely location of the barrier. Another way of identifying the most probable physical latitude of stratospheric barriers is to look at how the average tracer mixing ratios $\bar{\chi}$ (either the mean or the mode can be used here) change with respect to latitude ϕ. If we look at the rate of change $\frac{d\bar{\chi}(\phi)}{d\phi}$, then extrema in this function, corresponding to areas where mixing ratios are changing rapidly with respect to latitude, are likely to correspond to barriers [Sparling, 2000]. However, in the case of the vortex, its edge is often distorted and curved due to interactions with planetary waves, and the structure of the vortex is not always zonally symmetric. In these cases, just finding the approximate physical latitude of the vortex edge using these methods may not provide adequate information. Using equivalent latitude instead would solve this problem, but if this was calculated using potential vorticity, this would require the use of gridded wind data, which would remove the major advantage tracer-based techniques have of not requiring additional data.

Sparling [2000] also introduces the concept of chemical distinction. If tracer PDFs $P(\chi_a)$ and $P(\chi_b)$ are calculated for two adjoining regions of the atmosphere "a" and "b", we should expect that a smaller overlap between their distributions would be related to a stronger transport barrier between the two regions. Therefore it would be helpful to be able to define a quantitative measure, called "chemical distinction", to quantify this lack of overlap. Two different methods are given for calculating this quantity. The first is to compare the separation of the peaks of each sub-PDF with their standard deviations. If the peaks of each subdistribution are further apart than the sum of their standard deviations, then we can state that the distributions are chemically distinct. The chemical distinctness is then defined by

$$\delta \equiv \frac{|\bar{\chi_a} - \bar{\chi_b}|}{\sigma_a + \sigma_b},$$

where $\bar{\chi_a}$ and $\bar{\chi_a}$ are the modes of the tracer PDFs for each of the regions "a"

and "b" (the mixing ratios at the peak of each PDF), and σ_a and σ_b are the "inner" standard deviations of each PDF. These "inner" standard deviations are calculated only from tracer data with mixing ratios between $\bar{\chi_a}$ and $\bar{\chi_b}$. Tracer PDFs, especially those calculated over limited physical areas, can often be asymmetric and the "outer" standard deviations may not have anything to do with the overlap between the two distributions. The air masses described by $P(\chi_a)$ and $P(\chi_b)$ can then be considered to be chemically distinct and thus likely to be separated by a strong barrier if $\delta > 1$. Figure 2.6 shows an example of the use of this method from Sparling [2000] for finding the chemical distinction between the tropics and midlatitudes during a period (25 December 1992 - 5 January 1993) in the northern winter. The light grey area is the total tracer PDF for N_2O over latitudes from the equator to 55° N at 10 hPa (about 32 km), and $P_m(\chi)$ and $P_t(\chi)$ are the PDFs for the midlatitudes 15-55° N and tropical regions 0-15° N respectively. The modes (peaks) and inner standard deviations of the tropical and midlatitude PDFs are also marked on the plot. It can be seen that the difference between the peaks is greater than the sum of the standard deviations and therefore there is likely to be a transport barrier separating the tropical and midlatitude regions during this period. For this example, the chemical distinction between these two regions is $\delta = 1.3$.

Another way to calculate a quantity representing the chemical distinction of two air masses is to find the area of overlap A between their PDFs. Figure 2.6 shows this area for the example discussed above. This area represents the proportion of measurements in each region that are chemically similar to the other region. The larger the overlap, the less likely it is that the two regions are separated by a barrier to mixing. If the areas underneath the probability distributions for regions a and b are A_a and A_b, then the area of overlap can take any value from zero, when the two regions are completely disjoint, to $min(A_1, A_2)$, when one region's PDF is completely within the other. In order to calculate this area of overlap, it is first necessary to know which measurement belongs to each air mass so that a separate PDF for each region can be obtained. For example, if the regions corresponding to each air mass are defined on the basis of latitude, as is the case in Figure 2.6, the latitude of each measurement must be known.

Measurements from satellites are not generally evenly distributed around the globe, meaning by default that some regions will be more heavily represented than others in tracer distribution plots. However, it is possible to obtain an area-weighted PDF by enuring that the number of observations used in each latitude band $\Delta\phi$ is proportional to $\cos(\phi)$, either by removing some measurements or

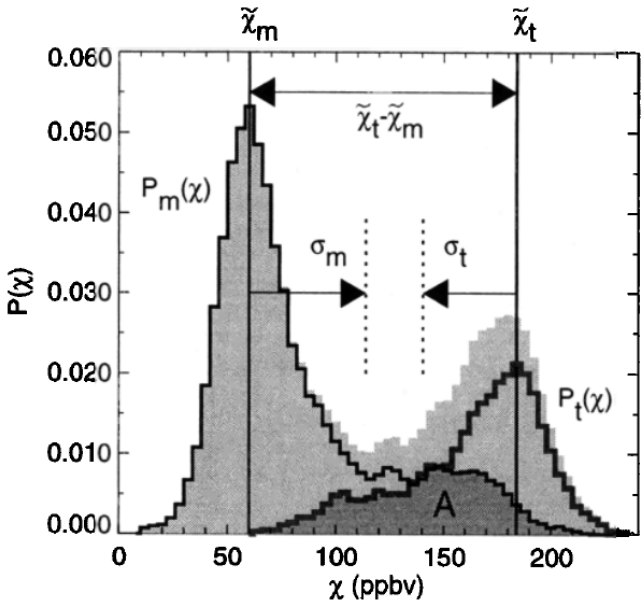

Figure 2.6: Example of how to calculate the chemical distinction between two air masses, taken from Sparling [2000]. This shows an N_2O tracer PDF based on measurements from the CLAES instrument onboard the UARS satellite for 25 Dec 1992 - 5 Jan 1993 over 0-55° N at 10 hPa. The PDFs $P_m(\chi)$ and $P_t(\chi)$ over the midlatitudes and tropical regions respectively are shown in this diagram, along with the locations of their modes and their "inner" standard deviations. The area of overlap A between the distributions $P_m(\chi)$ and $P_t(\chi)$ is also shown (in dark grey).

simply by applying a latitude-dependent weighting factor to them. For an area-weighted PDF obtained using measurements on a pressure or isentropic level in the stratosphere, the area $\int_{\chi_1}^{\chi_2} P(\chi)d\chi$ under the PDF function between two values of the tracer mixing ratio will be directly proportional to the geographical area occupied by air with tracer concentrations within that range. Also the area A of overlap between PDFs from different regions will be directly proportional to the geographical area over which chemical concentrations are characteristic of both regions.

Tracer PDFs usually have Gaussian cores, but if calculated over limited latitudinal regions can often have long, asymmetric, skewed, non-Gaussian tails. These are often associated with either mixing with other regions with different chemical signatures, perturbations by planetary waves causing the structure of the region to no longer be zonally symmetric, or in some cases, with air arriving vertically from a different isentropic or pressure level [Sparling, 2000, McDonald and Smith, 2013].

Neu et al. [2003] use PDFs to investigate the barriers at the edges of the "tropical pipe" region which separates the tropical stratosphere from the winter surf zone on one side and the summer hemisphere on the other. The tracer gradients between the tropics and the surf zone are much sharper than those between the tropics and the summer hemisphere, but for the purposes of this paper, it is still reasonable to treat both as edge regions since barriers exist in each location. They find the approximate physical latitude of the barriers using the method from Sparling [2000] in which the most probable latitude within the conditional PDF of latitudes corresponding to N_2O tracer concentrations near a minimum of the N_2O PDF is identified as the location of the barrier/s.

They also calculate the approximate area of the barrier regions. Because their PDFs are area-weighted, they can calculate the approximate area associated with tracer values over any given interval. Many of their calculated PDFs show a "valley" with relatively few measurements, associated with the subtropical edge, in between two peaks associated with tropical and midlatitude measurements. They then select an interval of tracer values which extends from midway between the tropical peak and the subtropical minimum, to midway between the midlatitude peak and the subtropical minimum. The measurements within this interval are then defined to be part of the subtropical edge region. They are then able to calculate the approximate area of the subtropical edge regions, showing that the area of the edge in the summer hemisphere is up to 60% of the entire hemisphere, while the edge region in the winter hemisphere is much narrower, presumably due

to its interactions with the surf zone, which causes sharp tracer gradients much as the interaction between the surf zone and the polar vortex does. Although the results they show are for the subtropical barriers, the methods they use could just as well be applied to the polar vortex edge barrier.

Palazzi et al. [2012] also use conditional PDFs of latitudes for measurements within the "subtropical barrier" region of N_2O and methane PDFs to investigate the behaviour of this barrier. They calculate these PDFs based on observations from four different satellites, Aura-MLS, MIPAS-Envisat, Odin-SMR and HALOE-UARS, and then compare the results. They find good agreement between the position of the subtropical barrier determined using data from each instrument over isentropic levels ranging from 520-1100 K. Using data from HALOE, they are also able to observe shifts in the position of the subtropical barrier at 600 K in response to changes in the phase of the quasi-biennial oscillation (QBO). It is also possible to use measures based on the complexity of tracer PDFs, such as Shannon entropy or the more generalized Rényi entropy [Krützmann et al., 2008], to identify locations where mixing may have occurred.

McDonald and Smith [2013] use a method similar to the area-based chemical distinction method introduced in Sparling [2000] to identify air belonging to the stratospheric polar vortex. Carbon monoxide measurements from the Aura-MLS satellite are used, with measurements being collected over 11 day periods in order to improve the statistical properties of the results. Over a wide range of altitudes, PDFs of carbon monoxide over the winter hemisphere are bimodal, and can approximately be described as the sum of two approximately Gaussian distributions which correspond to measurements within and outside the vortex, with the intra-vortex measurements having higher concentrations of CO. Figure 2.7 shows an example of the type of distribution which is commonly observed, and how it can be approximated by the sum of two Gaussian distributions. The main PDF, shown in black, is based on carbon monoxide measurements over the period from 10-20 July 2005 over the Southern Hemisphere at 0.3 hPa (approximately 57 km) and is clearly bimodal. The blue and red lines are Gaussians fitted to the two peaks of the distribution, and the green line shows the sum of the two Gaussians, which is a very good fit to the original PDF.

McDonald and Smith [2013] use an automatic process based on these distributions to identify tracer value thresholds corresponding to intra- and extra-vortex air. First, the intra and extra-vortex subdistributions are fitted to Gaussian curves using an algorithm, and then the PDF is divided into three sections, using the means of the Gaussian distributions as thresholds. A high proportion of

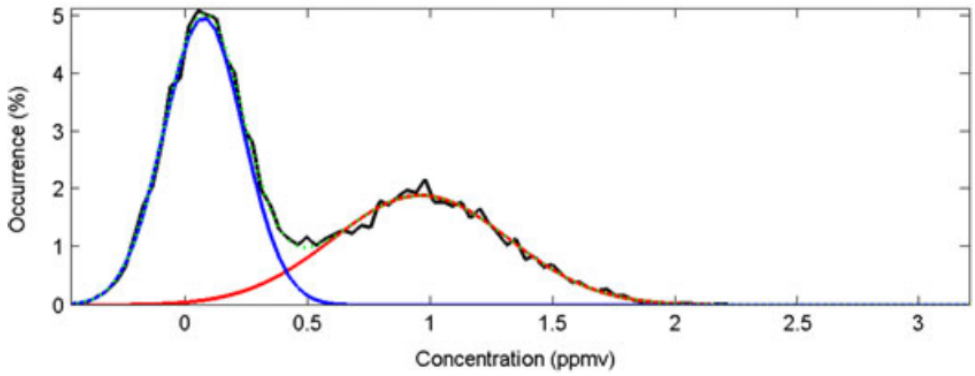

Figure 2.7: Example, taken from McDonald and Smith [2013], showing a PDF of Aura-MLS carbon monoxide volume mixing ratios (black line) over the Southern Hemisphere from 10-20 July at 0.3 hPa, as well as two Gaussians (blue and red lines) fitted to the upper and lower parts of the distribution. The green line shows the sum of the two Gaussians.

measurements above the uppermost threshold, which is the mean of the Gaussian distribution with the highest CO values, are shown to fit within the location of the vortex edge determined independently by finding the equivalent latitude contour which maximizes the impermeability function (see Chapter 2.2.2).

A trajectory-mapping technique is used to illustrate the results and increase the resolution of plots which visually compare the PDF-based results with the standard impermeability-based vortex edge. For each measurement within the 11-day period of observations that was used to assemble each PDF, a forwards or backwards trajectory is calculated to determine what position that measurement will have been advected to on the central date. These advected measurements can then all be shown together to create a high-resolution plot of the distribution of carbon monoxide on the central date. Figure 2.8 shows an example of such a plot for 15 August 2005 on the 900 K isentropic level, in the Southern Hemisphere. The vortex edge line found using impermeability is marked in green, measurements above the mean of the Gaussian distribution with the highest CO mixing ratios are shown in red, measurements below the mean of the other distribution are shown in blue, and intermediate measurements are shown in grey. It can be seen here that the measurements marked in red are all well within the vortex for this day, that the blue measurements are all outside, and that, although the grey measurements are in general widely distributed, there is a band of only grey measurements along the inner edge of the green vortex edge line. This suggests the existence of a distinct "vortex edge region" with CO concentrations intermediate between those of the vortex core and extra-vortex air. Plots from later on in the

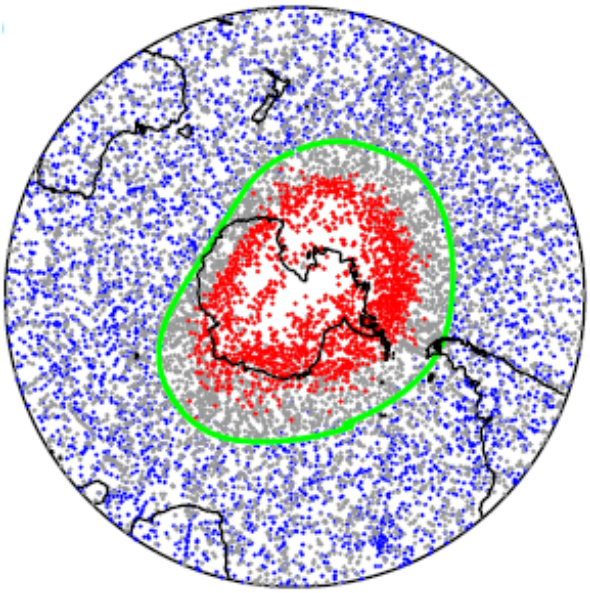

Figure 2.8: CO observations plotted for 15 August 2005 at 900 K based on data from 10-20 August (figure taken from McDonald and Smith [2013]). The results are colour coded according to which part of the CO PDF over 10-20 August they belong to: red measurements are those with CO concentrations above the mean of the higher Gaussian, blue measurements have concentrations below the mean of the lower Gaussian, and grey measurements have intermediate CO values. The standard impermeability-based vortex edge line is also shown in green.

season, as erosion by planetary waves sharpens the tracer gradients at the vortex edge, show this grey area diminishing and a more precise fit between the region occupied by red measurements and the impermeability-based vortex edge.

All of the methods for investigating stratospheric dynamics and identifying vortex air discussed so far in this section have used information from observations of a single chemical tracer. However, a considerable amount of research has been carried out using two (or more) tracers simultaneously. Much of this has focused on the strong linear correlations often observed between long-lived tracers in the stratosphere. The concentrations of long-lived tracers in the stratosphere are often highly correlated, with a linear relationship [Fahey et al., 1990, Plumb and Ko, 1992, Waugh and Polvani, 2010]. For tracers which originate in the troposphere and enter the stratosphere near the tropics, contours of constant tracer mixing ratio generally tend to slope downwards towards the pole relative to isentropic surfaces. The Brewer-Dobson circulation tends to sharpen this slope, while isentropic mixing occurring in areas such as the surf zone tends to flatten it. If the lifetime of two such chemical tracers is considerably greater than the typical

timescale of transport in the stratosphere, and the timescale over which isentropic mixing takes place is considerably faster than the timescale over which meridional transport occurs due to the Brewer-Dobson circulation, then concentrations of the two tracers will have a strong linear relationship [Plumb and Ko, 1992], which can be represented on a tracer-tracer scatter plot with a straight line. This linear relationship will still be visible even when measurements from different isentropic levels are shown on the same plot. If one or more of the tracers are not entirely conserved within the physical region being investigated, for example if there are sources or sinks there, then the scatter plot will instead show a curved line. These conditions hold within the surf zone, but since this is not wide enough to allow isentropic mixing over the entire globe, linear relationships will only occur in specific regions of the stratosphere [Plumb, 1996]. In the vicinity of the transport barriers at the polar vortex edge and on each side of the "tropical pipe", the conditions introduced in Plumb and Ko [1992] do not hold due to isentropic transport being impeded. Therefore, in practice, the correlation curves between two tracers will differ depending on the dynamical region they are calculated over. Figure 2.9 shows an example of this from Plumb et al. [2002]. The red dots and green markers plotted on this N_2O-CFC tracer-tracer plot are simulated observations from a 3D transport model driven by reanalysis wind data from the NASA Goddard Space Flight Center. The large blue, cyan and purple markers in Figure 2.9 are balloon and aircraft observations made on dates on or near 5 March during the Stratospheric Aerosol and Gas Experiment (SAGE) III Ozone Loss and Validation Experiment (SOLVE). In this case, the observed measurements do not entirely match the simulated measurements. For the purposes of this discussion, the simulated measurements will be focused on. All the simulated observations are from northwards of 40° N on 5 March 2000. Here, observations from a range of altitudes are amalgamated into a single plot, with the lowest-altitude observations being from the 100 hPa pressure level (corresponding to an altitude of approximately 16 km). It can be seen that the majority of data points are clustered around two lines. Within each line, there is a well-defined correlative relationship between mixing ratios of N_2O and CFCs, but for the topmost line, the relationship is more nearly linear than for the lowermost line. According to Plumb et al. [2002], the topmost line corresponds to intra-vortex air and the lowermost air corresponds to extra-vortex air, demonstrating that the exact details of the relationship between long-lived tracers can differ between different regions of the stratosphere. There are also a smaller number of data points in between the two main correlation curves, which according to Plumb et al. [2002] correspond to

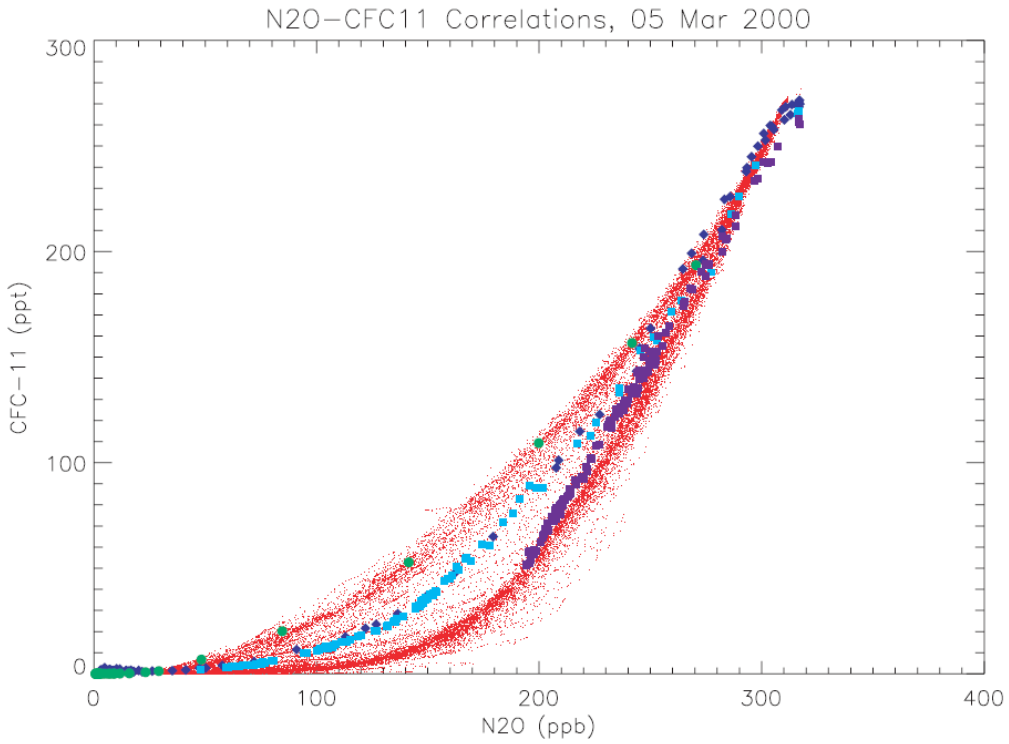

Figure 2.9: Tracer-tracer scatter plot of CFC-11 vs N_2O for 5 March 2000, taken from Plumb et al. [2002]. The red dots show simulated measurements of these tracers from a 3D transport model driven by reanalysis wind data from the NASA Goddard Space Flight Center. These are all from locations north of 40° N and from a range of altitudes with the lowest altitude corresponding to a pressure level of 100 hPa. The larger coloured markers shown here represent actual observations made during the SAGE III Ozone Loss and Validation Experiment (SOLVE), for dates on and near the 5 March.

air that has undergone mixing. Since the data points that represent intra- and extra-vortex air are separated spatially, this suggests that it should be possible to identify air that belongs to the vortex from tracer-tracer plots such as these.

When two regions have different chemical compositions, measurements belonging to them will be in different locations on a tracer-tracer scatter plot. When mixing occurs between the two regions, the mixed air will be located somewhere on a straight line between these regions. If a specific mixing event that affects a number of observations takes place, then a well-defined "mixing line" is sometimes observable on the tracer-tracer plot. If the original location of each measurement is known, these mixing lines can be used to identify where mixing between different regions is taking place. In Morgenstern et al. [2002], this approach is used to identify mixing between polar vortex and mid-latitude air.

If regions of intra-vortex, extra-vortex and mixed air can be distinctly identified on a tracer-tracer scatter plot, then if the original locations of the measurements are known, this information can be used to find the location and extent of the stratospheric polar vortex and the mixing region between it and the surf zone. Plumb et al. [2002] manually identify regions on a tracer-tracer plot of N_2O vs NO_y that correspond to each of these three regions. When the positions of measurements within these regions are plotted on polar stereographic maps for potential temperatures of 480 and 725 K, there is an impressive agreement between the locations of the measurements thought to correspond to vortex and "mixed" air, and the apparent position of the vortex and its edge on plots of N_2O concentrations.

Greenblatt et al. [2002a] also use the positions of measurements on a tracer-tracer scatter plot to identify intra-vortex, extra-vortex and mixed air, except that they use potential temperature as one of the tracers. Since potential temperature is conserved unless diabatic heat transfer takes place, it behaves as a tracer over short time scales, making this approach possible. They use scatter plots of N_2O vs potential temperature to identify mixed air from three different aircraft flights that took place as part of the SOLVE/THESEO 2000 (Stratospheric Aerosol and Gas Experiment III (SAGE III) Ozone Loss and Validation Experiment/Third European Stratospheric Experiment on Ozone 2000) campaign. For each flight, they compare the measurements made with measurements taken from a reference flight that took place on a similar date, but which never left the vortex. Measurements not belonging to the vortex could then be identified since they were separated from the reference measurements in N_2O–potential temperature space.

In Chapter 4 we will discuss research in which tracer-tracer scatter plots of CO vs N_2O and CO vs water vapour are used to identify air belonging to the polar vortex. A k-means clustering scheme is used to automatically sort the measurements into intra- and extra-vortex air. The results generally match well with the extent of the vortex determined using an impermeability-based algorithm to find the vortex edge. Carbon monoxide is a particularly useful tracer because during the polar vortex season, concentrations of CO are much higher inside than outside the vortex as high-CO air descends from the mesosphere, while in contrast concentrations of the other two tracers are in general higher outside the vortex.

As a result of this, the patterns shown in the Chapter 4 tracer-tracer plots are similar to those found in studies observing the barrier between the troposphere and stratosphere, in which tracer-tracer plots are also widely used [Pan et al., 2004, Patmore and Toumi, 2006, Pan et al., 2007]. In these studies, mea-

surements located within the tropopause are identified using tracer-tracer scatter plots in which a tracer (generally water vapour) that is prevalent in the troposphere but rare in the stratosphere is plotted against a different tracer for which these abundances are reversed, leading to a scatter plot which shows a characteristic pattern in which two tracer correlation lines meet near the origin in an "L" shape, with measurements in that region corresponding to locations near the tropopause barrier. In the case of the studies of strato-tropospheric coupling, the L shape is generally "smoothed" near the corner due to mixing occurring across the tropopause and thus the corner is replaced with a mixing line. However, the barrier between the stratospheric polar vortex and the surf zone is much stronger, and a sharp corner near the origin is commonly observed.

For the purposes of identifying air belonging to the stratospheric vortex from tracer-tracer scatter plots, the chemicals used do not necessarily actually need to be tracers. The only requirement is that the air inside the vortex is chemically different from the air outside in such a way that the two regions are clearly distinguished on a scatter plot based on concentrations of the chemicals. Different chemicals or tracers will be appropriate depending on the altitude, location, and time of year. For example, carbon monoxide is a very useful tracer for distinguishing stratospheric vortex air, but it is only useful during those times of the year in which strong descent causes CO-rich air to reach lower altitudes.

2.5 Summary

The stratosphere is divided into a number of dynamically distinct regions: the quiescent summer hemisphere, the tropical "pipe" region, the polar vortex within which air descends from higher altitudes, and the turbulent "surf zone" which surrounds it. The original motivation for the research contained in this thesis was to investigate the dynamical factors affecting the descent of air from the mesosphere and lower thermosphere (MLT) into the stratosphere through the stratospheric vortex.

There is a strong barrier to transport at the edge of the stratospheric polar vortex caused by powerful zonal winds. This confines the high-altitude air within the vortex as it descends and also protects some chemicals originating from higher altitudes, such as carbon monoxide (CO) and odd nitrogen (NO_x), from breakdown due to photolysis or photodissociation. However, in the Northern hemisphere, the stratosphere is periodically affected by dramatic dynamical

events called stratospheric sudden warmings (SSWs). During the most dramatic of these events, the barrier at the edge of the vortex can break down entirely, causing the air contained within the vortex to mix with extra-vortex air, and disrupting the descent of air within the vortex. However, after some of the most powerful SSW events, a particularly strong vortex reforms in the upper stratosphere, within which strong descent takes place.

It is clear that changes in the strength of the vortex edge transport barrier affect the descent of air through the vortex. It is therefore potentially very useful to develop methods for measuring the strength of this barrier. Many commonly-used methods for investigating transport barriers are based on Lagrangian trajectory models, in which the paths of air parcels are traced over time. In Chapter 2.2.2, we review methods based on this Lagrangian approach that have been used to locate the vortex edge and measure the strength of the associated barrier. In Chapter 3, we use a method based on the lengths of these trajectories to develop measures of barrier strength.

The Lagrangian trajectory-based methods used for investigating vortex dynamics all rely on the availability of reliable gridded wind velocity data, which is usually obtained from reanalyses. As discussed in Chapter 2.3.1, reanalysis data becomes less accurate at altitudes above the mid-stratosphere due to a lack of assimilated temperature and wind observations in these locations. This means that the trajectory-based methods discussed in Chapter 2.2.2 become less useful. However, measurements of chemical tracers from satellite instruments are still readily available at these altitudes. Therefore, we investigate methods based on measurements of tracer concentrations that could be used to identify the location of the polar vortex. In Chapter 2.3.2, we discuss a variety of satellite instruments that measure tracer mixing ratios in the stratosphere and mesosphere, including Aura-MLS, data from which was used in the tracer-based research described in Chapter 4. Chemical tracers that are potentially useful for locating and investigating the polar vortex include carbon monoxide (CO), nitrous oxide (N_2O), and water vapour (H_2O), as well as methane (CH_4) and methyl chloride (CH_3Cl).

In Chapter 2.4, we discuss how methods based on satellite chemical concentrations can be used to investigate polar vortex dynamics. The probability distribution functions (PDFs) of tracer measurements can be used to identify dynamically distinct regions within the stratosphere, such as the intra-vortex region. Once measurements of intra-vortex air have been identified in this way, the location of the vortex can be obtained from the physical location of the measurements. We discuss PDF-based methods that can be used to identify vortex air,

and also how more than one tracer can be used simultaneously to obtain extra information. In Chapter 4, we use a method based on clustering of CO and N_2O observations to identify air belonging to the vortex.

Chapter 3

A quantitative measure of polar vortex strength using the function M[1]

3.1 Introduction

During winter, strong winds associated with the stratospheric polar vortices form a transport barrier which isolates air in the stratospheric polar region from air at lower latitudes. Due to the Brewer-Dobson circulation, air within the polar vortex tends to descend to lower altitudes. Changes in the strength of the barrier and the rate of descent within the vortex have profound impacts on the composition of air in the polar stratospheric regions [Hood and Soukharev, 2005, Huck et al., 2005, Harvey et al., 2008, Randall et al., 2009, Olascoaga et al., 2012]. This is particularly evident during stratospheric sudden warmings (SSWs) [Matsuno, 1971], during which the polar vortex is severely disrupted and large-scale mixing between air inside and outside the vortex can occur.

In this paper, we will focus on finding quantitative measures of horizontal mixing and transport in the vicinity of the polar vortices. One aspect of vortex dynamics which it would be particularly useful to characterize is the permeability of the vortex barrier. A wider and stronger vortex barrier will contribute to larger differences in the chemical composition of air between the inside and outside of the vortex. Also, since the vortex forms during the polar night, it can prevent chemicals within it such as odd nitrogen (NO_x) from photodissociating.

[1] An edited version of this paper, Smith and McDonald [2014], was published by AGU.

Polar vortex dynamics are also known to have a modulating effect upon the energetic particle precipitation indirect effect (EPP IE), in which reactive chemical species such as NO_x produced by energetic particles from the solar wind in the mesosphere and lower thermosphere (MLT) descend to the stratosphere, where they can destroy ozone. Over the past decade, major SSWs in the northern stratospheric polar vortex during early 2004, 2006 and 2009 have been associated with large enhancements in the amount of EPP-produced NO_x reaching the stratosphere. Interestingly, for 2006 and 2009, geomagnetic activity was lower than usual, with the geomagnetic Ap index being significantly below the average since 1988 [Randall et al., 2009]. This suggests that under some circumstances vortex dynamics can have an effect on the EPP IE which is more significant than that of the amount of incoming EPP itself [Randall et al., 2009]. During the 2006 and 2009 SSWs, the stratopause broke down entirely before reforming at a very high altitude [Manney et al., 2009b, France and Harvey, 2013]. For both years, very strong diabatic descent occurred within the northern polar vortex as the stratopause reformed [Manney et al., 2009b] and it seems likely that this increased rate of descent is one of the causes of the enhanced EPP IE during these years. However, the precise mechanism by which SSWs and other changes in polar vortex dynamics affect the strength of the EPP IE is not yet fully understood. A better quantification of polar vortex dynamics will therefore be helpful when investigating this connection.

A variety of methods have been used in the past to investigate the dynamics of the polar vortices and the strength of the vortex barriers. Changes in the area and shape of the vortex can be captured by diagnostics based on elliptical diagnostics of potential vorticity (PV) contours [Butchart and Remsberg, 1986, Waugh, 1997, Waugh and Randel, 1999, Matthewman et al., 2009, Hannachi et al., 2011, Mitchell et al., 2010]. The amount of air entering and leaving the vortex can also be quantified by initializing an artificial tracer within the vortex, advecting the tracer using a Lagrangian trajectory model, and then measuring the quantity of the tracer which has left the vortex [Chen, 1994, Chen et al., 1994, Steinhorst et al., 2005, Grooßet al., 2008]. Steep gradients of potential vorticity can be used to identify mixing barriers [McIntyre and Palmer, 1984, Nash et al., 1996, Steinhorst et al., 2005]. Methods based on effective diffusivity [Nakamura, 1996, Haynes and Shuckburgh, 2000, Hauchecorne et al., 2002] and advection of material contours [Chen, 1994, Norton, 1994, Waugh and Plumb, 1994, Waugh et al., 1994] can also be used to identify the vortex edge by finding PV contours for which the rate of mixing and/or contour lengthening is at its

minimum. Others have used chemical constituent distributions to identify the vortex [Sparling, 2000, Krützmann et al., 2008, McDonald and Smith, 2013].

However, methods based on Lyapunov exponents are those most commonly used for investigating mixing and transport barriers in the stratosphere. These approaches include finite-size Lyapunov exponents (FSLEs) [Joseph and Legras, 2002], and finite-time Lyapunov exponents (FTLEs). These are both calculated by measuring how the distance between adjacent air parcels changes over time, with FTLE values being obtained from the separation between the parcels after a set time period, while FSLEs are found from the time taken for the distance between the parcels to reach a given threshold value. FTLEs have been used by Pierrehumbert and Yang [1993] and Bowman [1993] to analyze mixing, with Bowman [1993] applying this measure directly to the polar vortex. Later, Garny et al. [2007] calculated monthly fields of FTLEs from NCEP/NCAR reanalysis data at potential temperatures of 450-650 K and used these along with a regression model to identify the physical causes of trends and variability in stratospheric mixing. More recently, Beron-Vera et al. [2012] used FTLEs to identify transport barriers in the stratosphere. de la Camara et al. [2010] have also applied FTLEs to balloon flights and reanalysis data in order to analyze the breakup of the Southern hemisphere vortex in 2005.

In this paper we investigate polar vortex dynamics by applying a recently-conceived Lagrangian descriptor known as the "function M" [Jimenez Madrid and Mancho, 2009, de la Camara et al., 2012] to wind speed data from the MERRA reanalysis [Rienecker et al., 2011]. We use this, along with potential vorticity (PV) data from the MERRA reanalysis, to derive two quantitative measures of vortex dynamics which we can use to trace the dynamical evolution of the polar vortices as they evolve through time. We also describe a strong linear dependence observed between values of the function M in the vortex edge region calculated over different periods of time. It is possible that variations in this dependence could be used in future to investigate the coherence of dynamical structures in the stratosphere.

In Chapter 3.2 the function M and derived quantitative measures of vortex strength are described, along with details of the calculations. Chapter 3.3 presents results for these quantitative measures over a number of different time periods in both the Northern and Southern hemispheres, and the ability of these to capture changes in the dynamical properties of the stratospheric polar vortices are discussed. We also describe the linear dependence found between values of the function M calculated over different time periods. Chapter 3.4 presents a

summary and overview of our results.

3.2 Methodology

3.2.1 The function M

The function M is a measure based on the length of Lagrangian fluid parcel trajectories. On a two-dimensional surface, the value of M at a specific position and time (x_0, y_0, t_0) is the Euclidean arc length of a parcel trajectory calculated over an interval of time $(t_0 - \tau, t_0 + \tau)$ centered at t_0.

$$M_\tau(x_0, y_0, t_0) = \int_{t_0-\tau}^{t_0+\tau} dt \sqrt{\left(\frac{dx(t)}{dt}\right)^2 + \left(\frac{dy(t)}{dt}\right)^2} \tag{3.2.1}$$

In this paper, the value of M will be expressed in terms of the number of kilometers that the air parcel travels over the course of the time interval.

The function M was first defined in the paper Jimenez Madrid and Mancho [2009], in which the minima of M are used to find "distinguished trajectories" within dynamical systems. A distinguished trajectory is a type of trajectory that plays an organizing role within a time-dependent dynamical system [Ide et al., 2002]. Mendoza and Mancho [2010, 2012] then used the function M to investigate the structure and evolution of ocean flows in the vicinity of the Kuroshio current. The recent paper by de la Camara et al. [2012] was the first to use the function M to investigate horizontal transport in the atmosphere and specifically the southern polar vortex.

de la Camara et al. [2012] used the function M to create plots of the structure of the southern polar vortex during the 2005 southern spring. One of their main aims was to identify Lagrangian coherent structures (LCS) such as hyperbolic invariant manifolds and trajectories. Hyperbolic invariant manifolds are material lines which cannot be crossed by fluid parcels. They can be stable or unstable; stable manifolds repel fluid parcels near them while unstable manifolds attract them. In a time-dependent system, these material lines are advected by the fluid flow as time passes. When a stable and an unstable manifold intersect, their intersection point (or the path that the intersection point traces out as time passes) is a hyperbolic trajectory. A fluid parcel whose trajectory begins near the stable manifold and approaches a location near this crossing point cannot cross either manifold and so is advected away along the unstable manifold. Air parcels that

are close to each other but on different sides of the stable manifold can be advected in different directions and become widely separated [de la Camara et al., 2010]. Therefore hyperbolic trajectories are generally associated with mixing and also, near the vortex edge, with material entering and leaving the vortex. Hyperbolic trajectories and manifolds in general become more visible as the period over which M is calculated increases [de la Camara et al., 2012].

To calculate the function M it is necessary to first calculate Lagrangian parcel trajectories at each point. We used a 2D isentropic parcel trajectory model driven by MERRA reanalysis horizontal wind velocity data [Rienecker et al., 2011]. The MERRA data grid used has a resolution of $0.5°$ latitude by $0.66\dot{6}°$ longitude and the positions of the air parcels are calculated and saved at hourly intervals. The model uses a 4th order Runge-Kutta integration scheme to estimate the position of the air parcel after each time step. The starting points of the forward and backward trajectories are defined on a grid with the same resolution as the MERRA data. The value of the function M at each point is then the sum of the Euclidean arc lengths of the forward and backward trajectories. We calculate the great circle distances between the positions of each air parcel at successive time steps, and while doing so convert from positions measured with respect to latitude and longitude to distances in terms of kilometers. We then sum these to find M for each trajectory.

The process of calculating the function M is fairly computationally intensive. Although the computational time needed to calculate M compares favorably with that needed for the calculation of FTLEs [Mendoza and Mancho, 2010], it is still significant enough to make the calculation of the function M over climatological time scales difficult.

The results detailed were all derived on a 2D isentropic surface, which assumes that the movement of the air parcels is adiabatic over the function M calculation period. At the altitudes for which we calculate M the isentropic approximation may only be valid for periods of 7-10 days [Morris et al., 1995, 2002]. However, some studies have used isentropic approximations successfully in the lower stratosphere over periods of up to a month [Bowman, 1993, McKenna et al., 2002]. In addition, Morris et al. [2000] found that, for satellite tracer fields found by interpolation using Lagrangian trajectory mapping, the use of both forward and backward trajectories can help to minimize uncertainty and biases due to diabatic effects. For the calculations in this paper we have derived the function M over the course of a month ($\tau = 15$ days).

However, we will show later (in Chapter 3.3.2) that there is a strong correla-

tion between the values of the function M calculated over different time periods, which means that to a high degree of approximation our results differ from those that would be calculated over shorter time periods only by a scaling factor. Since the rate of descent within the vortex should increase at altitudes above 900 K [Shepherd, 2000], a 3D model will be needed in order to extend this methodology into the upper stratosphere and mesosphere. The recent paper by Mancho et al. [2013] contains some information on how the function M and other similar descriptors can be applied to 3D velocity fields.

For the purposes of this research, daily values of M have been calculated for two winter-spring periods in the Southern hemisphere with differences in their dynamics, August-October 2009 and August-October 2010. For the Northern hemisphere, values of M have been calculated over three different December-March periods, 2004-2005, 2008-2009 and 2009-2010. During the 2004-2005 period, the Northern hemisphere vortex was unusually strong and stable [El Amraoui et al., 2008], while major SSWs occurred during each of the two remaining periods [Randall et al., 2009, Ayarzagüena et al., 2011, Scheiben et al., 2012, Straub et al., 2012].

In a plot of the function M, areas where the value of M is high represent areas where parcels have traveled over long trajectories over the chosen time period. Stable and unstable manifolds are associated with sharp gradients in the function M and hyperbolic points can be identified by looking for points where lines with sharp gradients cross [de la Camara et al., 2012].

As an example, Figure 3.1 shows plots of the function M for the 15th of January in the Northern hemisphere (Figures 3.1a-d) and the 16th of August in the Southern hemisphere (Figures 3.1e-h) at a potential temperature of 900 K (which corresponds to a physical altitude of approximately 31 km) for 2006-2009. The highest values of M are located in a ring roughly centered on the pole. This ring is wider for the Southern hemisphere and the values of M within it are consistently higher than in the Northern Hemisphere. The dates in each set of plots have been chosen to be roughly analogous to each other in terms of their relative timing with respect to vortex evolution so that the dynamics can be compared. The differences in the plots of the function M between hemispheres therefore illustrate that the southern polar vortex tends to have higher wind speeds, a wider, more coherent region of high M values and a stronger barrier than the northern polar vortex. This is consistent with the results of Waugh and Randel [1999], who used elliptical diagnostics to show that in general the Antarctic vortex is stronger, more stable, and longer-lasting than the Arctic vortex.

Figure 3.1: This figure shows plots of the function M from the 15th of January in the Northern hemisphere for several different years (subfigures (a)-(d) show the years 2006-2009 respectively) and for the 15th of August in the Southern hemisphere for the same years (subfigures (e)-(h) show the years 2006-2009 respectively). The approximate location of the vortex edge is marked with a yellow line. All plots are at a potential temperature of 900 K.

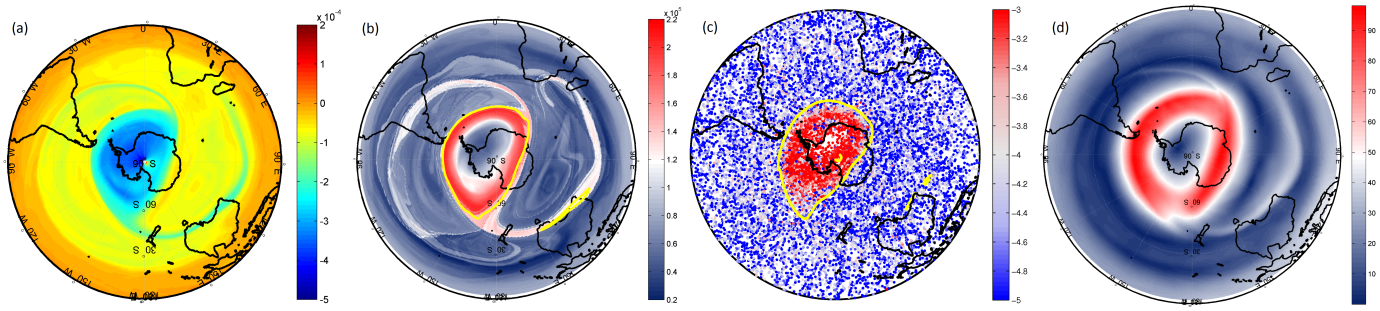

Figure 3.2: The potential vorticity (PV) in units of $(K \cdot m^2)/(kg \cdot s)$ (a), the function M (in km) (b), CO tracer concentrations (using a logarithmic scale) (c), and instantaneous wind speeds (in meters per second) (d) are shown for the 1st of October 2009 at a potential temperature of 700 K. For the CO tracer plot, the approximate location of the vortex edge is delineated by a yellow line.

Although the function M contains information from the entire time period over which the trajectories are derived (a month), the structures observable on a plot of M tend to correlate surprisingly well with those seen on instantaneous PV plots (also see de la Camara et al. [2012]). Since PV acts as a conserved tracer on isentropic surfaces, over time isolines of constant PV values will tend to be attracted to unstable manifolds. Therefore, structure associated with unstable manifolds should be visible on plots of potential vorticity, while both stable and unstable manifolds can be seen in plots of the function M [de la Camara et al., 2013]. Figures 3.2a and 3.2b show a PV plot and a plot of the function M for the 1st of October 2009 at 700 K. The PV plot shows a clearly defined area of low PV associated with the southern polar vortex, with high PV gradients at its boundary. The function M plot also shows a clear boundary at the same location, and both plots show two long streamers of air emanating from the vortex. However, the function M plot shows additional structure that is not observable in the PV plot.

On the function M plot (Figure 3.2b), there is a point visible to the east of New Zealand, at approximately 45° S and 195° E, where sharp gradients of M cross, creating a "crosshatched" feature which indicates the presence of a hyperbolic trajectory at this geographical position; this type of feature is in general associated with transport of fluid parcels across barriers. Out of the two sharp gradients of M which cross here, only one is visible on the potential vorticity plot (Figure 3.2a). The streamers of air leaving the vortex are longer in the function M plot than in the PV plot, which is as expected given that the function M plot incorporates information on air parcel behavior over a longer period of time. The function M is also foliated by many small filaments and streamers not clearly

visible in PV. These identify air parcels that will or have been traveling at a relatively high speed at some point during the function M calculation period. These include air parcels that will soon enter or have recently left the vortex, or alternatively the "collar" of stochastic mixing which immediately surrounds the vortex [Mariotti et al., 2000, de la Camara et al., 2013].

The location and extent of the vortex observed in Figure 3.2b also agrees very well with CO concentrations over the Southern hemisphere for the same date and potential temperature (Figure 3.2c), although the "streamers" observed in Figure 3.2b are not visible in CO. Each point in Figure 3.2c represents a measurement of CO concentration from the Microwave Limb Sounder (MLS) instrument on the Aura satellite. A domain-filling analysis has been used to improve the resolution of the plot (see McDonald and Smith [2013]). The position of the vortex edge, calculated using the method described in Chapter 3.2.2, is indicated by a yellow line. Due to the descent of CO-rich air from higher altitudes and the lack of photolysis during the polar night, concentrations of CO are higher inside the polar vortex (red area of Figure 3.2c). The interior of the vortex defined by the high CO concentrations matches well with the interior of the high M region in Figure 3.2.

An instantaneous horizontal wind speed plot (Figure 3.2d) for the same date and potential temperature also shows a vortex whose location agrees well with that shown in Figures 3.2a, 3.2b and 3.2c. It also shows small streamers of air leaving the vortex from the same locations as in the PV and function M plots (Figures 3.2a and 3.2b), but the streamers are short and otherwise the plot shows little structure. A comparison between Figures 3.2b and 3.2d shows how the function M incorporates information over the entire calculation period. The air parcels at the ends of the streamers in Figure 3.2b are linked dynamically to the vortex even though Figure 3.2d shows that their instantaneous speeds are low. The function M effectively averages the speed of each air parcel over the course of its trajectory in a Lagrangian framework; a corresponding Eulerian average over wind speed data would lead to a loss of information in the resulting plot.

In this paper, the equivalent latitude of the vortex edge was calculated each day during the case study periods using a method similar to that of Nash et al. [1996]. In this method, the location of the vortex edge is calculated by deriving the product of the PV gradient and average wind speeds as functions of equivalent latitude ϕ_e. The maximum of this function (known as the "impermeability") is at the equivalent latitude of the vortex edge and can be used to identify it.

We found that this impermeability function often has multiple peaks (see

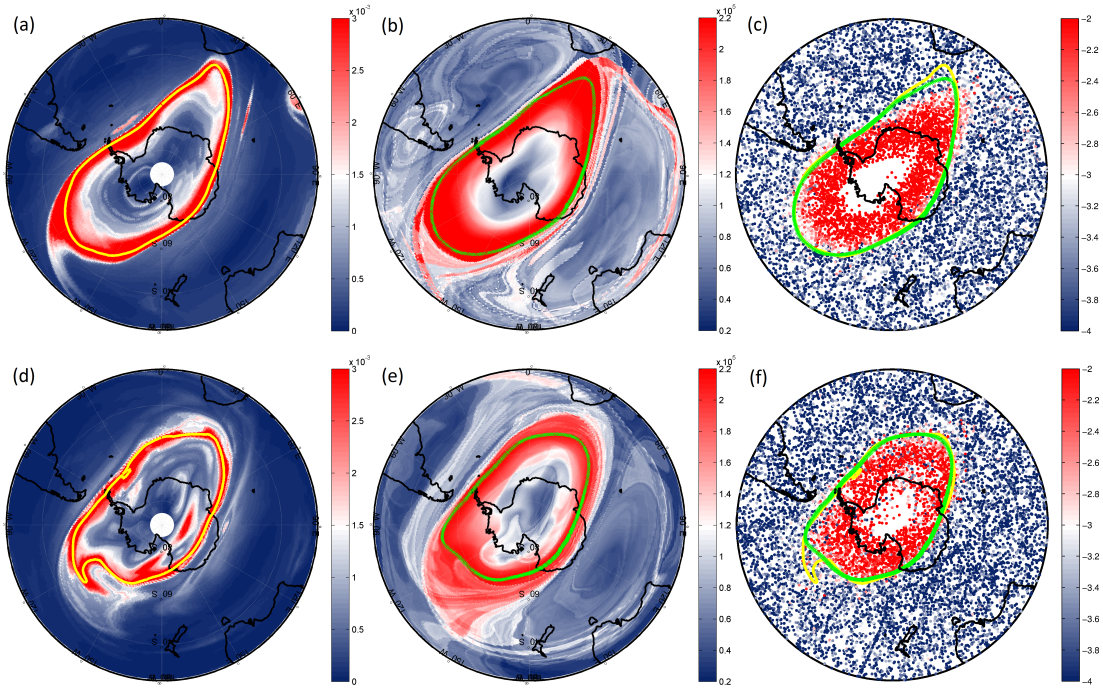

Figure 3.3: The impermeability function ($\frac{d(PV)}{d\phi_e}$ multiplied by wind speeds (meters per second)) plotted for the 13th of September 2009 (a) and 2010 (d), as well as the (b, e) function M (in km) and (c, f) CO concentrations (logarithmic scale) for the same dates. All plots are at 900 K. As in Figure 3.2, the location of the vortex edge calculated from the impermeability function is delineated by a yellow line. The green lines show the location of the maximum value of M for each longitude (smoothed using a 13-point moving window.)

Figures 3.3a and 3.3d), making the location of the vortex edge ambiguous. It is possible that this occurs because we are looking at higher potential temperatures than in Nash et al. [1996]. This is supported by the work of Mitchell et al. [2010], which suggests that at higher altitudes within the stratosphere more filamentation occurs, making the location of the vortex edge more difficult to find. In order to avoid ambiguity, a Gaussian fit was applied to the impermeability as a function of equivalent latitude, for equivalent latitudes between 55° and 80° and the location of the maximum of the Gaussian distribution was chosen to be the location of the vortex edge. The Gaussian fit was calculated iteratively using nonlinear regression. This improved the results, with the variation of equivalent latitude with time reducing greatly.

Figure 3.3a shows a plot of impermeability for the 13th of September 2009 at 900 K. For the same date, Figure 3.3b shows the function M and Figure 3.3c shows CO concentrations plotted using the same method as in Figure 3.2c.

Figures 3.3d, 3.3e and 3.3f show the same measures for the 13th of September 2010. On these plots, the equivalent latitudes of the vortex edge, calculated using the method described above, are delineated by yellow lines. Also shown are green lines displaying the location of the maximum value of M for each longitude. For both dates, all of the plots, as well as the yellow and green lines, agree closely on the position and extent of the vortex.

3.2.2 Quantitative measures based on the function M

In this section, we discuss a number of measures, derived using the function M, which can be used to quantify the dynamical properties of the polar stratospheric vortices.

Firstly, we discuss a measure based on the mean of the values of the function M near the vortex edge. Secondly, we discuss a measure of the area associated with values of M above a cutoff value, which will be correlated with the width of the vortex barrier; this should be correlated with barrier strength. An area with high values of M indicates that all air parcels within it have traveled consistently at high speed over the entire course of the calculation period. If values of M are high at the edge of the vortex, this means that the air parcels located there have all been traveling at high wind speeds in a coherent way along the entire length of their trajectories, implying the presence of a strong barrier. Therefore calculating the average value of M at the vortex edge should provide a measure that will be strongly correlated with the strength of the vortex barrier.

Once the equivalent latitude of the vortex edge was determined for each day in the case study periods, the average value of M at the vortex edge, denoted by $\bar{M}$, was determined by selecting those values of M which were located at points with equivalent latitudes within an interval of 4° centered on the vortex edge. Below an upper limit of 4°, the results are not sensitive to decreases in the equivalent latitude range, due to the limited resolution of the data used. The results were also smoothed using a 3-day running mean.

The measure described above depends on the use of potential vorticity data in order to determine the location of the vortex edge. However, PV data tends to be noisy [Allen and Nakamura, 2003] and using it for such purposes will inevitably cause extra uncertainty in the results. Also, above an altitude of approximately 60 km (or a potential temperature of 3000 K), methods based on equivalent latitude can no longer be used, as values of PV no longer vary monotonically with latitude [Harvey et al., 2009]. This means that any dynamical measure

based on equivalent latitude cannot be used in the mesosphere, which would be a limitation on its effectiveness. For this reason it is important to develop measures of vortex dynamics which are based solely on the function M.

Here we describe one such measure, denoted by A_M, which is based on the area associated with function M gridpoints for which the value of M is above a certain threshold. A high value of A_M should imply the existence of a wide region near the vortex edge where the air parcels are traveling at high speeds throughout the integration period, and therefore that there is a wide transport barrier near the vortex edge. It should also tend to be correlated with a large overall vortex area, since a larger vortex should have a larger circumference.

The threshold must be chosen so that values of M outside the vortex edge region are in general lower than it, and so that values of M inside the edge region are at or above it. In this paper, this threshold has been chosen based on an inspection of PDFs of the function M to be 1.0×10^5 km. PDFs of daily function M patterns usually appear to be comprised of two components, a group of lower M values which sometimes appear to have a Gaussian distribution, and a tail of higher values which grows longer when the vortex is stronger. For the Southern hemisphere periods we studied, and for the Northern hemisphere at 900 K, the 1.0×10^5 km threshold is often near the joining point of the two distributions. This threshold also approximately satisfies the above criteria and begins to register the presence of a vortex when a visual inspection confirms the presence of a clear vortex. We expect that this approximate measure of vortex jet area will be positively correlated with the strength of the vortex barrier, as a wide jet will be harder for an air parcel to cross.

Major stratospheric sudden warmings will be associated with large transfers of air across the vortex boundary, mixing, and a significant weakening of the vortex. A transfer of air across the boundary means that some values of M included in the $\bar{M}$ measure will not come from air parcels that have been traveling at the high wind speeds characteristic of the vortex edge; this should lead to lower values of the $\bar{M}$ measure over the course of the SSW and therefore to a dip in $\bar{M}$. A significant weakening of the vortex should be associated with a reduction in both the values of M near the vortex edge ($\bar{M}$) and the area with values of M above a certain value (A_M).

3.3 Results

3.3.1 Quantitative measures based on the function M

Figure 3.4 shows, over the period from August-October in 2009 for the Southern hemisphere, the measures $\bar{M}$ (Figure 3.4a) and A_M (Figure 3.4b), as well as the averaged eddy heat flux $\overline{v'T'}$ calculated over a 30-day moving window prior to each date (Figure 3.4c). In addition to the A_M measure calculated using the standard threshold of 1.0×10^5 km, Figure 3.4b also shows the same measure calculated using an alternative threshold, 1.4×10^5 km. The standard and the alternative thresholds are indicated on this plot by solid and dashed lines respectively. The general behaviour of the A_M measure is fairly similar for both thresholds and only the results using the standard threshold will be considered in the following discussion.

The eddy heat flux (Figure 3.4c) is calculated using data from the MERRA reanalysis, with the results also being averaged over latitudes of 45° S to 75° S. Eddy heat flux is an independent measure that is known to be associated with the amplitude of planetary waves, and so it should be useful to compare it with measures based on the function M. However, it often takes some time before an elevated level of eddy heat flux gives rise to obvious changes in vortex dynamics [Newman and Nash, 2005]. Therefore, using the 30-day moving window should give a better measure of how planetary waves are affecting vortex dynamics at any given time. The length of the time window is also consistent with that of the 30-day period that the measures $\bar{M}$ and A_M are calculated over.

Figure 3.5 shows plots of the function M for selected dates within this time period at potential temperatures of 600, 700, and 900 K (corresponding to altitudes in the lower-middle stratosphere of approximately 14-31 km). These dates, which have been chosen for their potential to be dynamically interesting, are 15th August, 29th August, 13th September and 3rd October, and are also highlighted by vertical lines in Figure 3.4.

Figures 3.5a, 3.5e and 3.5i show the vortex during mid-August where there was low variability in M near the vortex edge. During this period the vortex is nearly circular, which indicates that there is little planetary wave activity at this time. The magnitude of the averaged eddy heat flux is still quite low during this period (Figure 3.4c). From the 29th of August onwards (second vertical line, Figure 3.4c), the averaged eddy heat flux magnitude is consistently high. The plots of M on this date (Figures 3.5b, 3.5f and 3.5j) show a large anticyclone

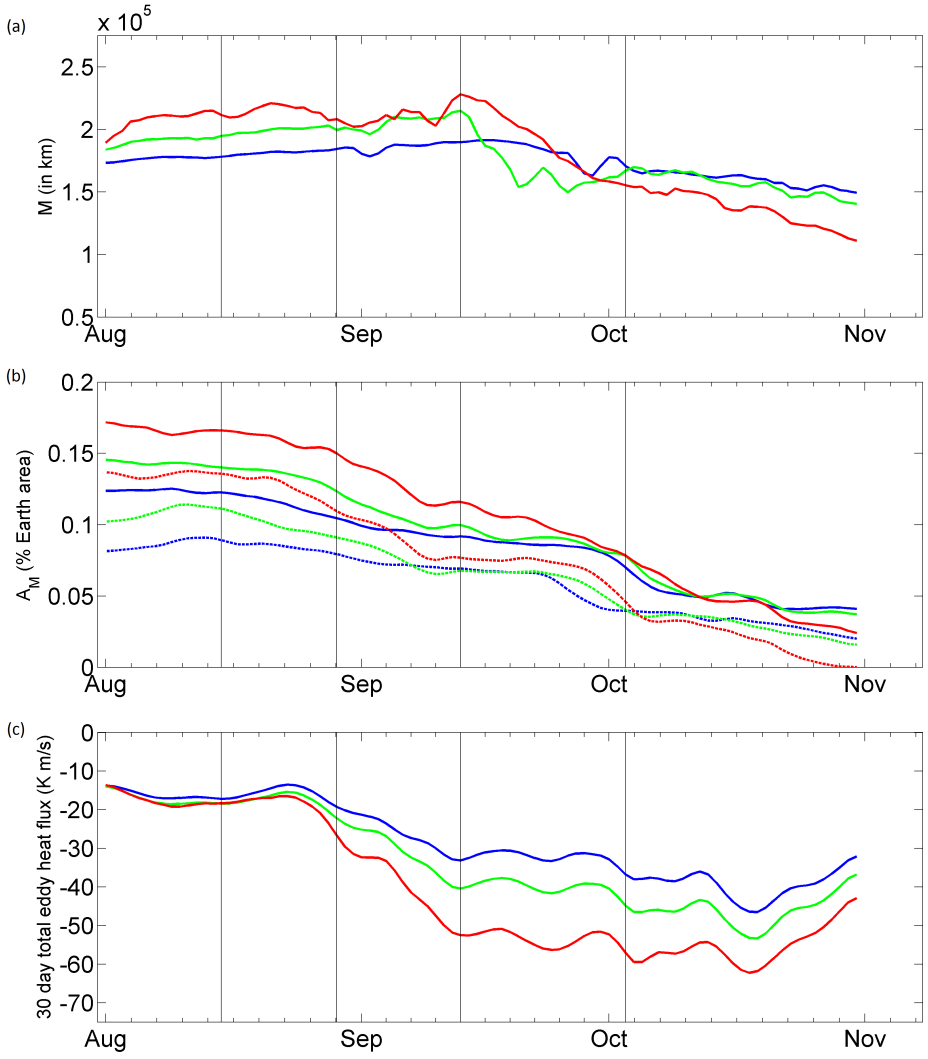

Figure 3.4: For potential temperatures of 600 K (blue lines), 700 K (green lines), and 900 K (red lines), these plots show the daily average of M within a band of 4° equivalent latitude centered on the vortex edge over August-October 2009 for three different potential temperature levels (a), as well as daily plots of the area associated with Southern hemisphere grid points with values of M above 1.0×10^5 km (solid lines) and 1.4×10^5 km (dashed lines) (b), and the eddy heat flux, averaged over 45° S to 75° S and also averaged over a 30-day period prior to each date shown (c). The dates examined in greater detail in Figure 3.5 are identified with dark lines. All measures are smoothed using a 3-day running mean.

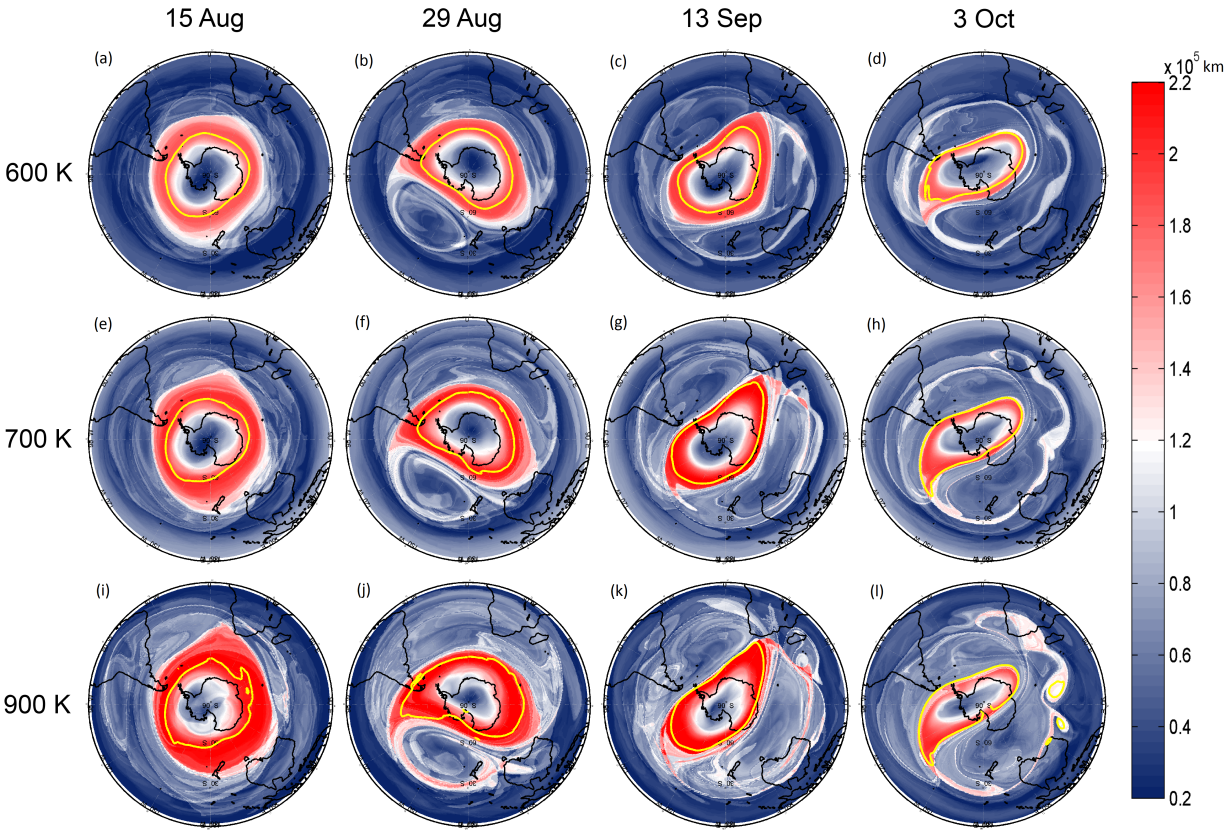

Figure 3.5: These plots show the function M over the Southern hemisphere at three different potential temperatures for a number of dates during August-October 2009. The vortex edge is marked with a yellow line. Figures (a)-(d) show the function M for 15th August, 29th August, 13th September and 3rd October, respectively, at 600 K. Figures (e)-(h) show function M plots for the same dates at 700 K and Figures (i)-(l) show plots for the same dates at 900 K.

centered to the east of New Zealand stretching from approximately 30° S to 60° S and between 160° E to 70° W which is clearly visible at all potential temperatures, but is strongest at 900 K (Figure 3.5j). A long streamer of high-M air can also be seen extending from the vortex along the edge of the anticyclone. Figures 3.5c, 3.5g and 3.5k show plots of M for the 13th of September. According to Figure 3.4, this is the date for which the average value of M near the vortex edge is at its maximum. The plots of M for this date show the effects of the continuing high average eddy heat flux values - an elliptical vortex with anticyclonic structures on either side, this being particularly clear at the higher potential temperatures (Figures 3.5g and 3.5k). By the 3rd of October, shown in Figures 3.5d, 3.5h and 3.5l, the vortex is noticeably smaller and weaker. This is a period of intense wave breaking, with long streamers of material leaving the vortex. The area measure also decreases sharply at this point (see Figure 3.4b).

At all altitudes, the $\bar{M}$ and A_M measures reach a peak early in the test period and then decrease thereafter. Their values are in general larger at higher altitudes over most of the test period, but during October, they decrease more sharply at higher than at lower altitudes (see Figures 3.4a and 3.4b). This suggests that values of M near the vortex edge are in general greater at higher altitudes. For 2009, Figure 3.5 shows more filamentary structure at higher altitudes. More filamentary structure is also observable as the season progresses, which suggests that more mixing may be occurring or has occurred.

During August to mid-September 2009, $\bar{M}$ increases very gradually at each of the potential temperature levels studied (Figure 3.4a) until it reaches a peak on approximately the 13th of September. It then begins to decline, with this being more rapid at higher potential levels; this might be expected since it is generally understood that the vortex breaks up at higher altitudes first while persisting for longer at lower altitudes [Harvey et al., 2002]. Large values of the $\bar{M}$ measure should be associated with a stronger vortex barrier, therefore this plot suggests that the strength of the vortex barrier reaches its maximum in mid-September. Note that until late September $\bar{M}$ is consistently higher at higher altitudes; this is because faster wind speeds at these levels cause air parcels to travel further over the 30-day calculation period.

The vortex edge area measure A_M behaves somewhat differently, with A_M being quite large to begin with, and then decreasing in an almost monotonic way at all potential temperature levels (Figure 3.4b). The decrease is particularly steep in early September and October but levels off for a time during mid-late September.

The average value of M near the vortex edge $\bar{M}$ and the area measure A_M should both be associated with the strength of the polar vortex and its barrier and so should be correlated with each other. In Figures 3.4a and 3.4b it can be seen that there is some similarity between these two measures over this time period. However there are some differences between them, which are most notable between mid-August and mid-September, during which $\bar{M}$ increases while A_M decreases. The first three columns of Figure 3.5 show plots of the function M for 3 days within this period. The area covered by the vortex does decrease during this time, but the values of M within the vortex do not reduce, meaning that $\bar{M}$ is at least partially independent of the size of the vortex edge region.

For August-October 2010 in the Southern hemisphere, Figure 3.6 shows the daily values of the function M measures and averaged eddy heat flux, while Figure 3.7 shows individual plots of M for the 12th and 20th of August, the 13th of September and the 12th of October, which are also highlighted by lines in Figure 3.6. Figures 3.6a and 3.6b show a strong similarity between the pattern of results for M and A_M over this time period. Both of these measures peak on approximately the 20th of August and then decline steadily thereafter. This decline, which accelerates after the 12th of October for 900 K, is steeper than the one that occurred in late October during 2009. Once more, the vortex area and average value of M are larger at higher altitudes over most of the Aug-Oct period, but later on, the measures suggest that the vortex breaks up more quickly at 900 K than at lower altitudes.

Compared to 2009, the value of the vortex edge area measure A_M for the 2010 period (Figure 3.6b) is significantly smaller to begin with, and after its peak it decreases more slowly and steadily than it did in 2009. These changes in A_M correspond well with what is known about the vortex dynamics during this period [Klekociuk et al., 2011]. A large eddy heat flux event disrupted the polar vortex in the mid-upper stratosphere during July 2010, and the effects of this disturbance continued into August (Figure 3.6c). This caused the area of the vortex at 850 K to be smaller than usual in August. The plots of $\bar{M}$ (Figure 3.6a) and A_M (Figure 3.6b) for 900 K shows a dip during this period. The eddy heat flux event in July occurred during an easterly phase of the Quasi-Biennial Oscillation (QBO) at 30 hPa. Such phases are often associated with increased planetary wave activity and disruption of the vortex. The QBO then moved into a positive (westerly) phase (generally associated with less disruption to the vortex) that became strong from September onwards. After this point, the vortex area at 850 K followed the climatological mean and broke up in early November,

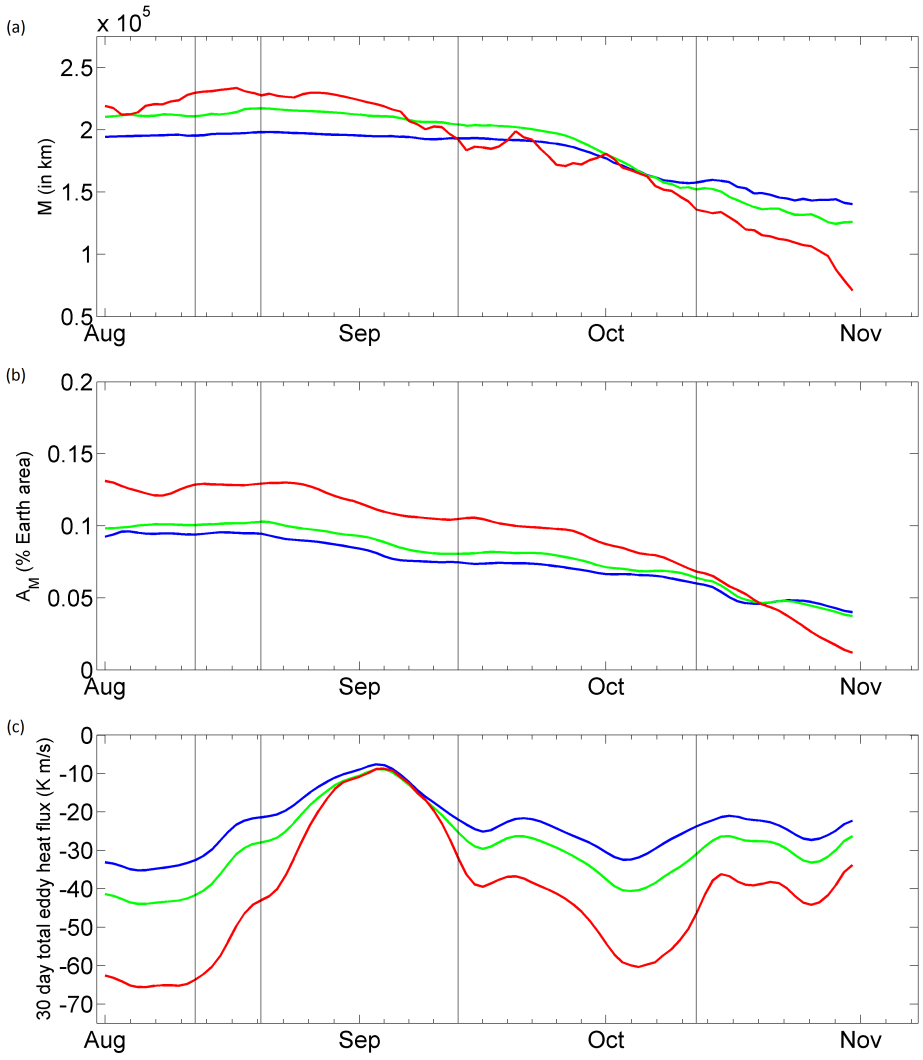

Figure 3.6: As in Figure 3.4, but for August-October 2010 and with only the 1.0×10^5 threshold shown in plot (b).

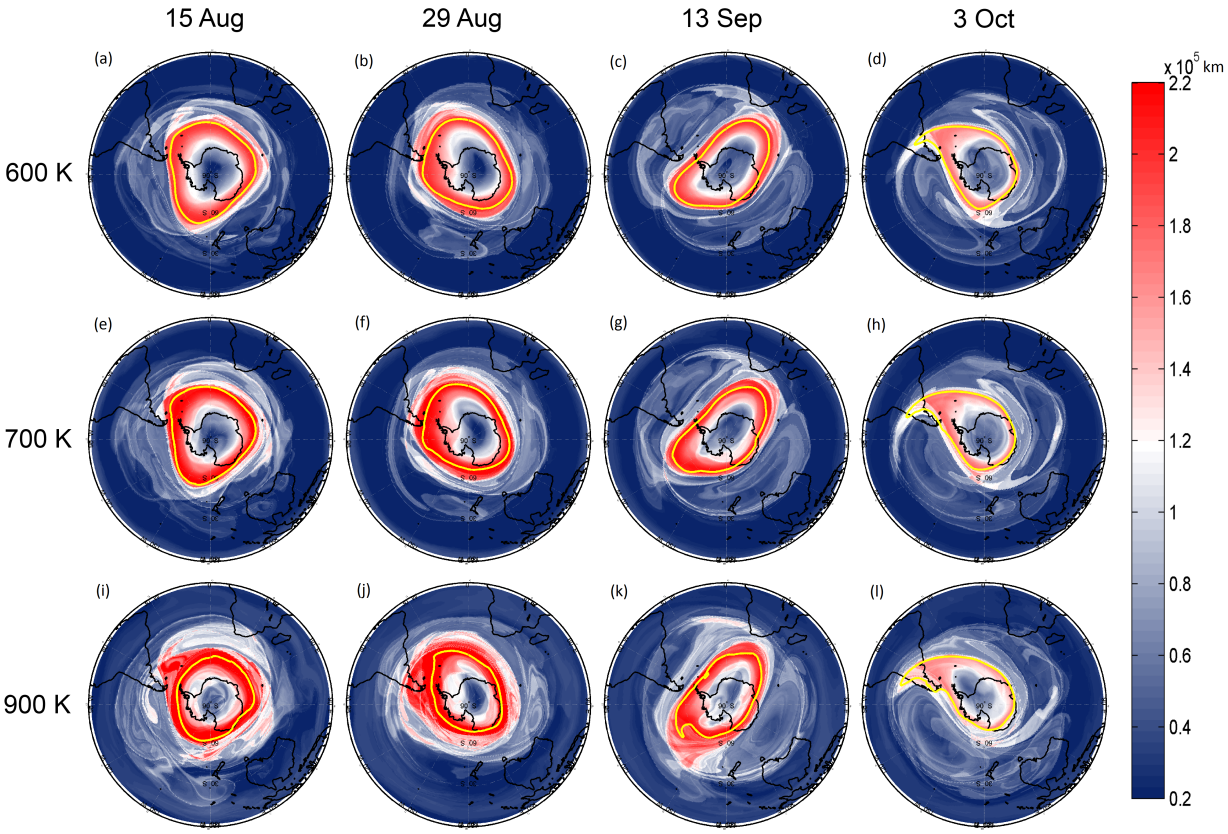

Figure 3.7: These plots show the function M over the Southern hemisphere at three different potential temperatures for a number of dates during August-October 2010. The vortex edge is marked with a yellow line. Figures (a)-(d) show the function M for 12th August, 20th August, 13th September and 12th October, respectively, at 600 K. Figures (e)-(h) show function M plots for the same dates at 700 K and Figures (i)-(l) show plots for the same dates at 900 K.

although at 450 K (approximately 17 km altitude) the vortex persisted well into December (see Figure 9 of Klekociuk et al. [2011]). The plot of A_M for 900 K (red line, Figure 3.6b) also indicates that the vortex is about to break up by the end of November 2010.

The first two columns of Figure 3.7 show plots of M for 600, 700 and 900 K for the 12th and 20th of August. During this period the values of $\bar{M}$ and A_M vary relatively little (Figures 3.6a and 3.6b). The values of M in the vortex edge ring also remain relatively constant between these dates. The magnitude of the eddy heat flux is high at the beginning of this period but then decreases sharply. However this does not appear to affect the vortex much, since it is rather calm and stable during this period. Figures 3.7c, 3.7g, and 3.7k show plots of M for the 13th of September. Although the eddy heat flux is increasing during this period (see Figure 3.6c), the values of the $\bar{M}$ and A_M measures have decreased only slightly from their peaks early in the season. For the final column of Figure 3.7, which displays plots of the function M for the 12th of October (Figures 3.7d, 3.7h, and 3.7l), we see that the vortex has decreased in size and intensity. It can be seen in Figure 3.6b that during this period the vortex edge area measure decreases rapidly. The area and intensity of the vortex appears to be the same at each potential temperature level, showing that this is the approximate date after which the vortex will begin to break down more rapidly at higher altitudes. The streamers of air emanating from the vortex, indicative of mixing and transport in the vortex periphery, are less evident than for the plots of M in Figures 3.5d, 3.5h, and 3.5l.

In general the plots in Figure 3.7 show a region of slightly elevated values of M stretching northwards of the vortex edge ring. However, it does not extend as far northwards as for 2009 (see Figure 3.5). This may be associated with the surf zone, a region of mixing and wave breaking surrounding the vortex [McIntyre and Palmer, 1984]. During 2010, the Quasi-Biennial Oscillation (QBO) at 30 hPa was in a westerly phase from August onwards [Klekociuk et al., 2011], while during the Southern hemisphere winter of 2009 the index was westerly from May onwards. It is possible that any differences between the two periods in the size of this area of elevated M and the amount of observed planetary wave breaking activity may be partially caused by the different QBO phases. An inspection of the 30-day averaged eddy heat flux over these two time periods (Figures 3.4c and 3.6c) confirms that values of the averaged eddy heat flux during September-October 2010 were in general lower than those for September-October 2009.

Polar vortex dynamics in the Northern hemisphere are in general markedly

more variable than in the Southern hemisphere, therefore it is worthwhile to investigate how much of this variability can be captured by measures based on the function M. Figures 3.8 and 3.9 show daily values of $\bar{M}$ and A_M over December-March in the Northern hemisphere winter periods of 2004/2005, 2008/2009 and 2009/2010 (Figures 3.8a and 3.8b), as well as the eddy heat flux averaged over a period of 30 days prior to each date (Figure 3.8c), and individual plots of M for the 21st of December, 10th and 24th of January and the 1st of February for each time period (Figure 3.9). These dates are again highlighted in Figure 3.8 for purposes of comparison. All measures and plots in these two figures are shown for a potential temperature level of 900 K (at an approximate altitude of 31 km). Major stratospheric sudden warmings (SSWs) occur during both the 2008/2009 and 2009/2010 periods, at approximately the same time in late January. The 2009 major SSW begins on the 24th of January [Ayarzagüena et al., 2011]. Although the 2010 SSW officially begins on the 26th of January [Scheiben et al., 2012], the 24th of January is the first date for which the zonal mean zonal winds reverse at 60° N and 10 hPa [Straub et al., 2012]; this is one of the conditions that must be satisfied in order for a major SSW to occur [Charlton and Polvani, 2007]. The 2008/2009 major SSW was a vortex splitting event, and one of the strongest SSWs on record [Randall et al., 2009, Ayarzagüena et al., 2011], while the 2009/2010 was a vortex displacement event [Straub et al., 2012]. By contrast, the polar vortex was unusually strong during the 2004/2005 Northern hemisphere winter [El Amraoui et al., 2008], and no major SSWs took place during this season (although two minor SSWs occurred in early and late February). The paper by Charlton and Polvani [2007] contains a set of criteria for automatically identifying vortex split events, while Mitchell et al. [2013] and Seviour et al. [2013] use a method based on elliptical diagnostics of PV contours (or geopotential height) to identify explicit criteria for both vortex displacements and splits.

For all three years, the average value of M near the vortex edge appears to increase fairly smoothly to a peak and then smoothly decline afterwards (Figure 3.8a). The maximum values of the $\bar{M}$ measure are similar for all years shown, but the date at which the $\bar{M}$ measure peaks varies considerably between the time periods. For 2008/2009, the period containing the most powerful SSW (green line), the measure peaks near the end of December, while for 2004/2005 (blue line) it does not reach its maximum value until the beginning of February. For 2009/2010 (red line) the peak value is at approximately the 10th of January.

Although for both 2008/2009 and 2009/2010 the polar vortex underwent an

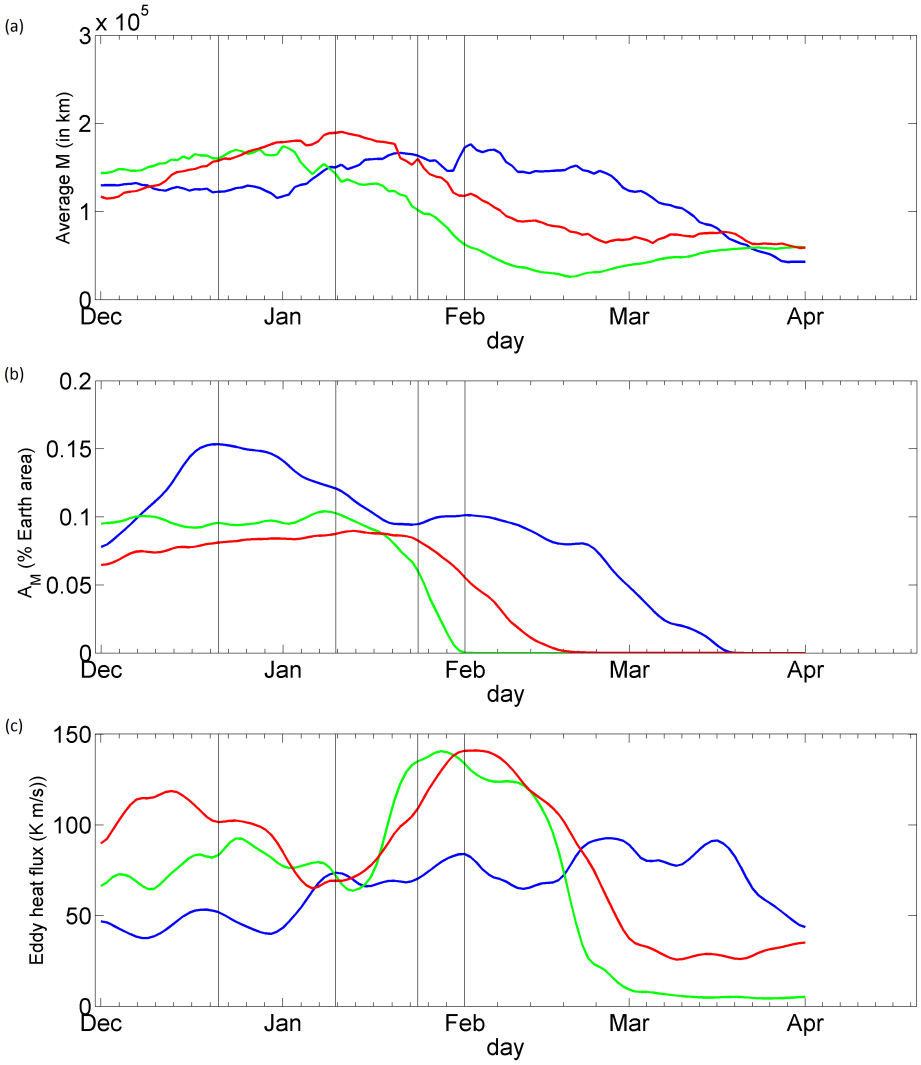

Figure 3.8: For 2004/2005 (blue lines), 2008/2009 (green lines), and 2009/2010 (red lines), these plots show the daily average of M within a band of 4° equivalent latitude centered on the vortex edge during the period from December - March for a potential temperature of 900 K (a), as well as a daily plot of the area associated with Northern hemisphere grid points with values M above 1.0×10^5 km (b), and the eddy heat flux, averaged over 45° N to 75° N and also averaged over a 30-day moving window period prior to each date shown (c). The dates examined in greater detail in Figure 3.9 are identified with dark lines. All measures are smoothed using a 3-day running mean.

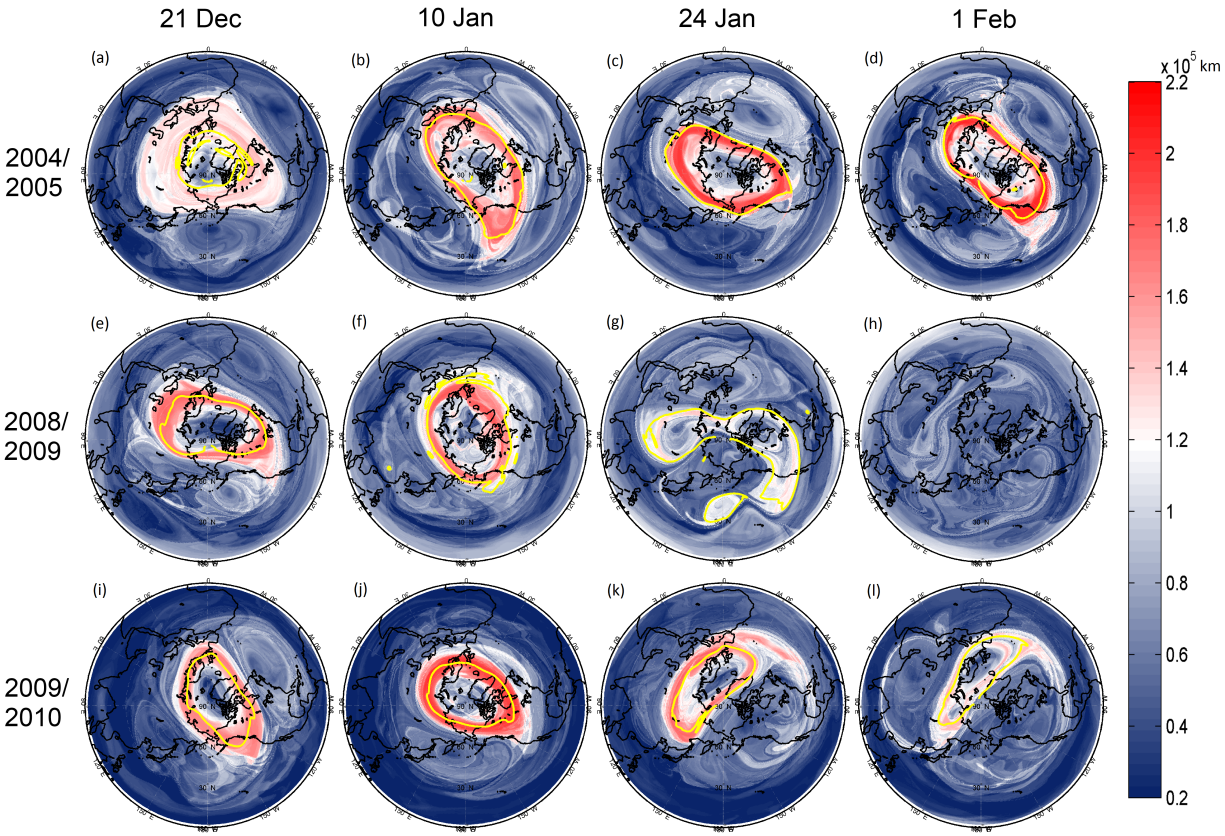

Figure 3.9: These plots show the function M over the Northern hemisphere for a number of dates during December - March. The vortex edge is marked with a yellow line. Figures (a)-(d) show the function M for 21st December, 10th January, 24th January and 1st February, respectively, for the 2004/2005 winter season. Figures (e)-(h) show function M plots for the same dates during 2008/2009 and Figures (i)-(l) show plots for the same dates during 2009/2010.

SSW from approximately the 24th of January onwards, no clear sign of this is visible in the $\bar{M}$ plots. The values of $\bar{M}$ do decline substantially during the SSW period for both years, and for 2008/2009 $\bar{M}$ decreases by approximately 40% over the period from 24th February - 1st March, but this is part of a sustained decline in values of $\bar{M}$ from their earlier peaks rather than a sudden drop. Possible reasons for these disappointing results are discussed in Chapter 3.3.3. Despite the official starting dates for the two SSWs only being two days apart, the decline in $\bar{M}$ begins considerably earlier in 2008/2009 than in 2009/2010. For 2008/2009, $\bar{M}$ begins to increase again during March, although it never reaches its former values. This suggests that a weak vortex may be beginning to reform. For 2004/2005, the average value of M at the vortex edge remains high well into March.

According to the vortex edge area measure A_M (Figure 3.8b), the area occupied by the vortex edge is consistently larger for 2004/2005 (blue line) than for the other two years. This is consistent with the vortex being unusually strong during the 2004/2005 winter season [El Amraoui et al., 2008]. For 2008/2009 (green line) and 2009/2010 (red line) the vortex breaks up due to the major stratospheric sudden warmings beginning on the 24th and 26th of January, respectively. Unlike $\bar{M}$, A_M shows behavior that is consistent with a vortex breakup for these time periods, with the measure decreasing sharply after the SSW. For the very strong 2008/2009 vortex split SSW, the decline in the area measure is particularly sharp.

At the beginning of December, the A_M measure is fairly similar in value for all time periods shown, but for the 2004/2005 period (blue line), the vortex edge area measure increases rapidly until it reaches a peak in mid-December (near the first line marked on the graph). The value of the area measure at this date is similar to those for A_M in the Southern hemisphere during August 2009/2010 for 900K (Figures 3.4b and 3.6b). The measure then decreases from this point, and by mid-late January is no longer greatly different than for the other two time periods. However for 2004/2005 the value of A_M then stays almost the same from that point until late February, while for the other two years the measure decreases sharply. The peak in A_M occurs in late December, well before the value of the $\bar{M}$ measure reaches its maximum (blue line, Figure 3.8b). This behavior is similar to that of the Southern hemisphere polar vortex in 2009, for which the highest values of A_M also occurred significantly before those for $\bar{M}$.

For 2009/2010, the vortex edge area measure decreases sharply once the SSW begins on the 26th of January. It continues to do so until it reaches approximately zero during mid-February, and does not recover after that point. This behavior is consistent with the description in Straub et al. [2012] of the evolution of the

vortex during the SSW at 10 hPa (∼900 K). For 2008/2009 the behavior is similar, except that the decline begins earlier, on approximately the 10th of January (second line marked on Figure 3.8b), and then becomes very steep after the major SSW begins. Even though the $\bar{M}$ measure for 2008/2009 shows signs of a vortex recovery beginning, A_M shows no sign of a vortex reforming after the SSW. This is potentially because the values of M within the reforming vortex never reach the threshold defined earlier.

An examination of the averaged eddy heat flux magnitudes (Figure 3.8c) shows that the eddy flux values for 2008/2009 (green line) reach their peak just after the major SSW begins on the 24th of January. For 2009/2010, the eddy flux peaks later, shortly after the 1st of February. For both of these years, the peaks appear to correspond to the midpoints of the sharp declines in A_M associated with the SSWs, rather than their official starting dates. After this point, eddy heat flux values begin to drop, relatively slowly at first and then steeply. For December-March 2004/2005, the averaged eddy heat flux magnitude is significantly smaller than for the years containing SSWs. It gradually increases until mid-March, which is the point at which the A_M measure stops identifying the presence of a vortex. The highest values of eddy flux do in general appear to be associated with drops in the function M-based measures for the time periods investigated here.

Figure 3.9 contains plots of M for a number of dates within each of the three Northern hemisphere periods studied. For each period, the same set of four dates is examined. Figure 3.9a shows the vortex for the 21st of December 2004. At this point, the vortex edge area is very wide, but values of M in the vortex edge area are still noticeably lower than for the corresponding dates in 2008 and 2009 (see Figures 3.9e and 3.9i). The values of the $\bar{M}$ and A_M measures on this date are consistent with this (Figures 3.8a and 3.8b). Figures 3.9b, 3.9c and 3.9d contain plots of M for the 10th and 24th of January 2005 and the 10th of February 2005, respectively. The strength and general appearance of the vortex remain roughly the same over this period, as no vortex breakup is occurring. Figures 3.9e and 3.9f show plots of M for the 21st of December 2008 and 10th of January 2009, while Figures 3.9i and 3.9j show plots for the same dates in 2009/2010. The general appearance of the plots look fairly similar for both time periods, although the values of M in the vortex barrier region appear generally larger for the 10th of January in 2010 than in 2009, as can also be seen in Figure 3.8a.

Figure 3.9g shows the polar vortex on the 24th of January 2009, the day on which the major SSW begins. It can be seen that the vortex has distinctly split

into two parts and has greatly weakened. By the 1st of February (Figure 3.9h), there is no longer any vortex structure visible.

Figure 3.9k shows the polar vortex on the 24th of January, which is the date on which zonal winds at 60° N and 10 hPa reverse prior to the 2010 SSW. Here the vortex is being shifted off the pole by a large anticyclone. Air can be observed leaving the vortex as it begins to break down. However, at this point the vortex structure itself is otherwise intact. Figure 3.9l shows the vortex for the 1st of February as it continues to break down once the SSW has passed its peak. Although the SSW still appears to be mostly a displacement event at this point, there are also hints of an emerging vortex split. The function M still shows a vortex-like structure on this date, although it is greatly distorted and weakened. This is in contrast to an instantaneous wind speed plot from the same day, which no longer shows any clear vortex structure (not shown).

3.3.2 Linear dependence of the function M upon τ

In general, there is a linear correlation between M calculated for different τ, which becomes strong within the polar vortex region. For each day in the December 2009 - March 2010 period, the function M was calculated for both $\tau = 2$ and $\tau = 15$ over all latitude/longitude points on the reanalysis grid. For each point, correlations between time series of daily values of M for both values of τ were calculated. The mean correlation coefficient between $M(2)$ and $M(15)$ was found to be 0.71 over the entire Northern hemisphere. When only grid points with physical latitudes between 60-80° N are considered, the mean correlation increases to 0.87. This very strong linear relationship means that, apart from a scaling factor proportional to time, quantitative measures based on the value of the function M in the vortex edge region are not very sensitive to changes in the amount of time they are calculated over. Therefore the results we have obtained for $\tau = 15$ are very similar to those that would have been found for a lower value of τ. This also suggests that the structure of the vortex is coherent over long periods of time. The ability of the function M to investigate the coherence of dynamical structures in this way was first discussed by Mendoza and Mancho [2010], who demonstrated how changes in the function M as τ changes can be used to indicate how long fluid parcels remain inside an oceanic eddy.

For function M plots of the polar vortices, the structures observed tend to alter relatively little as the period over which M is calculated changes, which implies that the polar vortex is usually coherent [de la Camara et al., 2012]. However,

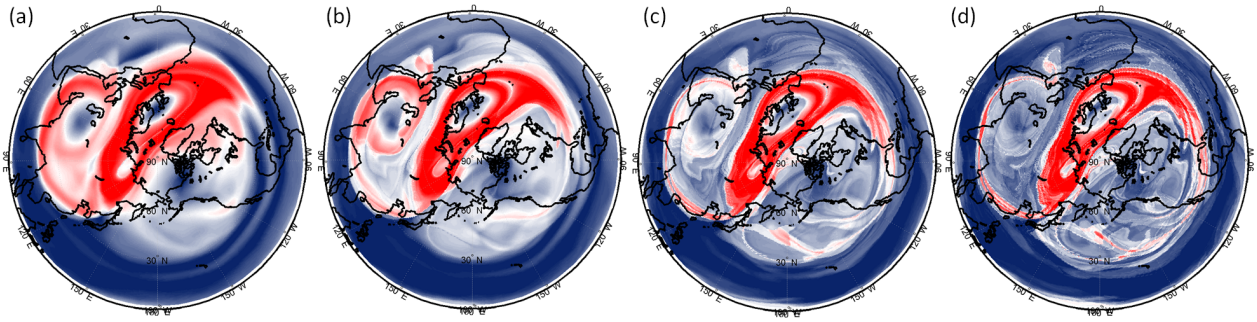

Figure 3.10: Plots of the function M for February 1st at 900 K, for a range of different values of τ. Subplots (a), (b), (c) and (d) show the function M for $\tau = 2$, $\tau = 5$, $\tau = 10$ and $\tau = 15$. For each plot, the colorbar limits are set to be equal to the 5th and 95th percentiles of the PDF (probability distribution function) of function M values.

during disturbed periods with rapidly changing dynamics, such as SSWs, this may not always be the case. Figure 3.10 shows plots of the function M on the 1st of February at 900 K, during the 2010 SSW, for $\tau = 2$ (Figure 3.10a), $\tau = 5$ (Figure 3.10b), $\tau = 10$ (Figure 3.10c) and $\tau = 15$ (Figure 3.10d). For all values of τ, a vortex-like structure is still clearly visible, although it is distorted and split. For $\tau = 2$, a prominent eddy is visible over western Asia stretching from approximately 20° S to 60° S and between 30° W to 90° W, but as τ increases, this becomes less obvious. By $\tau = 10$, the eddy is no longer clearly evident, although a long streamer of high M values can still be seen curling around its outer edge. This indicates that this particular eddy is short-lived rather than being a coherent structure.

In addition, as the value of τ increases, the area of high function M values associated with the disturbed vortex shrinks somewhat and its edges become much sharper and more well-defined. Some areas near the outer edge of the vortex have high M values in the $\tau = 2$ plot (Figure 3.10a), but low values when τ is larger. This indicates that although in the short term the air parcels at these locations on the 1st of February appear to be within the vortex, in the long term they are not dynamically linked to the vortex and so do not stay there for long. At $\tau = 10$ and 15 (Figures 3.10c and 3.10d), the sharp boundaries of the region of high M-values are likely to indicate the presence of the hyperbolic invariant manifolds discussed in de la Camara et al. [2012]. For these values of τ, the streamers of air emanating from the vortex become much clearer and longer, indicating that planetary wave breaking is occurring. Since the 1st of February

is firmly within the period of an SSW, it should be expected that a considerable amount of material will be entering and leaving the vortex. The plots in Figure 3.10 suggest that this is occurring only over a few, relatively small areas affected by the planetary wave breaking while in other areas the vortex barrier is still present.

Changes in observed structures when M is calculated over different time periods can also be seen during the very strong SSW in January 2009. On the 1st February 2009, a few days into the SSW, a plot of M (Figure 3.9h) shows little sign of vortex structure, while an instantaneous PV plot (not shown) shows three distinct areas of high PV. These areas correspond to faint structures visible in Figure 3.9h but are much more clearly visible in the PV. Since the PV is an instantaneous plot, while the Figure 3.9h plot of M is based on trajectory data from a period of 30 days centered on the 1st February, this suggests that the structures are short-lived.

3.3.3 Lack of an SSW signal

For January 2009 and 2010, the $\bar{M}$ measure does not show a clear SSW signal (Figure 3.8a). This is a puzzling result that needs further investigation. The most obvious possible explanation for this is that the long (30-day) period over which the function M is being calculated causes a "smoothing" effect in measures based on it which blurs the SSW signal. But the linear dependence of M upon τ discussed in Chapter 3.3.2 suggests this is not the case; when $\bar{M}$ is calculated based on function M values for $\tau = 2$, corresponding to a period of 4 days, there is no improvement in the SSW signal (plot not shown).

One factor that may be reducing the intensity of the SSW signals observed in Figures 3.8a and 3.8b is that the most common method for determining whether an SSW is occurring on a specific date is to calculate the zonal mean zonal winds at a physical latitude of 60° N [Charlton and Polvani, 2007]. If the average zonal wind velocity is westwards then a major SSW is occurring. However, for the $\bar{M}$ measure, the location of the vortex edge is identified by a PV contour, which can differ greatly from the 60° line of physical latitude, especially during an SSW. The A_M measure is based on the area associated with high values of M regardless of location.

When the polar vortex is distorted or split, the position of the vortex jets can shift away from a latitude circle as shown in Figure 3.10. Therefore the zonal mean zonal winds can be directed westwards and a major SSW can occur even

if the vortex itself still maintains some dynamical integrity. As long as there is a high PV gradient at the vortex edge, Rossby elasticity will still work towards reducing planetary wave breaking and maintaining the vortex edge barrier [Juckes and McIntyre, 1987]. Therefore measures such as $\bar{M}$ and A_M could be relatively insensitive to the SSW in some cases since they are not dependent on the shape of the vortex.

If the polar vortex does maintain dynamical integrity during an SSW, this should be observable in plots of tracer concentration values at that time. Figure 3.11a shows concentrations of CO measured by the Aura-MLS satellite on the 24th of January 2009, at the beginning of the major SSW, with domain-filling being used to improve the resolution. The color-coding of each point is based on a comparison with thresholds derived from the PDF (probability distribution function) of the results [McDonald and Smith, 2013]. High concentrations, characteristic of the region inside the vortex, are colored red, low concentrations are blue and intermediate concentrations are gray. For this date, although the vortex edge (outlined in yellow) has become distorted and broken by the beginning of the 2009 SSW, little high-CO air has crossed the vortex edge. In contrast, by the 1st of February (Figure 3.11b), there has been a large amount of mixing and there is no coherent vortex structure left. It was not possible to plot a vortex edge for this date. This shows that the 2009 SSW caused a complete breakdown in the vortex edge barrier. Plots of CO concentrations for corresponding dates during 2010 show that on the 1st of February, well into the SSW (Figure 3.11d), there is still a well-defined region of high CO values roughly corresponding to the area inside the vortex edge contour, and there is only slightly more mixing of high CO values outside the vortex than was visible on the 24th of January (Figure 3.11c), shortly before the major SSW began. The vortex is distorted but still coherent. In CO concentration plots at later dates, (not shown), areas of high CO mixing ratios associated with vortex remnants are still clearly visible until mid-February 2010.

In summary, the vortex maintains its dynamical integrity during the early stages of the 2010 major SSW but breaks up entirely during the 2009 SSW. This is reflected in the A_M measure (Figure 3.8b), which shows a much steeper decline between the 24th of January and the 1st of February for 2009 than for 2010. However the $\bar{M}$ measure shows little difference in the gradient of the decline (Figure 3.8a), which suggests that it is not particularly effective at measuring the effect of SSWs upon vortex barrier strength. The non-zero values of A_M in early-mid February are associated with vortex structure that persists at least

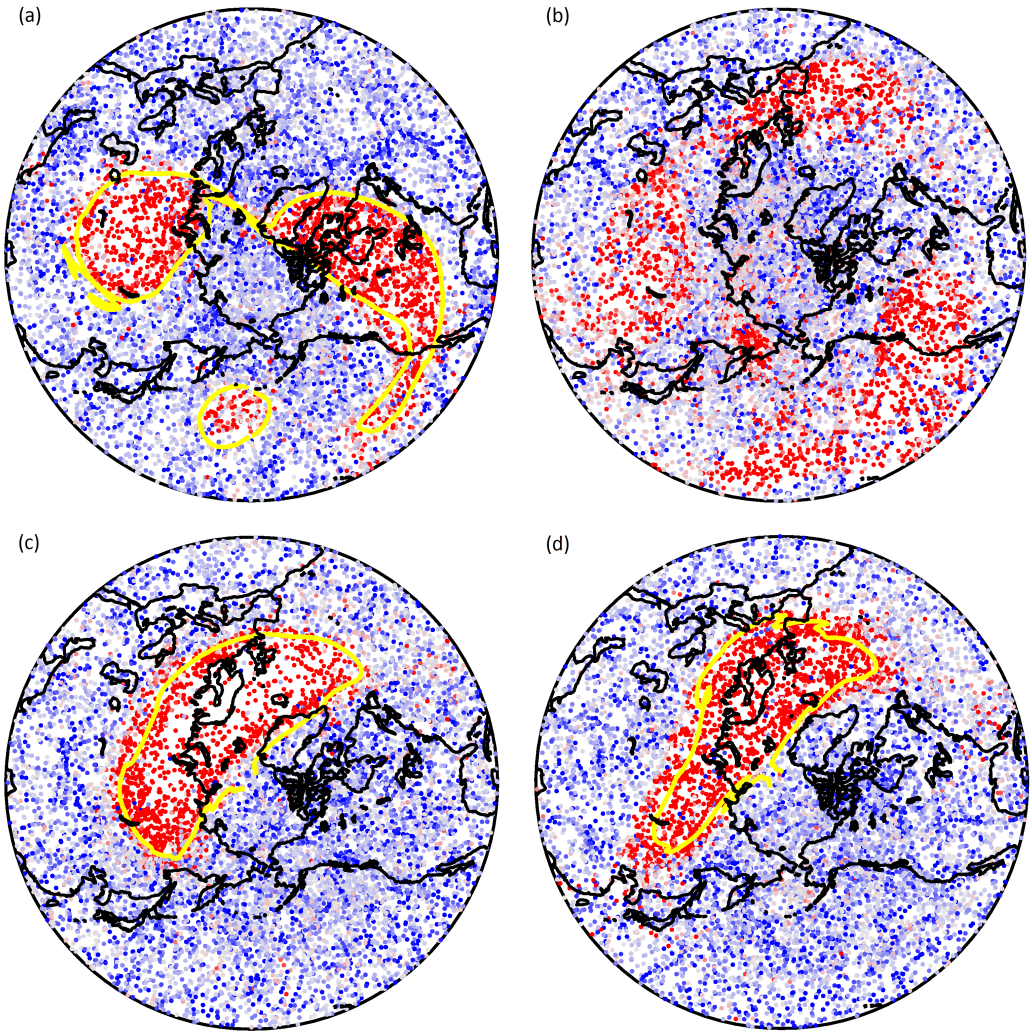

Figure 3.11: CO tracer concentration plots at 900 K for the 24th January 2009 (a), 1st February 2009 (b), 24th January 2010 (c) and 1st February 2010 (d). For the CO tracer plot, red areas correspond to high CO concentrations, blue areas to low CO concentrations, and intermediate values are shown in shades of gray. The approximate location of the vortex edge is delineated by a yellow line.

until mid-February. It should also be noted that during 2009 both the $\bar{M}$ and A_M measures begin their decline well before the SSW starts, while that is not the case for 2010. Although the breakup of the vortex during the SSW was sudden, these measures imply that the vortex began to weaken long before then.

3.4 Conclusions and future work

This paper shows that the function M can be used, not only to visualize the dynamics and structure of the stratospheric polar vortices in a detailed way, but also to provide a basis for quantitative measures that can capture important aspects of vortex dynamics. We have derived measures based on the function M that aim to quantitatively describe how different aspects of polar vortex dynamics change over time.

In general, the average value $\bar{M}$ near the vortex edge, and the vortex edge area A_M associated with values of M above a certain threshold value, are intended to be associated, respectively, with the strength of the vortex barrier and the area of the vortex barrier region. For the Southern hemisphere during August to October in 2010, both of these measures, taken together, show an apparent peak in the size and strength of the vortex in mid-August followed by a slow decline that becomes somewhat steeper from early October onwards. For the same period in 2009, the two measures do not agree in the same way, with the area measure declining significantly during the period from mid-August to early September, while the average value of M near the vortex edge is still increasing. The Northern hemisphere vortex also behaves in a similar way during the December 2004 - March 2005 winter season. The daily plots of M during these periods show the area of high function M values narrowing without a commensurate reduction in the magnitude of M within that region. This means that the $\bar{M}$ measure provides information about the vortex barrier strength that is not captured by the effective area A_M and the two measures are complementary in this case.

For the Northern hemisphere test period from December 2009 to March 2010, the $\bar{M}$ measure does not accurately show the sudden vortex breakup during the SSW event starting on the 24th of January, perhaps indicating a highly perturbed coherent vortex with little mixing. Instead it gradually reduces from this point until well into February. However, the A_M measure declines sharply from the 24th of January onwards, although it still does not reach its minimum until mid-February. This suggests that some remnant of the vortex structure persists

at least until this time and that A_M is potentially a useful measure of vortex strength.

The A_M measure also shows a sharper drop during the 2009 SSW than during the 2010 SSW. This makes sense given that the 2009 SSW was an unusually strong vortex split event that caused a rapid and complete breakdown of the vortex. For the December 2004 - March 2005 northern winter, the A_M measure shows the vortex edge barrier to be considerably wider than for these two disturbed years during late December and early January, and that it persists at least until early March.

One possible cause for the lack of a strong SSW signal from the $\bar{M}$ measure could be the large values of τ used in the calculations. However, the inability of $\bar{M}$ to capture the SSW event persists when the function M is calculated over a shorter time period. While investigating this, we found that there is, particularly near the vortex edge, a strong linear correlation between values of the function M calculated over different time periods. This means that the results found when calculating quantitative measures based on the function M (shown in Figures 3.4, 3.6 and 3.8) depend very little on the length of the time period, varying only by a scale factor proportional to time, which suggests that these dynamical structures are coherent over periods of at least 30 days. This correlation may weaken in the vicinity of hyperbolic invariant manifolds and trajectories since these features, which are associated with sharp gradients in the function M, are evident only when the period over which M is calculated is sufficiently long.

Plots of the function M show a vortex-like structure persisting well into the 2010 SSW period (Figures 3.10 and 3.11d), although the vortex is highly deformed. The existence of this structure may contribute to the less dramatic SSW signal observed using the A_M measure in 2010 as opposed to 2009. The standard definition of an SSW is affected by the shape of the vortex, while the function M-based measures are based on a Lagrangian framework, and therefore are able to pick up this remaining structure.

Of the two measures investigated here, the A_M measure appears much more effective at identifying SSWs and the differences in its behavior during the 2009 and 2010 major SSWs suggest that it may also be able to distinguish between different types of SSWs (for example, between displacement and split events). In order to verify this, A_M will need to be calculated over more time periods which include SSWs. The $\bar{M}$ measure, appears to be insensitive to SSWs, with no clear signal of them visible during any of the test periods. However it may still provide a useful measure of the time within a winter period when the vortex edge

barrier reaches its maximum. For the 2009 SH period, the maximum value of this measure is attained in mid-September after a long period of high values, while for 2010 it occurs in mid-August. For the three Northern hemisphere periods, the locations of the peaks in the $\bar{M}$ measure differ considerably from year to year. For the December 2008 - 2009 period, which contains the very large SSW, the measure peaks early, at the very beginning of January, while for the 2009 - 2010 period it peaks in early-mid January. For 2004 - 2005, within which the vortex is unusually strong and cold [El Amraoui et al., 2008], the measure does not peak until the beginning of February.

The function M can also be used to produce clear and detailed maps of the polar vortices that show the polar night jet, anticyclones, the signatures of planetary wave breaking as well as identifying specific locations where mixing across the vortex edge is likely to be occurring. These are surprisingly similar to plots obtained for the same times using potential vorticity (PV) (given that the function M is based on wind speeds over an extended period - in this case 30 days, while PV is based on instantaneous measurements) except that the function M plots contain more fine detail associated with the behavior of air parcels at other times within the period over which M is calculated. This is possibly because the function M is a Lagrangian measure which follows each air parcel over the calculation period, thus allowing long-term dynamics to be investigated without losing information due to Eulerian averaging. Coherent regions in which air parcels travel consistently at high wind speeds can be identified as being dynamically linked to the vortex. The location and extent of the polar vortices observed in the function M plots also agrees well with that observed in CO tracer plots.

For the purposes of this study, the function M was calculated throughout on two-dimensional isentropic surfaces, but extending the model to three dimensions may make it possible to extend the validity of this methodology to the upper stratosphere and mesosphere. The reanalysis data used here may also become less reliable at these higher altitudes, so it would be helpful to investigate alternative ways of obtaining wind speed data to use with the trajectory model such as the use of experimental measurements of tracer mixing ratios (see for example Rienecker et al. [2011] and McDonald and Smith [2013].

Acknowledgements.

MERRA data was disseminated by the Global Modeling and Assimilation Office (GMAO) and the 571 GES DISC. AJM would like to thank the EOS MLS team at the Jet Propulsion Laboratory/NASA for the provision of the EOS MLS data via their web site. This work was supported by the Royal Society of New Zealand Marsden Fund project "Evaluating the Impact of Excess Ionization on the Atmosphere".

Chapter 4

Identifying vortex air using Aura MLS tracer observations

4.1 Introduction

Energetic charged particles from the solar wind can produce a variety of chemical species when they interact with the atmosphere. Except during high intensity solar proton events (SPEs), these are primarily created in the mesosphere and lower thermosphere (MLT). Some, such as odd hydrogen and nitrogen (HO_x and NO_x), are capable of catalytically breaking down ozone. During the polar night, NO_x in particular can often be advected downwards into the stratosphere during the period when its lifetime is enhanced due to a lack of photodissociation. This is known as the energetic particle precipitation indirect effect (EPP IE) [Solomon et al., 1982, Seppala et al., 2004, Randall et al., 2007, 2009]. The dynamics of the polar vortex in the stratosphere and mesosphere can have a large impact on the magnitude of this effect, since the vortex transport barrier allows EPP-NO_x to be isolated within the polar night region, protecting it from photodissociation, while changes in the rate of diabatic descent within the vortex also affect the quantity of EPP-NO_x that reaches the stratosphere. More generally, the composition of air within the lower-middle stratosphere during the polar winter can be affected considerably by alterations in vortex dynamics that give rise to changes in the amount of air that arrives from higher altitudes.

Most reanalyses used in studies of the polar atmosphere represent dynamical fields well in the lower-middle stratosphere up to approximately 10 hPa [Manney et al., 2008b], but have more significant errors in the upper stratosphere and lower mesosphere (USLM) that increase with altitude [Manney et al., 2008b]. The errors

are particularly problematic during major stratospheric sudden warmings (SSWs) such as those in early 2006 and 2009 [Manney et al., 2008b, 2009b]. In order to understand the general dynamics of the upper stratosphere and mesosphere, as well as the EPP IE, it is important to obtain information about the dynamics of the polar vortex at high altitudes. Consequently, it is important to develop methods for studying the vortex that do not rely on reanalysis data. It would be particularly helpful to develop methods that determine the location of the vortex directly from satellite measurements.

The location of the polar vortex edge is most commonly determined using the isentropic potential vorticity (PV), which can be calculated from potential temperature and wind velocity fields. The PV field can be used to describe stratospheric dynamics in terms of an alternative set of coordinates in which PV increases monotonically with latitude; the new latitude coordinate is referred to as "equivalent latitude" [Butchart and Remsberg, 1986].

Over timescales of a few days to approximately a week, PV behaves as a conserved tracer in the stratosphere [Haynes and McIntyre, 1987, Baker and Cunnold, 2001, Waugh and Polvani, 2010]. Therefore PV contours align with the boundaries of dynamically distinct areas in the stratosphere, such as the polar vortex (e.g., Butchart and Remsberg [1986]). The polar vortex often deviates from zonal symmetry. This means that using a coordinate system including physical latitude to investigate the vortex can lead to issues where it becomes difficult to distinguish between vortex and extra-vortex air. For example, when calculating the mean concentration of a tracer as a function of physical latitude, for some latitudes both intra- and extra-vortex air contribute to the average, meaning that results for latitudes near the vortex edge are "smeared out". Using PV-equivalent latitude as a vortex-centered coordinate avoids these problems and as a result this coordinate system has been very widely used in studies of the polar vortex.

However above approximately 50 km, equivalent latitudes based on PV are no longer useful because the near monotonic relationship between PV values and physical latitude breaks down [Harvey et al., 2009]. Below this altitude, automated PV-based methods for locating the vortex edge work best when there is a single unambiguous region of strong PV gradients. This is most often the case during the winter, particularly in the Southern hemisphere, while it becomes more difficult to identify a clear vortex edge in the spring and fall [Manney et al., 2007]. The position of the vortex also becomes more ambiguous at higher altitudes within the stratosphere [Mitchell et al., 2010].

Another common set of methods used to locate the vortex edge and its

strength are those based on Lagrangian trajectory models. By initializing an artificial tracer at a chosen location and observing where air parcels at that location are later advected, it is often possible to observe the locations of barriers such as the one at the vortex edge [Chen, 1994, Chen et al., 1994, Grooßet al., 2008]. Such barriers can also be identified by advecting material contours comprised of many air parcels and observing the rate at which they lengthen, which is reduced in the vicinity of a barrier [Chen, 1994]. Lyapunov exponents can also be used to identify low rates of mixing associated with the vortex edge barrier [Bowman, 1993, Garny et al., 2007, Beron-Vera et al., 2012]. The recently developed "function M" measure, based on the length of Lagrangian fluid parcel trajectories, can also be used to map the polar vortex in detail and identify the vortex edge barrier [Jimenez Madrid and Mancho, 2009, de la Camara et al., 2012, Smith and McDonald, 2014]. These methods in general require reliable gridded wind velocity data to work, and so may not be suitable above the mid-stratosphere.

However, satellite observations of chemical tracer species are readily available at these higher altitudes. Satellite instruments such as ACE [Bernath et al., 2005], Aura-MLS [Waters et al., 2006], and Odin-SMR [Murtagh et al., 2002] can measure profiles of chemical species over wide altitude ranges. A number of these species are relatively inert and thus useful as tracers at altitudes above those accurately described by reanalysis data.

Because the vortex barrier isolates polar stratospheric air, the chemical composition of air within the vortex is often markedly different from that outside it, meaning that differences in tracer mixing ratios can be used to locate the polar vortex edge region [Greenblatt et al., 2002a, Plumb, 2002, McDonald and Smith, 2013]. In the stratosphere, concentrations of nitrous oxide are highest near the equator and lower near the poles, since nitrous oxide is primarily produced at the surface [Jin et al., 2009]. Although some N_2O is also produced in the mesosphere and lower thermosphere (MLT) as a result of reactions made possible by EPP, this has not been observed to descend to altitudes below 40 km and so does not generally reach the middle stratosphere [Sheese et al., 2016]. Carbon monoxide is produced both at the surface and in the mesosphere and thermosphere [Funke et al., 2009]. However, the majority of carbon monoxide in the stratosphere comes from higher altitudes via diabatic descent within the polar vortex during the winter. Therefore, in the mid-stratosphere, concentrations of CO within the vortex are markedly higher inside the vortex than outside, while concentrations of N_2O are lower within the vortex. Since the two tracers are produced in different regions, react differently to sunlight and have different sources and sinks, using

both of them may provide more detailed information about the vortex location than would otherwise be possible.

In the mid-stratosphere and above, methods based on probability distribution functions (PDFs) of tracer mixing ratios are potentially very useful for obtaining information on local dynamics since no additional information is needed to calculate them. This is discussed in detail by Sparling [2000] and Hu and Pierrehumbert [2001], while Neu et al. [2003] use a PDF-based method to locate the boundary of the stratospheric "tropical pipe" region. Krützmann et al. [2008] uses Rényi entropy, a measure that describes the complexity of a tracer PDF, to investigate stratospheric mixing, while McDonald and Smith [2013] use the PDF of carbon monoxide to identify vortex air.

A number of studies have shown that using more than one tracer can provide additional information. If two stratospheric tracers both have a lifetime considerably longer than the timescales of both diabatic and isentropic transport, and if there are no permanent transport barriers, then when their mixing ratios are plotted against each other, the result is a coherent curve (e.g., Plumb [2007]). Mixing events between different regions will cause some measurements to instead lie on a secant line intersecting this curve. This can be used to identify locations from which mixing has taken place [Morgenstern et al., 2002].

In this paper, we develop methods for identifying vortex air and thereby the location of the vortex edge in the middle stratosphere based on mixing ratios of carbon monoxide (CO) and nitrous oxide (N_2O). This builds upon work previously published in McDonald and Smith [2013] in which the PDF of CO concentrations was used to identify periods during which a polar vortex barrier exists. Mixing ratio thresholds derived from the PDF were then used to identify which measurements were within the vortex.

Tracer-tracer diagrams are used to provide a new perspective on chemistry and dynamics during the stratospheric winter. We use k-means clustering to divide the tracer-tracer diagrams into regions corresponding to intra– and extra–vortex air and identify the approximate location in tracer space that corresponds to the vortex edge. This method is applied on isentropic surfaces at 700, 900 and 1250 K; at these altitudes there are distinct differences in CO and N_2O concentrations across the vortex edge barrier during the vortex season. The k-means method is tested by comparing it statistically with the vortex edge location based on PV and wind speed data.

During winter, the lifetime of CO in and near the polar vortex is very long due to the lack of sunlight preventing the reactions with OH which are carbon

monoxide's major loss process from taking place. This lifetime reduces to about 20 days in the presence of sunlight [Minschwaner et al., 2010]. Therefore, when CO-rich air is advected to low altitudes as a result of a vortex breakdown, or when sunlight returns to the vortex region in spring, this will lead to some loss of CO [Minschwaner et al., 2010]. This may shorten the time period over which CO can be used to identify the vortex edge in some cases, since once the polar night ends the CO enhancement within the vortex will only last for a finite time, even if the vortex edge barrier still exists.

We also investigate the possibility of determining the provenance of air using an alternative tracer, namely water vapor, instead of nitrous oxide, since the reduction of nitrous oxide concentrations with altitude limits the range over which these measurements can be made by MLS. As a result of the maximum in water vapor mixing ratio in the upper stratosphere caused by its production by oxidation of methane (CH_4), the distribution of water within the stratosphere is relatively complicated [Lee et al., 2011]. When air descends through the polar vortex during winter, in the upper stratosphere concentrations of water become lower within the vortex than outside due to the descent of drier mesospheric air. By contrast, in the lower-middle stratospheric vortex water concentrations become higher than outside due to the descent of moister upper stratospheric air. But the altitudes reached by the moist upper stratospheric air and dry mesospheric air change with time as the vortex season progresses and descent continues, meaning that, especially in the middle stratosphere, there are some altitudes where the air within the vortex becomes first moister, then drier, than the surrounding air. This will make the process of using water vapor to identify vortex air at these altitudes more complex; therefore in the middle stratosphere it is likely preferable to use other tracers available at these altitudes, such as nitrous oxide, which do not have this problem. In the polar lower stratosphere, an additional complicating factor affecting the usefulness of water vapor is the formation of polar stratospheric clouds (PSCs) comprised of ice during the coldest parts of winter. This is an important sink of water vapor which causes air in this region to become considerably drier during these time periods [Nedoluha et al., 2003, McDonald et al., 2009].

In the upper stratosphere and mesosphere, water vapor concentrations are likely to be lower within the vortex than outside during the entire vortex season, except during major SSWs such as the one observed during January 2010 [Straub et al., 2012]. Then, although it is not in general useful as a tracer in the upper stratosphere [Lee et al., 2011], water vapor may still potentially be useful for

identifying vortex air in the upper stratosphere and mesosphere, especially in combination with carbon monoxide (CO), which remains a useful tracer at these altitudes.

By using different combinations of tracers, such as CO vs water vapor, it should be possible to apply a method similar to that used here to identify the vortex edge location over a wide variety of altitudes, including those where reliable reanalysis data is not available. If a k-means analysis based on CO and N_2O concentrations can be shown to agree well with a PV-based method in the middle stratosphere, this will provide some evidence that a similar method based on other tracers such as water vapor or methane will be effective in the upper stratosphere and lower mesosphere (USLM), a region where there is a lack of reliable reanalysis data and methods based on PV or wind velocities become less useful.

4.2 Methods

The carbon monoxide, nitrous oxide and water vapor profiles used in our analysis were obtained from the Aura-MLS instrument. Temperature data from this instrument were also used to interpolate the results to potential temperature surfaces using splines. The MLS instrument on the Aura satellite [Waters et al., 2006] orbits the Earth at an inclination of 98° and obtains approximately 3500 vertical profiles per day over physical latitudes between 82°N and 82°S by observing thermal microwave limb emissions. It measures a number of different chemical constituents, and also temperature and geopotential height. The Aura-MLS CO measurements are described and validated in Filipiak et al. [2005] for version 1.5 of the data and Pumphrey et al. [2007] for version 2.2. Pumphrey et al. [2007] indicates that the MLS CO mixing ratios have a positive bias of 25–50% in the mesosphere, a negative bias of up to 70% in the lower stratosphere, and are usable from the upper troposphere up to 90 km altitude. Lambert et al. [2007] discusses the quality of the version 2.2 product for both water vapor and nitrous oxide, concluding that the scientifically useful range of the H_2O data is from 316 to 0.002 hPa with the accuracy estimated to be 0.2-0.5 ppmv (4-11%) between 68-0.01 hPa. They also identify that the accuracy for the version 2.2 N_2O product is 3-70 ppbv (9-25%) in the pressure range 100-4.6 hPa. For all three tracers, Livesey et al. [2011] describes updates for the version 3.3 product utilized in this study.

Over the period from January 2005 – December 2010, these profiles were used

to derive two-dimensional histograms of carbon monoxide vs nitrous oxide on the 700, 900 and 1250 K isentropic surfaces. Each histogram contains measurements made over an 11-day period centered on the date identified. The length of this period was chosen to match that used in McDonald and Smith [2013]. Profiles for which both the CO and N_2O mixing ratios passed quality control were identified and results based on the Northern and Southern hemispheres were processed separately to avoid confusion. We do not weight the results here to give the results an equal-area spatial distribution as in Sparling [2000], since this would mean removing some results from the area near the pole which we are particularly interested in.

Since according to Sheese et al. [2016] N_2O produced in the MLT can under some circumstances descend to altitudes of 40-45 km, and the 1250 K isentropic surface corresponds to an approximate altitude of 40 km, there is a possibility that some of our results there could be affected by N_2O-enhanced air descending from above. However, if this were the case, we would expect to see some measurements on the 1250 K histograms corresponding to air with relatively high concentrations of both CO and N_2O. Since for all of the histograms at 1250 K, none of the high-N_2O measurements are associated with high CO concentrations, it appears that none of our results are affected by descending EPP-produced N_2O.

Figure 4.1(a) shows a scatter plot of observations in the Southern hemisphere for a period centered on 1 September 2005 at 900 K (equivalent to an average altitude of about 31 km) in CO/N_2O tracer-tracer space. This scatter plot shows two distinct clusters, within which each measurement is color-coded based on its silhouette value; this is a measure of the likelihood of the measurement being clustered correctly and will be discussed in more detail later in this section. These clusters can be more clearly identified in Figure 4.1(b), which shows a two–dimensional histogram, highlighting data density, for the same period. Figure 4.1(b) shows an "L-shaped" distribution, with the density of results being noticeably higher in the two clusters. One of these contains measurements with low values of CO, while the other contains measurements with low N_2O values and high CO values. Since these profiles were taken during the Southern hemisphere winter, these high CO values will be related to descent of high-CO air within the polar vortex. This distribution is similar in form to the relationships observed near the tropopause between two tracers where one is more common in the troposphere and the other is more prevalent in the stratosphere (such as ozone and carbon monoxide) [Pan et al., 2004]. This type of distribution in tracer-tracer space is likely to be common in situations where a transport barrier separates

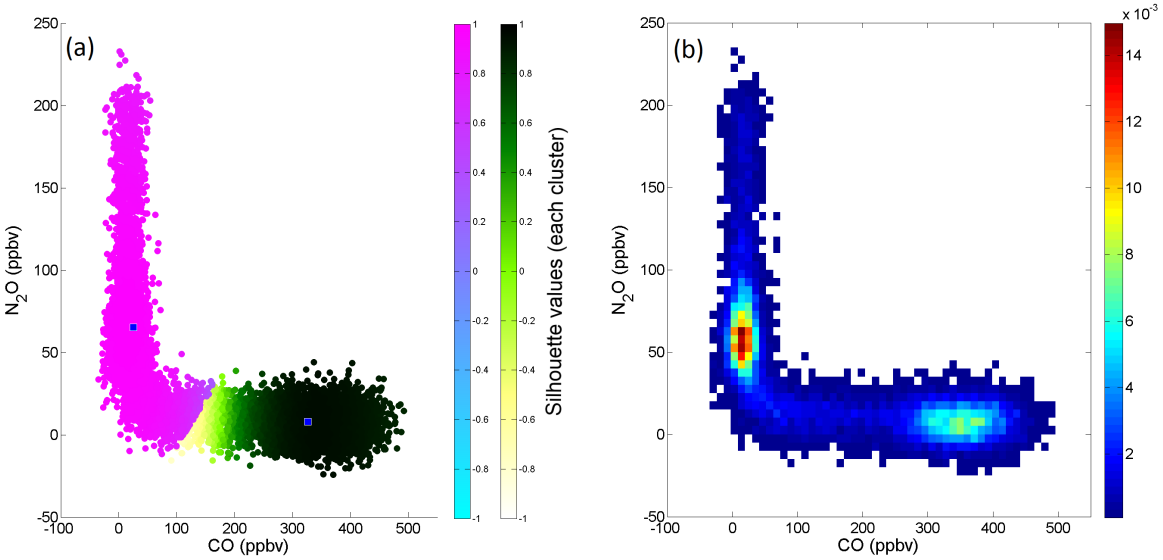

Figure 4.1: (a) Scatter plot divided into clusters using a k-means algorithm, with each cluster color coded based on silhouette values, for an 11-day period centered on 1 Sep 2005 at 900 K (SH). The blue squares show the mean CO and N_2O concentrations for each cluster. (b) Corresponding two-dimensional histogram in CO-N_2O tracer-tracer space.

two different atmospheric regions in which the two tracers used have opposing concentration patterns.

Since the high-CO measurements over the winter hemisphere in Figure 4.1 correspond to regions in and immediately around the polar vortex, it should be possible to develop a method for identifying a region in tracer-tracer space that corresponds to the polar vortex edge region. McDonald and Smith [2013] have already demonstrated that it is possible to identify intra- and extra-vortex air using CO concentrations alone. This study expands this idea by using multiple tracers and cluster analysis to take account of the distinctly different chemical properties of air inside and outside the vortex.

We use two different clustering algorithms to identify the approximate locations in tracer space associated with intra and extra-vortex air and will demonstrate in each case that these relate to geographically separate regions. The first algorithm is a k-means algorithm similar to that used in McDonald et al. [2009]. It iteratively searches for a predefined number (k) of clusters, two in this case, using the following scheme:

1. k elements of the data set of size N are selected at random and defined to

be seed points of distinct clusters;

2. each of the remaining N-k elements are assigned to the cluster with the nearest centroid (based on Euclidean distance in normalized tracer/tracer space) whereby after each assignment the centroid of the cluster is recalculated; and

3. after all elements have been assigned the centroid of each cluster is calculated. The algorithm is then iterated and the centroids used as new seed points.

In order to avoid distortions in the results caused by differing ranges of mixing ratios, these were normalized with respect to the length of the interval between the climatological maximum and minimum mixing ratios over Jan 2005–Dec 2010 for each tracer and potential temperature level. Outliers were manually identified and removed from consideration when calculating the interval lengths, but were not removed from the set of measurements used in the clustering. The algorithm is assumed to have converged once the concentrations of all tracers at the seed points differ by less than 0.5×10^{-12} between iterations. Wherever possible, we use the cluster centroids found by the algorithm for each day as the starting seed points for the next date. This tends to prevent random jumps in the results, and also helps speed up the computation. Where cluster centers from a previous day are not available, random values are chosen.

The second algorithm was designed with the intention of producing clustering results that more reliably represent the division of the measurements into intra and extra-vortex air. It is similar in many aspects to the first algorithm. Firstly, during step 2 of the algorithm, in which each of the data elements is assigned to the nearest cluster centroid, the cosine distance is used instead of an Euclidean metric. According to this measure, the distance between two points in CO-N_2O tracer-tracer space, $A = (CO_A, N_2O_A)$ and $B = (CO_B, N_2O_B)$, is given by

$$1 - \frac{CO_A \cdot CO_B + N_2O_A \cdot N_2O_B}{\sqrt{(CO_A)^2 + (N_2O_A)^2}\sqrt{(CO_B)^2 + (N_2O_B)^2}}$$

or $1 - \cos(\theta_{A \to B})$, where $\theta_{A \to B}$ is the included angle between the two points. Since the distance between two points according to this measure is based on the angle between the points measured from the origin, the position of this origin with respect to the data points is very important. Before the cluster seed points are chosen, the climatological minima of the CO and N_2O mixing ratios are subtracted

from all data points in order to ensure that all observations are in the upper-right quadrant with respect to the origin. The standard deviations of the CO and N_2O concentrations are then calculated. For the tracer with the highest standard deviation, the mean tracer mixing ratio over the 11-day period is then subtracted from all measurements. This has the effect of shifting the origin relative to the data in the direction of the tracer which has the highest standard deviation. This is necessary because the cosine distance-based clustering method generally divides the results into two clusters separated by a line beginning at the origin. However, there are a considerable number of cases where comparing the results to the two-dimensional histograms shows that this division gives suboptimal results. This is particularly likely to happen during periods when the clusters are more clearly distinguished with respect to one tracer than to the other. This will generally lead to that tracer having a larger standard deviation than the other tracer, so shifting the origin in that direction in usually leads to better results. For the cosine distance algorithm, the measurement ranges have not been normalized with respect to maximum and minimum mixing ratios. This is because initial attempts to do this led to extremely poor clustering results on some days. For example, for some days, nearly all the observations were placed into the vortex cluster while for others, hardly any were, even when two distinct clusters were clearly visible on the two-dimensional histograms. For our data set, cosine-norm algorithms appear to be less stable than algorithms based on the Euclidean norm, in that they are more prone to occasionally give wildly inaccurate results, with small changes in the algorithm causing marked differences in the frequency with which these issues occur. When the measurement ranges are not normalized and the origin is shifted relative to the data using the method described above, these issues become very rare for dates within the vortex period.

This method will be referred to as the "cosine clustering method" from here on.

For each clustering method, we can use silhouette scores [Rousseeuw, 1987] as a measure of the likelihood of each data point being correctly clustered. The silhouette score measures within-group and between-group differences and indicates how similar one point is to the other points within a cluster. The silhouette score can be written as:

$$S(i) = \frac{min\ b_i(k) - a_i}{max(a_i, min\ b_i(k))}, \tag{4.2.1}$$

where a_i is the average distance between point i and the other points in the

same cluster and $b_i(k)$ is the average distance between point i and the points in each of the other clusters k [Coughlin and Gray, 2009]. For each point, the silhouette value can range between -1 and 1, where negative values are associated with overlapping clusters and locations where specific data points may have been sorted into the wrong cluster. For a given day, the mean silhouette value over all the data can give insight into how well the division into clusters corresponds to the underlying structure of the data. It can also be used to help determine how many clusters a data set should be divided into and determine whether clustering is appropriate. For results obtained using both clustering methods, we use an un-normalized Euclidean metric for calculating the distances, since for the cosine clustering method, using cosine distances here led to there being too few points with low silhouette scores for the measure to be useful.

We also use a domain filling analysis, previously used in McDonald and Smith [2013], that projects observations taken over a time interval to their location at a particular time using a Lagrangian trajectory model to artificially improve sampling by utilizing observations acquired before and after the desired date via the use of forward and backward Lagrangian trajectories. This analysis allows us to plot the geographic position of cluster members at a higher resolution than would otherwise be possible in order to compare these with the vortex edge location. The domain filling analysis uses, as the input to the Lagrangian trajectory model, the MERRA reanalysis provided by the NASA GMAO (Global Modelling and Assimilation Office), which is based on the Goddard Earth Observing System Data Assimilation System (GEOS-5) [Rienecker et al., 2011]. The GEOS-5 model uses a $\frac{1}{2}^\circ$ latitude and $\frac{2}{3}^\circ$ longitude horizontal grid and 72 hybrid sigma/pressure model levels from the surface to 0.01 hPa [Rienecker et al., 2008]. The reanalyses data used in this study is the analyzed state on pressure levels product (inst6_3d_ana_Np), which uses the native horizontal grid, but with a reduced vertical resolution of 42 levels from 1000 to 0.1 hPa, and provides data at six hourly intervals. These horizontal wind data on pressure levels were then interpolated to potential temperature levels at each grid point for use in the Lagrangian model. This technique collects observations over an interval of 11 days centered on the desired date and assumes that, over the interval used, the passive tracer concentrations do not change. This is a reasonable assumption given that the longest trajectories used are taken over 5.5 days. Note that this analysis is limited to altitudes where the reanalyses are likely to be accurate and allows us to prove that the clustering technique works at these levels. All domain-filling plots shown in this chapter are at an isentropic level of 900 K. Each plot contains a mixture

of Aura-MLS data and MERRA reanalysis wind data used to advect the measurements to their current positions. The coherence of the plots shown later in Figures 4.3 and 4.4 and the observed match between observations belonging to the vortex cluster and the location of the vortex as obtained using the Manney et al. [2007] method then implies that the MERRA data is accurate enough to be useful for making such plots, since otherwise more points within the vortex cluster would be advected to locations outside the vortex than are seen here.

The technique also assumes that the motion of the air parcels is approximately adiabatic over the course of each trajectory. Since, according to Morris et al. [2002] and references therein, this approximation is valid for periods of 7-10 days at isentropic levels up to 800 K, it seems reasonable that it should also be valid over periods of 5.5 days at 900 K.

The simple Lagrangian trajectory model created at the University of Canterbury has been discussed previously in Alexander et al. [2013]. This model uses winds linearly interpolated in time and bilinearly interpolated in space as inputs to a fourth order Runge-Kutta algorithm applied at an hourly integration interval to derive particle trajectories on isentropic surfaces. A Euclidean coordinate system is used poleward of 70 degrees to avoid the singularity at the pole when using zonal and meridional wind components.

In order to test how well each of the clustering algorithms can identify measurements within the vortex, it is important to compare their results with those found using an alternative method. The most commonly used methods for determining the vortex edge location are based on PV-equivalent latitude. This can be calculated by finding, over either the Northern or Southern hemispheres, the area $A(q,t)$ associated with PV values above q at time t. This is a monotonic function of q that decreases as the value of PV increases. Then the equivalent latitude associated with that particular value of q is the latitude of the circle of latitude around the pole for which the area inside is equal to $A(q,t)$ [McIntyre and Palmer, 1984, Butchart and Remsberg, 1986, Haynes and Shuckburgh, 2000].

The most commonly used PV-equivalent latitude based method for determining the vortex edge location is described in Nash et al. [1996]. This method determines the equivalent latitude of the vortex edge using the gradient of PV and mean wind speed expressed as functions $dPV/d\phi_e$ and $v_{av}(\phi_e)$ of equivalent latitude ϕ_e. It identifies the peaks of each of these two functions and notes the value of the PV gradient and mean wind speed at each peak. It then multiplies together the PV gradient at each peak in $dPV/d\phi_e$ with the mean wind speed at each nearby peak of $v_{av}(\phi_e)$, and then chooses the pair of peaks that gives the

largest resultant value. The equivalent latitude associated with the chosen peak in PV gradient is then chosen to define the location of the vortex edge. A similar PV-based method, described by Manney et al. [2007] and used by Manney et al. [2009a], McDonald and Smith [2013] and Smith and McDonald [2014], simply multiplies the functions $dPV/d\phi_e$ and $v_{av}(\phi_e)$ together pointwise, and defines the equivalent latitude ϕ_e of the vortex edge to be where the resultant function is at its maximum. Other PV-based methods for locating the vortex edge include simply defining the vortex edge location to be at the maximum of $dPV/d\phi_e$ [Bauer et al., 1994].

We use the method described in Manney et al. [2007], McDonald and Smith [2013] and Smith and McDonald [2014] to provide an independent test of our clustering results, using PV and wind velocity data from the MERRA reanalysis to derive the potential vorticity at the vortex edge. Since we know the physical location of each of the tracer observations used by the clustering algorithms, we can find the PV value at the location of each measurement. This can then be used to determine, for each day, what proportion of results in the vortex cluster are in fact within the vortex, as well as what proportion of measurements geographically located within the vortex belong to the vortex cluster. The domain filling method is not used in this calculation; for each day, only measurements made on that day are included in the results. For each clustering method, statistics based on these daily proportions, as well as a similar analysis for the extra-vortex cluster, are shown in Chapter 4.3 for Northern and Southern winter periods during 2005-2010 at potential temperatures of 700, 900 and 1250 K.

During particularly strong major SSWs, noticeable errors in reanalyses can reach pressure levels as low in altitude as 10 hPa (approximately equivalent to 900 K). Therefore the PV-based position of the vortex edge could be affected to some degree by reanalysis errors at 900 and 1250 K. The agreement between analyses based on the GEOS-5 DAS and satellite data is considerably better, however, for dates not affected by SSWs [Manney et al., 2008a, Harvey et al., 2009]. The MERRA reanalysis is also based on GEOS-5, and therefore should be relatively unaffected by reanalysis errors except possibly for some dates during the 2006 and 2009 SSWs.

4.3 Results

4.3.1 Euclidean metric algorithm results

We will first discuss the results obtained using the k-means clustering scheme which uses a Euclidean metric. Figures 4.1(a), 4.2(a) and 4.2(c) display scatter plots in CO–N_2O tracer–tracer space at a number of different potential temperature levels and dates, and Figures 4.1(b), 4.2(b) and 4.2(d) show corresponding two-dimensional histograms. The points in the scatter plots are color-coded based on which cluster they are assigned to by the k-means algorithm, as well as on their silhouette values. The data points assigned to the low-CO/high-N_2O cluster are shown using a blue/purple color scale, representing the silhouette value of these cluster members, while the points assigned to the high-CO/low-N_2O cluster are shown using a white/yellow/green color scale.

While Figure 4.1 shows CO and N_2O concentrations during 1 September 2009, a period when there is a strong and stable stratospheric vortex, Figures 4.2(a) and (b) show results from 24 January 2009, identified as the start date of a major SSW in Labitzke and Kunze [2009] and Manney et al. [2009b]. Here, rather than an "L-shaped" distribution, we see a "cut-off corner", with measurements lying approximately on a line between the two lower clusters. According to Waugh et al. [1997], Michelsen et al. [1998] and Pan et al. [2004], as well as Plumb et al. [2000] and references within, such lines indicate the presence of mixing between the air masses at the line's endpoints. For this date, there are more points with lower silhouette scores than for 1 September 2005, with 10.9% of the measurements shown in Figure 4.2(a) having silhouette scores below 0.5 compared to 3.92% in Figure 4.2(a). This suggests that for 24 January 2009 there are more measurements for which there is some uncertainty about their cluster assignments. The areas with low silhouette scores are mostly within the "cut-off corner" with chemical concentrations that are between those observed in the cores of each cluster. Two-dimensional histograms on subsequent dates (not shown) display continued strong mixing and a complete disappearance of the vortex cluster by the end of February. Figures 4.2(c) and 4.2(d) show results at the higher potential temperature level of 1250 K for 15 January 2006. These show a large number of measurements with low values of both carbon monoxide and nitrous oxide. This is a common feature in Northern hemisphere winter tracer-tracer plots at 900 and 1250 K. The silhouette scores indicate that the majority of data points have been assigned reliably to their clusters, with only 2.95% of the measurements having

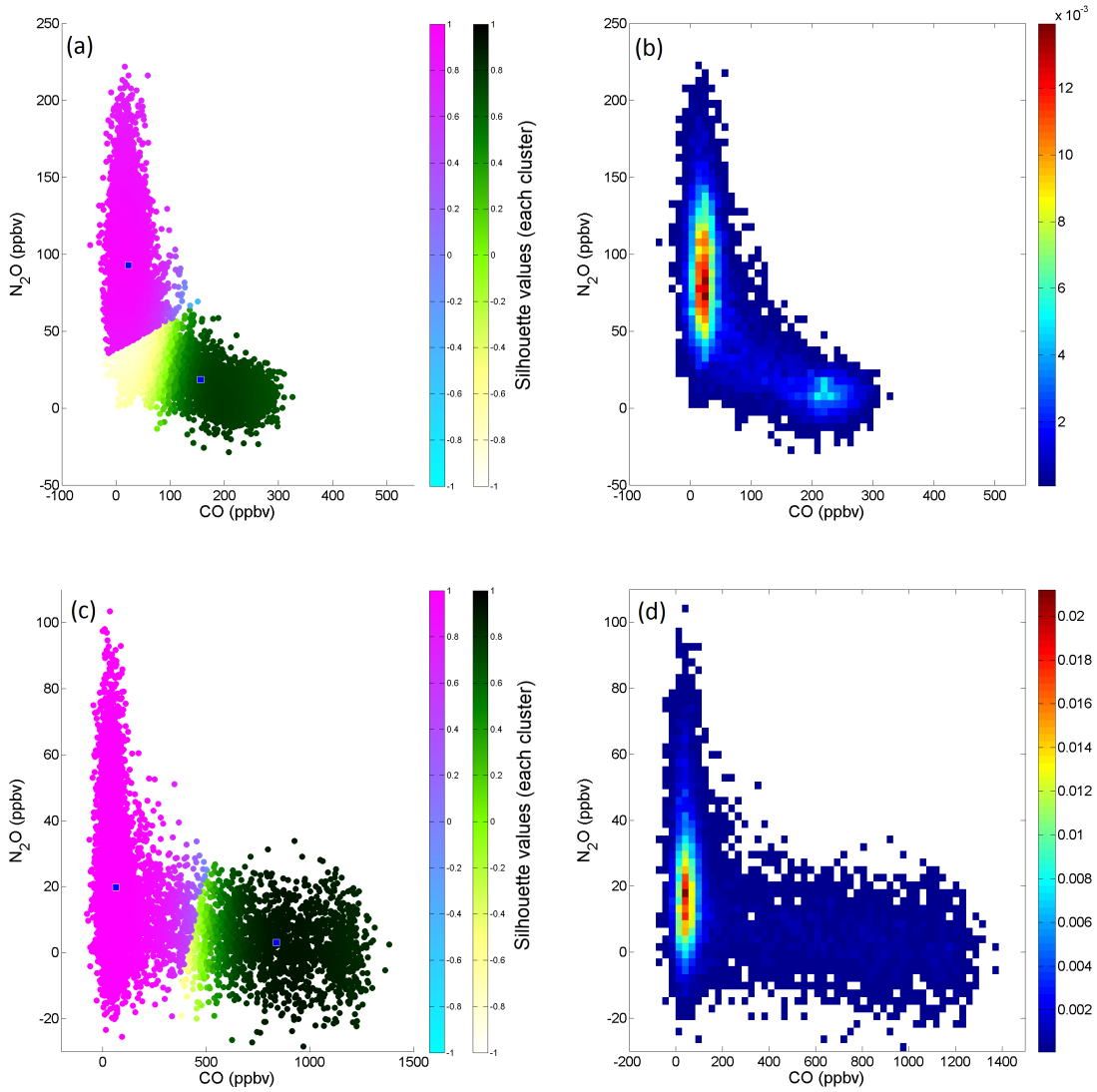

Figure 4.2: Scatter plots divided into two clusters using a k-means algorithm, with each cluster color coded based on silhouette values, for 11 day periods centered on (a) 24 Jan 2009 at 900 K (NH) and (c) 15 Jan 2006 at 1250 K (NH). (b, d) Corresponding two-dimensional histograms in tracer-tracer space.

silhouette scores below 0.5.

In the vortex edge region, concentrations of CO and N_2O should have values that are between those found in the intra- and extra-vortex clusters. Therefore it should be expected that measurements from this region should be positioned somewhere between these two clusters on a tracer-tracer plot. Since in Figures 4.1(a) and 4.2(a), the dividing lines between the clusters and the regions of low silhouette values surrounding them are neatly positioned between the two highest-density clusters (Figures 4.1(b) and 4.2(b)), it is likely that they are located within or near to the vortex edge region. The statistics that will be shown later in Tables 4.1-4.8 are intended to help provide evidence that this is the case by comparing our results to those obtained by a PV-based method for locating the vortex edge.

We now examine polar stereographic plots for a range of fields, using the domain filling scheme discussed in Chapter 4.2 to improve sampling. Figures 4.3(a) and (b) display polar stereographic plots of CO and N_2O concentrations, respectively, for 1st September 2005. The corresponding clustering plot and 2D histogram are shown in Figure 4.1. Figure 4.3(a) clearly shows that high values of CO are constrained to the inside of the vortex derived using the PV-equivalent latitude based scheme described in Chapter 4.2, with lower concentrations outside the polar vortex. Similarly, Figure 4.3(b) displays significant differences in N_2O concentrations between the inside and outside of the vortex, but with high values outside the vortex in this case. When approaching the vortex edge line from the inside, CO concentrations start to reduce, relative to values near the pole, before the vortex edge line is reached (Figure 4.3(a)), but N_2O concentrations do not change much relative to their polar values until after the vortex edge line has been passed (Figure 4.3(b)). This may highlight an intermediate mixing region such as that observed by Roscoe et al. [2012], but clearly identifies that the two tracers include different information. Thus, combining data from both these datasets within the k–means clustering scheme might be advantageous. Figure 4.3(c) displays the membership of the intra- and extra-vortex clusters found using the k-means method (light and dark gray, respectively). This clearly demonstrates that the clustering scheme can identify vortex air. For this date, the boundary between the intra- and extra-vortex clusters appears to match the edge of the region of high CO concentrations in Figure 4.3(a) more closely than the edge of the low-N_2O region in Figure 4.3(b).

A comparison of Figure 4.3(c) with Figure 6(b) in McDonald and Smith [2013] shows that for this case the k–means scheme has an ability to identify intra-vortex

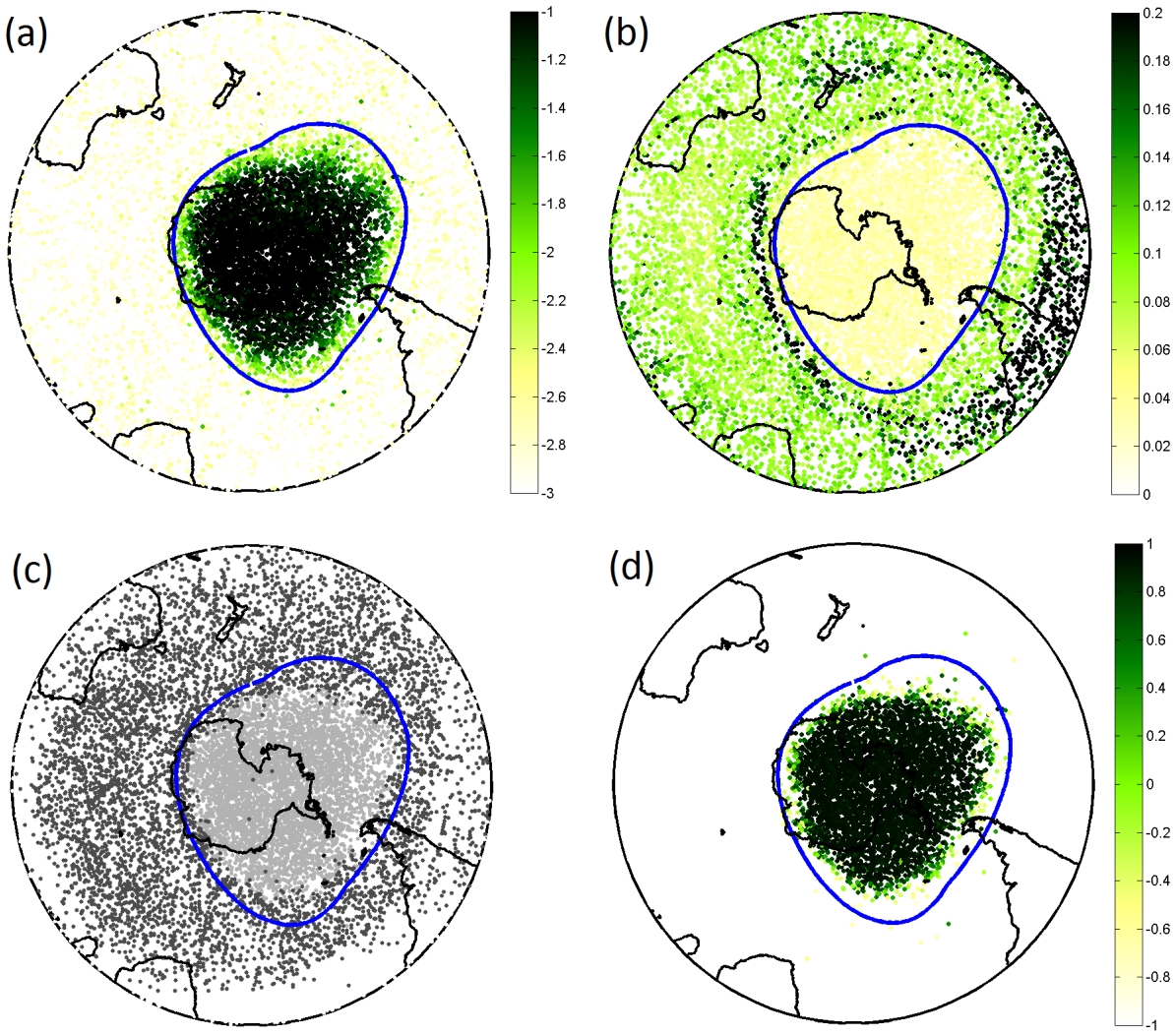

Figure 4.3: The polar stereographic maps show re-sampled observations on the 900 K isentropic level in the austral winter of 2005 for 1st September. The blue line on each map indicates the position of the vortex edge. Each colored dot in the map identifies the position of a resampled EOS-MLS observation (a) relates to the logarithm of CO concentrations and (b) shows N_2O concentrations (ppmv). In (c) the dark and light gray represent the intra- and extra vortex air clusters derived via k–means clustering and (d) displays the silhouette value for each member of the intra-vortex cluster.

air similar to that in McDonald and Smith [2013]. This point is further supported by the data discussed later in Tables 4.1-4.8. However, Figure 4.3(d) displays an additional useful property of the clustering scheme, namely that we can derive silhouette values for each member of the two clusters. An examination of Figure 4.3 (d) shows that in this case the highest silhouette values are found in the center of the vortex and the lower silhouette values, which are representative of measurements that are allocated to the vortex cluster with less certainty, occur close to the vortex edge derived using the scheme described in Chapter 4.2. The silhouette value for each cluster member therefore provides us with a useful statistical metric that relates to the structure observed in Figures 4.3(a) and (b).

This point is studied further in Figures 4.4(a), (c) and (e), which display individual silhouette values for observations within the intra-vortex cluster for 14, 21 and 28 January 2009 at 900K in the Northern hemisphere. This period encompasses the time of the 2009 Stratospheric Sudden Warming (SSW), which officially begins on 24 January [Labitzke and Kunze, 2009, Manney et al., 2009b]. On 14 January, before the warming, the scheme works well at identifying intra-vortex air even though the vortex edge (blue line) is complex (Figure 4.4 (a)). It also highlights that the streamer of air from the Arctic with its tip near Italy, has properties that are not as strongly related to intra-vortex air as other regions within the vortex, as shown by the low silhouette values. This may indicate that the PV-based vortex edge extends over a region where active mixing between intra- and extra-vortex air is occurring prior to the SSW. On 21 January, the vortex is already strongly distorted although the SSW has not yet begun, and the relationship between the intra-vortex cluster members and the vortex edge is not as clear (see Figure 4.4 (c)). But, again the intra-vortex silhouette values are lower in the filamentary structure over North America and the Pacific Ocean than elsewhere within the vortex. The relatively small number of cluster members outside the dynamic barrier also have low silhouette values, which may identify in this case that these observations represent air that has recently been mixed out of the vortex. Figure 4.4 (e) displays the silhouette values for 28th January 2009. These observations occur after the polar vortex has been strongly distorted and has split into two pieces (a vortex split event). In this case the clustering algorithm clearly identifies a large number of cluster members that are not within the rather complicated vortex edge. However, in this case the highest silhouette values again remain inside the vortex edge. It should also be noted that the mean silhouette values for these three days are 0.74, 0.78 and 0.39, respectively. The sharp difference between the values before and after the SSW suggests that the

silhouette score may be changing in response to SSW-induced alterations in the tracer distributions. However, as will be shown later (see Figure 4.5), although such sudden drops in Sil_{av} are often associated with major SSWs, they in fact only occur during periods where intra-vortex CO concentrations are declining near the end of the vortex season, and so could potentially be used to help find the vortex breakdown dates.

Figures 4.4(b), (d) and (f) display tracer-tracer scatter plots for the same dates shown in Figures 4.4(a), (c) and (e). On 14 January, the high-silhouette vortex cluster members shown in green (Figure 4.4(b)) almost all map to the region within the blue line in Figure 4.4(a) and are thus correctly classified. Most of the data points, shown in yellow, that are assigned to the vortex cluster with low silhouette values are physically located in a region near the streamer of air discussed above; this region appears to be a transitional region containing air with characteristics of both intra and extra-vortex air. This air has relatively low concentrations of both CO and N_2O. The angle between the high-CO and the high N_2O regions is fairly close to a right angle, suggesting that relatively little mixing is occurring between them over short time scales. On 21 January, the angle between these regions becomes more obtuse and individual detached points can be seen within it (Figure 4.4(d)). This implies that mixing between intra and extra-vortex air is occurring prior to the major SSW beginning on 24 January. The majority of points assigned to the vortex cluster with high silhouette values (shown in green) are physically located within the main body of the vortex shown in Figure 4.4(c). The yellow low silhouette value points are mostly located within the long filamentary structure in Figure 4.4(c) and outside the vortex. On 28 January (Figure 4.4(f)), the "L-shaped" structure seen in earlier clustering points appears to have broken down as a result of strong mixing between air assigned to the vortex and extra-vortex clusters. A large proportion of the air assigned to the vortex cluster with low silhouette values appear to be physically located outside the vortex and the number of such points has markedly increased since 21 January. This suggests that the majority of the points marked in yellow in Figure 4.4(f) have been incorrectly assigned to the vortex cluster. It appears that for 28 January, the effects of the SSW have caused the clustering algorithm to assign many points to the vortex cluster incorrectly. However the majority of points marked in green are assigned to locations within the vortex remnants. In Figure 4.4(f) it can be seen that the low daily mean silhouette value for this day's clustering results is due to the silhouette values in the high-CO region of the scatter plot being lower than on previous days.

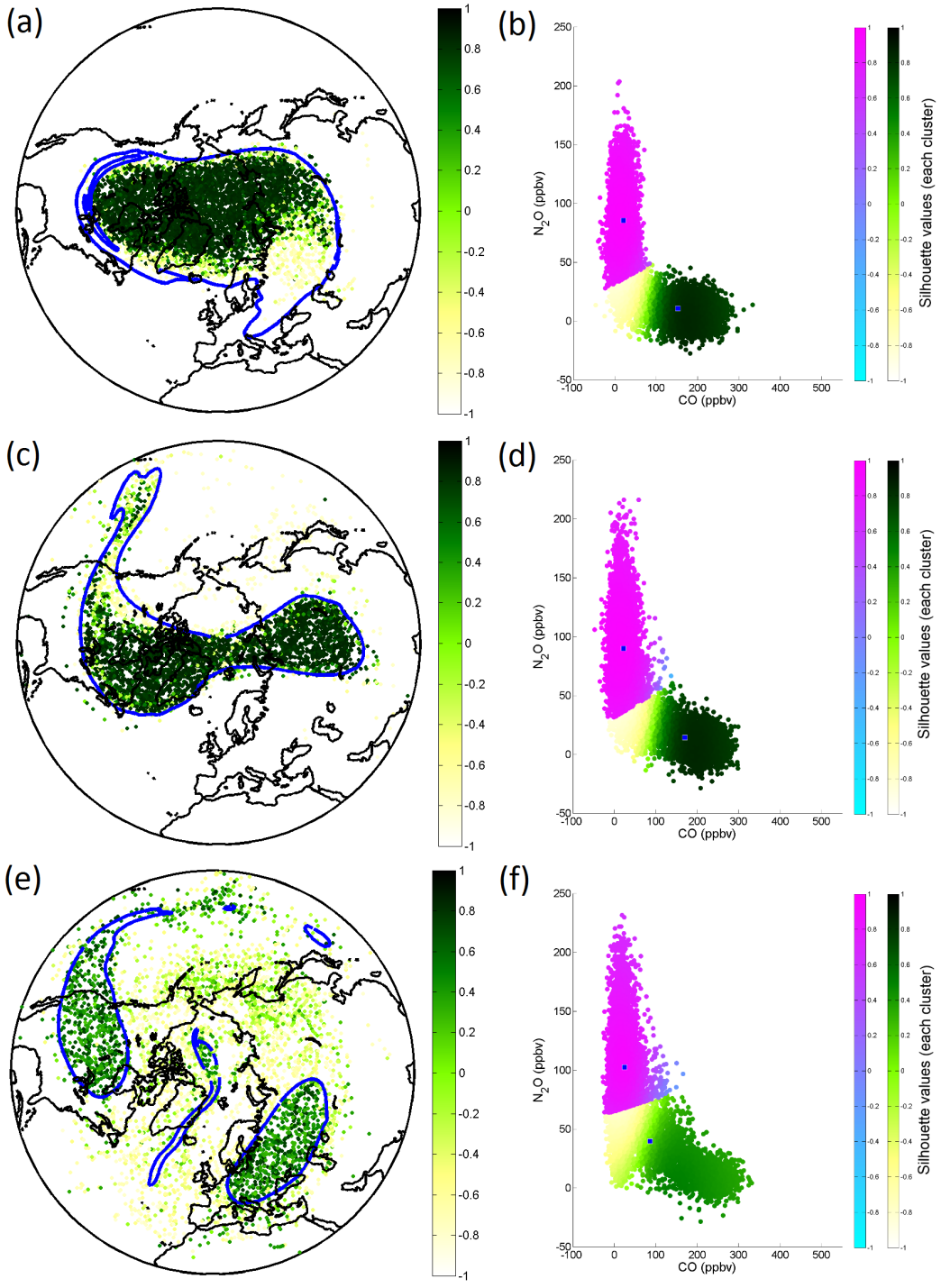

Figure 4.4: Silhouette values for the intra-vortex cluster members for 14 (a), 21 (c), and 28 January 2009 (e) on the 900 K isentropic level in the Northern hemisphere. The blue line on each map indicates the position of the vortex edge. (b, c, f) Scatter plots divided into two clusters using a k-means algorithm, with measurements color coded according to silhouette values.

Figures 4.5 and 4.6 show, for the 2005-2010 winter spring periods, CO concentrations at the centroids of the low-N_2O (solid red line) and high-N_2O (dotted red line) clusters, the daily mean silhouette scores Sil_{av} averaged over all data points in each cluster (blue line), and, for selected dates, the proportions of measurements assigned to the low-N_2O cluster that were later found, using a PV-based method, to be within the vortex (red, blue, and purple markers). These will be discussed in detail later on in connection with the statistics shown in Tables 4.1 and 4.5. Figure 4.5 shows this information for the Northern hemisphere during December-March 2005-2010 on the 700, 900 and 1250 K isentropic surfaces, while Figure 4.6 shows the same information for the Southern hemisphere during June-November 2005-2010. For the Northern hemisphere plots, the approximate start dates of major SSWs within this period are marked by vertical green lines. The dates marked here are 21 January 2006, 24 February 2007, 22 February 2008, 24 January 2009 and 26 January 2010 [Manney et al., 2008a, 2009b, Labitzke and Kunze, 2009, Ayarzagüena et al., 2011, Kuttippurath and Nikulin, 2012, Scheiben et al., 2012].

In all plots, concentrations of carbon monoxide are clearly enhanced within the low-N_2O cluster during a well defined period within the winter, while concentrations at the other cluster centroid show little or no enhancement. The only exception to this is for the Northern hemisphere 2005/2006 and 2008/2009 winter periods, where high concentrations of CO never reach 700 K (Figure 4.5); this may be because the early SSWs during these seasons disrupt the vortex before the high-CO air is able to descend to this level. As would be expected for carbon monoxide descending from higher altitudes, the enhancement period is later at lower altitudes. The period of CO enhancement is also noticeably longer in the Southern than in the Northern hemisphere (Figure 4.6). For some plots at the two higher altitudes, the CO enhancement appears to peak twice during the vortex season. The clearest example of this can be seen during the 2006 Southern hemisphere vortex season at 1250 K. During 2005 and 2006, two-dimensional histograms (not shown) show that the maximum concentrations of CO do peak twice during winter.

Immediately prior to the enhancement period, there is often a dip in CO values at the low-N_2O cluster centroid. According to Livesey et al. [2011], the Aura-MLS version 3.3 CO data used in this study is affected by an issue where negative CO values are observed at pressure levels immediately below those where there are large positive values, with this being particularly evident in the vicinity of the winter polar vortex. Therefore these low CO values should not be considered

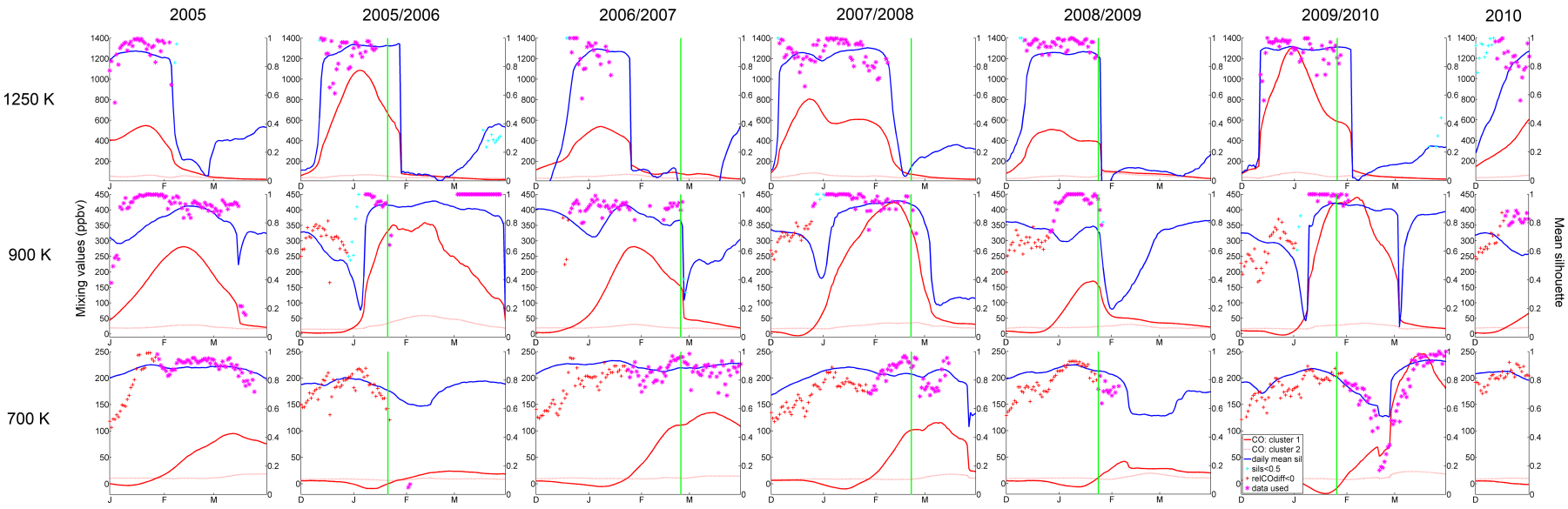

Figure 4.5: CO mixing ratios at the centroids of the low-N_2O (solid red line) and high-N_2O (dotted red line) clusters, as well as daily mean silhouette values for k=2 clusters (blue line), for the Northern hemisphere at potential temperatures of 700, 900 and 1250 K, during each year within the 2005-2010 period. Individual markers show proportions of measurements assigned to the low-N_2O cluster that are inside the vortex. Purple markers indicate dates included in the statistics shown in Tables 4.1 and 4.5. Blue markers indicate dates ruled out due to low daily mean silhouette values and red markers indicate dates ruled out because CO concentrations in the low-N_2O cluster are not greater than in the other cluster. The start dates of major SSWs within this period are marked by vertical green lines.

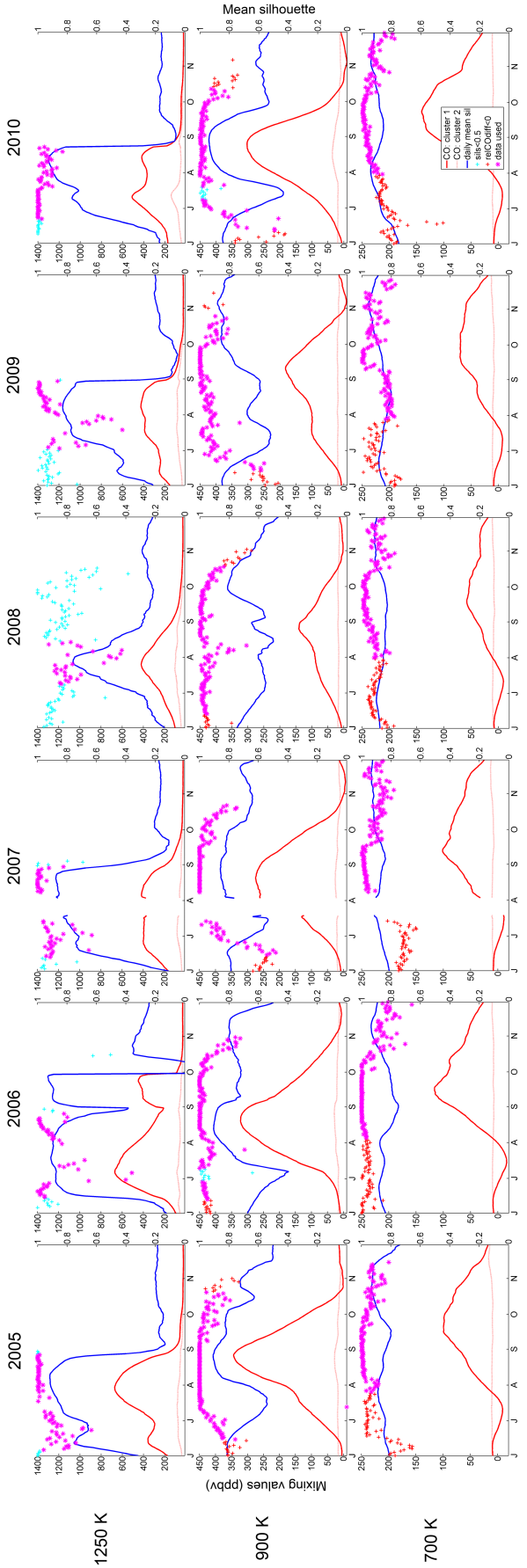

Figure 4.6: As for Figure 4.5, but in the Southern hemisphere.

to be physical. During this period, measurements from the low-N_2O cluster are located physically at high latitudes while measurements from the other cluster are at lower latitudes. This has informed our decision to identify the low-N_2O cluster as the "vortex cluster", as this leads to a more consistent identification with vortex air. From this point, the low-N_2O cluster will be referred to as the "vortex cluster", while the high-N_2O cluster will be referred to as the "extra-vortex cluster".

In the Northern hemisphere at 900 K (Figure 4.5), the major SSW start dates are often associated with sharp drops in both vortex cluster centroid CO concentrations and daily mean silhouettes Sil_{av}. This is not surprising, since the most common set of criteria used to identify major SSWs, the WMO definition, depends on temperatures and wind speeds at 10 hPa, which is at approximately the same altitude as 900 K [Charlton and Polvani, 2007]. However, for the 2005/2006 and 2009/2010 seasons, this is not the case. For these seasons, the SSW occurs while intra-vortex CO concentrations are still increasing. In these cases, CO concentrations within the vortex are not greatly affected by the SSWs. When an SSW occurs, Sil_{av} values are only substantially affected in cases where there is a sharp drop in intra-vortex CO concentrations as a result. If the SSW begins sufficiently early in the vortex season, the resultant perturbation in CO concentrations is not large enough to cause a sharp drop in Sil_{av} values. Therefore, the behaviour of the mean silhouette values is more closely linked to changes in CO concentrations caused by SSWs than to the SSWs themselves.

In both the Northern and Southern hemispheres at 1250 K (Figures 4.5 and 4.6), the k=2 silhouette scores are high (reaching peaks of 0.8-1.0) during the periods where CO values in the vortex cluster are enhanced, showing that at these times the measurements can be divided into two clusters naturally. At the two lower potential temperatures, although daily mean silhouette values are still high during the CO enhancement periods, they are also high during other times within the periods shown. When daily mean silhouette values are high, the results in each cluster appear distinct when plotted geographically (not shown), with results from the low N_2O cluster in nearly all cases being nearer to the pole. In these cases, it is difficult to tell whether the algorithm is detecting differences in N_2O concentrations across the vortex edge barrier as the vortex forms prior to the arrival of high-CO air from above, or whether it is detecting the barrier at the edge of the "tropical pipe" region [Plumb, 1996].

As described in Chapter 4.2, it is possible to determine how many vortex cluster measurements are physically within the vortex boundary and vice versa

by comparing the PV values at the location of each measurement with the PV at the vortex edge as determined using the method of Manney et al. [2007]. The relative differences between the CO concentrations in each cluster, as well as the daily mean silhouette values, can be used as thresholds to identify dates when it makes sense to carry out this comparison. Ruling out dates for which the daily mean silhouette score Sil_{av} is low removes dates for which there is no clear distinction between the two clusters. An inspection of Figures 4.5 and 4.6 suggests that applying a Sil_{av}-based threshold may be an effective way to identify dates with a clear distinction between the vortex and extra-vortex clusters, but at 700 and 900 K is unlikely to be sufficient on its own to do this. However, the threshold based on the relative difference between CO concentrations at each of the two cluster centroids should be effective at these lower altitudes. This can be used to identify dates within the periods when high-CO air enters the vortex from higher altitudes. Here, we calculate the relative difference by subtracting the CO concentration at the centroid of the extra-vortex cluster from the concentration at the vortex cluster centroid, and then dividing this difference by the concentration at the extra-vortex cluster centroid.

Table 4.1 displays statistics on the daily percentages of measurements from the vortex cluster that are in fact within the vortex, for a range of potential temperature levels and both hemispheres. For each date included, the observations belonging to the vortex cluster are identified and the percentage of these observations that are within the vortex is calculated by comparing the PV associated with each measurement with the PV value at the vortex edge. Conversely, Table 4.2 displays statistics about the daily percentages of measurements within the vortex that actually belong to the vortex cluster. When calculating these statistics, we first remove any individual points from the vortex cluster that have silhouette scores less than 0.5; this removes points that have potentially been incorrectly clustered. The dates investigated are those from winter to spring in each hemisphere (December–March inclusive in the Northern hemisphere and June–November inclusive in the Southern hemisphere), that satisfy the thresholds described immediately below. We only include dates for which the mean daily silhouette score Sil_{av} is above 0.5 when the data is divided into two clusters; this removes dates for which there is no clear distinction between the clusters corresponding to intra– and extra–vortex air. We remove any dates for which the CO concentration is lower in the vortex cluster than the extra-vortex cluster in order to ensure that all dates used are within the CO enhancement period. For 900 and 1250 K, the algorithm used upon the PV data to identify the location

Location	mean (%)	standard deviation (%)	lower decile (%)	upper decile (%)	percentage of dates used	mean no. dates/year
NH 700 K	81.7	16.3	67.4	95.5	41.9	40.6
NH 900 K	92.2	12.2	82.6	100	63.8	47.6
NH 1250 K	90.7	9.18	78.6	99.2	63.5	42.3
SH 700 K	92.6	6.23	83.1	99.4	66.3	118.5
SH 900 K	93.6	9.38	83.6	100	82.6	122.8
SH 1250 K	89.7	12.5	72.6	100	49.5	53.5

Table 4.1: Statistics applied to the daily percentages of vortex cluster observations (in CO-N_2O tracer-tracer space) that are inside the vortex, for dates within the vortex periods December-March (NH) or June-November (SH) 2005-2010 with mean silhouette scores $Sil_{av} > 0.5$ and with mean values of CO that are higher within the vortex cluster than outside. Only measurements with individual silhouette values above 0.5 are considered here to be part of the vortex cluster. After dates where the PV-based vortex edge line is unavailable and/or at an equivalent latitude above 70 degrees are removed from the vortex periods, the percentages of the remaining dates that satisfy the thresholding criteria and are included in the statistics are shown in the penultimate column. The final column shows the average number of dates per year that are incorporated in the statistics.

of the vortex edge occasionally encounters a problem, most commonly early in the season, where the equivalent latitude jumps rapidly between equivalent latitudes in the range of 55°-60° to >70°. In these cases, when the vortex edge equivalent latitude is >70°, the shape and size of the "vortex edge" identified by it often do not correspond to anything that might be expected for the polar vortex. This issue is not unexpected since it is known that when using automated PV-based methods for locating the vortex edge, it becomes more difficult to locate the vortex edge unambiguously at higher altitudes within the stratosphere [Manney et al., 2007, Mitchell et al., 2010]. To avoid these problems affecting the results, we do not consider any dates for these potential temperatures for which the equivalent latitude found for the vortex edge is polewards of ± 70°. The statistical information summarized in Table 4.1 is also plotted in Figures 4.5 and 4.6. This information will be discussed in detail later on, after a general overview of the results in Tables 4.1-4.4.

The last two columns in Tables 4.1-4.4 show information on the numbers and proportions of dates within the time period investigated that satisfy the thresholds introduced above and therefore contribute to the statistics. The average number of dates per year that are used in the calculated statistics is shown in the final column. The "percentage of dates used" column contains the percentage of dates within the total investigation period that are used. Before calculating

Location	mean (%)	standard deviation (%)	lower decile (%)	upper decile (%)	percentage of dates used	mean no. dates/year
NH 700 K	93.2	7.24	82.8	99.7	41.9	40.6
NH 900 K	78.8	19.6	45.8	95.7	63.8	47.6
NH 1250 K	80.2	11.9	67.9	92.2	63.5	42.3
SH 700 K	93.1	6.87	85.1	99.4	66.3	118.5
SH 900 K	84.0	9.06	72.1	95.5	82.6	122.8
SH 1250 K	73.8	14.1	50.1	89.4	49.5	53.5

Table 4.2: As for Table 4.1 but statistics are applied to daily percentages of observations within the vortex that belong to the vortex cluster.

the percentages, dates for which the vortex edge equivalent latitude is either undefined or (for 900 and 1250 K) above 70° are removed. The results in these columns are the same for all tables, since the same dates are used throughout the analysis. The mean number of dates used per year is greatest for 700 and 900 K in the Southern hemisphere, at approximately 4 months or 120 days per year. This is likely to be because the period over which CO concentrations are enhanced is longer in the Southern than the Northern hemisphere (Figures 4.5 and 4.6), and therefore the number of days satisfying the CO relative difference threshold criterion is greater. The period of CO enhancement is also long at 1250 K in the Southern hemisphere, but the mean number of dates used in the statistics is smaller because no dates are used outside the periods when Sil_{av} is high.

A comparison of Table 4.1 and Table 4.2 shows that in general the mean daily percentages, both of vortex cluster measurements that are within the vortex and vice–versa, are fairly high. They range from 73–93%, but are above 80% in most cases. The percentages of vortex cluster measurements that are within the vortex, shown in Table 4.1, are lowest for 700 K in the Northern hemisphere, with the percentages for all other altitude levels and hemispheres being close to or above 90%. The Northern hemisphere at 700 K also shows the greatest variation in daily percentages over the study period, with the standard deviation and lower decile of the distribution of percentages being 16.3% and 67.4% respectively. This implies that there are some dates when a substantial proportion of the measurements assigned to the vortex cluster are not located within the vortex.

For Table 4.2, the mean percentage of observations within the vortex that belong to the vortex cluster is lowest for the Southern hemisphere at 1250 K; when this is removed from consideration the remaining mean percentages range from approximately 80-90%. In general, the statistics in Table 4.1 and 4.2 show that the majority of measurements within the vortex cluster are within the vortex

on dates that satisfy the thresholds introduced earlier. Also, the majority of measurements within the PV-based vortex edge on these dates are within the vortex cluster.

Compared to similar results calculated using CO concentrations alone in McDonald and Smith [2013] (for the Southern Hemisphere winter), the proportion of the vortex cluster observations chemically identified to be within the vortex edge is lower (92.6% relative to 98.9% at 700 K, 93.6% relative to 98.4% at 900 K and 89.7% relative to 93.1% at 1250 K), but at the two lower potential temperatures the proportion of measurements within the vortex that are assigned to the vortex cluster is higher (93.1% relative to 79.0% at 700 K and 84.0% relative to 83.6% at 900 K), although this is not the case for 1250 K (73.8% relative to 83.4%). Thus, when identifying which measurements are within the vortex, this method gives more false positives, but fewer false negatives than the method used in McDonald and Smith [2013]. For 700 and 900 K, the observations within the vortex are nearly all linked to the intra-vortex cluster derived using the k-means scheme. Figures 4.3(a) and (b) show distinct differences in the position of the change in gradient at the vortex edge for CO and N_2O observations, which might explain why the current scheme that uses N_2O data identifies some air outside the vortex edge as intra-vortex air. Overall, though, it is not yet clear whether or not the vortex edge determined using this method is more reliable than that found using the method of McDonald and Smith [2013].

Tables 4.3 and 4.4 show statistics calculated using the same method as in Tables 4.1 and 4.2, but for the extra-vortex cluster. Table 4.3 shows results based on the daily percentages of extra-vortex cluster members that are found to be located outside the vortex, and Table 4.4 shows statistics calculated from the daily percentages of measurements located outside the vortex that are found to be within the extra-vortex cluster. For the results in these tables, we only count observations with individual silhouette scores of 0.5 or more as being within the extra-vortex cluster. Otherwise, the dates included in these statistics, and the thresholds used to identify them, are the same as those used in Tables 4.1 and 4.2.

According to Table 4.3, the mean percentage of extra-vortex cluster measurements that are found to be outside the vortex is very high; above 94% for all hemispheres and altitude levels except for the Southern hemisphere at 1250 K, for which the percentage is 85.3%. The mean percentages of observations located outside the vortex that are found to be within the extra-vortex cluster, shown in Table 4.4, range between 81-93%. These percentages are not as high as in Ta-

Location	mean (%)	standard deviation (%)	lower decile (%)	upper decile (%)	percentage of dates used	mean no. dates/year
NH 700 K	99.4	0.819	98.4	100	41.9	40.6
NH 900 K	94.8	7.98	86.8	100	63.8	47.6
NH 1250 K	94.0	4.71	87.7	98.7	63.5	42.3
SH 700 K	98.1	2.09	95.8	100	66.3	118.5
SH 900 K	96.3	4.6	89.2	100	82.6	122.8
SH 1250 K	85.3	12.5	74.9	97.2	49.5	53.5

Table 4.3: As for Table 4.1, but shows statistics applied to the daily percentages of extra-vortex cluster observations (in CO-N_2O tracer-tracer space) that are located outside the vortex.

Location	mean (%)	standard deviation (%)	lower decile (%)	upper decile (%)	percentage of dates used	mean no. dates/year
NH 700 K	88.2	11.4	73.2	97.3	41.9	40.6
NH 900 K	89.6	14.5	71.0	99.7	63.8	47.6
NH 1250 K	93.0	5.90	84.7	98.4	63.5	42.3
SH 700 K	90.2	6.89	82.1	96.6	66.3	118.5
SH 900 K	81.5	15.9	59.6	98.5	82.6	122.8
SH 1250 K	85.0	13.7	63.0	98.9	49.5	53.5

Table 4.4: As for Table 4.1, but shows statistics applied to the daily percentages of observations geographically outside the vortex that belong to the extra-vortex cluster.

ble 4.3 but are comparable to the results shown for the vortex cluster in Tables 4.1 and 4.2. The most striking feature of the results in Tables 4.3 and 4.4 is the high mean percentages in Table 4.3, relative to those in the three other tables. In addition, the mean of the percentages shown in Table 4.4, 87.9%, is higher than the corresponding mean for Table 4.2, which is 83.9%. This suggests that our k-means clustering method is particularly good at identifying extra-vortex air. Comparing the statistics shown in Tables 4.3 and 4.4 with those in Tables 4.1 and 4.2 suggests that the k-means method can identify extra-vortex air with a greater accuracy than intra-vortex air. The percentages in these two tables are also higher on average than the percentages from McDonald and Smith [2013] quoted above for intra-vortex air.

In addition to CO centroid mixing values and daily mean silhouette values Sil_{av}, Figures 4.5 and 4.6 also show information about the daily proportions of measurements within the vortex cluster found to be within the vortex. The purple markers show proportions for the dates that contribute to the Table 4.1 statistics. The blue markers indicate dates ruled out by the $Sil_{av} > 0.5$ condition and the red markers indicate dates ruled out because CO concentrations are lower in the vortex cluster than in the extra-vortex cluster. There are a number of dates for

which no markers are shown. These correspond to dates ruled out either because the vortex edge equivalent latitude is polewards of $\pm 70^{\circ}$ or undefined, or to dates ruled out because there are no vortex cluster measurements with individual silhouette values greater than 0.5. In the former case, we do not have a reliable vortex edge to compare our clustering analysis against, and so cannot calculate the proportion of vortex cluster measurements that belong to the vortex. We also cannot do this in the latter case, because when calculating our statistical results we only count data points with silhouette values greater than 0.5 as truly belonging to the vortex cluster.

In the Northern hemisphere (Figure 4.5) at 700 K, the proportions of vortex cluster measurements found to belong to the vortex are reasonably high, apart from during mid-late February 2010, when they drop dramatically. After the particularly large SSWs in early 2006 and 2009, the amount of descending CO that reaches 700 K is greatly reduced, and as a consequence of this few dates within these periods satisfy the requirement that mean CO concentrations in the vortex cluster be larger than in the extra-vortex cluster. In general, at 700 K, a considerable number of dates (shown in red) are ruled out due to this condition, generally those early in the season. Few if any dates are ruled out based on their Sil_{av} scores. The proportions shown for the dates ruled out by the CO relative difference condition appear lower on average than those for the dates actually used in the statistics once the February 2010 period is excluded. This indicates that if the CO relative difference threshold criterion were not applied, the statistical results shown in Table 4.1 for the NH at 700 K would worsen to some degree, although not dramatically.

At 900 K, the proportions of vortex cluster measurements belonging to the vortex, as indicated by the purple markers, appear higher on average than for 700 K. A few dates are ruled out by the $Sil_{av} > 0.5$ condition (blue markers), and considerably more dates are ruled out by the CO relative difference condition (red markers). For this level, the CO relative difference condition appears effective at ruling out dates for which the proportions are low.

At 1250 K, few if any dates are ruled out due to the CO relative difference condition. Also, based on Figure 4.5 few dates appear to have been ruled out due to the $Sil_{av} > 0.5$ condition alone. However, a brief investigation of the reasons for this found that for most dates where $Sil_{av} < 0.5$, there are no measurements assigned to the vortex cluster with silhouette scores above 0.5. This means that in our statistics, no measurements are recognized as being part of the vortex cluster, therefore these dates are automatically ruled out and results are not plotted for

these dates. It can be seen in Figure 4.5 that for 1250 K few markers are visible during periods when $Sil_{av} < 0.5$. For the dates marked in purple as contributing to the statistics, there appears to be some variability in the results and the overall results are not as good as for 900 K.

In the Southern hemisphere (Figure 4.6), it can be seen that for 700 K, many more dates are used in the statistics than in the Northern hemisphere and the proportions of vortex cluster measurements belonging to the vortex are high overall for these dates. However, they are also generally high for the dates ruled out using the CO relative difference condition. As in the Northern hemisphere, removing this condition would make only a modest difference to the statistical results. At 900 K, the overall results appear good. Few dates are ruled out due to the Sil_{av} condition, and the proportions plotted for these appear no different from those for the dates used in the statistics. Some dates are screened out due to the CO relative difference condition, and these do show lower proportions. An inspection of the results for the dates passing all threshold criteria suggests that tightening the CO relative difference condition so that a higher mean relative CO concentration in the vortex cluster is needed may improve the statistical results at this level. At 1250 K, a considerable number of results are screened out by the Sil_{av} condition, especially during 2008, but the statistical results for these dates are not noticeably better than for the days that are kept. This is because the results for the dates used in the statistics are in general relatively poor at this level, with a considerable degree of variability and some low proportions observed even at the height of the CO enhancement period. This variability is also observable to a lesser degree in the Northern hemisphere at 1250 K (Figure 4.5). At 1250 K, especially in the Southern hemisphere, the vortex edge identification algorithm was affected by sudden jumps in location to a worse degree than elsewhere. Although removing dates for which the equivalent latitude found for the vortex edge was polewards of $\pm$ 70° is likely to have ameliorated the problem to some degree, it is likely that some uncertainty remains in the vortex edge location for a number of the remaining dates. This makes the task of validating the k-means clustering method by comparison with a PV-based vortex location method more difficult and is the most likely explanation for the poorer results at this level.

Overall, for both hemispheres, the CO relative difference threshold condition appears most effective at identifying dates appropriate for use in the clustering analysis at 700 and 900 K. At 700 K, the proportions of vortex cluster measurements that belong to the vortex are often high even outside the CO enhancement period. However, the physical meaning of some of these results, in particular

those further from the CO enhancement period, is doubtful and it is appropriate to remove them. In general, the $Sil_{av} > 0.5$ condition rules out fewer dates than would be expected, even at 1250 K, where it appears that the majority of the dates not included in the statistics are in fact rejected on the basis of the condition that only measurements with individual silhouette scores above 0.5 are to be considered as part of the vortex cluster.

Figure 4.5 shows that the relatively poor Table 4.1 statistical results are in large part due to the event in mid-late February 2010 during which the proportions of vortex cluster measurements found to be within the vortex dip dramatically. This dip begins a few days after the vortex at 700 K undergoes a splitting event on 12 February, which is visible on a polar stereographic plot of the vortex edge line (not shown). The statistical results worsen further as one of the remnant subvortices resulting from this event dissipates on 20 February. On this date the proportion of vortex cluster measurements found to be within the vortex reaches a minimum of 16.8%, suggesting that the chemical distinction between intra- and extra-vortex air is too low for the clustering algorithm to recognize which measurements should be assigned to each cluster. On 27 February, the statistical results improve and CO concentrations in the vortex cluster continue their increase. During 12-27 February, two-dimensional histograms (not shown) show evidence of strong mixing between high-CO/low-N_2O and low-CO/high-N_2O air. The poor statistical results during the dip appear to be associated with the mixing and unusual dynamics during this period. Polar stereographic plots showing the locations of the vortex cluster measurements for each day show that after this date, most of the vortex cluster measurements are located within or near to the remaining subvortex. This unusually small reformed vortex persists until well after the period shown in Figure 4.5 and, during March, mean CO concentrations within the vortex cluster reach higher values than are observed during any other winter/spring period in either the Northern or Southern hemispheres (Figures 4.5 and 4.6) at 700 K.

In Figures 4.5 and 4.6, it can be seen that there is considerable variation from year to year in the statistical results summarized in Table 4.1. It is therefore worthwhile to break down the results shown in Tables 4.1-4.4 and show statistics for each year in order to understand this variability. Tables 4.5-4.8 show the same results that are in Tables 4.1-4.4, except that they are divided into years. The results listed next to each year contain statistics based on data from January-March and December (for the Northern hemisphere), or data from June-November (for the Southern hemisphere). This means that for the Northern hemisphere,

the results for each year contain January-March data from one vortex season and then December data from the next season.

Table 4.5 shows statistical results from Table 4.1, but for each year. In the Northern hemisphere, the statistical results for 700 K during 2006 and 2009 are poor, presumably due to the impact of the particularly powerful major SSWs occurring during these periods. However the CO relative difference threshold condition screens out most dates during these periods so that the impact on the overall statistical results in Table 4.1 is low. The relatively low mean percentage for 2010 at 700 K, due to the large dip in February 2010 discussed earlier, has a larger impact on the overall statistics. In the Southern hemisphere, the yearly means shown in Table 4.5 appear higher than for the Northern hemisphere and more consistent between years. Exceptions to this are the results for 2008 and 2009, for which the means are lower. The percentages at the lower decile of the probability distribution for these years are 48.6% and 59.4%, which are considerably lower than for the other years, implying that there are more low-percentage outliers for these years than the others. In Figure 4.6 it can be seen that for 2008 and 2009, the proportions of vortex cluster measurements found to be within the PV-based vortex dip sharply in late July-early August. A similar dip is also present in July 2006, but appears to affect fewer dates. An investigation into the 2008 and 2009 dates affected by the dips found that at these times the PV-based vortex edge is highly distorted. This causes a poor match between the vortex cluster measurements and the location of the PV-based vortex.

The number of dates included in the statistics for each year appears to vary depending on the potential temperature and hemisphere being investigated, and the dynamics occurring that year. In the Southern hemisphere, more dates per year are used at 700 and 900 K than at 1250 K. The "percentage of dates used" column also shows lower percentages at 1250 K than at the two lower levels, but not as low as would be expected from a comparison with the "no. dates" column. The discrepancy between the two columns comes about because at 1250 K many dates are removed from the results due to issues with the vortex edge equivalent latitude. These dates are removed from the Jun-Nov period before the "percentage of dates used" column is calculated, but the "no. dates" column is unaffected. The clearest example of this discrepancy is during 2006 in the Southern hemisphere at 1250 K.

In the Northern hemisphere, the number of dates used in the statistical analysis of the k-means clustering algorithm is lower overall. At 700 K, as mentioned above, the number of dates used appears to vary dramatically depending on the

dynamical situation, with very few dates being used from the years affected by the most powerful major SSWs, in 2006 and 2009. During these years, not much CO reaches 700 K, so the CO relative difference threshold condition is effectively screening out dates for which there is little distinction between CO values inside and outside the vortex. At 900 K, the dynamical situation also appears to affect the number of dates used. According to Figure 4.5, during most winter/spring periods, the statistics include results from very few dates after each of the major SSWs. Therefore the timing of each SSW has a strong effect upon the number of dates used each season. At 1250 K, the differences in the dynamical situation for each year appear to have less effect on the results. However, the number of dates used per year is still smaller on average than in the Southern hemisphere. This may be because the length of the CO enhancement period is shorter. In general, the number of dates used per year appears to be mostly constrained at lower levels by the length of the CO enhancement period and variations in dynamics during each vortex season. At 1250 K, conditions based on silhouette scores and issues with detecting the PV-based vortex edge reliably appear to play a greater role in constraining the number of dates used.

Table 4.6 shows the same statistical results summarized in Table 4.2, but divided into years. In Table 4.6, the lowest yearly mean percentage is 44.0%, which occurs at 900 K during 2006 in the Northern hemisphere. An investigation into the cause of these poor statistics found that the daily percentages of intra-vortex measurements found to belong to the vortex cluster were very low for 3-28 March 2006. Plots of PV and vortex cluster measurement locations during this period (not shown) suggest that the vortex is reforming after the 2006 major SSW and that the vortex measurements are localized within the PV-based vortex but cover a smaller area than it. In addition, two-dimensional histograms and clustering plots show that over this period the k-means algorithm correctly divides measurements into high- and low-CO clusters, but that relatively few measurements exhibit high CO values. This implies that as the vortex reforms, enhanced CO concentrations are confined within the vortex core, causing a discrepancy between the clustering results and the PV-derived vortex edge.

Table 4.7 shows the same results as in Table 4.3, again divided into years. The mean percentages of extra-vortex cluster observations found to be located outside the vortex are in general very high. However, at 900 K in the Northern hemisphere during 2006, and at 1250 K in the Southern hemisphere for a number of different years, the mean percentages are somewhat lower. For the 2006 Northern hemisphere at 900 K, this is likely related to some of the March results

Northern Hemisphere

Year	Isentropic level	mean (%)	standard deviation (%)	lower decile (%)	upper decile (%)	percentage of dates used	no. dates
2005	700 K	89.7	5.58	80.5	95.1	46.3	56
2005	900 K	87.3	19.8	55.8	99.6	63.6	77
2005	1250 K	90.1	10.9	74.5	99.0	67.5	52
2006	700 K	5.94	1.46	4.91	6.98	3.64	2
2006	900 K	97.1	7.23	92.2	100	67.7	44
2006	1250 K	90.8	9.52	78.6	100	49.0	24
2007	700 K	86.6	6.69	76.9	94.5	52.1	63
2007	900 K	91.6	3.57	88.0	95.4	63.3	38
2007	1250 K	88.8	7.82	78.9	98.3	59.7	37
2008	700 K	83.8	8.85	72.1	95.4	44.8	47
2008	900 K	95.2	6.01	88.5	100	60.8	48
2008	1250 K	92.3	7.65	80.4	99.7	83.3	55
2009	700 K	73.2	3.23	69.5	78.1	12.1	8
2009	900 K	95.5	7.65	89.7	100	44.3	27
2009	1250 K	93.9	8.60	86.8	99.3	56.6	43
2010	700 K	71.8	22.9	34.3	97.8	52.1	63
2010	900 K	95.8	9.68	92.0	100	40.6	26
2010	1250 K	88.3	9.02	78.4	99.3	54.3	38

Southern Hemisphere

Year	Isentropic level	mean (%)	standard deviation (%)	lower decile (%)	upper decile (%)	percentage of dates used	no. dates
2005	700 K	95.3	4.35	88.9	99.8	67.1	112
2005	900 K	94.6	10.3	84.6	100	84.2	128
2005	1250 K	92.5	8.76	79.8	100	62.5	70
2006	700 K	93.4	8.02	81.0	100	70.0	128
2006	900 K	96.7	4.10	92.0	100	76.0	114
2006	1250 K	88.1	13.9	72.3	98.4	60.0	45
2007	700 K	92.1	5.39	85.2	98.6	65.4	119
2007	900 K	90.7	12.9	69.0	100	79.2	114
2007	1250 K	92.0	8.69	81.7	100	52.5	64
2008	700 K	92.3	5.10	85.2	98.4	70.2	127
2008	900 K	95.2	5.21	88.5	99.4	83.6	127
2008	1250 K	73.9	14.2	48.6	87.4	24.2	31
2009	700 K	88.5	6.75	80.5	98.3	68.9	122
2009	900 K	92.4	8.75	82.9	100	84.8	128
2009	1250 K	85.7	15.4	59.4	99.1	46.2	48
2010	700 K	93.5	4.76	86.6	98.6	69.9	128
2010	900 K	93.7	8.36	82.7	99.6	79.0	113
2010	1250 K	96.4	3.99	90.5	100	58.3	63

Table 4.5: As for Table 4.1, this shows statistics based on the daily percentages of vortex cluster observations that were found to be within the vortex, except that here individual sets of statistics calculated for each year are shown. The results for each year are based on data from January-March and December for the Northern hemisphere, and June-November for the Southern hemisphere.

Northern Hemisphere

Year	Isentropic level	mean (%)	standard deviation (%)	lower decile (%)	upper decile (%)	percentage of dates used	no. dates
2005	700 K	97.2	2.77	93.8	100	49.1	56
2005	900 K	90.3	6.05	83.5	97.2	71.3	77
2005	1250 K	85.3	7.62	73.6	93.3	67.5	52
2006	700 K	98.1	2.62	96.3	100	3.64	2
2006	900 K	44.0	22.7	16.6	74.8	67.7	44
2006	1250 K	74.0	17.3	45.3	89.4	49.0	24
2007	700 K	94.1	5.20	86.3	99.4	52.1	63
2007	900 K	89.2	5.71	80.2	95.3	63.3	38
2007	1250 K	81.2	7.81	69.0	90.7	59.7	37
2008	700 K	90.2	8.50	77.9	99.3	44.8	47
2008	900 K	80.3	11.1	62.2	91.9	60.8	48
2008	1250 K	80.9	8.87	68.6	92.1	83.3	55
2009	700 K	86.5	6.72	78.3	95.2	12.1	8
2009	900 K	77.9	12.1	62.3	92.9	44.3	27
2009	1250 K	71.9	15.9	46.1	86.8	56.6	43
2010	700 K	91.6	9.00	76.8	100	52.1	63
2010	900 K	73.4	8.78	63.6	85.3	40.6	26
2010	1250 K	82.6	8.07	72.1	93.3	54.3	38

Southern Hemisphere

Year	Isentropic level	mean (%)	standard deviation (%)	lower decile (%)	upper decile (%)	percentage of dates used	no. dates
2005	700 K	92.0	6.31	85.1	98.6	61.2	112
2005	900 K	84.6	8.87	73.2	95.6	70.0	128
2005	1250 K	72.9	11.8	57.8	85.4	38.3	70
2006	700 K	88.2	10.9	70.9	98.4	70.0	128
2006	900 K	79.7	9.34	65.7	90.0	76.0	114
2006	1250 K	85.0	8.39	72.9	95.1	60.0	45
2007	700 K	94.3	4.92	86.3	98.8	65.4	119
2007	900 K	86.9	7.70	75.5	99.4	79.2	114
2007	1250 K	75.2	6.56	65.1	83.9	52.5	64
2008	700 K	94.1	4.67	89.3	98.4	70.2	127
2008	900 K	81.4	10.0	68.4	96.2	83.6	127
2008	1250 K	75.5	8.05	65.1	87.3	24.2	31
2009	700 K	97.0	3.55	93.2	100	68.9	122
2009	900 K	86.3	7.30	76.1	95.2	84.8	128
2009	1250 K	70.6	14.2	50.4	87.7	46.2	48
2010	700 K	94.2	3.78	89.4	99.3	69.9	128
2010	900 K	82.1	9.30	69.3	92.4	79.0	113
2010	1250 K	67.4	20.4	41.6	90.4	58.3	63

Table 4.6: As for Table 4.2, this shows statistics based on the daily percentages of observations within the vortex that were found to be within the vortex cluster, except that here individual sets of statistics calculated for each year are shown.

mentioned above for which there was a poor fit between the tracer-based and PV-based vortex edges as the vortex reformed. The lower mean percentages in the Southern hemisphere at 1250 K are likely due to problems with the PV-based vortex edge detection algorithm. Table 4.8 shows the same results as in Table 4.4, but divided into years. There are not many notable deviations in this table from the values shown in Table 4.4, apart from in the Northern hemisphere at 700 K during 2006, where the mean percentage is very low. This is likely due to the disruption caused by the major SSW in 2006.

Figure 4.7(a) displays the daily percentages of measurements from the vortex cluster that are within the vortex after individual observations with silhouette scores below a threshold value are removed, over a range of thresholds. The same thresholds and dates are used here as in Tables 4.1 and 4.2. As the threshold silhouette value for individual observations increases, measurements assigned to the vortex cluster with low certainty are removed from it, and the percentage of the refined cluster members that are within the vortex steadily increases. Note that the methodology has a success rate of approximately 90% for high thresholds except at 700 K in the Northern hemisphere. However, the success rate improves faster as a function of threshold silhouette value in this case. This may be because the 700 K Northern hemisphere results are disproportionately affected by the event in February 2010 in which many measurements are incorrectly assigned to the vortex cluster; during this period clustering plots and two-dimensional histograms (not shown) show that a considerable proportion of the misclassified measurements had low silhouette scores.

Figure 4.7(b) shows, for intra-vortex measurements, how the mean daily percentages of measurements found to be within the vortex cluster change as a function of the individual silhouette threshold. As expected, removing cluster members that have low silhouette values means that the total percentage of observations within the vortex edge that are within the vortex cluster reduces. Apart from at the 1250 K potential temperature level in the Northern hemisphere, these percentages are greater than 85% when the silhouette threshold is low. However, as the threshold silhouette value is increased the percentages typically reduce. The rate of decline steepens considerably after the threshold reaches approximately 0.5, implying that there are relatively few measurements in the vortex cluster with silhouette values above 0.5.

Thus, the individual silhouette threshold can be altered in order to provide an adaptive tuning of the clustering scheme. For example, if the user wished to identify air that is rather certain of having its origin in the vortex it would be

Northern Hemisphere

Year	Isentropic level	mean (%)	standard deviation (%)	lower decile (%)	upper decile (%)	percentage of dates used	no. dates
2005	700 K	99.5	0.705	98.9	100	49.1	56
2005	900 K	98.3	1.59	95.9	100	63.6	77
2005	1250 K	94.6	2.85	90.5	97.5	43.0	52
2006	700 K	100	0.00	100	100	3.64	2
2006	900 K	82.3	13.5	60.6	96.5	67.7	44
2006	1250 K	93.1	6.52	81.0	98.6	49.0	24
2007	700 K	99.3	0.790	98.1	100	52.1	63
2007	900 K	98.6	1.16	97.4	99.8	63.3	38
2007	1250 K	95.6	2.67	91.9	98.9	59.7	37
2008	700 K	99.1	1.07	98.2	100	44.8	47
2008	900 K	95.1	3.65	89.6	98.8	60.8	48
2008	1250 K	94.2	4.71	87.7	98.4	83.3	55
2009	700 K	98.8	0.752	97.8	99.6	12.1	8
2009	900 K	94.9	5.19	87.6	87.6	44.3	27
2009	1250 K	89.9	5.51	81.3	81.3	56.6	43
2010	700 K	99.6	0.677	99.2	100	52.1	63
2010	900 K	93.6	3.44	89.0	98.1	40.6	26
2010	1250 K	96.0	3.04	91.1	99.2	54.3	38

Southern Hemisphere

Year	Isentropic level	mean (%)	standard deviation (%)	lower decile (%)	upper decile (%)	percentage of dates used	no. dates
2005	700 K	98.0	1.59	95.7	99.7	67.1	112
2005	900 K	94.5	6.84	82.6	100	84.2	128
2005	1250 K	86.2	6.49	76.5	93.4	62.5	70
2006	700 K	97.3	3.56	91.8	99.9	70.0	128
2006	900 K	94.1	5.47	84.8	99.6	76.0	114
2006	1250 K	92.5	5.79	84.1	98.7	60.0	45
2007	700 K	98.1	1.69	95.6	99.8	65.4	119
2007	900 K	96.5	4.24	89.4	100	79.2	114
2007	1250 K	90.1	4.73	84.7	96.4	52.5	64
2008	700 K	98.7	1.37	96.8	100	70.2	127
2008	900 K	97.0	2.45	93.4	99.7	83.6	127
2008	1250 K	90.3	6.00	83.0	98.3	24.2	31
2009	700 K	99.0	1.26	97.3	100	68.9	122
2009	900 K	99.0	1.52	96.7	100	84.8	128
2009	1250 K	88.1	5.95	79.5	97.3	46.2	48
2010	700 K	98.0	1.47	96.2	99.8	69.9	128
2010	900 K	96.2	3.15	92.0	100	79.0	113
2010	1250 K	70.7	27.4	34.6	97.0	58.3	63

Table 4.7: As for Table 4.3, this shows statistics based on the daily percentages of extra-vortex cluster observations that were found to be outside the vortex, except that here individual sets of statistics calculated for each year are shown.

Northern Hemisphere

Year	Isentropic level	mean (%)	standard deviation (%)	lower decile (%)	upper decile (%)	percentage of dates used	no. dates
2005	700 K	90.2	3.82	84.2	94.0	49.1	56
2005	900 K	83.4	21.0	48.8	96.0	63.6	77
2005	1250 K	91.4	7.28	81.3	97.7	43.0	52
2006	700 K	26.8	2.16	25.3	28.3	3.64	2
2006	900 K	98.6	3.12	96.5	100	67.7	44
2006	1250 K	94.0	5.72	86.3	98.8	49.0	24
2007	700 K	92.1	3.56	87.0	96.3	52.1	63
2007	900 K	90.9	3.82	85.1	95.5	63.3	38
2007	1250 K	92.9	3.34	89.0	97.3	59.7	37
2008	700 K	90.4	6.08	80.4	97.3	44.8	47
2008	900 K	96.4	4.00	92.7	99.7	60.8	48
2008	1250 K	94.2	4.03	87.1	98.4	83.3	55
2009	700 K	89.9	0.867	88.9	91.2	12.1	8
2009	900 K	88.7	12.0	77.9	97.9	44.3	27
2009	1250 K	97.1	2.14	93.2	99.1	56.6	43
2010	700 K	82.1	16.6	57.0	99.4	52.1	63
2010	900 K	94.1	17.4	96.7	99.7	40.6	26
2010	1250 K	89.6	7.60	79.4	98.3	54.3	38

Southern Hemisphere

Year	Isentropic level	mean (%)	standard deviation (%)	lower decile (%)	upper decile (%)	percentage of dates used	no. dates
2005	700 K	92.4	4.30	86.3	96.7	67.1	112
2005	900 K	83.8	16.5	62.0	100	84.2	128
2005	1250 K	89.3	9.79	76.4	99.0	62.5	70
2006	700 K	92.0	5.14	85.9	99.0	70.0	128
2006	900 K	89.0	10.6	66.9	98.4	76.0	114
2006	1250 K	83.2	10.5	70.3	95.7	60.0	45
2007	700 K	92.0	3.45	87.0	96.1	65.4	119
2007	900 K	79.6	21.5	45.7	98.9	79.2	114
2007	1250 K	86.4	10.5	72.4	98.9	52.5	64
2008	700 K	87.7	5.20	79.9	94.2	70.2	127
2008	900 K	79.7	8.70	65.2	88.2	83.6	127
2008	1250 K	60.2	9.87	45.0	70.9	24.2	31
2009	700 K	84.1	11.9	67.2	96.4	68.9	122
2009	900 K	75.6	14.7	56.7	95.3	84.8	128
2009	1250 K	81.7	14.0	57.6	97.3	46.2	48
2010	700 K	91.6	3.73	86.9	95.7	69.9	128
2010	900 K	82.4	16.8	61.2	98.6	79.0	113
2010	1250 K	95.0	4.34	89.1	100	58.3	63

Table 4.8: As for Table 4.4, this shows statistics based on the daily percentages of observations outside the vortex that were found to be within the extra-vortex cluster, except that here individual sets of statistics calculated for each year are shown.

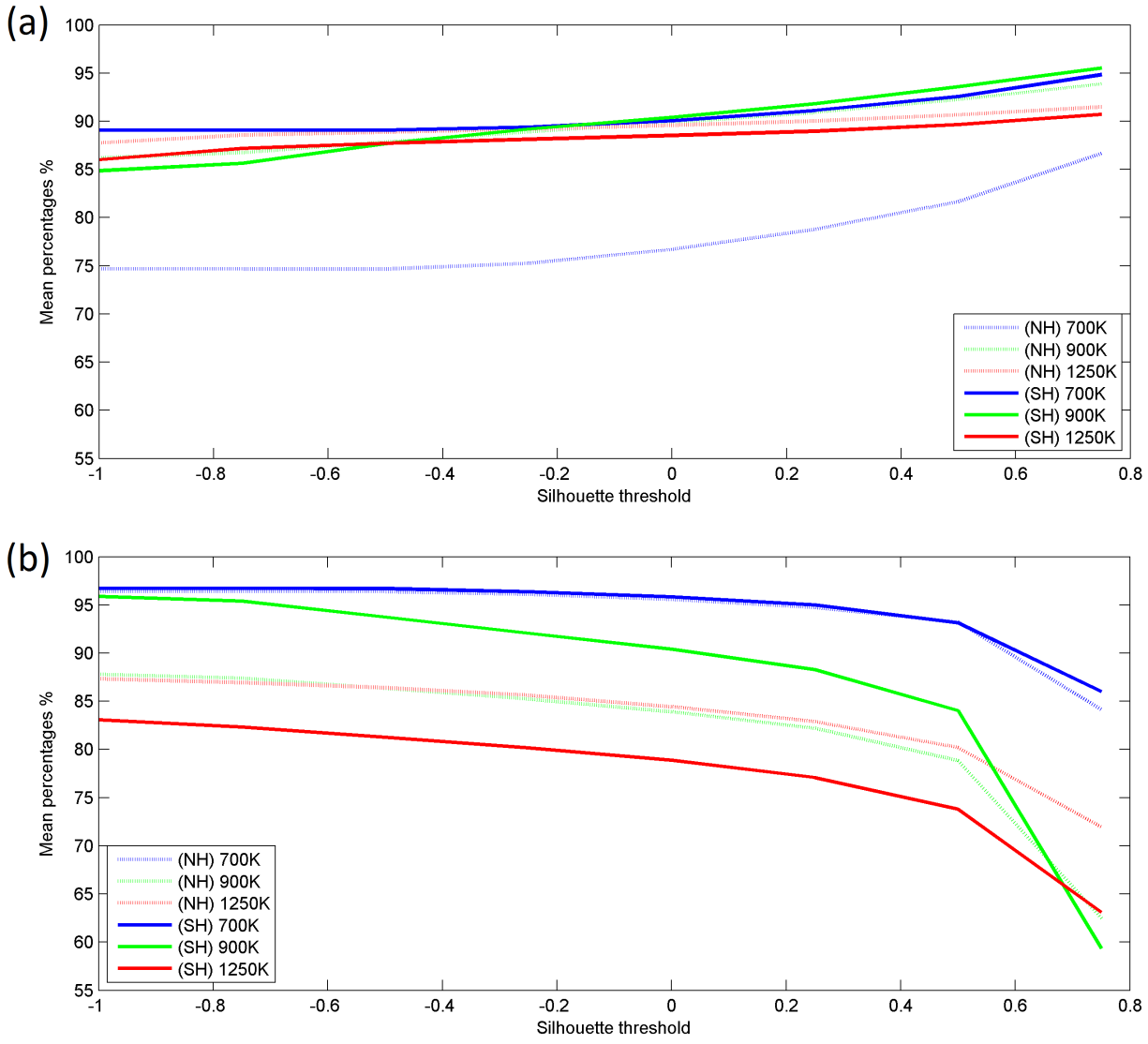

Figure 4.7: Mean daily percentages, over the periods described in Tables 1 and 2, of (a) vortex cluster observations that are within the vortex and (b) observations within the vortex that belong to the vortex cluster, as a function of the silhouette value below which individual observations are removed.

sensible to use a conservative silhouette threshold, while if you wanted to be more certain of identifying as many observations within the vortex edge as possible in a particular cluster then a lower silhouette value could be used. The statistical results shown in Tables 4.1-4.8 are calculated using an individual silhouette threshold of 0.5. This maximizes the percentage of vortex cluster observations found to be within the vortex, while avoiding the steep reduction in the percentage of intra-vortex measurements found to belong to the vortex cluster that occurs when the individual silhouette score threshold is increased above 0.5.

Figures 4.8(a) and 4.8(b) show results from 1750 K for an 11-day period centered on 1 Aug 2005 in the Southern hemisphere. The 1750 K isentropic layer (corresponding to a mean pressure of approximately 1.3 hPa) is located in the upper stratosphere. Here, since nitrous oxide concentrations are unavailable at higher altitudes, the water vapor mixing ratio is used as an alternative. Although concentrations of water vapor are only slightly lower in the high-CO cluster than elsewhere, the clustering algorithm still clearly divides the results into two clusters. Since throughout the middle atmosphere, the chemical composition of vortex air is affected by the descent of high-CO air from above, it can safely be assumed that the high-CO/low-H_2O cluster shown here corresponds to intra-vortex air. Figure 4.8(c) shows the locations of Aura-MLS observations for the central date, color-coded according to their silhouette scores and the clusters they are assigned to. The locations of the high-CO/low-H_2O cluster measurements appear consistent with those expected for intra-vortex air.

Within the stratosphere, concentrations of H_2O generally increase with height. However, due to the effect of photolysis, H_2O concentrations decrease with altitude in the mesosphere [Lee et al., 2011, Straub et al., 2012]. Therefore, in the upper stratosphere, air descending through the polar vortex is likely to be drier than air outside the vortex, explaining why the high-CO cluster shown in Figure 4.8 has a lower water vapor concentration than the low-CO cluster. The presence of an intermediate region between the areas of highest measurement density may suggest that mixing is occurring across the vortex boundary. The production of water vapor in the upper stratosphere, and its loss in the lower stratosphere caused by dehydration linked to polar stratospheric cloud (PSC) formation [Kelly et al., 2009], mean that water vapor is not a perfect tracer at these altitudes. However, the clustering algorithm can still clearly provide useful results as long as there is chemical distinction between intra– and extra–vortex air.

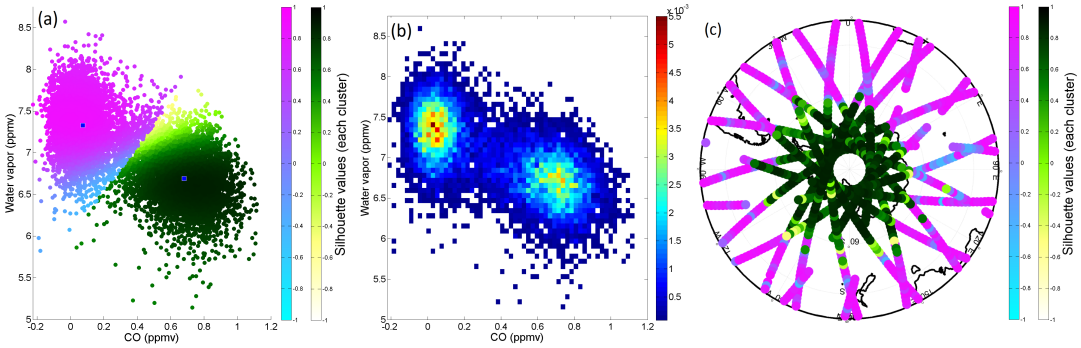

Figure 4.8: (a) A clustering plot in CO-water vapor tracer-tracer space for an 11-day period centered on 1 Aug 2005 (SH) at 1750 K. (b) Corresponding two-dimensional histogram. (c) Locations of observations for the central date color-coded according to cluster assignment and silhouette score.

4.3.2 Cosine distance algorithm results

All of the results discussed up to this point have used the k-means clustering algorithm based on a Euclidean distance. Although they certainly show that this method is useful for identifying intra and extra-vortex air within the middle stratosphere, and is particularly good at identifying extra-vortex air, any improvement in accuracy would be welcome. Here, we examine whether the alternative "cosine clustering" algorithm can produce improved statistical results. As part of this algorithm, for each day of results, the origin is shifted, in relation to the plotted measurements, along the axis in tracer-tracer space corresponding to the tracer with the highest standard deviation for that day. This is done with the aim of biasing the algorithm so that it divides the measurements into clusters primarily on the basis of information about the tracer for which there is the clearest distinction between intra and extra-vortex air.

Figure 4.9(a) shows a tracer-tracer scatter plot for 28 January 2009 at 900 K in the Northern hemisphere, demonstrating how the cosine clustering algorithm divides the results into clusters. Figure 4.4(f) shows the results for the same date and location that were obtained using the original Euclidean metric k-means clustering algorithm, in which a large number of measurements were assigned to the vortex cluster with low silhouette scores (shown in yellow). Figure 4.4(e) shows that these low-silhouette measurements are mostly located outside the vortex edge line and therefore were wrongly assigned to the vortex cluster. The cosine clustering algorithm instead assigns these measurements correctly to the extra-vortex cluster. Figure 4.9(b) shows a two-dimensional histogram for 28 January, on which it can be seen that most of the measurements that were assigned to the

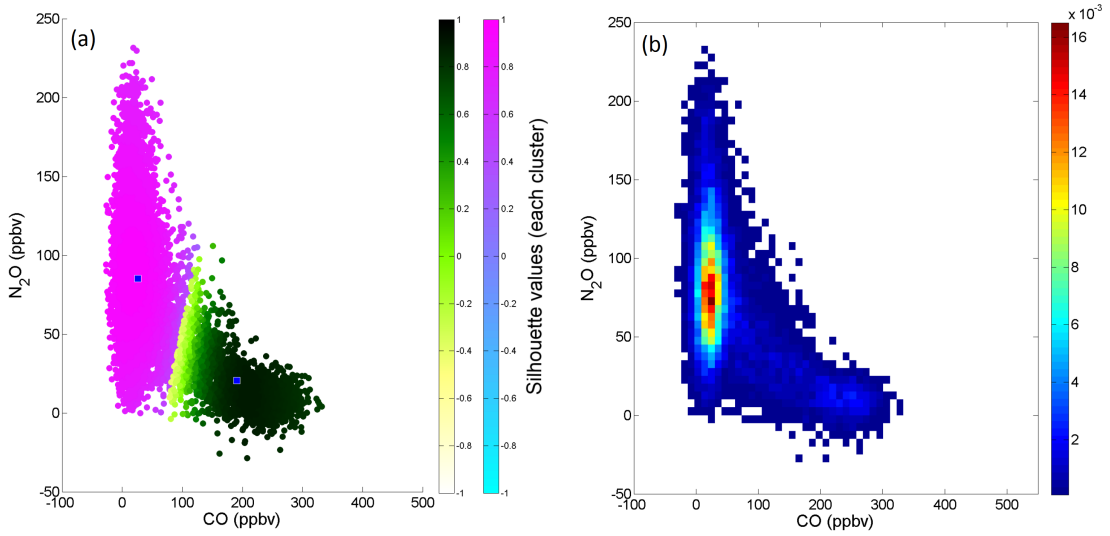

Figure 4.9: (a) As for Figure 4.4(f) but shows clustering results found using the "cosine clustering" algorithm for an 11-day period centered on 28 January 2009 at the 900 K isentropic level. (b) Corresponding two-dimensional histogram in tracer-tracer space.

vortex cluster in Figure 4.4 but were not assigned to it in Figure 4.9 are part of a region of high measurement density which clearly belongs to the extra-vortex cluster. For this date, and a number of other example dates, the cosine clustering algorithm divides the measurements into intra and extra-vortex clusters more accurately than the Euclidean metric clustering.

However, in order to determine whether this method is truly an improvement on the previous algorithm, it is necessary to study the results produced by it in more detail. Figures 4.10 and 4.11 show results similar to those shown in Figures 4.5 and 4.6, except using the cosine clustering algorithm. The statistical results shown in these plots were calculated using the same thresholds that were used for the Euclidean algorithm. This was done in order to make the comparison between the two algorithms as consistent as possible. However, as will be shown later, these thresholds are not an ideal choice, and altering them leads to improved statistical results.

In the Northern hemisphere (Figure 4.10), the change in methodology affects the clustering process so that, at 900 and 1250 K, the sudden sharp changes in Sil_{av} score often observed near the beginning and end of each CO enhancement period are removed. This is potentially beneficial since those sudden changes were not linked to any change in the underlying physical situation on those dates, but merely identified the time period over which the Euclidean metric clustering

method was able to give sensible results. However, for 700 K there are more sudden jumps in Sil_{av} and CO vortex cluster centroid values than was the case when the Euclidean metric method was used. For the Euclidean metric results, Sil_{av} values varied over a much wider range at the higher isentropic levels than at the lower levels. Using the cosine clustering method, Sil_{av} varies over a similar range at all levels. This is helpful when attempting to choose a Sil_{av}-based threshold that will work consistently at each level.

The overall effect of these changes upon the statistical results is that many more results are included in the statistics (plotted using purple markers) for 1250 K, while slightly more results at 700 K are screened out by the $Sil_{av} > 0.5$ condition (blue markers). At 900 K, slightly fewer results are screened out by the Sil_{av} condition. The extra dates included in the 1250 K statistics include many dates that were not plotted at all in Figure 4.5 because no measurements for those dates had silhouette scores above 0.5. For those dates that are included in the statistics for both clustering methods, there appears to be little difference between the proportions shown here. This is the case even in late January 2009 at 900 K after the major SSW, the time period which includes the results for 28 January plotted in Figure 4.9. This may be be because the results shown here only count measurements with individual silhouette scores above 0.5 as being part of the vortex cluster. The measurements that were incorrectly assigned to the vortex cluster using the Euclidean metric-based algorithm mostly had silhouette scores below 0.5, as can be seen in Figures 4.4(e) and (f). Therefore, although the cosine clustering algorithm assigns these measurements to the correct, extra-vortex cluster, this is not reflected by the statistical results shown in Figure 4.10. It may be possible to ameliorate or resolve this issue by reducing the silhouette score threshold for individual results. The cosine algorithm is useful over a wider time range than the Euclidean algorithm, since it screens out fewer dates.

In the Southern hemisphere (Figure 4.11), there are also no sharp changes in Sil_{av} values at 1250 K. At 700 and 900 K, the results shown in Figure 4.11 are very similar to those in Figure 4.6, although again at 900 K slightly fewer measurements are screened out by the $Sil_{av} > 0.5$ condition. At 1250 K, many more dates are used in the statistics than was the case with the Euclidean algorithm, and for some of these dates the proportions of vortex cluster measurements that belong to the vortex is low. In particular, near the end of each CO enhancement period there is a descending tail of dates where these proportions are very low and this has a negative impact on the overall statistical results. This implies that altering the Sil_{av} threshold would improve these results.

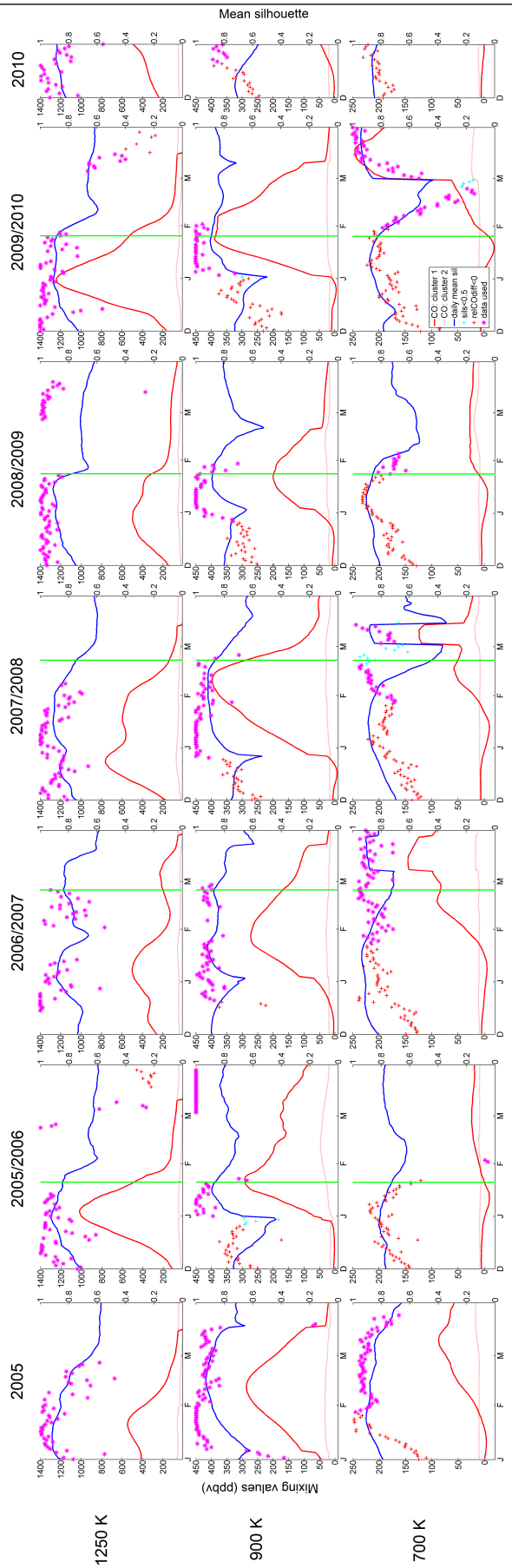

Figure 4.10: As for Figure 4.5, but shows results for the Northern hemisphere found using the cosine clustering algorithm.

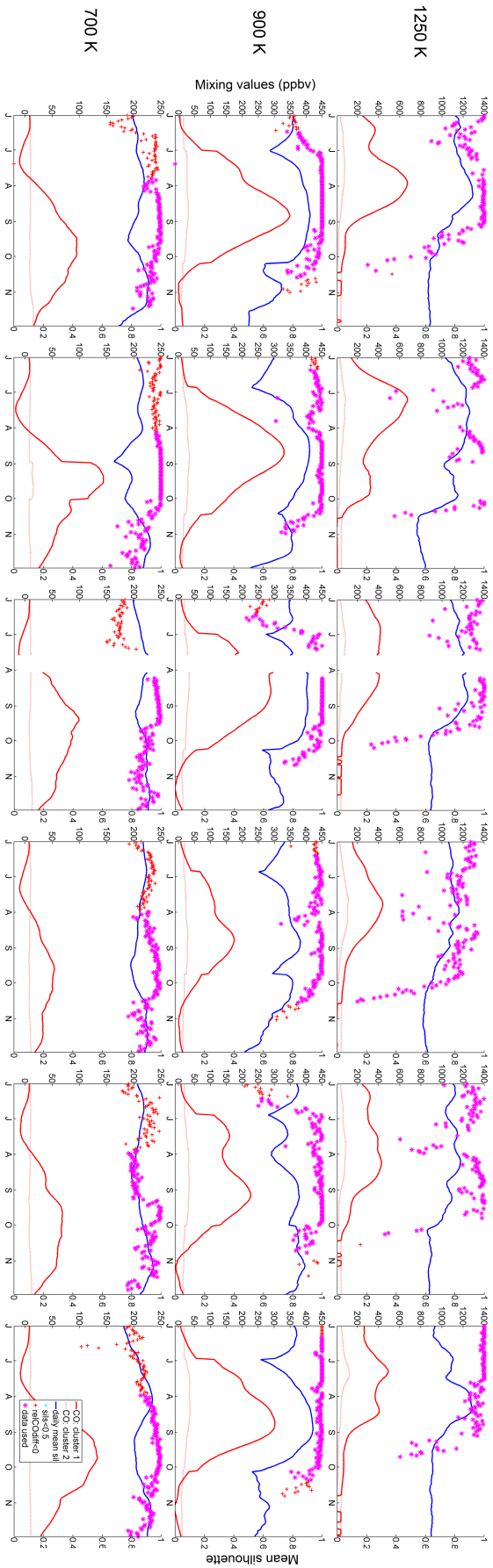

Figure 4.11: As for Figure 4.10, but in the Southern hemisphere.

In fact, Figures 4.10 and 4.11 show that the $Sil_{av} > 0.5$ condition is screening out very few dates in either hemisphere at any isentropic level. It appears that the new cosine clustering method leads to higher Sil_{av} values, particularly at 1250 K, making the $Sil_{av} > 0.5$ condition less effective. A higher threshold for this condition may more effectively constrain the statistical results to include only dates when the distributions of tracers inside and outside the vortex are clearly defined and distinct. In order to screen out the "tails" of bad results shown for the Southern hemisphere at 1250 K (Figure 4.11), the Sil_{av} threshold would need to be above 0.6.

Tables 4.9-4.12 contain statistical results calculated using the cosine clustering algorithm over Dec-Mar 2005-2010 for the Northern hemisphere and Jun-Nov 2005-2010 for the Southern hemisphere. Table 4.9 contains statistics applied to the daily percentages of vortex cluster observations found within the vortex. The same daily percentages are also plotted in Figures 4.10 and 4.11. The mean percentages listed here for the cosine clustering method are slightly better than those found using the Euclidean metric clustering algorithm at 900 K in both hemispheres, but slightly worse at 700 and 1250 K. Fewer dates per year are used for 700 K in the Northern hemisphere, which is probably due to a period in February-March 2008 where sudden changes in Sil_{av} cause a number of dates to be ruled out (Figure 4.10). For all other locations and altitudes, though, the number of dates used in the statistics is greater as the $Sil_{av} > 0.5$ condition rules out fewer days. At 1250 K, many more dates are used than was the case with the Euclidean metric clustering. The lower mean percentages at this level are due to the addition of these new days, for which the percentages of vortex cluster measurements found to be within the vortex tend to be lower. However, even though many such days of results are included, the overall mean percentages for 1250 K reduce only slightly from those shown in Table 4.1.

Based on the results in Tables 4.1 and 4.9, it is not entirely clear which algorithm is the most effective overall at identifying intra-vortex air. The mean percentages shown in Table 4.9 are overall slightly lower than those in Table 4.1. However, the cosine clustering metric can find useful results over a considerably wider range of dates at 1250 K with only a modest decrease in accuracy.

In Table 4.10, which contains statistics about the percentages of measurements within the vortex that are found to be within the vortex cluster, the results are, overall, worse than those in Table 4.2, especially at 1250 K in the Southern hemisphere. This implies that when results from both Tables 4.9 and 4.10 are taken into account, the cosine clustering algorithm is worse at identifying intra-

Location	mean (%)	standard deviation (%)	lower decile (%)	upper decile (%)	percentage of dates used	mean no. dates/year
NH 700 K	80.9	17.7	63.8	94.8	39.0	37.8
NH 900 K	92.9	10.4	83.8	100	68.5	51.1
NH 1250 K	88.5	12.8	72.9	99.4	94.3	62.7
SH 700 K	92.4	6.28	82.9	99.5	66.3	118.5
SH 900 K	94.3	8.98	83.6	100	85.4	127.0
SH 1250 K	85.5	16.7	62.6	99.7	97.5	105.5

Table 4.9: Statistics applied to the daily percentages of vortex cluster observations that are inside the vortex, calculated as for Table 4.1, but using a clustering algorithm based on an alternative "cosine" metric. The time periods over which the results are obtained, the thresholds used to select dates suitable for inclusion are the same, and the silhouette value threshold above which a measurement is considered to be part of the vortex cluster are the same as for Table 4.1.

Location	mean (%)	standard deviation (%)	lower decile (%)	upper decile (%)	percentage of dates used	mean no. dates/year
NH 700 K	93.8	7.02	84.1	99.7	39.0	37.8
NH 900 K	74.9	22.1	35.7	95.3	68.5	51.1
NH 1250 K	73.3	17.2	45.1	90.8	94.3	62.7
SH 700 K	93.0	8.39	86.4	99.4	66.3	118.5
SH 900 K	79.2	12.8	62.8	95.2	85.4	127.0
SH 1250 K	64.8	17.2	42.5	86.2	97.5	105.5

Table 4.10: As for Table 4.9 but statistics are applied to daily percentages of observations within the vortex that belong to the vortex cluster, using clusters determined with the cosine "metric".

vortex air than the k-means clustering algorithm using a Euclidean metric.

In Table 4.11, which shows statistics about the percentages of extra-vortex cluster measurements found outside the vortex, the results are also overall poorer than for Table 4.3, with the greatest discrepancies found at 1250 K. The comparison between Tables 4.4 and 4.12 is more complicated, since the cosine-clustering statistical results are considerably better at 900 K than those for the Euclidean algorithm. However, this is not the case at the other isentropic levels. In summary, the statistical results in Tables 4.9-4.12 suggest that when using this set of thresholds the cosine clustering algorithm is overall not as successful as the original Euclidean metric k-means clustering algorithm. However, the differences are generally small except at 1250 K, where the lack of constraint by the $Sil_{av} > 0.5$ condition causes the inclusion of dates for which the algorithm's results are less reliable.

Tables 4.13-4.16 show a more detailed year-by-year statistical analysis of the results from Tables 4.9-4.12. For each yearly period listed, the differences between the results in Tables 4.5-4.8 and Tables 4.13-4.16 are small. The one major

Location	mean (%)	standard deviation (%)	lower decile (%)	upper decile (%)	percentage of dates used	mean no. dates/year
NH 700 K	99.5	0.639	98.8	100	39.0	37.8
NH 900 K	93.2	7.92	81.1	99.8	68.5	51.1
NH 1250 K	90.8	11.5	77.6	98.6	94.3	62.7
SH 700 K	98.2	2.69	96.1	100	66.3	118.5
SH 900 K	91.2	7.68	79.1	99.7	85.4	127.0
SH 1250 K	81.2	15.8	69.3	95.3	97.5	105.5

Table 4.11: As for Table 4.9, but shows statistics applied to the daily percentages of extra-vortex cluster observations that are located outside the vortex, using clusters determined with the cosine "metric".

Location	mean (%)	standard deviation (%)	lower decile (%)	upper decile (%)	percentage of dates used	mean no. dates/year
NH 700 K	83.9	14.8	63.3	97.1	39.0	37.8
NH 900 K	92.2	12.0	80.0	99.6	68.5	51.1
NH 1250 K	89.6	12.4	80.6	98.2	94.3	62.7
SH 700 K	89.0	6.83	81.5	95.9	66.3	118.5
SH 900 K	88.8	14.7	63.6	99.8	85.4	127.0
SH 1250 K	83.7	14.7	63.4	98.5	97.5	105.5

Table 4.12: As for Table 4.9, but shows statistics applied to the daily percentages of observations geographically outside the vortex that belong to the extra-vortex cluster, using clusters determined with the cosine "metric".

difference between the results shown in the two sets of tables is that the number of dates used in each yearly period is much larger at 1250 K for the cosine clustering results.

For the cosine clustering algorithm, Figure 4.12(a) shows how the mean percentages of vortex cluster measurements found to be within the vortex vary as a function of the individual silhouette threshold. The same dates and thresholds as for Tables 4.9-4.10 are used. As for Figure 4.7, the percentages are lowest for the Northern hemisphere at 700 K and increase at all isentropic levels as measurements assigned to the vortex cluster with low silhouette scores are removed. However, for 900 K in both hemispheres, the mean percentages are higher when using the cosine algorithm than was the case for the Euclidean algorithm, while the reverse is true for 700 and 1250 K.

Figure 4.12(b) shows the mean percentage of intra-vortex measurements that belong to the vortex cluster as a function of individual silhouette threshold. The overall pattern of results is similar to that found for the Euclidean algorithm, except that for 900 and 1250 K the percentages are lower overall, with this difference being more marked in the Southern hemisphere. Also, for 900 K in the Southern hemisphere, the mean percentages drop less steeply at individual

Northern Hemisphere

Year	Isentropic level	mean (%)	standard deviation (%)	lower decile (%)	upper decile (%)	percentage of dates used	no. dates
2005	700 K	89.0	6.33	78.8	94.8	49.1	56
2005	900 K	89.3	16.4	83.0	99.8	71.3	77
2005	1250 K	86.9	12.4	67.5	99.1	100	77
2006	700 K	5.92	1.44	4.91	6.94	3.64	2
2006	900 K	95.3	7.43	87.6	100	93.8	61
2006	1250 K	86.8	19.1	58.1	100	75.5	37
2007	700 K	86.6	6.31	77.5	94.3	55.4	67
2007	900 K	92.1	4.22	87.9	97.5	64.8	46
2007	1250 K	85.8	9.54	73.9	97.0	100	62
2008	700 K	83.8	8.02	72.5	93.8	33.3	35
2008	900 K	94.3	7.16	85.7	100	67.1	53
2008	1250 K	92.5	7.42	80.2	99.7	100	66
2009	700 K	71.3	5.08	66.0	79.6	18.2	12
2009	900 K	95.2	6.85	87.7	100	49.2	30
2009	1250 K	93.9	10.5	87.2	100	100	76
2010	700 K	69.0	26.3	27.8	97.8	45.5	55
2010	900 K	93.7	7.92	80.8	100	62.5	40
2010	1250 K	83.1	15.6	59.6	99.1	84.3	59

Southern Hemisphere

Year	Isentropic level	mean (%)	standard deviation (%)	lower decile (%)	upper decile (%)	percentage of dates used	no. dates
2005	700 K	95.1	4.38	88.9	99.6	67.1	112
2005	900 K	95.6	6.28	85.2	100	83.6	127
2005	1250 K	86.9	16.5	64.2	100	99.1	111
2006	700 K	93.0	8.02	80.2	100	64.5	118
2006	900 K	95.4	6.85	87.0	100	92.7	139
2006	1250 K	86.8	14.6	67.9	98.4	100	75
2007	700 K	91.8	5.53	84.8	98.4	65.4	119
2007	900 K	91.0	13.3	68.2	100	81.3	117
2007	1250 K	85.5	18.0	63.4	99.4	88.5	108
2008	700 K	92.4	4.96	85.2	98.0	66.3	120
2008	900 K	95.9	4.70	89.5	99.8	84.2	128
2008	1250 K	76.4	17.7	48.1	92.7	100	128
2009	700 K	88.5	6.86	80.0	98.3	67.2	119
2009	900 K	93.6	9.41	83.0	100	86.8	131
2009	1250 K	87.4	14.6	64.3	98.8	99.0	103
2010	700 K	93.5	4.68	86.8	98.6	67.2	123
2010	900 K	93.8	10.9	81.9	100	83.9	120
2010	1250 K	92.4	12.9	69.6	100	100	108

Table 4.13: As for Table 4.9, this shows statistics based on the daily percentages of vortex cluster observations that were found to be within the vortex using a clustering method based on a cosine "metric", except that here individual sets of statistics calculated for each year are shown.

Northern Hemisphere

Year	Isentropic level	mean (%)	standard deviation (%)	lower decile (%)	upper decile (%)	percentage of dates used	no. dates
2005	700 K	97.3	2.70	94.1	100	49.1	56
2005	900 K	88.2	9.13	73.8	96.7	71.3	77
2005	1250 K	81.5	10.6	66.4	92.1	100	77
2006	700 K	98.1	2.62	96.3	100	3.64	2
2006	900 K	51.9	28.2	19.2	96.0	93.8	61
2006	1250 K	60.5	25.3	24.6	89.1	75.5	37
2007	700 K	94.4	4.86	86.7	99.6	55.4	67
2007	900 K	82.0	16.8	55.7	94.5	64.8	46
2007	1250 K	76.9	12.7	61.3	88.4	100	62
2008	700 K	92.7	7.94	78.2	99.7	33.3	35
2008	900 K	80.8	12.5	59.7	93.5	67.1	53
2008	1250 K	78.8	11.0	65.1	92.3	100	66
2009	700 K	90.1	6.03	81.2	97.3	18.2	12
2009	900 K	73.1	12.9	54.8	92.2	49.2	30
2009	1250 K	62.4	17.4	40.6	84.5	100	76
2010	700 K	90.9	9.82	75.4	100	45.5	55
2010	900 K	67.2	23.3	20.1	87.4	62.5	40
2010	1250 K	75.0	16.5	45.7	92.9	84.3	59

Southern Hemisphere

Year	Isentropic level	mean (%)	standard deviation (%)	lower decile (%)	upper decile (%)	percentage of dates used	no. dates
2005	700 K	92.4	6.09	86.3	98.6	67.1	112
2005	900 K	83.1	9.35	71.3	95.4	83.6	127
2005	1250 K	68.8	12.3	55.6	85.1	99.1	111
2006	700 K	85.3	15.4	60.2	98.5	64.5	118
2006	900 K	75.8	14.2	52.4	91.0	92.7	139
2006	1250 K	72.3	21.5	32.9	93.4	100	75
2007	700 K	94.5	4.74	86.8	98.8	65.4	119
2007	900 K	84.5	9.43	72.4	99.5	81.3	117
2007	1250 K	68.3	12.9	47.4	82.9	88.5	108
2008	700 K	94.2	4.68	89.5	98.4	66.3	120
2008	900 K	76.3	13.1	57.7	95.5	84.2	128
2008	1250 K	64.1	12.1	50.1	78.9	100	128
2009	700 K	97.1	3.38	93.4	100	67.2	119
2009	900 K	79.9	11.1	65.1	95.8	86.8	131
2009	1250 K	62.8	14.3	44.2	83.6	99.0	103
2010	700 K	94.3	3.58	89.6	99.2	67.2	123
2010	900 K	76.8	15.6	51.3	93.9	83.9	120
2010	1250 K	55.0	23.7	21.9	88.5	100	108

Table 4.14: As for Table 4.10, this shows statistics based on the daily percentages of observations within the vortex that were found to be within the vortex cluster using a clustering method based on a cosine "metric", except that here individual sets of statistics calculated for each year are shown.

Northern Hemisphere

Year	Isentropic level	mean (%)	standard deviation (%)	lower decile (%)	upper decile (%)	percentage of dates used	no. dates
2005	700 K	99.6	0.683	98.9	100	49.1	56
2005	900 K	96.1	3.61	90.2	99.7	71.3	77
2005	1250 K	94.7	2.92	90.8	98.1	100	77
2006	700 K	100	0.00	100	100	3.64	2
2006	900 K	87.1	11.3	72.7	98.7	93.8	61
2006	1250 K	84.5	16.2	56.2	99.4	75.5	37
2007	700 K	99.7	4.73	99.0	100	55.4	67
2007	900 K	96.9	4.70	94.6	99.9	64.8	46
2007	1250 K	96.0	2.77	92.4	99.2	100	62
2008	700 K	99.4	0.645	98.5	100	33.3	35
2008	900 K	94.4	6.79	82.6	99.8	67.1	53
2008	1250 K	94.4	4.97	87.2	98.8	100	66
2009	700 K	99.0	0.574	98.3	99.6	18.2	12
2009	900 K	89.5	7.15	79.6	99.0	49.2	30
2009	1250 K	84.6	14.3	66.0	97.7	100	76
2010	700 K	99.5	0.737	99.1	100	45.5	55
2010	900 K	93.2	7.08	80.0	100	62.5	40
2010	1250 K	88.3	15.4	59.6	99.2	84.3	59

Southern Hemisphere

Year	Isentropic level	mean (%)	standard deviation (%)	lower decile (%)	upper decile (%)	percentage of dates used	no. dates
2005	700 K	98.3	1.49	98.9	100	67.1	112
2005	900 K	90.4	8.23	90.2	99.9	83.6	127
2005	1250 K	85.2	6.83	90.8	90.8	99.1	111
2006	700 K	96.2	5.38	88.7	100	64.5	118
2006	900 K	90.2	8.60	75.6	99.6	92.7	139
2006	1250 K	89.1	7.62	79.8	98.6	100	75
2007	700 K	98.4	14.5	96.1	99.8	65.4	119
2007	900 K	93.6	5.83	83.9	100	81.3	117
2007	1250 K	87.3	7.59	76.4	95.7	88.5	108
2008	700 K	98.7	1.36	96.8	100	66.3	120
2008	900 K	89.3	8.02	78.9	99.4	84.2	128
2008	1250 K	81.0	6.84	72.9	91.4	100	128
2009	700 K	99.0	1.20	97.3	100	67.2	119
2009	900 K	92.9	5.95	82.8	100	86.8	131
2009	1250 K	84.1	8.47	71.6	94.4	99.0	103
2010	700 K	98.4	1.40	96.6	99.8	67.2	123
2010	900 K	91.0	7.96	77.6	99.8	83.9	120
2010	1250 K	63.4	28.0	28.9	96.0	100	108

Table 4.15: As for Table 4.11, this shows statistics based on the daily percentages of extra-vortex cluster observations that were found to be outside the vortex using a clustering method based on a cosine "metric", except that here individual sets of statistics calculated for each year are shown.

Northern Hemisphere

Year	Isentropic level	mean (%)	standard deviation (%)	lower decile (%)	upper decile (%)	percentage of dates used	no. dates
2005	700 K	87.0	3.28	82.8	90.6	49.1	56
2005	900 K	88.9	17.6	86.6	98.5	71.3	77
2005	1250 K	89.5	7.87	78.4	97.6	100	77
2006	700 K	26.8	2.16	25.2	28.3	3.64	2
2006	900 K	94.6	7.15	81.1	99.7	93.8	61
2006	1250 K	86.4	20.6	56.9	99.5	75.5	37
2007	700 K	88.5	4.40	83.2	94.7	55.4	67
2007	900 K	92.6	6.55	83.5	97.3	64.8	46
2007	1250 K	89.2	5.32	80.8	95.3	100	62
2008	700 K	84.3	8.13	71.8	96.8	33.3	35
2008	900 K	94.0	8.86	88.0	100	67.1	53
2008	1250 K	93.9	3.74	89.1	98.3	100	66
2009	700 K	86.6	2.76	81.8	88.9	18.2	12
2009	900 K	95.2	7.39	84.9	99.9	49.2	30
2009	1250 K	92.3	11.8	86.3	98.7	100	76
2010	700 K	76.6	25.1	38.3	99.5	45.5	55
2010	900 K	89.9	14.5	63.9	99.5	62.5	40
2010	1250 K	84.0	18.8	49.2	97.8	84.3	59

Southern Hemisphere

Year	Isentropic level	mean (%)	standard deviation (%)	lower decile (%)	upper decile (%)	percentage of dates used	no. dates
2005	700 K	91.6	4.41	85.1	96.1	67.1	112
2005	900 K	89.2	15.3	62.8	100	83.6	127
2005	1250 K	86.5	13.7	68.4	99.0	99.1	111
2006	700 K	91.0	6.13	84.8	100	64.5	118
2006	900 K	90.2	11.3	67.6	99.5	92.7	139
2006	1250 K	84.4	11.1	71.3	96.1	100	75
2007	700 K	91.1	3.73	86.0	95.5	65.4	119
2007	900 K	83.8	21.4	44.8	100	81.3	117
2007	1250 K	85.3	15.7	59.7	98.3	88.5	108
2008	700 K	87.2	4.90	81.2	93.9	66.3	120
2008	900 K	90.8	6.28	81.5	98.4	84.2	128
2008	1250 K	71.2	13.5	53.0	85.9	100	128
2009	700 K	82.9	11.7	66.6	96.0	67.2	119
2009	900 K	89.3	12.6	70.6	99.0	86.8	131
2009	1250 K	86.1	11.5	64.9	96.3	99.0	103
2010	700 K	90.1	2.49	86.7	93.3	67.2	123
2010	900 K	88.3	17.5	59.7	99.1	83.9	120
2010	1250 K	91.2	12.3	70.7	100	100	108

Table 4.16: As for Table 4.12, this shows statistics based on the daily percentages of observations geographically within the vortex that were found to belong to the extra-vortex cluster using a clustering method based on a cosine "metric", except that here individual sets of statistics calculated for each year are shown.

Location	mean (%)	standard deviation (%)	lower decile (%)	upper decile (%)	percentage of dates used	mean no. dates/year
NH 700 K	83.2	9.79	68.9	93.5	33.7	32.6
NH 900 K	93.8	6.65	86.3	100	60.9	45.4
NH 1250 K	89.2	10.2	76.1	99.0	87.5	58.3
SH 700 K	91.0	6.67	80.4	98.3	65.9	117.8
SH 900 K	94.1	9.88	83.0	100	69.1	102.6
SH 1250 K	89.0	11.1	75.7	99.5	79.8	86.3

Table 4.17: As for Table 4.9, but using a daily mean silhouette threshold of $Sil_{av} > 0.7$ and a silhouette threshold for individual measurements of 0.25.

Location	mean (%)	standard deviation (%)	lower decile (%)	upper decile (%)	percentage of dates used	mean no. dates/year
NH 700 K	94.7	6.08	86.4	99.7	33.7	32.6
NH 900 K	76.9	20.8	39.2	96.4	60.9	45.4
NH 1250 K	79.2	14.0	56.3	92.9	87.5	58.3
SH 700 K	94.5	7.83	89.1	99.7	65.9	117.8
SH 900 K	82.8	10.9	68.6	97.8	69.1	102.6
SH 1250 K	73.2	14.0	52.5	89.6	79.5	86.3

Table 4.18: As for Table 4.10, but using a daily mean silhouette threshold of $Sil_{av} > 0.7$ and a silhouette threshold for individual measurements of 0.25.

thresholds above 0.5 than was the case for the Euclidean algorithm. Overall, one of the most notable differences between Figures 4.12 and 4.7 is that for 900 K, the mean percentages in Figure 4.12(a) are higher than was the case using the Euclidean algorithm and the percentages in Figure 4.12 are lower. This implies that on average the cosine algorithm assigns a smaller number of measurements to the vortex cluster than was the case for the Euclidean algorithm. For 700 K, there is not much difference between the two sets of results, and for 1250 K the results shown in Figures 4.12(a) and 4.12(b) are worse for all individual silhouette thresholds, especially for the Southern hemisphere.

The results above clearly show that when using the cosine k-means algorithm the Sil_{av} threshold must be increased in order for it to be effective. It may also be helpful to reduce the individual silhouette threshold. This is because it is possible that the individual silhouette threshold used so far has worsened the statistical results by causing measurements assigned to the correct clusters by the cosine algorithm to be ignored. In order to test whether altering these thresholds can improve the cosine algorithm's results, the calculations used to produce Tables 4.9-4.12 have been repeated with the Sil_{av} threshold set to 0.7 and the individual silhouette threshold reduced to 0.25. The results are shown in Tables 4.17-4.20, with Tables 4.17 and 4.18 showing results for the intra-vortex cluster while Tables 4.19 and 4.20 show results for the extra-vortex cluster.

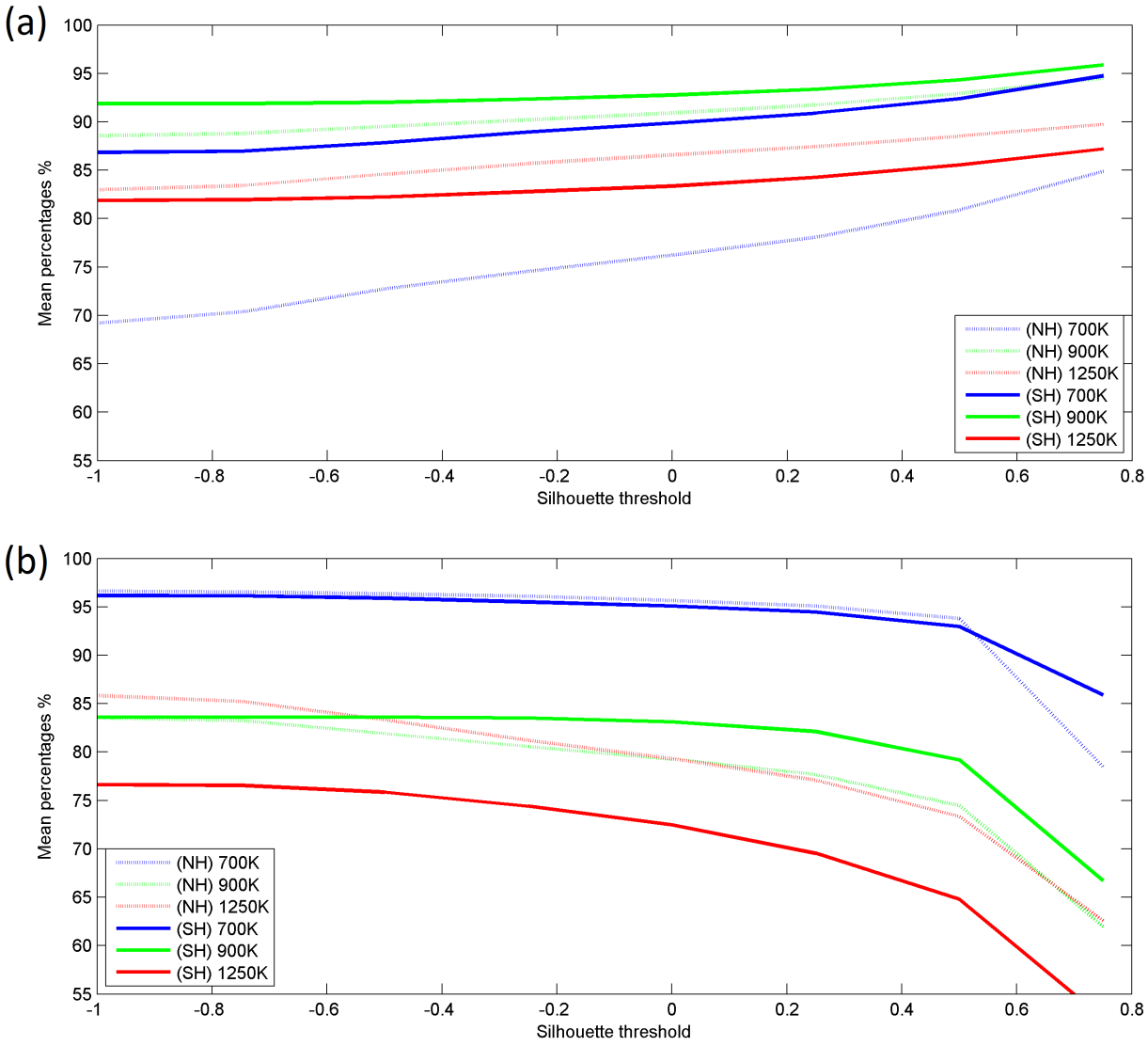

Figure 4.12: As for Figure 4.7 but for the cosine clustering algorithm.

Location	mean (%)	standard deviation (%)	lower decile (%)	upper decile (%)	percentage of dates used	mean no. dates/year
NH 700 K	99.4	0.659	98.7	100	33.7	32.6
NH 900 K	92.2	8.24	80.0	99.2	60.9	45.4
NH 1250 K	92.8	7.45	83.1	98.8	87.5	58.3
SH 700 K	98.0	3.35	96.0	100	65.9	117.8
SH 900 K	89.2	8.21	77.6	99.4	69.1	102.6
SH 1250 K	81.7	14.3	70.0	95.2	79.8	86.3

Table 4.19: As for Table 4.11, but using a daily mean silhouette threshold of $Sil_{av} > 0.7$ and a silhouette threshold for individual measurements of 0.25.

Location	mean (%)	standard deviation (%)	lower decile (%)	upper decile (%)	percentage of dates used	mean no. dates/year
NH 700 K	89.5	5.50	83.0	97.9	33.7	32.6
NH 900 K	95.8	4.71	91.1	99.7	60.9	45.4
NH 1250 K	92.3	5.56	84.8	98.3	87.5	58.3
SH 700 K	89.6	5.90	82.9	96.0	65.9	117.8
SH 900 K	92.8	12.9	82.4	100	69.1	102.6
SH 1250 K	88.9	9.19	76.2	98.8	79.5	86.3

Table 4.20: As for Table 4.12, but using a daily mean silhouette threshold of $Sil_{av} > 0.7$ and a silhouette threshold for individual measurements of 0.25.

As the Sil_{av} threshold is increased, it is expected that the statistical results will improve, but that the number of dates used will decrease. If the Sil_{av} threshold is set too high, then the range of dates over which the clustering algorithm is usable will be too limited for the results to be scientifically useful. The $Sil_{av} > 0.7$ threshold has been chosen because it improves the statistical results as much as possible while keeping the numbers of dates used per year roughly comparable with those for the Euclidean algorithm. It can be seen from Figure 4.12 that reducing the individual silhouette threshold increases the percentage of intra-vortex observations found to belong to the vortex cluster, but decreases the percentage of vortex cluster observations found to be within the vortex. This will improve the mean percentages in Table 4.18 at the expense of those in Table 4.17, but the magnitude of the change in the Table 4.18 results will in general be larger than for Table 4.17. For these tables, the individual silhouette threshold has been chosen in order to improve the Table 4.18 results as much as possible while ensuring that the Table 4.17 results are no worse than those found using the previous set of thresholds.

In Table 4.17, altering these thresholds causes the majority of the mean percentages to improve by approximately 1-2%. However, for the Southern hemisphere at 700 and 900 K, the percentages instead decrease slightly. For Table 4.18, the results are less ambiguous, with all percentages improving. The improvement is larger at the higher isentropic levels, and reaches a maximum of 8.4% for the Southern hemisphere at 1250 K. Overall, these results are a clear improvement upon those displayed in Tables 4.9 and 4.10, and show that the altered thresholds are more appropriate for the cosine algorithm than those previously used.

Increasing the Sil_{av} threshold has reduced the number of dates used in the analysis. However, in most cases the mean number of dates used per year is comparable to that used in the Euclidean algorithm statistics, although for the Northern hemisphere at 700 K, an average of 8 fewer days per year are used.

The mean percentages shown in Tables 4.17 and 4.18 are now very similar to the Euclidean algorithm results from Tables 4.1 and 4.2. All mean percentages match to within 2% and overall there is no clear increase or decrease in percentages relative to the Table 4.1-4.2 results. Using a more appropriate set of thresholds has improved the cosine algorithm's statistical results to the point where they are comparable with those from the Euclidean algorithm. Of these two methods, the cosine algorithm uses more dates per year at 1250 K with only a very small decrease in the associated mean percentages, so it could be argued that it is the best method to use at that level. The same is true for the Euclidean method at 700 K. However, it appears that when an appropriate set of thresholds is chosen for each algorithm, there is little overall difference in how closely their results correspond with those obtained using the PV-based method.

Tables 4.19 and 4.20 show that, for the cosine algorithm, altering the individual silhouette and Sil_{av} thresholds also leads to clear improvements in the statistical results for the extra-vortex cluster. Relative to the results found for the Euclidean algorithm, the mean percentages of extra-vortex cluster observations found to be located outside the vortex are worse (Table 4.19) while the mean percentages of measurements outside the vortex that are assigned the extra-vortex cluster are better. These differences may be because the change in individual silhouette threshold from 0.5 to 0.25 has caused the results in Table 4.20 to improve at the expense of those from Table 4.19. The overall statistical results indicate that with these new thresholds the cosine algorithm is very good at identifying extra-vortex air, to such an extent that its performance is roughly comparable to that of the Euclidean algorithm.

4.4 Conclusion

This study describes a method, applied to Aura-MLS measurements of carbon monoxide (CO) and nitrous oxide (N_2O), which allows the identification of intra– and extra–vortex air. It builds on research carried out by McDonald and Smith [2013], in which vortex air was identified using a method based on probability distribution functions (PDFs) of carbon monoxide (CO) mixing ratios. The new method discussed here uses two different clustering schemes applied to measurements of chemical concentrations represented in CO-N_2O tracer-tracer space. Both schemes generally identify a sharp boundary in tracer-tracer space between low-CO/high-N_2O and high-CO/low-N_2O measurements during the polar win-

ter, with the high-CO measurements being found within the vortex. The two-dimensional histograms in tracer-tracer space shown (Figures 4.1(b), 4.2(b) and 4.2(d)) clearly identify distinct distributions linked to intra–and extra–vortex air and air that is mixed. By applying k-means clustering to the data in tracer-tracer space we have demonstrated on a case study basis and statistically that we can identify populations of intra– and extra–vortex air with reasonable certainty. The two-dimensional histograms can also be used in a qualitative way to gain insight into the chemistry and dynamics of the stratosphere. For example, mixing across the stratospheric polar vortex edge during major stratospheric warmings can often be clearly observed, as shown in Figure 4.2 (b).

Of the two different clustering algorithms used, one is a k-means algorithm in which the distances between measurements in tracer-tracer space are calculated using a normalized Euclidean metric. The other is a modified k-means algorithm in which these distances are instead calculated using the cosine distance, and in which the data in tracer-tracer space is shifted with respect to the origin in order to give more weight to the tracer which, over each time period, has the largest standard deviation, and which therefore is likely to have a clearer bimodality in its distribution. Each algorithm is applied to data collected over an 11-day moving window.

In order to produce detailed polar stereographic plots containing information on the physical locations of cluster members over an entire 11-day period, a domain filling scheme is used to project the MLS observations, collected over the entire period, to their location on the central date using a Lagrangian trajectory model to artificially improve sampling at that time. This allows us to examine the geographical distribution of the observations linked to the two clusters identified by the k-means clustering scheme. This analysis allows us to more closely examine the performance of the clustering algorithm and clearly shows that it performs well at identifying vortex air. We also show that the silhouette value, a measure of the within-group and between-group differences between clusters which is an indication of the likelihood of each measurement being assigned to the correct cluster, can be used to represent our confidence in a particular observation being intra– or extra–vortex air. It is also found that during the 2009 SSW, measurements identified as belonging to the vortex with a high silhouette value are prevalent within the vortex remnants identified using the standard PV-based method in a geographical sense (see Figures 4.4(a), (c) and (e)). This therefore suggests that silhouette values offer the potential to identify mixed air. This is also confirmed on visual inspection of Figures 4.4(b), (d) and (f), which clearly show that the

mixed region in tracer-tracer space is linked to low silhouette values.

In Figures 4.3(a) and (b), the boundary between tracer values that are typical of intra- and extra-vortex air appears to be within the impermeability-based vortex edge line for CO and outside it for N_2O. This clearly indicates that the two tracers can provide different independent information, and may also indicate the existence of an intermediate mixing region similar to that identified by Roscoe et al. [2012]. The possibility of obtaining more information about the location of the vortex edge by using multiple tracers is one of the motivations behind this study.

A combination of thresholds based on relative differences between CO concentrations at the cluster centroids and daily mean silhouette scores Sil_{av} can be used to identify dates for which there are likely to be two chemically distinct clusters corresponding to air inside and outside the polar vortex. For the Euclidean-metric clustering algorithm, the silhouette–based threshold is most effective at the higher altitudes used in this study, while the threshold based on relative differences between CO concentrations is more effective at lower levels. For the cosine distance clustering algorithm, the effectiveness of the Sil_{av} condition is more consistent between levels.

For the Euclidean-metric algorithm, major SSWs over the 2005-2010 period are often associated with sudden drops in daily mean silhouette values, which raises the possibility of these being used to identify periods where mixing is occurring. During seasons where the SSW begins after vortex cluster CO concentrations have peaked, the SSW start date coincides with a sharp drop in daily mean silhouette scores at 900 K (Figure 4.5). At 1250 K (Figure 4.5), the drop in Sil_{av} precedes the official SSW start date, while at 700 K (Figure 4.5), there is a dip shortly after the start date. This is what would be expected if the reduction in Sil_{av} were linked to a disturbance in the vortex propagating downwards. However, this relationship does not always hold. At 700 and 900 K, the major SSWs in early 2006 and 2010 are not associated with drops in Sil_{av}. These are also the two SSWs for which, at 900 K, the SSW begins before CO values in the vortex cluster have reached their peak. This suggests that there is a strong relationship between steep drops in Sil_{av} and major SSWs, but that this only applies under certain circumstances.

A statistical analysis applied to a comparison between the Euclidean–metric k–means clustering method and the PV-based method as used in Manney et al. [2007], McDonald and Smith [2013], and Smith and McDonald [2014] shows that the clustering method does well at identifying vortex air at all isentropic levels

investigated. A comparison of these results with similar statistics obtained by McDonald and Smith [2013] using a method based on probability distribution functions (PDFs) of CO shows that they are roughly equivalent. However, the addition of N_2O information has not led to a clear improvement in the fit between the vortex location determined using the tracer based method and that found using the more standard PV/wind speed based approach. The differences between CO and N_2O distributions in the stratosphere still suggest that it should be possible to obtain extra information about the dynamics and location of the vortex edge location by incorporating N_2O data. More research needs to be done in order to determine whether this is the case. In addition, this method can be tuned to be more or less conservative in identifying vortex air by altering the silhouette threshold value below which individual tracer measurements are not identified as belonging to the vortex air mass.

Interestingly, the best statistical results for the algorithms are based on the percentages of measurements assigned to the extra-vortex cluster found outside the vortex according to the PV-based method. This implies that they can identify air located outside the vortex with a high degree of accuracy.

The cosine distance clustering method was designed with the intention of providing an improved statistical fit between the clustering results and the vortex location obtained using the PV-based method. During periods such as the days immediately after the 2009 major SSW, this method does appear to produce a more realistic division of measurements into clusters corresponding to intra– and extra–vortex air, as can be seen from a comparison between Figures 4.4(e) and (f), and Figure 4.9. The statistical results produced using the cosine clustering method appeared at first to be worse than those from the Euclidean algorithm. However, this was found to be caused by the thresholds, which were initially set to the same values used by the Euclidean algorithm. After the Sil_{av} threshold was increased to 0.7 and the individual silhouette threshold decreased to 0.25, the results improved considerably. If appropriate thresholds are used for both algorithms, the statistical results produced by them are approximately equivalent. This may imply that the statistical results may be relatively insensitive to changes in the k-means clustering algorithm.

One approach that could help improve the results found using the cosine distance method would be to normalize the data before clustering using the maximum and minimum tracer values over each 11-day period being clustered over. The cosine clustering algorithm is highly sensitive to the shape of the distribution of the results in tracer-tracer space that is input to it. Therefore this normaliza-

tion may improve the consistency of the clustering results.

At the two highest potential temperatures used in this study, 900 and 1250 K, some difficulties were experienced with obtaining a consistent vortex edge location, in terms of equivalent latitude, to compare our clustering results against. These difficulties were most acute at 1250 K, especially in the Southern hemisphere, where they caused a large number of dates within the period investigated to be removed from the results. In general the statistical results were worse and more variable at 1250 K than at the two lower isentropic levels, for both clustering methods. It is also possible that ambiguity in the equivalent latitude of the vortex edge could have affected statistical results at the two lower potential temperature levels. These difficulties are not unexpected, since it is stated in Manney et al. [2007] that it is more difficult to obtain an unambiguous equivalent latitude for the vortex edge at higher altitudes, particularly in the Southern hemisphere. However they do cause problems when attempting to test our tracer-based method for identifying vortex air at these altitudes against the known position of the vortex edge. It may be helpful to test the tracer-tracer based clustering methods developed here at lower altitudes within the stratosphere such at 600 K, since it is easier to obtain a clear equivalent latitude for the vortex edge there.

It is possible that the difficulty in obtaining a consistent vortex edge at higher altitude may be due to there being an intermediate region of mixing between air inside and outside the vortex rather than a sharp boundary. In this case it may be more appropriate to identify measurements belonging to this mixing region rather than to look for a clear, well defined vortex edge based on the tracer data. An obvious approach to take, based on our current methodology, would be to define all measurements with individual silhouette scores below a certain threshold score to be part of a group of measurements likely to be connected with the intermediate mixing region. However, some care would need to be taken to test whether the low-silhouette measurements are indeed part of such a mixing region.

Currently, when calculating the percentages of, for example, measurements located within the vortex that are found to belong to the vortex cluster, only measurements with individual silhouette scores above 0.5 (or 0.25 for the cosine algorithm) are considered to belong to the vortex cluster. This means that measurements located within the vortex that belong to the vortex cluster, but with silhouette scores below that threshold are counted as misclassified air. This may cause the statistical results to appear worse than they truly are, since in actuality these measurements should either be within the vortex or belong to the vortex

edge region. This issue could be resolved by, as discussed above, instead assigning these measurements to a low-silhouette/mixing region and not counting them as misclassified air. This would improve the statistical results as well as better reflecting the physical structure of the vortex.

The tracer-based clustering methodology described here can also potentially be used with chemicals that are not long-term tracers, such as water vapor, as shown in Figure 4.8. By using different sets of chemicals that are more or less prevalent at different altitudes, it should be possible to apply this method at different levels in the atmosphere. For example, at 1750 K applying a k-means algorithm based on concentrations of carbon monoxide and water vapor identifies an area with a shape, extent and location consistent with the polar vortex, although no PV-based vortex edge is available to test against. This suggests that k-means clustering in tracer-tracer space could be used to locate the vortex and its edge at altitudes where it is hard to obtain reliable reanalysis data, such as in the upper stratosphere and lower mesosphere.

Chapter 5

Conclusions and further work

5.1 Summary of results

The main aim of this research has been to develop new methods for investigating the location and strength of the transport barrier at the edge of the stratospheric polar vortex. These could lead to a better understanding of how changes in the strength of the vortex edge barrier, such as those caused by dynamical events such as SSWs, affect the rate at which air descends through the vortex. Changes in this descent rate affect the strength of the energetic particle precipitation indirect effect (EPP IE), in which reactive chemicals such as odd nitrogen (NO_x), produced by EPP in the mesosphere and lower thermosphere, descend into the stratosphere where they can break down ozone [Solomon et al., 1982, Siskind et al., 2000, Jackman et al., 2009]. The strength of the vortex edge barrier also affects lower stratospheric ozone concentrations more generally, since a stronger barrier leads to colder intra-vortex temperatures that are necessary in order for large-scale breakdown of ozone to occur. For example, during the 2010-2011 Arctic vortex season, an unusually strong vortex edge barrier led to the formation of an unprecedented "ozone hole" [Manney et al., 2011, Olascoaga et al., 2012]. Changes in vortex dynamics can also affect tropospheric weather [Baldwin and Dunkerton, 2001] and information about events such as SSWs can be used in some circumstances to improve weather prediction in the troposphere [Sigmond et al., 2013].

To begin with, we developed two quantitative measures based on reanalysis wind speed data that are related to the strength of the vortex edge barrier and the dynamics of the vortex more generally. We then investigated methods for locating the vortex edge based on satellite tracer data, since this data is likely to be more

reliable at high altitudes within the middle atmosphere than the reanalysis data.

The quantitative measures based on wind speed data made use of a Lagrangian descriptor known as the "function M", which is based on the arc length traced by fluid parcel trajectories derived from reanalysis data over a period of days or weeks. The fluid parcel trajectories used were calculated using a model developed by our research group. The first measure, $\bar{M}$, is based on the average value of M near the vortex edge, and the second, A_M, is based on the area over which values of M are above a certain threshold. The $\bar{M}$ measure is intended to be strongly correlated with the strength of the vortex edge barrier, while A_M is intended to measure the area occupied by the vortex edge region. These measures were calculated over a number of Northern and Southern hemisphere winter periods for isentropic levels ranging from 600-900 K (corresponding to altitudes of approximately 14-31 km).

The area-based measure, A_M, appears to be the most useful in practice and can identify periods when the vortex edge barrier breaks down. After the major SSWs of 2009 and 2010, this measure sharply decreases. The A_M measure also appears to be good at identifying periods when the vortex is strong. For example, during the 2004/2005 Northern hemisphere winter period, when the vortex was unusually strong [El Amraoui et al., 2008], the A_M measure has a considerably larger value throughout most of the vortex season than is the case for the other two seasons studied. This means that the A_M measure could be very useful as a quantitative measure of vortex edge barrier strength.

The $\bar{M}$ measure is much less sensitive to the effects of major SSWs. However, it appears to be better at identifying periods when the transport barrier is narrow but relatively impermeable, such as when erosion by planetary wave breaking leads to a sharp PV gradient near the vortex edge. This indicates that the $\bar{M}$ measure provides information about the vortex edge barrier that complements that obtained using A_M and that using both measures simultaneously will lead to a better understanding of changes in the barrier's behaviour than would be possible using just one measure.

An investigation into the insensitivity of the $\bar{M}$ measure to major SSWs led to some interesting results. At first, it appeared that the most obvious possible explanation for this insensitivity was that the long time period (30 days) over which M was calculated led to an overly smoothed result. However, this was found not to be the case, since reducing the period over which M was calculated did not lead to any appreciable improvement in sensitivity. In fact, it was found that over the 2009/2010 vortex season there is a strong linear correlation between

values of M calculated over periods of different lengths, particularly near the vortex edge. This explains why the sensitivity of the function M-based measures does not alter much when the period over which M is calculated changes. It also implies that the structure of the polar vortex is coherent over long periods of time.

Another factor which affects the sensitivity of both measures to the effects of SSWs is due to the fact that, according to the most commonly used definition [Charlton and Polvani, 2007], a major SSW begins when the zonal mean zonal winds reverse at 60°N. Since the function M-based measures follow the edge of the vortex, they can detect the dynamical structure of the vortex even when it becomes distorted, as often occurs during a major SSW. This is why values of A_M drop off more rapidly after the 24 January 2009 SSW than after the 26 January 2010 SSW, as can be seen in Figure 3.8. For 2009, the SSW is a splitting event and the post-SSW breakdown of the vortex is much more sudden and complete than is the case for 2010. After the 2010 SSW, which was a vortex displacement event, a vortex-like structure persists at least until 1 February, and this is reflected in the value of the A_M measure.

As was first discussed in de la Camara et al. [2012], the function M can be used qualitatively to create detailed plots of the stratospheric polar vortex and the surrounding region. In these plots, it is possible to observe the polar night jet, as well as anticyclones and and locations where material is likely to be entering or leaving the vortex.

In Chapter 3, the function M-based analysis was applied to the isentropic levels ranging from 600-900 K during a number of different winter seasons in both hemispheres. At altitudes higher than this, the reanalysis wind data used to calculate the function M becomes less reliable. Therefore we investigated alternative data sources that could be used to provide information about the location of the vortex edge, and the strength of the barrier there. We decided to focus on methods that could be used to find the location of the polar vortex and its edge, and developed a methodology for doing this based on applying k-means clustering to satellite observations in order to identify intra- and extra-vortex air. Two closely related k-means algorithms were developed. When choosing which measurements to assign to each cluster, one algorithm uses a Euclidean metric to calculate the distances between points, and the other uses cosine distance to do this (see Chapter 4.2).

We started developing and testing the k-means clustering algorithms in the middle stratosphere at isentropic levels between 700-1250 K, since these are the

highest altitudes at which the algorithms can be reliably validated against PV-based vortex edge detection methods. The algorithms were based on measurements of carbon monoxide (CO) and nitrous oxide (N_2O), since these are prevalent enough at these altitudes to be used as tracers. Since N_2O generally enters the middle stratospheric winter hemisphere from lower altitudes and latitudes, concentrations of it are higher outside the vortex than inside. The reverse is true for CO, as this generally arrives in the middle stratospheric winter hemisphere via descent from higher altitudes within the vortex. Therefore if the vortex edge transport barrier is of non-negligible width, the location of the barrier obtained using N_2O data may be different from that found using CO data: in general it would be expected that the barrier location found using N_2O data will be equatorwards of that found using CO data. This is because N_2O attempting to enter the vortex from outside would be stopped by the outermost edge of the barrier region, while CO attempting to leave the vortex would be stopped at the innermost edge of the barrier region, meaning that there would be a region within the barrier with low concentrations of both tracers. One of the main motivations for developing methods based on more than one tracer is that doing so may provide additional information about the vortex edge, leading to a more reliable determination of its location.

It should be possible to apply this methodology at different altitudes by using different combinations of tracers. For example, in the upper stratosphere it may be possible to use measurements of CO and H_2O to identify vortex air, although the relatively complicated distribution of H_2O in the stratosphere will need to be taken into account when carrying this out. Figure 4.8 shows an example of how our methodology can be used to divide measurements of these tracers into clusters for a sample date within the vortex season at an isentropic level of 1750 K.

The algorithms were tested, for the winter seasons of both hemispheres during 2005-2010, by comparing their results with the vortex edge location determined using a PV-based method. The comparisons showed that both algorithms are good at identifying intra- and extra-vortex air at the altitude levels studied. However, there is so far no clear evidence that either of these methods is better at identifying vortex air than the method described in McDonald and Smith [2013], which only uses measurements of CO.

However, the algorithms were found to be especially successful at identifying air which is located outside the vortex. The proportions of measurements assigned to the extra-vortex cluster that are located outside the vortex according to the

PV-based criteria are very high, particularly for the Euclidean algorithm. This may be due to the fact that data from measurements of N_2O are incorporated into the results. Since the location of the barrier as determined using N_2O data should be equatorwards of that found using CO, the inclusion of N_2O data may tend to bias the tracer-derived vortex edge towards lower latitudes, leading to a set of clustering algorithms that are better at identifying extra-vortex air than at identifying intra-vortex air.

Two-dimensional histograms in CO-N_2O tracer-tracer space can also be used qualitatively to observe changes in stratospheric chemistry and dynamics. For example, during events such as major SSWs, when the vortex barrier weakens or breaks down, signs of mixing across the vortex barrier can often be seen, as shown in Figures 4.2 (a) and (b). Further qualitative information can be obtained from the results of the clustering algorithms. Plots showing how the mean CO value in the vortex cluster centroid changes over time can show, for each altitude, the time period over which CO-rich air is descending from above, as well as how major SSWs affect this descent.

When calculating the statistical results, only measurements assigned to the intra- or extra-vortex clusters with silhouette scores above a threshold value were considered to belong to the clusters. A set of threshold conditions were also applied to the clustering results to rule out dates for which there was likely too little distinction between the chemical compositions in each cluster for the algorithms to work correctly. The first condition ruled out dates for which mean CO values were smaller in the intra- than the extra-vortex cluster, while the second condition ruled out dates for which the mean silhouette scores Sil_{av} averaged over all measurements were less than a threshold value. For the Euclidean-metric algorithm, the Sil_{av} threshold was 0.5, while for the cosine distance algorithm the threshold for the Sil_{av} condition needed to be raised to 0.7 in order to maintain its effectiveness. For both algorithms, applying these conditions led to a modest improvement in the results.

The cosine distance clustering method was designed with the aim of improving upon the Euclidean metric clustering algorithm. However, when the division of measurements into clusters produced by both of these algorithms was compared with the location of the PV-based vortex edge, there was little difference between the statistical results found for each algorithm. This suggests that these results may be rather insensitive to the changes in the k-means clustering algorithm. This insensitivity may be due to difficulty in classifying air belonging to the vortex edge region in cases where the boundary between intra- and extra-vortex

air is not sharp. In Chapter 5.2, possible methods for accounting for this air and improving the statistical results are discussed.

For both clustering algorithms, the statistical match between their results and those found using the PV-based method was poorest at the highest altitude level studied, 1250 K. At this level it was difficult to obtain a consistent PV-based vortex edge location to compare our results against, since this location often appeared to jump considerably from day to day, particularly in the earlier part of the vortex season studied and in the Southern hemisphere. Although a number of dates for which the PV-based vortex edge was not considered likely to be realistic were screened out, it seems probable that these issues affected our statistical results at 1250 K.

In summary, we have developed two different methods, based on a dynamical measure known as the "function M", which capture different aspects of vortex dynamics. The area-based measure, A_M, is a useful measure of the strength of the polar vortex, can be used to identify major SSWs, and can detect the dynamical structure of the polar vortex even when its shape has been greatly distorted. The measure $\bar{M}$, which is based on the average value of M near the PV-based vortex edge, is less effective at identifying SSWs, but captures other aspects of vortex dynamics that complement the information that can be obtained from A_M. Recent improvements to the trajectory model used by our group to calculate M may open up new possible avenues for useful research. The two function M-based measures work well at isentropic levels up to 900 K, and it may be possible to extend this range upwards, but the lack of reliable reanalysis data in the upper stratosphere and above means that it is necessary to look for alternative approaches at these altitudes.

Therefore, we have investigated methods for investigating polar vortex dynamics that are based on satellite tracer data, since this is readily available at higher altitudes. We decided to focus on methods that can be used to identify the location of the vortex edge, and developed two k-means clustering algorithms that can be used to identify intra- and extra-vortex air based on measurements of CO and N_2O from the Aura-MLS instrument. Although we tested these algorithms in the middle stratosphere, at isentropic levels ranging from 700-1250 K, once their accuracy has been verified it should be possible to extend this methodology in order to locate the polar vortex at higher altitudes by using tracer combinations such as CO vs H_2O. Comparisons between the clustering algorithms and the vortex edge location derived using a PV-based method show that our method in general works well. However, there is not yet any clear evidence that either of

these algorithms is better at identifying vortex air than the one used by McDonald and Smith [2013], although they are very good at identifying extra-vortex air. A number of different approaches, discussed in these conclusions, could be used to improve the accuracy and reliability of these algorithms and/or the reliability of the reanalysis data-based vortex edge against which their results are tested. It seems very likely that doing this would lead to a method or methods that could be very useful for locating the polar vortex in the upper stratosphere and possibly also the mesosphere, which would lead to a better understanding of polar vortex dynamics in these regions.

5.2 Further work

Both of the function M-based quantitative measures developed over the course of this research could be useful for producing time series describing how the dynamics of the vortex change over time. These could then be compared with descent rates in order to investigate how those are affected by changes in the strength of the vortex edge barrier, leading to a better knowledge of the effects of dynamical events such as SSWs.

By comparing plots of the function M that are calculated over short and long time periods, it is possible to distinguish long-lived dynamical structures from transient ones, since long-lived structures persist when the period over which M is calculated increases while shorter-lived structures dissipate. The strong correlation between values of the function M calculated over periods of different lengths which was found over the Dec 2009-March 2010 vortex season may also be worth investigating further. For example, a similar calculation could be carried out for the Dec 2008-March 2009 period, for which there is evidence that the January 2009 SSW caused a sudden and complete breakdown of vortex structure, to see whether that affects the correlation.

Recently, an improved parcel trajectory model has been developed by our research group. This new model is considerably faster than the model used previously, and can also calculate three dimensional trajectories rather than being limited to isentropic surfaces. The speed improvements will make it easier to carry out function M-based research over climatological time scales, and may also make it worthwhile to carry out function M-based computations that would otherwise have been prohibitively time-consuming. Since the descent rate of air through the vortex increases above 900 K (the highest potential temperature sur-

face investigated by the work in Chapter 3), and the isentropic approximation is valid over shorter time scales, the ability to calculate three-dimensional trajectories may also help to extend the vertical range over which function M-based methods are applicable. However, this will still be limited by the availability of reliable reanalysis data at these higher altitudes.

It may be possible to use the function M to develop an improved method for determining the location of the vortex edge barrier. For 600-900 K, the isentropic levels studied in Chapter 3, the most commonly-used methods for identifying the location of the vortex edge are based on finding the maximum mean gradient of potential vorticity (PV) as a function of equivalent latitude. Even at these altitudes, the function can have multiple peaks, making the detection of an unambiguous vortex edge more challenging. At higher levels, such as 1250 K, these issues can cause significant problems with the PV-based calculation of the vortex edge, as was seen in Chapter 4 (also see Randall et al. [2007]). Since values of the function M are largest in the vicinity of the polar night jet, when mean values of M are calculated as a function of equivalent latitude, this function should usually have a single well-defined peak at or close to the vortex edge barrier. This means that, if this peak is found to correspond to the vortex edge barrier location, a function M-based method could be a more reliable way of locating it than a PV-based method. This approach will be more computationally expensive than standard methods, but since speed improvements have recently been made to our trajectory model it is likely to be worth testing.

There are a number of possible avenues for future research following on from our study of tracer-based methods for identifying intra- and extra-vortex air. For example, it may be worthwhile to calculate the vortex edge location using data from each individual tracer and then investigate where the PV-based vortex edge is in relation to each of these, since this may provide additional information about the structure of the vortex edge region. Another possible method for obtaining such information would be identify the physical locations corresponding to measurements for which concentrations of CO and N_2O are both low, since these may be associated with the vortex edge barrier, and to compare these with plots of PV and other meteorological variables. An improved understanding of the edge region's structure may lead to alternative methods for determining the vortex edge location.

In addition, since tracer-tracer histograms can provide useful qualitative information about the chemistry and dynamics of the vortex, a study of how these evolve over the course of each vortex season and how they are related to known

dynamical events may provide a useful insight into the life-cycle of the stratospheric polar vortex.

There are also a number of possible modifications that could be made to the k-means clustering algorithms that may improve the statistical results found when comparing our results to the vortex edge determined using standard PV-based methods. For example, it may be possible to improve the consistency of the results from the cosine algorithm by applying a pre-clustering normalization to the measurements in order to avoid large changes over time in the shape of the measurement's distribution in tracer-tracer space.

Also, the PV-based method used in our statistical comparisons defines the vortex edge to be at a single equivalent latitude. However, this may not always be realistic, since the actual vortex edge barrier region may often have a non-negligible width. Rather than a sharp edge separating intra- and extra-vortex air, it may be more realistic to think of the vortex edge as an intermediate mixing region (as identified by Lee et al. [2001] and Roscoe et al. [2012] etc) of finite size. It may then not be ideal to divide all satellite tracer observations neatly into two clusters corresponding to intra- and extra-vortex air, since some observations will correspond to locations that cannot truly be considered to be either inside or outside the vortex. This may cause a certain amount of arbitrariness in the division into intra- and extra-vortex air produced by the clustering algorithms and therefore also make it difficult to obtain a perfect fit between this division into clusters and the PV-based vortex edge. However, since we have calculated a silhouette score for each measurement, this can be used to help identify which measurements are most likely to have been assigned to the correct clusters. Measurements with silhouette scores above a certain threshold can then be confidently assigned to the intra- or extra-vortex clusters, while a third "cluster" is defined that is comprised of measurements with lower silhouette scores. This "cluster" should include measurements that are linked with the vortex edge barrier region, although some testing will need to be carried out before it can confidently be stated that this is the case. These changes in the clustering methodology could lead to improved algorithms that will better account for those cases where the vortex edge barrier is not sharply defined but instead has a finite width or a more complicated dynamical structure.

So far, we have focused on the results obtained by our k-means clustering algorithms and how they might be improved. However, there may be other related tracer-based methods for identifying vortex air that are also worth looking into. For example, since the location found to correspond to the vortex edge may differ

depending on whether CO or N_2O tracer data is used, it may be possible to identify the vortex edge region by first using CO data alone to determine which measurements belong to the vortex, and then doing the same using N_2O data. It should then be possible to identify which measurements are likely to be part of the vortex edge region by looking for observations which are assigned to the vortex when using data from one of the tracers but which are placed outside the vortex when the other tracer is used. Another potentially useful approach is to calculate gradients of tracer concentrations as has been done by Harvey et al. [2015], since the vortex edge barrier should be associated with sharp tracer gradients. Harvey et al. [2015] use gradients of CO to identify the location of the vortex edge, and it should be possible to carry out this method for different tracers and then compare the results obtained.

Bibliography

J. Ajtić, B. J. Connor, C. E. Randall, B. N. Lawrence, G. E. Bodeker, J. E. Rosenfield, and D. N. Heuff. Antarctic air over New Zealand following vortex breakdown in 1998. *Annales Geophysicae*, 21(11):2175–2183, 2003.

J. Ajtić, B. J. Connor, B. N. Lawrence, G. E. Bodeker, K. W. Hoppel, J. E. Rosenfield, and D. N. Heuff. Dilution of the Antarctic ozone hole into southern midlatitudes, 1998-2000. *Journal of Geophysical Research-Atmospheres*, 109: D17107, 2004. doi: 10.1029/2003JD004500.

S. P. Alexander, A. R. Klekociuk, A. J. McDonald, and M. C. Pitts. Quantifying the role of orographic gravity waves on polar stratospheric cloud occurrence in the Antarctic and the Arctic. *Journal of Geophysical Research-Atmospheres*, 118(20):15, 2013. doi: 10.1002/2013jd020122.

D. R. Allen and N. Nakamura. A seasonal climatology of effective diffusivity in the stratosphere. *Journal of Geophysical Research - Atmospheres*, 106(D8): 7917–7935, 2001. doi: 10.1029/2000JD900717.

D. R. Allen and N. Nakamura. Tracer Equivalent Latitude: A Diagnostic Tool for Isentropic Transport Studies. *Journal of the Atmospheric Sciences*, 60(2): 287–304, 2003. doi: 10.1175/1520-0469(2003)060<0287:TELADT>2.0.CO;2.

D. R. Allen, J. L. Stanford, M. A. López-Valverde, N. Nakamura, D. J. Lary, A. R. Douglass, M. C. Cerniglia, J. J. Remedios, and F. W. Taylor. Observations of Middle Atmosphere CO from the UARS ISAMS during the Early Northern Winter 1991/92. *Journal of the Atmospheric Sciences*, 56(4):563–583, 1999. doi: 10.1175/1520-0469(1999)056¡0563:OOMACF¿2.0.CO;2.

D. R. Allen, J. L. Stanford, N. Nakamura, M. A. López-Valverde, M. López-Puertas, F. W. Taylor, and J. J. Remedios. Antarctic polar descent and planetary wave activity observed in ISAMS CO from April to July 1992. *Geophysical Research Letters*, 27(5):665–668, 2000. doi: 10.1029/1999GL010888.

D. R. Allen, A. R. Douglass, G. E. Nedoluha, and L. Coy. Tracer transport during the Arctic stratospheric final warming based on a 33-year (1979-2011) tracer equivalent latitude simulation. *Geophysical Research Letters*, 39:L12801, 2012. doi: 10.1029/2012GL051930.

David G. Andrews. *An introduction to atmospheric physics*. Cambridge University Press, 2010.

David G. Andrews, James R. Holton, and Conway B. Leovy. *Middle Atmosphere Dynamics*. Academic Press, 1987.

C. Appenzeller, H. C. Davies, and W. A. Norton. Fragmentation of stratospheric intrusions. *Journal of Geophysical Research-Atmospheres*, 101(D1):1435–1436, 1996. doi: 10.1029/95JD02674.

B. Ayarzagüena, U. Langematz, and E. Serrano. Tropospheric forcing of the stratosphere: A comparative study of the two different major stratospheric warmings in 2009 and 2010. *Journal of Geophysical Research-Atmospheres*, 116:D18114, 2011. doi: 10.1029/2010JD015023.

M. N. Baker and D. M. Cunnold. The Uses and Limitations of Contour Advection as a Technique for Examining Arctic Vortex Dynamics. *Journal of the Atmospheric Sciences*, 58(15):2210–2221, 2001. doi: 10.1175/1520-0469(2001)058¡2210:TUALOC¿2.0.CO;2.

M. P. Baldwin and T. J. Dunkerton. Stratospheric Harbingers of Anomalous Weather Regimes. *Science*, 294(5542):581–584, 2001. doi: 10.1126/science.1063315.

R. Bauer, A. Engel, H. Franken, E. Klein, G. Kulessa, C. Schiller, and U. Schmidt. Monitoring the vertical structure of the Arctic polar vortex over northern Scandinavia during EASOE: Regular N_2O profile observations. *Geophysical Research Letters*, 21(13):1211–1214, 1994. doi: 10.1029/93GL01053.

P. F. Bernath, C. T. McElroy, M. C. Abrams, C. D. Boone, M. Butler, C. Camy-Peyret, M. Carleer, C. Clerbaux, P. H. Coheur, R. Colin, P. DeCola, M. DeMazière, J. R. Drummond, D. Dufour, W. F. J. Evans, H. Fast, D. Fussen, K. Gilbert, D. E. Jennings, E. J. Llewellyn, R. P. Lowe, E. Mahieu, J. C. McConnel, M. McHugh, S. D. McLeod, R. Michaud, C. Midwinter, R. Nassar, F. Nichitiu, C. Nowlan, C. P. Rinsland, Y. J. Rochon, N. Rowlands, K. Semeniuk, P. Simon, R. Skelton, J. J. Sloan, M. A. Soucy, K. Strong, P. Tremblay,

D. Turnbull, K. A. Walker, I. Walkty, D. A. Wardle, V. Wehrle, R. Zander, and J. Zou. Atmospheric Chemistry Experiment (ACE): Mission overview. *Geophysical Research Letters*, 32(15):L15S01, 2005. doi: 10.1029/2005GL022386.

F. J. Beron-Vera, M. J. Olascoaga, and M. G. Brown. Zonal Jets as Meridional Transport Barriers in the Subtropical and Polar Lower Stratosphere. *Journal of the Atmospheric Sciences*, 69(2):753–767, 2012. doi: 10.1175/JAS-D-11-084.1.

P. Berrisford, D. Dee, P. Poli, R. Brugge, K. Fielding, M. Fuentes, P. Kållberg, S. Kobayashi, S. Uppala, and A. Simmons. The ERA-Interim archive Version 2. Technical report, ECMWF, 2011. available from http://old.ecmwf.int/publications/library/do/references/show?id=90276.

M. G. Bosilovich, S. Akella, L. Coy, R. Cullather, C. Draper, R. Gellaro, R. Kovach, Q. Liu, A. Molod, P. Norris, K. Wargan, W. Chao, R. Reichle, L. Takacs, Y. Vikhliaev, S. Bloom, A. Collow, S. Firth, G. Labow, G. Partyka, S. Pawson, O. Reale andS. D. Schubert, and M. Suarez. MERRA-2:Initial Evaluation of the Climate. Technical report, Goddard Space Flight Center - NASA, 2015. Technical Report Series on Global Modeling and Data Assimilation, Volume 43 (NASA/TM2015-104606/Vol. 43), available from https://gmao.gsfc.nasa.gov/pubs/tm/docs/Bosilovich803.pdf.

K. P. Bowman. Large-Scale Isentropic Mixing Properties of the Antarctic Polar Vortex from Analyzed Winds. *Journal of Geophysical Research-Atmospheres*, 98(D12):23013–23027, 1993. doi: 10.1029/93JD02599.

A. W. Brewer. Evidence for a world circulation provided by the measurements of helium and water vapour distribution in the stratosphere. *Quarterly Journal of the Royal Meteorological Society*, 75(326):351–363, 1949.

N. Butchart. The Brewer-Dobson circulation. *Reviews of Geophysics*, 52(2): 157–184, 2014. doi: 10.1002/2013RG000448.

N. Butchart and E. E. Remsberg. The Area of the Stratospheric Polar Vortex as a Diagnostic for Tracer Transport on an Isentropic Surface. *Journal of the Atmospheric Sciences*, 43(13):1319–1339, 1986. doi: 10.1175/1520-0469(1986)043<1319:TAOTSP>2.0.CO;2.

A. H. Butler, D. J. Seidel, S. C. Hardiman, N. Butchart, T. Birner, and A. Match. Defining sudden stratospheric warmings. *Bulletin of the American Meteorological Society*, 96(11):1913–1928, 2015. doi: 10.1175/BAMS-D-13-00173.1.

A. RJ. Charlton and L. M. Polvani. A New Look at Stratospheric Sudden Warmings. Part I: Climatology and Modeling Benchmarks. *Journal of Climate*, 20 (3):449–469, 2007. doi: 10.1175/JCLI-D-11-00348.1.

J. G. Charney and P. G. Drazin. Propagation of Planetary-Scale Disturbances from the Lower into the Upper Atmosphere. *Journal of Geophysical Research*, 66(1):83–&, 1961. doi: 10.1029/JZ066i001p00083.

P. Chen. The permeability of the Antarctic vortex edge. *Journal of Geophysical Research - Atmospheres*, 99(D10):20563–20571, 1994. doi: 10.1029/94JD01754.

P. Chen, J. R. Holton, A. O'Neill, and R. Swinbank. Quasi-horizontal trnasport and mixing in the Antarctic stratosphere. *Journal of Geophysical Research - Atmospheres*, 99(D8):16851–16866, 1994. doi: 10.1029/94JD00784.

N. Y. Cohen, E. P. Gerber, and O. Bühler. What Drives the Brewer-Dobson Circulation? *Journal of the Atmospheric Sciences*, 71(10):3837–3855, 2014. doi: 10.1175/JAS-D-14-0021.1.

K. Coughlin and L. J. Gray. A continuum of sudden stratospheric warmings. *Journal of the Atmospheric Sciences*, 66(2):531–540, 2009. doi: 10.1175/2008jas2792.1.

L. Coy, S. D. Eckermann, K. W. Hoppel, and F. Sassi. Mesospheric Precursors to the Major Stratospheric Sudden Warming of 2009: Validation and Dynamical Attribution Using a Ground-to-Edge-of-Space Data Assimilation System. *Journal of Advances in Modeling Earth Systems*, 3:M10002, 2011. doi: 10.1029/2011MS000067.

A. de la Camara, C. R. Mechoso, K. Ide, R. Walterscheid, and G. Schubert. Polar night vortex breakdown and large-scale stirring in the southern stratosphere. *Climate Dynamics*, 35(6):965–975, 2010. doi: 10.1007/s00382-009-0632-6.

A. de la Camara, A. M. Mancho, K. Ide, E. Serrano, and C. R. Mechoso. Routes of Transport across the Antarctic Polar Vortex in the Southern Spring. *Journal of the Atmospheric Sciences*, 69(2):741–752, 2012. doi: 10.1175/JAS-D-11-0142.1.

A. de la Camara, C. R. Mechoso, A. M. Mancho, E. Serrano, and K. Ide. Isentropic Transport within the Antarctic Polar-Night Vortex: Rossby Wave Breaking Evidence and Lagrangian Structures. *Journal of the Atmospheric Sciences*, 70 (9):2982–3001, 2013. doi: 10.1175/JAS-D-12-0274.1.

D. P. Dee, S. M. Uppala, A. J. Simmons, P. Berrisford, P. Poli, S. Hobayashi, U. Andrae, M. A. Balmaseda, G. Balsamo, P. Bauer, P. Bechtold, A. C. M. Beljaars, L. van de Berg, J. Bidlot, N. Bormann, C. Delsol, R. Dragani, M. Fuentes, A. J. Geer, L. Haimberger, S. B. Healey, H. Hersbach, E. V. Hólm, L. Isaksen, P. Kållberg, M. Köhler, M. Matricardi, A. P. McNally, B. M. Monge-Sanz, J.-J. Morcrette, B.-K. Parl, C. Paubey, P. de Rosnay, C. Tavolato, J.-N. Thépaut, and F. Vitart. The ERA-Interim reanalysis: configuration and performance of the data assimilation system. *Quarterly Journal of the Royal Meteorological Society*, 137:553–597, 2011. doi: 10.1002/qj.828.

G. M. B. Dobson. Origin and distribution of the polyatomic molecules in the atmosphere. *Proceedings of the Royal Society of London Series A-Mathematical and Physical Sciences*, 236(1205):187–193, 1956.

T. Dunkerton. On the Mean Meridional Mass Motions of the Stratosphere and Mesosphere. *Journal of the Atmospheric Sciences*, 35(12):2325–2333, 1978. doi: 10.1175/1520-0469(1978)035¡2325:OTMMMM¿2.0.CO;2.

S. D. Eckermann, K. W. Hoppel, L. Coy, J. P. McCormack, D. E. Siskind, K. Nielsen, A. Kochenash, M. J. Stevens, C. R. Englert, W. Singer, and M. Hervig. High-altitude data assimilation system experiments for the northern summer mesosphere season of 2007. *Journal of Atmospheric and Solar-Terrestrial Physics*, 71(3-4 SI):531–551, 2008. doi: 10.1016/j.jastp.2008.09.036.

L. El Amraoui, N. Semane, V. H. Peuch, and M. L. Santee. Investigation of dynamical processes in the polar stratospheric vortex during the unusually cold winter 2004/2005. *Geophysical Research Letters*, 35(3):L03803, 2008. doi: 10.1029/2007GL031251.

A. Engel, T. Möbius, H.-P. Haase, H. Bönisch, T. Wetter, U. Schmidt, I. Levin, T. Reddnamm, H. Oelhaf, G. Wetzel, K. Grunow, N. Huret, and M. Pirre. Observation of mesospheric air inside the arctic stratospheric polar vortex in early 2003. *Atmospheric Chemistry and Physics*, 6:267–282, 2006.

D. W. Fahey, S. Solomon, S. R. Kawa, M. Loewenstein, J. R. Podolske, S. E. Strahan, and K. R. Chan. A diagnostic for denitrification in the winter polar stratospheres. *Nature*, 345(6277):698–702, 1990. doi: 10.1038/345698a0.

M. J. Filipiak, R. S. Harwood, J. H. Jiang, Q. B. Li, N. J. Livesey, G. L. Manney, W. G. Read, M. J. Schwartz, J. W. Waters, and D. L. Wu. Carbon monox-

ide measured by the EOS Microwave Limb Sounder on Aura: First results. *Geophysical Research Letters*, 32:L14825, 2005. doi: 10.1029/2005GL022765.

H. Fischer, M. Birk, C. Blom, B. Carli, M. Carlotti, T. von Clarmann, L. Delbouille, A. Dudhia, D. Ehhalt, M. Endemann, J. M. Flaud, R. Gessner, A. Kleinert, R. Koopman, J. Langen, M. López-Puertas, P. Mosner, H. Nett, H. Oelhaf, G. Perron, J. Remedios, M. Ridolfi, G. Stiller, and R. Zander. MIPAS: an instrument for atmospheric and climate research. *Atmospheric Chemistry and Physics*, 8(8):2151–2188, 2008.

M. Fisher and A. O'Neill. Rapid descent of mesospheric air into the stratospheric polar vortex. *Geophysical Research Letters*, 20(12):1267–1270, 1993. doi: 10.1029/93GL01104.

E. L. Fleming, S. Chandra, J. J. Barnett, and M. Corney. Chapter 2: Zonal mean temperature, pressure, zonal wind and geopotential height as functions of latitude. *Advances in Space Research*, 10(12):(12)11–(12)59, 1990. doi: 10.1016/0273-1177(90)90386-E.

T. Flury, K. Hocke, A. Haefele, N. Kämpfer, and R. Lehmann. Ozone depletion, water vapor increase, and PSC generation at midlatitudes by the 2008 major stratospheric warming. *Journal of Geophysical Research - Atmospheres*, 114 (D18302), 2009. doi: 10.1029/2009JD011940.

J. A France and V. L. Harvey. A climatology of the stratopause in WACCM and the zonally asymmetric elevated stratopause. *Journal of Geophysical Research - Atmospheres*, 118(5):2241–2254, 2013. doi: 10.1002/jgrd.50218.

B. Funke, M. García-Comas, M. López-Puertas, N. Glatthor, G. P. Stiller, T. von Clarmann, K. Semeniuk, and J. C. McConnell. Enhancement of N_2O during the October-November 2003 solor proton events. *Atmospheric Chemistry and Physics*, 8(14):3805–3815, 2008.

B. Funke, M. López-Puertas, M. García-Comas, G. P. Stiller, T. von Clarmann, M. Höpfner, N. Glatthor, U. Grabowski, S. Kellmann, and A. Linden. Carbon monoxide distributions from the upper troposphere to the mesosphere inferred from 4.7 μm non-local thermal equilibrium emissions measures by MIPAS on Envisat. *Atmospheric Chemistry and Physics*, 9(7):2387–2411, 2009.

H. Garny, G. E. Bodeker, and M. Dameris. Trends and variability in stratospheric mixing: 1979-2005. *Atmospheric Chemistry and Physics*, 7(21):5611–5624, 2007.

J. Gille and L. Gray. High Resolution Dynamics Limb Sounder Earth Observing System (EOS) data description and quality version 7 (v7) (HIRDLS version 7.00.00) June 2013. Technical report, NASA, 2013. 82 pp, available from http://gmao.gsfc.nasa.gov/pubs/office_notes.

N. Glatthor, T. von Clarmann, H. Fischer, B. Funke, U. Grabowski, M. Höpfner, S. Kellmann, M. Kiefer, A. Londen, M. Milz, T. Steck, G. P. Stiller, G. Mengistu Tsidu, and D.-Y. Wang. Mixing Processes during the Antarctic Vortex Split in September-October 2002 as Inferred from Source Gas and Ozone Distributions from ENVISAT-MIPAS. *Journal of the Atmospheric Sciences*, 62(3):787–800, 2005. doi: 10.1175/JAS-3332.1.

J. B Greenblatt, H-J. Jost, M. Loewenstein, J. R. Podolske, T. P Bui, D. F. Hurst, J. W. Elkins, R. L. Herman, C. R. Webster, S. M. Schauffler, E. L. Atlas, P. A. Newman, L. R. Lait, M. Müller, A. Engel, and U. Schmidt. Defining the polar vortex edge from an N_2O:potential temperature correlation. *Journal of Geophysical Research - Atmospheres*, 107(D20):8268, 2002a. doi: 10.1029/2001JD000575.

J. B Greenblatt, H-J. Jost, M. Loewenstein, J. R. Podolske, D. F. Hurst, J. W. Elkins, S. M. Schauffler, E. L. Atlas, R. L. Herman, C. R. Webster, T. P Bui, R. L. Moore, E. R. Ray, S. Oltmans, H. Vömel, J-F. Blavier, B. Sen, R. A. Stachnik, G. C. Toon, A. Engel, M. Müller, U. Schmidt, H. Bremer, R. B. Pierce, B-M. Sinnhuber, M. Chippperfield, and F. Lefèvre. Tracer-based determination of vortex descent in the 1999/2000 Arctic winter. *Journal of Geophysical Research - Atmospheres*, 107(D20):8279, 2002b. doi: 10.1029/2001JD000937.

J. U. Grooß, R. Müller, P. Konopka, A. Engel, T. Möbius, and C. M. Volk. The impact of transport across the polar vortex edge on Match ozone loss estimates. *Atmospheric Chemistry and Physics*, 8(3):565–578, 2008.

G. Haller. Lagrangian Coherent Structures. *Annual Review of Fluid Mechanics*, 47:137–162, 2015. doi: 10.1146/annurev-fluid-010313-141322.

A. Hannachi, D. Mitchell, L. Gray, and A. Charlton-Perez. On the Use of Geometric Moments to Examine the Continuum of Sudden Stratospheric Warmings. *Journal of the Atmospheric Sciences*, 68(3):657–674, 2011. doi: 10.1175/2010JAS3585.1.

V. Lynn Harvey, R. B. Pierce, T. B. Fairlie, and T. D. Hitchman. A climatology of stratospheric polar vortices and anticyclones. *Journal of Geophysical Research - Atmospheres*, 107(D20):4442, 2002. doi: 10.1029/2001JD001471.

V. Lynn Harvey, C. E. Randall, G. L. Manney, and C. S. Singleton. Low-ozone pockets observed by EOS-MLS. *Journal of Geophysical Research - Atmospheres*, 113(D17):D17112, 2008. doi: 10.1029/2007JD009181.

V. Lynn Harvey, C. E. Randall, and M. H. Hitchman. Breakdown of potential vorticity based equivalent latitude as a vortex-centered coordinate in the polar winter mesosphere. *Journal of Geophysical Research - Atmospheres*, 114: D22105, 2009. doi: 10.1029/2009JD012681.

V. Lynn Harvey, C. E. Randall, and R. L. Collins. Chemical definition of the mesospheric polar vortex. *Journal of Geophysical Research - Atmospheres*, 120 (19), 2015. doi: 10.1002/2015JD023488.

A. Hauchecorne, S. Godin, M. Marchand, B. Heese, and C. Souprayen. Quantification of the transport of chemical constituents from the polar vortex to midlatitudes in the lower stratosphere using the high-resolution advection model MIMOSA and effective diffusivity. *Journal of Geophysical Research - Atmospheres*, 107(D20):8289, 2002. doi: 10.1029/2001JD000491.

P. Haynes and E. Shuckburgh. Effective diffusivity as a diagnostic of atmospheric transport 1. Stratosphere. *Journal of Geophysical Research-Atmospheres*, 105 (D18):22777–22794, 2000. doi: 10.1029/2000JD900093.

P. H. Haynes and M. E. McIntyre. On the Evolution of Vorticity and Potential Vorticity in the Presence of Diabatic Heating and Frictional or Other Forces. *Journal of the Atmospheric Sciences*, 44(5):828–841, 1987. doi: 10.1175/1520-0469(1987)044<0828:OTEOVA>2.0.CO;2.

A. Hertzog, P. Cocquerez, C. Basdevant, G. Boccara, J. Bordereau, B. Brioit, A. Cardonne, R. Guilbon, A. Ravissot, E. Schmitt, J-N. Valdivia, S. Venel, and F. Vial. Stratéole/Vorcore - Long-duration, Superpressure Balloons to

Study the Antarctic Lower Stratosphere during the 2005 Winter. *Journal of Atmospheric and Oceanic Technology*, 24(12):2048–2061, 2007.

M. H. Hitchman, J. C. Gille, C. D. Rodgers, and G. Brasseur. The Separated Polar Winter Stratopause: A Gravity Wave Driven Climatological Feature. *Journal of the Atmospheric Sciences*, 46(3):410–422, 1989. doi: 10.1175/1520-0469(1989)046¡0410:TSPWSA¿2.0.CO;2.

J. R. Holton. *An introduction to dynamic meteorology, 3rd edition*. International geophysics series; v.48. San Diego: Academic Press, 1992.

J. R. Holton, P. H. Haynes, M. E. McIntyre, A. R. Douglass, R. B. Rood, and L. Pfister. Stratosphere-troposphere exchange. *Reviews of Geophysics*, 33(4): 403–439, 1995. doi: 10.1029/95RG02097.

L. L. Hood and B. E. Soukharev. Interannual Variations of Total Ozone at Northern Midlatitudes Correlated with Stratospheric EP Flux and Potential Vorticity. *Journal of the Atmospheric Sciences*, 62(10):3724–3740, 2005. doi: 10.1175/JAS3559.1.

K. W. Hoppel, N. L. Baker, L. Coy, S. D. Eckermann, J. P. McCormack, G. E. Nedoluha, and E. Siskind. Assimilation of stratospheric and mesospheric temperatures from MLS and SABER into a global NWP model. *Atmospheric Chemistry and Physics*, 8(20):6103–6116, 2008.

Y. Hu and R. T. Pierrehumbert. The Advection-Diffusion Problem for Stratospheric Flow. Part I: Concentration Probability Distribution Function. *Journal of the Atmospheric Sciences*, 58(12):1493–1510, 2001. doi: 10.1175/1520-0469(2001)058¡1493:TADPFS¿2.0.CO;2.

P. E. Huck, A. J. McDonald, G. E. Bodeker, and H. Struthers. Interannual variability in Antarctic ozone depletion controlled by planetary waves and polar temperature. *Geophysical Research Letters*, 32(13):L13819, 2005. doi: 10.1029/2005GL022943.

R. Hughes and P. Bernath. ACE Mission Information for Public Data Release. Technical report, Atmospheric Chemistry Experiment Science Operations Center, Department of Chemistry, University of Waterloo, 2012. Document Number ACE-SOC 0025, available from http://www.ace.uwaterloo.ca/public.html.

K. Ide, D. Small, and S. Wiggins. Distinguished hyperbolic trajectories in time-dependent fluid flows: analytical and computational approach for velocity fields defined as data sets. *Nonlinear Processes in Geophysics*, 9(3-4):237–263, 2002.

C. H. Jackman, M. C. Cerniglia, J. E. Nielsen, D. J. Allen, J. M. Zawodny, R. D. McPeters, A. R. Douglass, J. E. Rosenfield, and R. B. Rood. Two-dimensional and three-dimensional model simulations, measurements, and interpretation of the influence of the October 1989 solar proton events on the middle atmosphere. *Journal of Geophysical Research*, 100(D6):11641–11660, 1995.

C. H. Jackman, Richard D. McPeters, Gordon J. Labow, E. L. Fleming, C. J. Praderas, and J. M. Russell. Northern Hemisphere atmospheric effects due to the July 2000 solar proton event. *Geophysical Research Letters*, 28(15): 2883–2886, 2001.

C. H. Jackman, D. R. Marsh, F. M. Vitt, R. R. Garcia, C. E. Randall, E. L. Fleming, and S. M. Frith. Long-term middle atmospheric influence of very large solar proton events. *Journal of Geophysical Research-Atmospheres*, 114, 2009.

C. H. Jackman, D. R. Marsh, F. M. Vitt, R. G. Roble, C. E. Randall, P. E. Bernath, B. Funke, S. Versick, G. P. Stiller, A. J. Tyler, and E. L. Fleming. Northern Hemisphere atmospheric influence of the solar proton events and ground level enhancement in January 2005. *Atmospheric Chemistry and Physics*, 11:6153–6166, 2011.

J. A. Jimenez Madrid and A. M. Mancho. Distinguished trajectories in time dependent vector fields. *Chaos*, 19:013111, 2009. doi: 10.1063/1.3056050.

J. J. Jin, K. Semeniuk, S. R. Beagley, V. I. Fomichev, A. I. Jonsson, J. C. McConnel, J. Urban, D. Murtagh, G. L. Manney, C. D. Boone, P. F. Bernath, K. A. Walker, B. Batter, P. Ricaud, and E. Dupuy. Comparison of CMAM simulations of carbon monoxide (CO), nitrous oxide (N_2O), and methane (CH_4) with observations from Odin/SMR, ACE-FTS, and Aura/MLS. *Atmospheric Chemistry and Physics*, 9(10):3233–3252, 2009. doi: 10.5194/acp-9-3233-2009.

B. Joseph and B. Legras. Relation between Kinematic Boundaries, Stirring, and Barriers for the Antarctic Polar Vortex. *Journal of the Atmospheric Sciences*, 59(7):1198–1212, 2002. doi: 10.1175/1520-0469(2002)059<1198:RBKBSA>2.0.CO;2.

M. N. Juckes and M. E. McIntyre. A high-resolution one-layer model of breaking planetary waves in the stratosphere. *Nature*, 328(6131):590–596, 1987. doi: 10.1038/328590a0.

N. Kawamoto, H. Kanzawa, and M. Shiotani. Time variations of descent in the Antarctic vortex during the early winter of 1997. *Journal of Geophysical Research-Atmospheres*, 109(D18):D18309, 2004. doi: 10.1029/2004JD004650.

K. K. Kelly, A. F. Tuck, D. M. Murphy, M. H. Profitt, D. W. Fahey, R. L. Jones, D. S. McKenna, M. Loewenstein, J. R. Podolske, S. E. Strahan, G. V. Ferry, K. R. Chan, J. F. Vedder, G. L. Gregory, W. D. Hypes, M. P. McCormick, E. V. Browell, and L. E. Heidt. Dehydration in the lower Antarctic stratosphere during late winter and early spring, 1987. *Journal of Geophysical Research-Atmospheres*, 94(D9):11317–11357, 2009. doi: 10.1029/JD094iD09p11317.

G. Kishore Kumar, K. Kishore Kumar, G. Baumgarten, and G. Bamkumar. Validation of MERRA reanalysis upper-level winds over low latitudes with independent rocket sounding data. *Journal of Atmospheric and Solar-Terrestrial Physics*, 123:48–54, 2014. doi: 10.1016/j.jastp.2014.12.001.

A. R. Klekociuk, M. B. Tully, S. P. Alexander, R. J. Dargaville, L. L. Deschamps, P. J. Fraser, H. P. Gies, S. I. Henderson, J. Javorniczky, P. B. Krummel, S. V. Petelina, J. D. Shanklin, J. M. Siddaway, and K. A. Stone. The Antarctic ozone hole during 2010. *Australian Meteorological and Oceanographic Journal*, 61(4):253–267, 2011.

S. Kobayashi, M. Matricardi, D. Dee, and S. Uppala. Toward a consistent reanalysis of the upper stratosphere based on radiance measurements from SSU and AMSU-A. *Quarterly Journal of the Royal Meteorological Society*, 135(645): 2086–2099, 2009. doi: 10.1002/qj.514.

S. Kobayashi, Y. Ota, Y. Harada, A. Ebita, M. Moriya, H. Onoda, K. Onogi, H. Kamahori, C. Kobayashi, H. Endo, K. Miyaoka, and K. Takahashi. The JRA-55 Reanalysis: General Specifications and Basic Characteristics. *Journal of the Meteorological Society of Japan*, 93(1):5–48, 2015. doi: 10.2151/jmsj.2015-001.

N. C. Krützmann, A. J. McDonald, and S. E. George. Identification of mixing barriers in chemistry-climate model simulations using Rényi entropy. *Geophysical Research Letters*, 35:L06806, 2008. doi: 10.1029/2007GL032829.

J. Kuttippurath and G. Nikulin. A comparative study of the major sudden stratospheric warmings in the Arctic winters 2003/2004-2009/2010. *Atmospheric Chemistry and Physics*, 12(17):8115–8129, 2012. doi: 10.5194/acp-12-8115-2012.

K. Labitzke. The Interaction Between Stratosphere and Mesosphere in Winter. *Journal of the Atmospheric Sciences*, 29(7):1395–&, 1972. doi: 10.1175/1520-0469(1972)029¡1395:TIBSAM¿2.0.CO;2.

K. Labitzke and M. Kunze. On the remarkable Arctic winter in 2008/2009. *Journal of Geophysical Research-Atmospheres*, 114:D00I02, 2009. doi: 10.1029/2009JD012273.

A. Lambert, W. G. Read, N. J. Livesey, M. L. Santee, G. L. Manney, L. Froidevaux, D. L. Wu, M. J. Schwartz, H. C. Pumphrey, C. Jimenez, G. E. Nedoluha, R. E. Cofield, D. T. Cuddy, W. H. Daffer, B. J. Drouin, R. A. Fuller, R. F. Jarnot, B. W. Knosp, H. M. Pickett, V. S. Perun, W. V. Snyder, P. C. Stek, R. P. Thurstans, P. A. Wagner, J. W. Waters, K. W. Jucks, G. C. Toon, R. A. Stachnik, P. F. Bernath, C. D. Boone, K. A. Walker, J. Urban, D. Murtagh, J. W. Elkins, and E. Atlas. Validation of the Aura Microwave Limb Sounder middle atmosphere water vapor and nitrous oxide measurements. *Journal of Geophysical Research-Atmospheres*, 112(D24):24, 2007. doi: 10.1029/2007jd008724.

A. Le Pichon, J. D. Assink, P. Heinrich, E. Blanc, A. Charlton-Perez, C. F. Lee, P. Keckhut, A. Hauchecorne, R. Rüfenacht, N. Kämpfer, D. P. Drob, P. S. M. Smets, L. G. Evers, L. Ceranna, C. Pilger, O. Ross, and C. Claud. Comparison of co-located independent ground-based middle atmospheric wind and temperature measurements with numerical weather prediction models. *Journal of Geophysical Research - Atmospheres*, 120(16):8318–8331, 2015. doi: 10.1002/2015JD023273.

A. M. Lee, H. K. Roscoe, A. E. Jones, P. H. Haynes, E. F. Shuckburgh, M. W. Morrey, and H. C. Pumphrey. The impact of the mixing properties within the Antactic stratospheric vortex on ozone loss in spring. *Journal of Geophysical Research-Atmospheres*, 106(D3):3203–3211, 2001. doi: 10.1029/2000JD900398.

J. N. Lee, D. L. Wu, G. L. Manney, M. J. Schwartz, A. Lambert, N. J. Livesey, K. R. Minschwaner, H. C. Pumphrey, and W. G. Read. Aura Microwave Limb

Sounder observations of the polar middle atmosphere: Dynamics and transport of CO and H_2O. *Journal of Geophysical Research-Atmospheres*, 116:D05110, 2011. doi: 10.1029/2010JD014608.

V. Limpusavan, D. L. Wu, M. J. Schwartz, J. W. Waters, Q. Wu, and T. L. Killeen. The two-day wave in EOS MLS temperature and wind measurements during 2004-2005 winter. *Geophysical Research Letters*, 32(17):L17809, 2005. doi: 10.1029/2005GL023396.

N. J. Livesey, W. G. Read, L. Froidevaux, A. Lambert, G. L. Manney, H. C. Pumphrey, M. L. Santee, M. J. Schwartz, S. Wang, R. E. Cofeld, D. T. Cuddy, R. A. Fuller, R. F. Jarnot, J. H. Jiang, B. W. Knosp, P. C. Stek, P. A. Wagner, and D. L. Wu. Earth Observing System (EOS) Aura Microwave Limb Sounder (MLS) Version 3.3 Level 2 data quality and description document. Technical report, NASA, 2011.

N. J. Livesey, W. G. Read, P. A. Wagner, L. Froidevaux, A. Lambert, G. L. Manney, L. F. Millán Valle, H. C. Pumphrey, M. L. Santee, M. J. Schwartz, S. Wang, R. A. Fuller, R. F. Jarnot, B. W. Knosp, and E. Martinez. Earth Observing System (EOS) Aura Microwave Limb Sounder (MLS) Version 4.2x Level 2 data quality and description document. Technical report, NASA, 2015.

R. Lucchesi. File Specification for MERRA Products. GMAO Office Note No. 1 (Version 2.3). Technical report, NASA, 2012. 82 pp, available from http://gmao.gsfc.nasa.gov/pubs/office_notes.

Amanda H. Lynch and John J. Cassano. *Applied Atmospheric Dynamics*. John Wiley & Sons, Ltd, 2006.

A. M. Mancho, S. Wiggins, J. Curbelo, and C. Mendoza. Lagrangian descriptors: A method for revealing phase space structures of general time dependent dynamical systems. *Communications in Nonlinear Science and Numerical Simulation*, 18(12):3530–3557, 2013. doi: 10.1016/j.cnsns.2013.05.002.

G. L. Manney, R. W. Zurek, M. E. Gelman, A. J. Miller, and R. Nagatani. The anomalous Arctic lower stratospheric polar vortex of 1992-1993. *Geophysical Research Letters*, 21(22):2405–2408, 1994a. doi: 10.1029/94GL02368.

G. L. Manney, R. W. Zurek, A. O'Neill, and R. Swinbank. On the Motion of Air through the Stratospheric Polar Vortex. *Journal of the*

Atmospheric Sciences, 51(20):24973–2994, 1994b. doi: 10.1175/1520-0469(1994)051¡2973:OTMOAT¿2.0.CO;2.

G. L. Manney, D. R. Allen, K. Krüger, B. Naujokat, M. L. Santee, J. L. Sabutis, S. Pawson, R. Swinbank, C. E. Randall, A. J. Simmons, and C. Long. Diagnostic Comparison of Meteorological Analyses during the 2002 Antarctic Winter. *Monthly Weather Review*, 133(5):1261–1278, 2005a. doi: 10.1175/MWR2926.1.

G. L. Manney, K. Kruger, J. Sabutis, S. A. Sena, and S. Pawson. The remarkable 2003-2004 winter and other recent warm winters in the Arctic stratosphere since the late 1990s. *Journal of Geophysical Research - Atmospheres*, 110:D04107, 2005b.

G. L. Manney, W. H. Daffer, J. M. Zawodny, P. F. Bernath, K. W. Hoppel, K. A. Walker, B. W. Knosp, C. Boone, E. E. Remsberg, M. L. Santee, V. L. Harvey, S. Pawson, D. R. Jackson, L. Deaver, C. T. McElroy, C. A. McLinden, J. R. Drummond, H. C. Pumphrey, A. Lambert, M. J. Schwartz, L. Froidevaux, S. McLeod, L. L. Takacs, M. J. Suarez, C. R. Trepte, D. C. Cuddy, N. J. Livesey, R. S. Harwood, and J. W. Waters. Solar occulatation satellite data and derived meterological products: Sampling issues and comparisons with Aura Microwave Limb Sounder. *Journal of Geophysical Research - Atmospheres*, 112 (D24):D24S50, 2007. doi: 10.1029/2007JD008709.

G. L. Manney, W. H. Daffer, K. B. Strawbridge, K. A. Walker, C. D. Boone, P. F. Bernath, T. Kerzenmacher, M. J. Schwartz, K. Strong, R. J. Sica, K. Krüger, H. C. Pumphrey, A. Lambert, M. L. Santee, N. J. Livesey, E. E. Remsberg, M. G. Mlynczak, and J. R. Russell III. The high Arctic in extreme winters: vortex, temperature, and MLS and ACE-FTS trace gas evolution. *Atmospheric Chemistry and Physics*, 8(3):505–522, 2008a.

G. L. Manney, K. Krüger, S. Pawson, K. Minschwaner, M. J. Schwartz, W. H. Daffer, N. J. Livesey, M. G. Mlynczak, E. E. Remsberg, J. M. Russell, and J. W. Waters. The evolution of the stratopause during the 2006 major warming: Satellite data and assimilated meteorological analyses. *Journal of Geophysical Research - Atmospheres*, D113:D11115, 2008b. doi: 10.1029/2007JD009097.

G. L. Manney, R. S. Harwood, I. A. MacKenzie, K. Minschwaner, D. R. Allen, M. L. Santee, K. A. Walker, M. I. Hegglin, A. Lambert, H. C. Pumphrey, P. F. Bernath, C. D. Boone, M. J. Scwartz, N. J. Livesey, W. H. Daffer, and

R. A. Fuller. Satellite observations and modeling of transport in the upper troposphere through the lower mesosphere during the 2006 major stratospheric sudden warming. *Atmospheric Chemistry and Physics*, 9(14):4775–4795, 2009a. doi: 10.5194/acp-9-4775-2009.

G. L. Manney, M. J. Schwartz, K. Kruger, M. L. Santee, S. Pawson, J. N. Lee, W. H. Daffer, R. A. Fuller, and N. J. Livesey. Aura Microwave Limb Sounder observations of dynamics and transport during the record-breaking 2009 Arctic stratospheric major warming. *Geophysical Research Letters*, 36, 2009b. doi: 10.1029/2009GL038586.

G. L. Manney, M. L. Santee, M. Rex, N. J. Livesey, M. C. Pitts, P. Veefkind, E. R. Nash, I. Wohltmann, R. Lehmann, L. Froidvaux, L. R. Poole, M. R. Schoeberl, D. P. Haffner, J. Davies, V. Dorokhov, H. Gernandt, B. Johnson, R. Kivi, E. Kyrö, N. Larsen, P. F. Levelt, A. Makshtas, C. T. McElroy, H. Nakajima, M. C. Parrondo, D. W. Tarasick, P. von der Gathen, K. A. Walker, and N. S. Zinoviev. Unprecedented Arctic ozone loss in 2011. *Nature*, 478(7370):469–U–65, 2011. doi: 10.1038/nature10556.

A. Mariotti, C. R. Mechoso, B. Legras, and V. Daniel. The Evolution of the Ozone "Collar" in the Antarctic Lower Stratosphere during Early August 1994. *Journal of the Atmospheric Sciences*, 57(3):402–414, 2000. doi: 10.1175/1520-0469(2000)057¡0402:TEOTOC¿2.0.CO;2.

Taroh Matsuno. A Dynamical Model of the Stratospheric Sudden Warming. *Journal of the Atmospheric Sciences*, 28(8):1479–1494, 1971. doi: 10.1175/1520-0469(1971)028<1479:ADMOTS>2.0.CO;2.

N. J. Matthewman, J. G. Esler, A. J. Charlton-Perez, and L. M. Polvani. A New Look at Stratospheric Sudden Warmings. Part III: Polar Vortex Evolution and Vertical Structure. *Journal of Climate*, 22(6):1566–1585, 2009. doi: 10.1175/2008JCLI2365.1.

A. J. McDonald and M. Smith. A technique to identify vortex air using carbon monoxide observations. *Journal of Geophysical Research - Atmospheres*, 118 (D22):12719–12733, 2013. doi: 10.1002/2012JD019257.

A. J. McDonald, S. E. George, and R. M. Woollands. Can gravity waves significantly impact PSC occurrence in the Antarctic? *Atmospheric Chemistry and Physics*, 9(22):8825–8840, 2009.

A. J. McDonald, R. E. Hibbins, and M. J. Jarvis. Properties of the quasi 16 day wave derived from EOS MLS observations. *Journal of Geophysical Research - Atmospheres*, 116:D06112, 2011. doi: 10.1029/2010JD014719.

R. McInturff. Stratospheric warmings: Synoptic, dynamic and general-circulation aspects. Technical report, NASA, National Meteorological Center., Washington, D. C., 1978. NASA Reference Publication NASA-RP-1017.

M. E. McIntyre and T. N. Palmer. Breaking planetary waves in the stratosphere. *Nature*, 305(5935):593–600, 1983. doi: 10.1038/305593a0.

M. E. McIntyre and T. N. Palmer. The surf zone in the stratosphere. *Journal of Atmospheric and Terrestrial Physics*, 46(9):825–849, 1984. doi: 10.1016/0021-9169(84)90063-1.

D. S. McKenna, J. U. Grooß, G. Gunther, P. Konopka, R. Muller, G. Carver, and Y. Sasano. A new Chemical Lagrangian Model of the Stratosphere (CLaMS) - 2. Formulation of chemistry scheme and initialization. *Journal of Geophysical Research - Atmospheres*, 107(D15):4256, 2002. doi: 10.1029/2000JD000113.

C. Mendoza and A. M. Mancho. Hidden geometry of ocean flows. *Physical Review Letters*, 105(3):038501, 2010. doi: 10.1103/PhysRevLett.105.038501.

C. Mendoza and A. M. Mancho. The Lagrangian description of aperiodic flows: a case study of the Kuroshio Current. *Nonlinear Processes in Geophysics*, 19 (4):449–472, 2012. doi: 10.5194/npg-19-449-2012.

H. A. Michelsen, G. L. Manney, M. R. Gunson, C. P. Rinsland, and R. Zander. Correlations of stratospheric abundances of CH_4 and N_2O derived from ATMOS measurements. *Geophysical Research Letters*, 25(15):2777–2780, 1998. doi: 10.1029/98GL01977.

K. Minschwaner, G. L. Manney, N. J. Livesey, H. C. Pumphrey, H. M. Pickett, L. Froidevaux, A. Lambert, M. J. Schwartz, P. F. Bernath, K. A. Walker, and C. D. Boone. The photochemistry of carbon monoxide in the stratosphere and mesosphere evaluated from observations by the Microwave Limb Sounder on the Aura satellite. *Journal of Geophysical Research - Atmospheres*, 115 (D13303), 2010. doi: 10.1029/2009JD012654.

D. M. Mitchell, A. J. Charlton-Perez, and L. J. Gray. Characterizing the Variability and Extremes of the Stratospheric Polar Vortices Using 2D Moment

Analysis. *Journal of the Atmospheric Sciences*, 68(6):1194–1213, 2010. doi: 10.1175/2010JAS3555.1.

D. M. Mitchell, L. J. Gray, J. Anstey, M. P. Baldwin, and A. J. Charlton-Perez. The Influence of Stratospheric Vortex Displacements and Splits on Surface Climate. *Journal of Climate*, 26(8):2668–2682, 2013. doi: 10.1175/JCLI-D-12-00030.1.

A. Molod, L. Takacs, M. Suarez, and J. Bacmeister. Development of the GEOS-5 atmospheric general circulation model: evolution from MERRA to MERRA2. *Geoscientific Model Development*, 8(5):1339–1356, 2015. doi: 10.5194/gmd-8-1339-2015.

O. Morgenstern, J. A. Pyle, A. M. Iwi, W. A. Norton, J. W. Elkins, D. F. Hurst, and P. A. Romashkin. Diagnosis of mixing between middle latitudes and the polar vortex from tracer-tracer correlations. *Journal of Geophysical Research - Atmospheres*, 107(D17):4321, 2002. doi: 10.1029/2001JD001224.

G. A. Morris, M. R. Schoeberl, L. C. Sparling, P. A. Newman, L. R. Lait, L. Elson, J. Waters, R. A. Suttie, A. Roche, J. Humer, and J. M. Russell III. Trajectory mapping and applications to data from the Upper Atmosphere Research Satellite. *Journal of Geophysical Research - Atmospheres*, 100(D8):16491–16505, 1995. doi: 10.1029/95JD01072.

G. A. Morris, J. F. Gleason, J. Ziemke, and M. R. Schoeberl. Trajectory mapping: A tool for validation of trace gas observations. *Journal of Geophysical Research - Atmospheres*, 105(D14):17875–17894, 2000. doi: 10.1029/1999JD901118.

G. A. Morris, J. F. Gleason, J. M. Russell III, M. R. Schoeberl, and M. Patrick. McCormick. A comparison of HALOE V19 with SAGE II V6.00 ozone observations using trajectory mapping. *Journal of Geophysical Research - Atmospheres*, 107(D13):4177, 2002. doi: 10.1029/2001JD000847.

R. Müller and G. Günther. A Generalized Form of Lait's Modified Potential Vorticity. *Journal of the Atmospheric Sciences*, 60(17):2229–2237, 2003. doi: 10.1175/1520-0469(2003)060¡2229:AGFOLM¿2.0.CO;2.

D. Murtagh, U. Frisk, F. Merino, M. Ridal, A. Jonsson, J. Stegman, G. Witt, P. Eriksson, C. Jiménez, G. Megie, J. de la Noë, P. Ricaud, P. Baron, J. R. Pardo, A. Hauchcorne, E. J. Llewellyn, D. A. Degenstein, R. L. Gattinger,

N. D. Lloyd, W. F. J. Evans, I. C. McDade, C. S. Haley, C. Sioris, C. von Savigny, B. H. Solheim, J. C. McConnell, K. Strong, E. H. Richardson, G. W. Leppelmeier, E. Kyrölä, H. Auvinen, and L. Oikarinen. An overview of the Odin atmospheric mission. *Canadian Journal of Physics*, 80(4):309–319, 2002. doi: 10.1139/P01-157.

N. Nakamura. Two-dimensional mixing, edge formation, and permeability diagnosed in an area coordinate. *Journal of the Atmospheric Sciences*, 53(11):1524–1537, 1996. doi: 10.1175/1520-0469(1996)053<1524:TDMEFA>2.0.CO;2.

N. Nakamura and J. Ma. Modified Lagrangian-mean diagnostics of the stratospheric polar vortices: 2. Nitrous oxide and seasonal barrier migration in the cryogenic limb array etalon spectrometer and SKYHI general circulation model. *Journal of Geophysical Research - Atmospheres*, 102(D22):25721–25735, 1997. doi: 10.1029/97JD02153.

E. R. Nash, P. A. Newman, J. E. Rosenfield, and M. R. Schoeberl. An objective determination of the polar vortex using Ertel's potential vorticity. *Journal of Geophysical Research - Atmospheres*, 101(D5):9471–9478, 1996. doi: 10.1029/96JD00066.

J. Nash and R. Saunders. A review of Stratospheric Sounding Unit radiance observations for climate trends and reanalyses. *Quarterly Journal of the Royal Meteorological Society*, 141(691):2103–2113, 2015. doi: 10.1002/qj.2505.

G. E. Nedoluha, R. M. Bevilacqua, M. D. Fromm, K. W. Hoppel, and D. R. Allen. POAM measurements of PSCs and water vapor in the 2002 Antarctic vortex. *Geophysical Research Letters*, 30(15):1796, 2003. doi: 10.1029/2003GL017577.

J. L. Neu, L. C. Sparling, and R. A. Plumb. Variability of the subtropical "edges" in the stratosphere. *Journal of Geophysical Research - Atmospheres*, 108(D15): 4482, 2003. doi: 10.1029/2002JD002706.

P. A. Newman and E. R. Nash. The Unusual Southern Hemisphere Stratosphere Winter of 2002. *Journal of the Atmospheric Sciences*, 62(3):614–628, 2005. doi: 10.1175/JAS-3323.1.

W. A. Norton. Breaking Rossby Waves in a Model Stratosphere Diagnosed by a Vortex-Following Coordinate System and a Technique for Advecting Material Contours. *Journal of the Atmospheric Sciences*, 51(4):654–673, 1994. doi: 10.1175/1520-0469(1994)051<0654:BRWIAM>2.0.CO;2.

J. Oberheide, G. A. Lehmacher, D. Offermann, K. U. Grossmann, A. H. Manson, C. E. Meek, F. J. Schmidlin, W. Singer, P. Hoffmann, and R. A. Vincent. Geostrophic wind fields in the stratosphere and mesosphere from satellite data. *Journal of Geophysical Research - Atmospheres*, 107(D23):8175, 2002. doi: 10.1029/2001JD000655.

M. J. Olascoaga, M. G. Brown, F. J. Beron-Vera, and H. Koçak. Stratospheric winds, transport barriers and the 2011 Arctic ozone hole. *Nonlinear Processes in Geophysics*, 19(6):687–692, 2012. doi: 10.5194/npg-19-687-2012.

A. O'Neill, W. L. Grose, V. D. Pope, H. Maclean, and R. Swinbank. Evolution of the Stratosphere during Northern Winter 1991/92 as Diagnosed from U.K. Meteorological Office Analyses. *Journal of the Atmospheric Sciences*, 51(20): 2800–2817, 1994. doi: 10.1175/1520-0469(1994)051¡2800:EOTSDN¿2.0.CO;2.

E. Palazzi, F. Fierli, G. P. Stiller, and J. Urban. Probability density functions of long-lived tracer observations from satellite in the subtropical barrier region: data intercomparison. *Atmospheric Chemistry and Physics*, 11(20): 10579–10598, 2012. doi: 10.5194/acp-11-10579-2011.

F. M. Palmeiro, D. Barriopedro, R. García-Herrara, and N. Calvo. Comparing Sudden Stratospheric Warming Definitions in Reanalysis Data. *Journal of Climate*, 28(17):6823–6840, 2015. doi: 10.1175/JCLI-D-15-0004.1.

L. L. Pan, W. J. Randel, B. L. Gary, M. J. Mahoney, and E. J. Hintsa. Definitions and sharpness of the extratropical tropopause: A trace gas perspective. *Journal of Geophysical Research-Atmospheres*, 109(D23):D23103, 2004. doi: 10.1029/2004JD004982.

L. L. Pan, K. P. Bowman, M. Shapiro, W. J. Randel, R. S. Gao, T. Campos, C. Davis, S. Schauffler, B. A. Ridley, J. C. Wei, and C. Barnet. Chemical behaviour of the tropopause observed during the Stratosphere-Troposphere Analyses of Regional Transport experiment. *Journal of Geophysical Research-Atmospheres*, 112(D18):D18110, 2007. doi: 10.1029/2007JD008645.

N. Patmore and R. Toumi. An entropy-based measure of mixing at the tropopause. *Quarterly Journal of the Royal Meteorological Society*, 132(619): 1949–1967, 2006. doi: 10.1256/qj.05.84.

N. M. Pedatella, K. Raeder, J. L. Anderson, and H.-L. Liu. Ensemble data assimilation in the Whole Atmosphere Community Climate Model. *Journal of Geophysical Research-Atmospheres*, 119(16):9779–9809, 2014. doi: 10.1002/2014JD021776.

R. B. Pierce, W. L. Grose, J. M. Russell III, and A. F. Tuck. Evolution of Southern Hemisphere spring air masses observed by HALOE. *Geophysical Research Letters*, 21(3):213–216, 1994. doi: 10.1029/93GL02997.

R. T. Pierrehumbert and H. Yang. Global chaotic mixing on isentropic surfaces. *Journal of the Atmospheric Sciences*, 50(15):2462–2480, 1993. doi: 10.1175/1520-0469(1993)050<2462:GCMOIS>2.0.CO;2.

R. A. Plumb. A "tropical pipe" model of stratopsheric transport. *Journal of Geophysical Research-Atmospheres*, 101(D2):3957–3972, 1996. doi: 10.1029/95JD03002.

R. A. Plumb. Stratospheric Transport. *Journal of the Meteorological Society of Japan*, 80(4B):793–803, 2002. doi: 10.2151/jmsj.80.793.

R. A. Plumb. Tracer interrelationships in the stratosphere. *Reviews of Geophysics*, 45(4):RG4005, 2007. doi: 10.1029/2005RG000179.

R. A. Plumb. Planetary Waves and the Extratropical Winter Stratosphere. In L. M. Polvani, A. H. Sobel, and D. W. Waugh, editors, *The Stratosphere: Dynamics, Transport, and Chemistry*. American Geophysical Union, Washington, D. C., 2010. doi: 10.1002/9781118666630.ch3.

R. A. Plumb and M. K. W. Ko. Interrelationships between mixing ratios of long-lived stratospheric constituents. *Journal of Geophysical Research-Atmospheres*, 97(D9):10145–10156, 1992.

R. A. Plumb, D. W. Waugh, and M. P. Chipperfield. The effects of mixing on tracer relationships in the polar vortices. *Journal of Geophysical Research-Atmospheres*, 105(D8):10047–10062, 2000. doi: 10.1029/1999JD901023.

R. A. Plumb, W. Heres, J. L. Neu, N. M. Mahowald, J. del Corral, G. C. Toon, E. Ray, F. Moore, and A. E. Andrews. Global tracer modeling during SOLVE: High-latitude descent and mixing. *Journal of Geophysical Research-Atmospheres*, 107:8309, 2002. doi: 10.1029/2001JD001023. [printed *108*(D5), 2003].

A. Podglajen, A. Hertzog, R. Plougonven, and N. Žagar. Assessment of the accuracy of (re)analyses in the equatorial lower stratosphere. *Journal of Geophysical Research-Atmospheres*, 119(19):11166–11188, 2014. doi: 10.1002/2014JD021849.

S. Polavarapu, S. Ren, Y. Rochon, D. Sankey, N. Ek, J. Koshyk, and D. Tarasick. Data assimilation with the Canadian middle atmosphere model. *Atmosphere-Ocean*, 43(1):77–100, 2005. doi: 10.3137/ao.430105.

H. C. Pumphrey, M. J. Filipiak, N. J. Livesey, M. J. Schwartz, C. Boone, K. A. Walker, P. Bernath, P. Ricaud, B. Barret, C. Clerbaux, R. F. Jarnot, G. L. Manney, and J. W. Waters. Validation of middle-atmosphere carbon monoxide retrievals from the Microwave Limb Sounder on Aura. *Journal of Geophysical Research-Atmospheres*, 112(D24):D24S38, doi:10.1029/2007JD008723, 2007.

F. Rabier, A. Bouchard, E. Brun, A. Doerenbecher, S. Guedj, V. Guidard, F. Karbou, V-H. Peuch, L. El Amraoui, D. Puech, C. Genthon, G. Picard, M. Town, A. Hertzog, F. Vial, P. Cocquerez, S. A. Cohn, T. Hock, J. Fox, H. Cole, D. Parsons, J. Powers, K. Romberg, J. VanAndel, T. Deshler, J. Mercer, J. S. Haase, L. Avallone, L. Kalnajs, C. R. Mechoso, A. Tangborn, A. Pellegrini, Y. Frenot, J-N. Thépaut, A. McNally, G. Balsamo, and P. Steinle. The Concordiasi Project in Antarctica. *Bulletin of the American Meteorological Society*, 91(1):69–+, 2010.

C. E. Randall, D. W. Rusch, R. M. Bevilacqua, K. W. Hoppel, and J. D. Lumpe. Polar Ozone and Aerosol Measurement (POAM) II stratospheric NO, 1993-1996. *Journal of Geophysical Research*, 103(D21):28361–28371, 1998.

C. E. Randall, D. E. Siskind, and R. M. Bevilacqua. Stratospheric NOx enhancements in the southern hemisphere vortex in winter/spring of 2000. *Geophysical Research Letters*, 28(12):2385–2388, 2001.

C. E. Randall, V. L. Harvey, C. S. Singleton, P. F. Bernath, C. D. Boone, and J. U. Kozyra. Enhanced NO_x in 2006 linked to strong upper stratospheric arctic vortex. *Geophysical Research Letters*, 33(18), 2006.

C. E. Randall, V. L. Harvey, C. S. Singleton, S. M. Bailey, P. F. Bernath, M. Codrescu, H. Nakajima, and J. M. Russell III. Energetic particle precipitation effects on the Southern Hemisphere stratosphere in 1992-2005. *Journal of Geophysical Research*, 112:D08308, 2007.

C. E. Randall, V. L. Harvey, D. E. Siskind, J. France, P. F. Bernath, C. D. Boone, and K. A. Walker. NO(x) descent in the Arctic middle atmosphere in early 2009. *Geophysical Research Letters*, 36, 2009. doi: 10.1029/2009GL039706.

W. J. Randel, F. Wu, J. M. Russell III, A. Riche, and J. W. Waters. Seasonal Cycles and QBO Variations in Stratospheric CH_4 and H_2O Observed UARS HALOE Data. *Journal of the Atmospheric Sciences*, 55(2):163–185, 1998. doi: 10.1175/1520-0469(1998)055¡0163:SCAQVI¿2.0.CO;2.

E. Remsberg, G. Lingenfelser, V. L. Harvey, W. Grose, J. Russell III, M. Mlynczak, L. Gordley, and B. T. Marshall. On the verification of the quality of SABER temperature, geopotential height, and wind fields by comparison with Met Office assimilated analyses. *Journal of Geophysical Research - Atmospheres*, 108(D20):4628, 2003. doi: 10.1029/2003JD003720.

E. Remsberg, B. T. Marshall, M. Garcia-Comas, D. Krueger, G. S. Lingenfelser, J. Martin-Torres, M. G. Mlynczak, J. M. Russell III, A. K. Smith, Y. Zhao, C. Brown, L. L. Gordley, M. J. Lopez-Gonzalez, M. Lopez-Puertas, C.-Y. She, M. J. Taylor, and R. E. Thompson. Assessment of the quality of the Version 1.07 temperature-versus-pressure profiles of the middle atmosphere from TIMED/SABER. *Journal of Geophysical Research - Atmospheres*, 113(D17): D17101, 2008. doi: 10.1029/2008JD010013.

M. M. Rienecker, M. J. Suarez, R. Todling, J. Bacmeister, L. Takacs, H.-C Liu, W. Gu, M. Sienkiewicz, R. D. Koster, R. Gelaro, I. Stajner, and J. E. Nielsen. The GEOS-5 Data Assimilation System - Documentation of Versions 5.0.1, 5.1.0, and 5.2.0. Technical report, NASA, 2008. NASA/TM-2008-104606, Technical Report Series on Global Modeling and Data Assimilation, Volume 27.

M. M. Rienecker, M. J. Suarez, R. Gelaro, R. Todling, J. Bacmeister, E. Liu, M. G. Bosilovich, S. D. Schubert, L. Takacs, G. K. Kim, S. Bloom, J. Y. Chen, D. Collins, A. Conaty, A. Da Silva, W. Gu, J. Joiner, R. D. Koster, R. Lucchesi, A. Molod, T. Owens, S. Pawson, P. Pegion, C. R. Redder, R. Reichle, F. R. Robertson, A. G. Ruddick, M. Sienkiewicz, and J. Woolen. MERRA: NASA's Modern-Era Retrospective Analysis for Research and Applications. *Journal of Climate*, 24(14):3624–3648, 2011. doi: 10.1175/JCLI-D-11-00015.1.

C. P. Rinsland, M. R. Gunson, R. J. Salawitch, H. A. Michelsen, R. Zander, M. J. Newchurch, M. M. Abbas, M. C. Abrams, G. L. Manney, A. Y. Chang,

F. W. Irion, A. Goldman, and E. Mahieu. ATMOS/ATLAS-3 measurements of stratospheric chlorine and reactive nitrogen partitioning inside and outside the November 1994 Antarctic vortex. *Geophysical Research Letters*, 23(17): 2365–2368, 1996.

C. P. Rinsland, C. Boone, R. Nassar, K. Walker, P. Bernath, J. C. McConnell, and L. Chiou. Atmospheric Chemistry Experiment (ACE) Arctic stratospheric measurements of NO_x during February and March 2004: Impact of intense solar flares. *Geophysical Research Letters*, 32(16):L16S05, 2005. doi: 10.1029/2005GL022425.

H. K. Roscoe, W. Feng, M. P. Chipperfield, M. Trainic, and E. F. Shuckburgh. The existence of the edge region of the Antarctic stratospheric vortex. *Journal of Geophysical Research - Atmospheres*, 117:D04301, 2012. doi: 10.1029/2011JD015940.

J. E. Rosenfield, P. A. Newman, and M. R. Schoeberl. Computations of diabatic descent in the stratospheric polar vortex. *Journal of Geophysical Research - Atmospheres*, 99(D8):16677–16689, 1994. doi: 10.1029/94JD01156.

P. J. Rousseeuw. Silhouettes: a graphical aid to the interpretation and validation of cluster analysis. *Journal of Computational and Applied Mathematics*, 20: 53–65, 1987. doi: 10.1016/0377-0427(87)90125-7.

A. Ruiz-Herrera. Some examples related to the method of Lagrangian descriptors. *Chaos*, 25(6):063112, 2015. doi: 10.1063/1.4922182.

D. W. Rusch, J.-C. Gerard, S. Solomon, P. J. Crutzen, and G. C. Reid. The effect of particle precipitation events on the neutral and ion chemistry of the middle atmosphere - I. Odd nitrogen. *Planetary Space Science*, 29(7):767–774, 1981.

J. M. Russell, III, S. Solomon, L. L. Gordley, E. E. Remsberg, and L. B. Callis. The variability of stratospheric and mesospheric NO_2 in the polar winter night observed by LIMS. *Journal of Geophysical Research*, 89(D5):7267–7275, 1984.

J. M. Russell, III, A. F. Tuck, L. L. Gordley, J. H. Park, S. R. Drayson, J. E. Harries, R. J. Cicerone, and P. J. Crutzen. HALOE Antarctic observations in the spring of 1991. *Geophysical Research Letters*, 20(8):719–722, 1993. doi: 10.1029/93GL00497.

S. Saha, S. Moorthi, H-L. Pan, X. Wu, J. Wang, S. Nadiga, P. Tripp, R. Kistler, J. Woolen, D. Behringer, H. Lu, D. Stokes, R. Grumbine, G. Gayno, J. Wang, Y-T. Hou, H-Y. Chuang, H-M. H. Juang, J. Sela, M. Iredell, R. Treadon, D. Kleist, P. van Delst, D. Keyder, J. Derber, M. Ek, J. Meng, H. Wei, R. Yang, S. Lord, H. van den Dool, A. Kumar, W. Wang, C. Long, M. Chelliah, Y. Xue, B. Huang, J-K. Schemm, W. Ebisuzaki, R. Lin, P. Xie, M. Chen, S. Zhou, W. Higgins, C-Z. Zou, Q. Liu, Y. Chen, Y. Han, L. Cucurull, R. W. Reynolds, G. Rutledge, and M. Goldberg. The NCEP Forecast System Reanalysis. *Bulletin of the American Meteorological Society*, 91(8):1015–1057, 2010.

S. Saha, S. Moorthi, X. Wu, J. Wang, S. Nadiga, P. Tripp, D. Behringer, Y-T. Hou, H-Y. Chuang, M. Iredell, M. Ek, J. Meng, R. Yang, M. Peña Mendez, H. van den Dool, Q. Zhang, W. Wang, M. Chen, and E. Becker. The NCEP Climate Forecast System Version 2. *Bulletin of the American Meteorological Society*, 91(8):1015–1057, 2014.

D. Scheiben, C. Straub, K. Hocke, P. Forkman, and N. Kämpfer. Observations of middle atmospheric H_2O and O_3 during the 2010 major sudden stratospheric warming by a network of microwave radiometers. *Atmospheric Chemistry and Physics*, 12(16):7753–7765, 2012. doi: 10.5194/acp-12-7753-2012.

M. R. Schoeberl, S. R. Kawa, A. R. Douglass, T. J. McGee, E. V. Browell, J. Waters, N. Livesey, W. Read, L. Froidvaux, H. C. Pumphrey, L. R. Lait, and L. Twigg. Chemical observations of a polar vortex intrusion. *Journal of Geophysical Research - Atmospheres*, 111(D20):D20306, 2006. doi: 10.1029/2006JD007134.

M. J. Schwartz, A. Lambert, G. L. Manney, W. G. Read, N. J. Livesey, L. Waters, N. Livesey, W. Read, L. Froidevaux, C. O. Ao, P. F. Bernath, C. D. Boone, R. E. Cofield, W. H. Daffer, B. J. Drouin, E. J. Fetzer, R. A. Fuller, R. F. Jarnot, J. H. Jiang, Y. B. Jiang, B. W. Knosp, K. Krüger, J.-L. F. Li, M. G. Mlynczak, S. Pawson, J. M. Russell III, M. L. Santee, W. V. Snyder, P. C. Stek, R. P. Thurstans, A. M. Tompkins, P. A. Wagner, K. A. Walker, J. W. Waters, and D. L. Wu. Validation of the Aura Microwave Limb Sounder temperature and geopotential height measurements. *Journal of Geophysical Research - Atmospheres*, 114(D15):D15S11, 2008. doi: 10.1029/2007JD008783.

A. Seppala, P. T. Verronen, E. Kyrola, S. Hassinen, L. Backman, A. Hauchecorne, J. L. Bertaux, and D. Fussen. Solar proton events of October November 2003:

Ozone depletion in the Northern Hemisphere polar winter as seen by GOMOS/Envisat. *Geophysical Research Letters*, 31:L19107, 2004.

W. J. M. Seviour, D. M. Mitchell, and L. J. Gray. A practical method to identify displaced and split stratospheric polar vortex events. *Geophysical Research Letters*, 40(19):5268–5273, 2013. doi: 10.1002/grl.50927.

P. E. Sheese, K. A. Walker, C. D. Boone, P. F. Bernath, and B. Funke. Nitrous oxide in the atmosphere: First measurements of a lower thermospheric source. *Geophysical Research Letters*, 43(6):2866–2872, 2016. doi: 10.1002/2015GL067353.

T. G. Shepherd. The middle atmosphere. *Journal of Atmospheric and Solar-Terrestrial Physics*, 62(17-18):1587–1601, 2000. doi: 10.1016/S1364-6826(00)00114-0.

T. G. Shepherd. Large-Scale Atmospheric Dynamics for Atmospheric Chemists. *Chemical Reviews*, 103(12):4509–4531, 2003. doi: 10.1021/cr020511z.

R. J. Sica, M. R. M. Izawa, K. A. Walker, C. Boone, S. V. Petelina, P. S. Argall, P. Bernath, G. B. Burns, V. Catoire, R. L. Collins, W. H. Daffer, C. De Clerc, Z. Y. Fan, B. J. Firanski, W. J. R. French, P. Gerard, M. Gerding, J. Granville, J. L. Innis, P. Keckhut, T. Kerzenmacher, A. R. Klekociuk, E. Kyrö, J. C. Lambert, E. J. Llewellyn, G. L. Manney, I. S. McDermid, K. Mizutani, Y. Murayama, C. Piccolo, P. Raspollini, M. Ridolfi, C. Robert, W. Steinbrecht, K. Strong, R. Stübi, and B. Thurairajah. Validation of the Atmospheric Chemistry Experiment (ACE) version 2.2 temperature using ground-based and space-borne measurements. *Atmospheric Chemistry and Physics*, 8 (1):35–62, 2008.

T. G. Sigmond, J. F. Scinnocca, V. V. Kharin, and T. G. Shepherd. The middle atmosphere. *Nature Geoscience*, 6(2):98–102, 2013. doi: 10.1038/NGEO1698.

A. Simmons, M. Hortal, G. Kelly, A. McNally, A. Untch, and S. Uppala. ECMWF Analyses and Forecasts of Stratospheric Winter Polar Vortex Breakup: September 2002 in the Southern Hemisphere and Related Events. *Journal of the Atmospheric Sciences*, 62(3):668–689, 2004. doi: 10.1175/JAS-3322.1.

M. Sinnhuber, H. Nieder, and N. Wieters. Energetic Particle Precipitation and the Chemistry of the Mesosphere/Lower Thermosphere. *Surveys in Geophysics*, 33(6):1281–1334, 2012. doi: 10.1007/s10712-012-9201-3.

D. E. Siskind, G. E. Nedoluha, J. M. Russell, C. E. Randall, M. Fromm, and J. M. Russell III. An assessment of Southern Hemisphere stratospheric NO_x enhancements due to transport from the upper atmosphere. *Geophysical Research Letters*, 27(3):329–332, 2000.

D. E. Siskind, S. D. Eckermann, L. Coy, J. P. McCormack, and C. E. Randall. On recent interannual variability of the Arctic winter mesosphere: Implications for tracer descent. *Geophysical Research Letters*, 34(9):L09806, 2007. doi: 10.1029/2007GL029293.

A. K. Smith. Interactions Between the Lower, Middle and Upper Atmosphere. *Space Science Reviews*, 168(1-4):1–21, 2012. doi: 10.1007/s11214-011-9791-y.

M. L. Smith and A. J. McDonald. A quantitative measure of polar vortex strength using the function M. *Journal of Geophysical Research - Atmospheres*, 119(10): 5966–5985, 2014. doi: 10.1002/2013JD020572. To view the published open abstract, go to http://dx.doi.org and enter the DOI.

S. Solomon. Stratospheric ozone depletion: a review of concepts and history. *Reviews of Geophysics*, 37(3):275–316, 2010. doi: 10.1029/1999RG900008.

S. Solomon, P. J. Crutzen, and R. M. Roble. Photochemical coupling between the thermosphere and the lower atmosphere: 1. Odd nitrogen from 50 to 120 km. *Journal of Geophysical Research*, 87(C9):7206–7220, 1982.

L. C. Sparling. Statistical perspectives on stratospheric transport. *Reviews of Geophysics*, 38(3):417–436, 2000. doi: 10.1029/1999RG000070.

H-M. Steinhorst, P. Konopka, G. Günther, and R. Müller. How permeable is the edge of the Arctic vortex: Model studies of winter 1999-2000. *Journal of Geophysical Research - Atmospheres*, 110(D6):D06105, 2005. doi: 10.1029/2004JD005268.

C. Straub, B. Tschanz, K. Hocke, N. Kampfer, and A. K. Smith. Transport of mesospheric H_2O during and after the stratospheric sudden warming of January 2010: observation and simulation. *Atmospheric Chemistry and Physics*, 12(12): 5413–5427, 2012. doi: 10.5194/acp-12-5413-2012.

R. T. Sutton, H. Maclean, R. Swinbank, A. O'Neill, and F. W. Taylor. High-Resolution Stratospheric Tracer Fields Estimated from Satellite Observations Using Lagrangian Trajectory Calculations. *Journal of*

the Atmospheric Sciences, 51(20):2995–3005, 1994. doi: 10.1175/1520-0469(1994)051¡2995:HRSTFE¿2.0.CO;2.

S. Tegtmeier, K. Krüger, I. Wohltmann, K. Schoellhammer, and M. Rex. Variations of the residual circulation in the Northern Hemispheric winter. *Journal of Geophysical Research - Atmospheres*, 113(D16):D16109, 2008. doi: 10.1029/2007JD009518.

R. M. Thorne. The importance of energetic particle precipitation on the chemical composition of the middle atmosphere. *Pure Applied Geophysics*, 118:129–151, 1980. doi: 10.1007/BF01586448.

S. M. Uppala, P. W. Kållberg, A. J. Simmons, U. Andrae, V. da Costa Bechtold, M. Fiorino, J. K. Gibson, J. Haseler, A. Hernandez, G. A. Kelly, X. Li, K. Onogi, S. Saarinen, N. Sokka, R. P. Allan, E. Andersson, K. Arpe, M. A. Balmaseda, A. C. M. Beljaars, L. van de Berg, J. Bidlot, N. Bormann, S. Caires, F. Chevallier, A. Dethof, M. Dragosavac, M. Fisher, M. Fuentes, S. Hagemann, E. Hólm, B. J. Hoskins, L. Isaksen, P. A. E. M. Janssen, R. Jenne, A. P. McNally, J.-F. Mahfouf, J.-J. Morcrette, N. A. Rayner, R. W. Saunders, P. Simon, A. Sterl, K. E. Trenberth, A. Untch, D. Vasiljevic, P. Viterbo, and J. Woolen. The ERA-40 re-analysis. *Quarterly Journal of the Royal Meteorological Society*, 131(612):2961–3012, 2005. doi: 10.1256/qj.04.176.

C. Varotsos. The Southern Hemisphere Ozone Hole Split in 2002. *Environmental Science and Pollution Research*, 9(6):375–376, 2002. doi: 10.1007/BF02987584.

J. W. Waters, L. Froidevaux, R. S. Harwood, R. F. Jarnot, H. M. Pickett, W. G. Read, P. Siegel, R. E. Cofield, M. J. Filipiak, D. A. Flower, J. R. Holden, G. K. Lau, N. J. Livesey, G. L. Manney, H. C. Pumphrey, M. L. Santee, D. L. Wu, D. T. Cuddy, R. R. Lay, M. S. Loo, V. S. Perun, M. J. Schwartz, P. C. Stek, R. P. Thurstans, M. A. Boyles, K. M. Chandra, M. C. Chavez, G-S. Chen, B. V. Chudasama, R. Dodge, R. A. Fuller, M. A Girard, J. H. Jiang, Y. Jiang, B. W. Knosp, R. C. LaBelle, J. C. Lam, K. A. Lee, D. Miller, J. E. Oswald, N. C. Patel, D. M. Pukala, O. Quintero, D. M. Scaff, W. Van Snyder, M. C. Tope, P. A. Wagner, and M. J. Walch. The Earth Observing System Microwave Limb Sounder (EOS MLS) on the Aura satellite. *Quarterly Journal of the Royal Meteorological Society*, 44(5):1075–1092, 2006. doi: 10.1109/TGRS.2006.873771.

D. W. Waugh. Elliptical diagnostics of stratospheric polar vortices. *Quarterly*

Journal of the Royal Meteorological Society, 123(542):1725–1748, 1997. doi: 10.1002/qj.49712354213.

D. W. Waugh and R. A. Plumb. Contour Advection with Surgery: A Technique for Investigating Finescale Structure in Tracer Transport. *Journal of the Atmospheric Sciences*, 51(4):530–540, 1994. doi: 10.1175/1520-0469(1994)051<0530:CAWSAT>2.0.CO;2.

D. W. Waugh and L. M. Polvani. Stratospheric Polar Vortices. In L. M. Polvani, A. H. Sobel, and D. W. Waugh, editors, *The Stratosphere: Dynamics, Transport, and Chemistry*. American Geophysical Union, Washington, D. C., 2010. doi: 10.1002/9781118666630.ch3.

D. W. Waugh and W. J. Randel. Climatology of Arctic and Antarctic Polar Vortices Using Elliptical Diagnostics. *Journal of the Atmospheric Sciences*, 56(11): 1594–1613, 1999. doi: 10.1175/1520-0469(1999)056¡1594:COAAAP¿2.0.CO;2.

D. W. Waugh, R. A. Plumb, R. J. Atkinson, M. R. Schoeberl, L. R. Lait, P. A. Newman, M. Loewenstein, D. W. Toohey, L. M. Avallone, C. R. Webster, and R. D. May. Transport out of the lower stratospheric Arctic vortex by Rossby-wave breaking. *Journal of Geophysical Research - Atmospheres*, 99 (D1):1071–1088, 1994. doi: 10.1029/93JD02556.

D. W. Waugh, R. A. Plumb, J. W. Elkins, D. W. Fahey, K. A. Boering, , G. S. Dutton, C. M. Volk, E. Keim, R.-S. Gao, B. C. Daube, S. C. Wofsy, M. Loewenstein, J. R. Podolske, K. R. Chan, M. H. Profitt, K. K. Kelly, P. A. Newman, and L. R. Lait. Mixing of polar vortex air into middle latitudes as revealed by tracer-tracer scatterplots. *Journal of Geophysical Research - Atmospheres*, 102 (11D):13119–13134, 1997. doi: 10.1029/96JD03715.

S. Wiggins and A. M. Mancho. Barriers to transport in aperiodically time-dependent two-dimensional velocity fields: Nekhoroshev's theorem and "Nearly Invariant" tori. *Nonlinear Processes in Geophysics*, 21(1):165–185, 2014. doi: 10.5194/npg-21-165-2014.

D. L. Wu, M. J. Schwartz, J. W. Waters, V. Limpusavan, Q. Wu, and T. L. Killeen. Mesospheric doppler wind measurements from Aura Microwave Limb Sounder. *Advances in Space Research*, 42(7):1246–1252, 2008. doi: 10.1016/j.asr.2007.06.014.